SAINT PETERSBURG STATE UNIVERSITY

Sofya Vladimirovna Demina

NOVEL SOLID SOLUTIONS BASED ON Ba-CONTAINING BORATES Bi and Y: THERMAL BEHAVIOR, CRYSTAL STRUCTURE AND PHOTOLUMINESCENCE

Scientific specialty 1.6.4. Mineralogy, Crystallography.
Geochemistry, geochemical methods of mineral exploration

DISSERTATION
submitted for the degree of
Candidate of Chemical Sciences

Translation from Russian

Scientific supervisor:
Doctor of Geological and Mineralogical Sciences,
Prof. S.K. Filatov

Saint Petersburg
2024

Table of contents

Introduction 6
Chapter 1. Crystal chemistry of borates in the BaO–M_2O_3–B_2O_3 (M = Y, Eu^{3+}, Bi^{3+}) systems ...16
1.1 General features of borate crystal chemistry 16
1.2 Classification of borates.....16
1.3 Main boron-oxygen groups.....17
1.4 Thermal expansion of borates with isolated triangular BO_3 radicals and triborate B_3O_6 groups 18
1.5 Basic principles of high-temperature crystal chemistry of borates.....18
1.6 Borates in nature 19
1.6.1 Alkaline earth metal borates.....20
1.6.2 Rare earth borates.....22
1.7 Borates in the BaO– Bi_2O_3–B_2O_3 system 23
1.7.1 Synthetic borates in the BaO– Bi_2O_3–B_2O_3 system 23
1.7.2 Borates of the $ABi_2B_2O_7$ (A = Ca, Sr, Ba) family 26
1.7.3 Behavior of borates in the $ABi_2B_2O_7$ (A = Ca, Sr, Ba) family at high temperatures 31
1.7.4 Luminescent properties of borates of the $ABi_2B_2O_7$ (A = Ca, Sr, Ba) family, activated by REE^{3+} ions.....33
1.8 Borates in the BaO–M_2O_3–B_2O_3 (M = Y, Eu) systems.....34
1.8.1 Synthetic borates of the BaO–M_2O_3–B_2O_3 (M = Y, Eu) systems 34
1.8.2 Borates of the $A_3M_2(BO_3)_4$ (A = Ca, Sr, Ba, M = *REE*, Bi^{3+}) family 37
1.8.3 Thermal expansion of borates of the $A_3M_2(BO_3)_4$ (A = Ca, Sr, Ba, M = *REE*, Bi^{3+}) family 40
1.8.4 Luminescent properties of borates of the $A_3M_2(BO_3)_4$ (A = Ca, Sr, Ba, M = *REE*, Bi^{3+}) family 43
1.8.5 Natural and synthetic compounds isostructural to $A_3M_2(BO_3)_4$ (A = Ca, Sr, Ba, M = *REE*, Bi^{3+}) borates.....44
1.9 Conclusion to the chapter 1 46

Chapter 2. Experimental part and research methodology.....48
2.1 Synthesis Methods.....48
2.1.1 Crystallization from Glass-Ceramics.....50
2.1.2 Obtaining Poly- and Monocrystals from Melt.....51
2.2 Investigation Methods.....51
2.2.1 X-ray Diffraction Methods.....51
2.2.1.1 X-ray Powder diffraction (XRD).....51
2.2.1.2 Single crystal X-ray diffraction.....52
2.2.1.3 High-temperature powder X-ray diffraction.....53
2.2.2 Thermal Analysis: Thermogravimetry (TG) and Differential Scanning Calorimetry (DSC).....54
2.2.3 Spectroscopic Methods.....54
2.2.3.1 Light Scattering Spectroscopy (LSS).....54
2.2.3.2 Infrared Spectroscopy (IR Spectroscopy).....54
2.2.3.3 Luminescent Spectroscopy.....54
Chapter 3. The $BaBi_2B_2O_7$ borates, activated and co-activated by REE^{3+} Ions. Results and Discussion.....56
3.1 The BaBi2−xEuxB2O7 (x = 0.05, 0.1, 0.15, 0.2, 0.3, 0.4, 0.5) borates.....56
3.1.1 Results of Powder X-ray Diffraction of Borates BaBi2−xEuxB2O7.....56
3.1.2 Results of refinement of crystal structures of the $BaBi_{2-x}Eu_xB_2O_7$ (x = 0.1, 0.2, 0.4) borates.....58
3.1.3 Distribution of Eu^{3+} cations over *M*1, *M*2, *M*3 sites.....62
3.1.4 Results of light scattering spectroscopy of $BaBi_{2-x}Eu_xB_2O_7$ borates.....63
3.1.5 Results of luminescent spectroscopy of $BaBi_{2-x}Eu_xB_2O_7$ borates.....63
3.2 The $BaBi_{2-x}Sm_xB_2O_7$ (x = 0.05, 0.1, 0.15, 0.2, 0.3, 0.4, 0.5) borates.....66
3.2.1 Results of powder X-ray diffraction of $BaBi_{2-x}Sm_xB_2O_7$ borates.....66
3.2.2 Results of refinement of crystal structures of $BaBi_{2-x}Sm_xB_2O_7$ (x = 0.05, 0.3) borates.....68
3.2.3 Distribution of Sm^{3+} cations over *M*1, *M*2, *M*3 sites.....70

3.2.4 Results of High-temperature powder X-ray diffraction of $BaBi_{1.7}Sm_{0.3}B_2O_7$ borate 70

3.2.5 Results of thermal analysis of $BaBi_{1.7}Sm_{0.3}B_2O_7$ borate 74

3.2.6 Results of luminescent spectroscopy of $BaBi_{2-x}Sm_xB_2O_7$ borates.....75

3.3 The $BaBi_{2-x-0.05}Eu_xSm_{0.05}B_2O_7$ (x = 0.35, 0.4, 0.45) borates.....77

3.3.1 Results of powder X-ray diffraction of the $BaBi_{2-x-0.05}Eu_xSm_{0.05}B_2O_7$ borates77

3.3.2 Results of luminescent spectroscopy of $BaBi_{2-x-0.05}Eu_xSm_{0.05}B_2O_7$ borates ...78

3.4 The $BaBi_{2-0.15-y}Eu_{0.15}Sm_yB_2O_7$ (y = 0.05, 0.1, 0.15, 0.2, 0.3) borates.....79

3.4.1 Results of powder X-ray diffraction of $BaBi_{2-0.15-y}Eu_{0.15}Sm_yB_2O_7$ borates 79

3.4.2 Results of luminescent spectroscopy of $BaBi_{2-0.15-y}Eu_{0.15}Sm_yB_2O_7$ borates ...81

3.5 The $BaBi_{2-x}Tb_xB_2O_7$ (x = 0.05, 0.1, 0.15, 0.2, 0.3, 0.4, 0.5) borates.....84

3.5.1 Results of powder X-ray diffraction of the$BaBi_{2-x}Tb_xB_2O_7$ borates.....84

3.5.2 Results of refinement of crystal structures of the $BaBi_{2-x}Tb_xB_2O_7$ (x = 0.1, 0.3, 0.4) borates 86

3.5.3 Distribution of Tb^{3+} cations over *M*1, *M*2, *M*3 sites 88

3.5.4 Results of luminescent spectroscopy of the $BaBi_{2-x}Tb_xB_2O_7$ borates.....89

3.6 The $BaBi_{2-x-0.3}Eu_xTb_{0.15}Tm_{0.15}B_2O_7$ (x = 0.05, 0.1, 0.15, 0.2) borates.....91

3.6.1 Results of powder X-ray diffraction of the $BaBi_{2-x-0.3}Eu_xTb_{0.15}Tm_{0.15}B_2O_7$ borates 91

3.6.2 Results of luminescent spectroscopy of the $BaBi_{2-x-0.3}Eu_xTb_{0.15}Tm_{0.15}B_2O_7$ borates 92

3.7 Results and discussion 94

3.7.1 Areas of continuous solid solutions existence $BaBi_{2-x-y-z}REE_{x,x,z}B_2O_7$ (*REE* = Eu^{3+}, Sm^{3+}, Tb^{3+}, Tm^{3+}).....94

3.7.2 Analysis of the occupancies of crystallographic sites of the $BaBi_{2-x}REE_xB_2O_7$ (*REE* = Eu^{3+}, Sm^{3+}, Tb^{3+}) borates.....96

3.7.3 Chemical deformations in the $BaBi_{2-x}REE_xB_2O_7$ (*REE* = Eu^{3+}, Sm^{3+}, Tb^{3+}) borates 97

3.8 Conclusion for the section 3 99

Chapter 4. The $Ba_3Eu_2(BO_3)_4$ and $Ba_3Y_{2-x}Er_x(BO_3)_4$ borates. Results and discussion.....101

4.1 Results of powder X-ray diffraction of the $Ba_3Eu_2(BO_3)_4$ and $Ba_3Y_{2-x}Er_x(BO_3)_4$ borates 101

4.2 Results of refinement of the crystal structure of the $Ba_3Y_2(BO_3)_4$ borate 102

4.3 Results of High-temperature powder X-ray diffraction of the $Ba_3Eu_2(BO_3)_4$ and $Ba_3Y_2(BO_3)_4$ borates.....105

4.4 Results of refinement of the crystal structure of the $Ba_3Y_2(BO_3)_4$ borate at high temperatures using the Rietveld method 109

4.5 Results of Raman spectroscopy of and infrared spectroscopy of the $Ba_3Y_{2-x}Er_x(BO_3)_4$ borates.....110

4.6 Results of luminescent spectroscopy of the $Ba_3Y_{2-x}Er_x(BO_3)_4$ borates.....111

4.7 Results of thermoluminescent spectroscopy of the $Ba_3Y_{2-x}Er_x(BO_3)_4$ borates..113

4.8 Results and discussion 114

4.8.1 Crystal structures of the $A_3M_2(BO_3)_4$ borates at room temperature 114

4.8.2 Crystal structures of the $A_3M_2(BO_3)_4$ borates at high temperatures.....117

4.9 Conclusion for the chapter 4.....123

Conclusion.....125

List of abbreviations and symbols.....128

References 129

Other publications with the main scientific results of the dissertation.....139

Supplementary materials 143

Introduction

The relevance of the topic at hand lies in the development of new materials based on known inorganic compounds with beneficial properties, essential for the advancement of various industrial sectors. These new materials have the potential to exhibit enhanced characteristics compared to existing analogues, fostering the development of innovative technologies such as cutting-edge electronics, energy storage systems, and environmental remediation solutions. The continuous exploration and research of new inorganic materials stimulate progress, enhance material durability, and meet the growing societal needs. Material properties can often be altered or modified by substituting one chemical element for another, highlighting the importance of understanding the "composition-structure-properties" relationship of materials.

The development of new phosphors – an important component of LEDs – holds significant scientific and industrial potential. As technology advances and scientific progress accelerates, there is a constant need to improve the characteristics and properties of luminescent materials, such as increasing efficiency and intensity of luminescence, color rendering, and enhancing chemical, mechanical, and thermal stability. In terms of sustainable resource management, it is noteworthy that LED technology is characterized by low energy consumption, rapidly replacing traditional lighting sources. According to the International Energy Agency (iea.org), lighting accounts for 19% of global electricity consumption. The implementation of modern lighting technologies could reduce electricity consumption by 40%, leading to an annual savings of approximately 106 billion euros worldwide. From an environmental perspective, this translates to a reduction of carbon dioxide emissions by 555 million tons per year, saving 2 terawatt-hours of electricity annually, and conserving 1.5 billion barrels of oil.

White light-emitting diodes (w-LEDs) possess such virtues as compactness, durability, high luminous intensity, excellent color rendition, and the ability for color-tuning. However, many commercial phosphors have several serious drawbacks: "atypical" emission wavelengths not perceived by the human eye, sensitivity to changing environmental factors such as temperature and humidity, as well as the high toxicity of raw materials and synthesis conditions, including their costliness (obtaining certain commercial phosphors requires the application of heat and pressure to the raw components). The most well-known commercial phosphors include: red-emitting yttrium aluminum garnet (YAG) (Juansheng, 2004), widely used in lighting and displays, strontium aluminate $SrAl_2O_4$:Eu (Li et al., 2008), known for its long-lasting phosphorescent glow, and green-emitting zinc sulfide ZnS (Reddy, Northrop, 2000), used in some lighting sources. All mentioned commercial phosphors have limitations in color rendition and energy transfer efficiency. The advantages of borates, as promising matrices for photoluminophores, include: good

chemical, thermal, and mechanical stability, cost-effectiveness of their synthesis (often requiring only heat treatment of raw materials), transparency in UV and visible ranges, good polarizability, high optical damage threshold, high luminescence efficiency when activated by rare earth ions, as well as crystallographic diversity, stemming from the multitude of possible combinations of various boron-oxygen groups (Chen, Li, 1988; Schubert, 2003; Xia, Liu, 2016a; Zhang, Chen, Bai, 2013). The extensive structural diversity of borates allows for their application as functional materials in various industrial sectors: modern optoelectronic systems and devices (Konidakis et al., 2022), nonlinear optical materials (Mutailipu et al., 2019b; Sasaki et al., 2000), laser "host materials" (Kumar et al., 2013), matrices for phosphors (Lin, Liu, 2011; Ye et al., 2010), flame retardants (Shen et al., 2008), detergents (Yu, Zhao, Bayly, 2008), and others.

Due to their long service life and excellent optical characteristics, borate materials activated by rare-earth ions are used as traditional light sources, in currency marking, in the field of forensics and customs control, in lasers, scintillators for radiation detectors, and in other applications.

It is known that phosphors suitable for use in LEDs must possess a number of characteristics: 1) High absorption when excited by near UV (360-420 nm) or blue light (420-480 nm); 2) Luminescence efficiency and high quantum yield; 3) High resistance to atmospheric conditions, carbon dioxide, chemicals, and moisture; 4) Relatively simple synthesis conditions, including easy control of particle morphology, low toxicity, and energy consumption during synthesis (Xia, Liu, 2016).

Additionally, an important property of a phosphor is thermal stability, as prospective white LED devices (w-LED) can reach temperatures exceeding 150 °C due to the thermal effect from the *p-n* junction. Most materials with thermal stability require high nitrogen pressure in the atmosphere and high synthesis temperatures, leading to high production costs. When using materials in variable temperature conditions, controlling their thermal expansion is necessary in many modern industrial technologies, as even a slight temperature change significantly degrades the characteristics of high-precision devices and products.

Therefore, the search for new phosphors among borates activated by rare-earth ions and the study of the "composition-structure-properties" relationships is a current task.

In the present study, **the focus of research** is on the novel obtained $BaBi_{2-x}Eu_xB_2O_7$, $BaBi_{2-x}Sm_xB_2O_7$, $BaBi_{2-x}Tb_xB_2O_7$, $BaBi_{2-x-0.05}Eu_xSm_{0.05}B_2O_7$, $BaBi_{2-0.15-y}Eu_{0.15}Sm_yB_2O_7$, $BaBi_{2-x-0.3}Eu_xTb_{0.15}Tm_{0.15}B_2O_7$, $Ba_3Y_{2-x}Er_x(BO_3)_4$ series of solid solutions, as well as known $Ba_3M_2(BO_3)_4$ (M = Y, Eu^{3+}) borates.

The aim of the study is the synthesis, investigation of the crystalline structure and thermal expansion of borates in the $BaO–M_2O_3–B_2O_3$ (M = Y, Eu^{3+}, Bi^{3+}) systems, as well as the luminescent properties of these borates activated by rare earth ions.

The main objectives are as follows: **1.** Synthesis of new $Ba_3Y_{2-x}Er_x(BO_3)_4$, $BaBi_{2-x}Eu_xB_2O_7$, $BaBi_{2-x}Sm_xB_2O_7$, $BaBi_{2-x}Tb_xB_2O_7$, $BaBi_{2-x-0.05}Eu_xSm_{0.05}B_2O_7$ (x = 0.35, 0.4), $BaBi_{2-0.15-y}Eu_{0.15}Sm_yB_2O_7$ (y = 0.05—0.2), $BaBi_{2-x-0.3}Eu_xTb_{0.15}Tm_{0.15}B_2O_7$ (x = 0.05—0.2) series of solid solutions, conducting powder X-ray diffraction, refining parameters of the unit cell, determining regions of continuous solid solutions. **2**. Study of the thermal expansion of $Ba_3Eu_2(BO_3)_4$, $Ba_3Y_2(BO_3)_4$, $BaBi_{1.7}Sm_{0.3}B_2O_7$ borates (analysis of temperature dependence graphs of unit cell parameters, calculation of thermal expansion coefficients) using High-temperature powder X-ray diffraction. **3.** Determination of melting and crystallization temperatures of $BaBi_{1.7}Sm_{0.3}B_2O_7$ borate based on thermal analysis data. **4.** Refinement of crystal structures and cation distribution over sites using single-crystal X-ray diffraction data ($Ba_3Y_2(BO_3)_4$, $BaBi_{2-x}Eu_xB_2O_7$ (x = 0.10, 0.20, 0.40), $BaBi_{2-x}Sm_xB_2O_7$ (x = 0.05, 0.3), $BaBi_{2-x}Tb_xB_2O_7$ (x = 0.10, 0.30, 0.40)) and HT-XRD data at different temperatures ($Ba_3Y_2(BO_3)_4$). **5.** Investigation of luminescent properties of $Ba_3Y_{2-x}Er_x(BO_3)_4$, $BaBi_{2-x}Eu_xB_2O_7$, $BaBi_{2-x}Sm_xB_2O_7$, $BaBi_{2-x}Tb_xB_2O_7$, $BaBi_{2-x-0.05}Eu_xSm_{0.05}B_2O_7$, $BaBi_{2-0.15-y}Eu_{0.15}Sm_yB_2O_7$, $BaBi_{2-x-0.3}Eu_xTb_{0.15}Tm_{0.15}B_2O_7$ solid solution series and thermoluminescent properties of $Ba_3Y_{2-x}Er_x(BO_3)_4$. **6.** Measurement of vibrational spectra of $Ba_3Y_{2-x}Er_x(BO_3)_4$ and $BaBi_{2-x}Eu_xB_2O_7$ borates using light scattering spectroscopy (LSS) and infrared spectroscopy (IR spectroscopy).

Methods of synthesis and research. To conduct a comprehensive analysis of the studied photoluminophores based on borate matrices, experimental research methods were used to identify the influence of chemical composition and crystalline structure on thermal expansion and luminescent properties. **1.** Borate synthesis was carried out using crystallization methods from melt and glass-ceramics. The synthesis was conducted at the branch of the National Research Center "Kurchatov Institute" - Petersburg Institute of Nuclear Physics - I.V. Grebenshchikov Institute of Silicate Chemistry (branch of the National Research Center KI - PINP - ISC). **2.** Phase composition determination, refinement of unit cell parameters of 42 crystalline phases and solid solutions were performed using powder X-ray diffraction on the Rigaku MiniFlex II diffractometer (St. Petersburg State University research park "Centre for X-ray Diffraction Studies" – "Centre XRD"). **3.** The crystal structure of $Ba_3Y_2(BO_3)_4$ borate at room temperature was refined using single crystal data obtained with the Bruker Smart APEX II diffractometer (Mo Kα, branch of the National Research Center KI - PINP - ISC), and over a wide temperature range using powder data with the Rigaku Ultima IV diffractometer with a thermal attachment ("Centre XRD"). Arrays of experimental data for refining the crystal structures of $BaBi_{2-x}Eu_xB_2O_7$ (x = 0.10, 0.20, 0.40), $BaBi_{2-x}Sm_xB_2O_7$ (x = 0.05, 0.30), $BaBi_{2-x}Tb_xB_2O_7$ (x = 0.10, 0.30, 0.40) borates were obtained on the Rigaku XtaLAB Synergy-S diffractometer (Mo Kα, "Centre XRD"). **4.** High-temperature X-

ray diffraction experiments were conducted to check for phase transitions, crystal structure deformations, and determine the thermal stability of materials using the Rigaku Ultima IV powder diffractometer with an SHT-1500 thermal attachment ("Centre XRD"). **5.** Refinement of crystal structures over a wide temperature range, determination of unit cell parameters, calculation of the principal values of the thermal expansion tensor, and visualization of characteristic tensor surfaces were carried out using the Rietveld To Tensor software package (Bubnova et al. 2018) at the branch of the National Research Center KI - PINP - ISC. **6.** Thermal analysis (DSC + TG), determination of melting and crystallization temperatures (endo- and exothermic effects) were performed on the STA 429 CD NETZSCH instrument (branch of the National Research Center KI - PINP - ISC). **7.** Fluorescence spectra, excitation spectra, kinetic curves, and luminescence kinetics were measured using the Fluorolog-3 spectrofluorimeter (Horiba Jobin Yvon) (St. Petersburg State University research park "OLMIV"). **8.** Raman scattering spectra were obtained using the Horiba LabRam spectrometer equipped with a confocal microscope ("OLMIV"). **9.** Infrared spectra were obtained using the Nicolet 8700 spectrometer (Thermo Scientific) ("OLMIV").

Scientific novelty.

1. For the first time, 6 series of solid solutions based on $BaBi_2B_2O_7$, activated and co-activated with rare earth elements (*REE* = Sm, Eu, Tb, Tm), were synthesized by crystallization from glass-ceramics: 32 new representatives; for all series, the existence limits of continuous solid solutions were established.

1.1. The crystal structures were refined based on single crystal data, including the distribution of cations on three non-equivalent sites, in $BaBi_{2-x}Eu_xB_2O_7$ (x = 0.1, 0.2, 0.4), $BaBi_{2-x}Sm_xB_2O_7$ (x = 0.05, 0.3), $BaBi_{2-x}Tb_xB_2O_7$ (x = 0.1, 0.3, 0.4) solid solutions, for $BaBi_{2-x}Eu_xB_2O_7$ structural data were confirmed by light scattering spectra.

1.2. The thermal properties of the borate $BaBi_{1.7}Sm_{0.3}B_2O_7$ were studied using high-temperature powder X-ray diffraction and thermal analysis (DSC+TG); the difference in the nature of thermal expansion upon activation of the $BaBi_2B_2O_7$ crystalline matrix with rare earth element atoms was analyzed, and the crystallization and melting temperatures were determined.

1.3. Based on the luminescence spectra of $BaBi_{2-x}Eu_xB_2O_7$, $BaBi_{2-x}Sm_xB_2O_7$, $BaBi_{2-x}Tb_xB_2O_7$, $BaBi_{2-x-0.05}Eu_xSm_{0.05}B_2O_7$, $BaBi_{2-0.15-y}Eu_{0.15}Sm_yB_2O_7$, $BaBi_{2-x-0.3}Eu_xTb_{0.15}Tm_{0.15}B_2O_7$ concentration series, it was established that the maximum optimal concentration of activator ions is achieved with the simultaneous entry of rare earth element ions into *M*1 and *M*2 sites; bright examples of this phenomenon are $BaBi_{2-x}Eu_xB_2O_7$ and $BaBi_{2-0.15-y}Eu_{0.15}Sm_yB_2O_7$ solid solutions.

2. A new series of solid solutions $Ba_3Y_{2-x}Er_x(BO_3)_4$ (x = 0.01—0.3) was obtained by crystallization from a melt.

2.1. The crystal structure of the $Ba_3Y_2(BO_3)_4$ borate was refined for the first time in an anisotropic approximation based on single crystal data. Based on the analysis of occupancies of crystallographic sites in the crystal structure of borates of the $A_3M_2(BO_3)_4$ (A = Ca, Sr, Ba, M = *Ln*, Y, Bi) family, a regularity of occupancy of sites with smaller polyhedral volume by atoms with smaller ionic radius was revealed, and a description of isomorphism schemes from the perspective of structural diversity factor was proposed.

2.2. The thermal expansion of $Ba_3Eu_2(BO_3)_4$ and $Ba_3Y_2(BO_3)_4$ borates was studied using high-temperature powder X-ray diffraction, bends were detected in the temperature dependencies of unit cell parameters. The crystal structure of $Ba_3Y_2(BO_3)_4$ was refined in the temperature range of 600—800 °C (40 points), including sites occupancies; it was established that the previously detected bends in the temperature dependencies of unit cell parameters for borates of the $A_3M_2(BO_3)_4$ family occur due to cation redistribution among sites with increasing temperature.

2.3. The vibrational spectra, luminescent, and thermoluminescent properties of the series of solid solutions $Ba_3Y_{2-x}Er_x(BO_3)_4$ were studied.

The reliability of the results and conclusions of this study is ensured by: **1.** The use of a combination of experimental research methods and conducting experiments using modern certified equipment. **2.** Consistency of research results obtained by different methods. **3.** High accuracy of the obtained data. **4.** Reproducibility of results. **5.** Discussion of the obtained results with leading specialists.

Practical significance. The borates investigated in this study, activated by rare earth ions, have the potential to be utilized as matrices for phosphors. The $Ba_3Y_{2-x}Er_x(BO_3)_4$ borates exhibit temperature-dependent luminescence and can be employed as luminescent thermometers. The $BaBi_{2-x}Eu_xB_2O_7$, $BaBi_{2-x}Sm_xB_2O_7$, $BaBi_{2-x}Tb_xB_2O_7$, $BaBi_{2-x-0.05}Eu_xSm_{0.05}B_2O_7$, $BaBi_{2-0.15-y}Eu_{0.15}Sm_yB_2O_7$, $BaBi_{2-x-0.3}Eu_xTb_{0.15}Tm_{0.15}B_2O_7$ borates represent promising matrices for white light-emitting diodes. Furthermore, the $BaBi_{2-x}Eu_xB_2O_7$, $BaBi_{2-0.15-y}Eu_{0.15}Sm_yB_2O_7$, and $BaBi_{2-x-0.3}Eu_xTb_{0.15}Tm_{0.15}B_2O_7$ solid solutions may find application in high-tech devices requiring precise color tuning, as the increase in Eu^{3+} ion concentration in these materials leads to color changes. The thermal stability of all synthesized phosphors is a key criterion in the industrial sector. Based on the investigation of the thermal expansion of various borates, it can be concluded that these borates are stable within the operational temperature range of high-precision devices.

Data on the thermal expansion of the studied borates have been deposited into the TensorBase database of thermal expansion coefficients, while data on the crystal structures have been stored in the ICSD database of crystal structures (2163168, 2163167, 2163169).

Validation of the study. The results of this research have been presented at various international and all-Russian conferences in the form of oral and poster presentations: XX International Conference on Crystal Chemistry, X-ray Diffraction, and Mineral Spectroscopy and VI International Conference on Organic Mineralogy (St. Petersburg, 2024), XIV All-Russian Scientific Conference "Minerals: Structure, Properties, Research Methods" with a youth school (Yekaterinburg, 2024), X All-Russian Conference (with international participation) "High-Temperature Chemistry of Oxide Systems and Materials" (St. Petersburg, 2023), International Scientific Student Conference "ISSC" (Novosibirsk, 2021, 2022, 2023, 2024), Geological International Student Summit "GISS" (St. Petersburg, 2022, 2023), Youth Scientific Conference of ISC RAS "Functional Materials: Synthesis, Properties, Application" (St. Petersburg, 2020, 2022, 2023), Youth International Scientific Conference "Modern Trends in the Development of Functional Materials" (Sochi, 2022, 2023), Scientific-Practical Conference "Rare Metals and Materials Based on Them: Technologies, Properties, and Applications" (Moscow, 2021), National Crystal Chemical Conference (2021, 2024), Conference and School for Young Scientists "Thermo X-ray Diffraction and X-ray Diffraction of Nanomaterials (TRRN-4)" (St. Petersburg, 2021), "Crystal Chemistry in Space and Time" (Moscow, 2019). All abstracts of the presentations have been published.

Publications. On the topic of the dissertation, 28 works have been published, including 3 articles in peer-reviewed scientific journals listed in the HAC, Web Of Science, and Scopus systems (1 - Ceramics International, 1 - Journal of Solid State Chemistry, 1 - Glass Physics and Chemistry).

The author's personal contribution lies in the synthesis of all the borates studied in the work, conducting powder X-ray diffraction with subsequent determination of the phase composition, calculation of unit cell parameters; capturing and refining a series of crystalline structures based on single crystal data; processing data obtained by – High-temperature powder X-ray diffraction method, refining unit cell parameters over a wide temperature range, calculating coefficients of thermal expansion. Luminescence data, Raman spectroscopy, and IR spectroscopy were interpreted with the direct participation of the author of this work. Discussion and interpretation of the obtained results were carried out jointly with the scientific supervisor and co-authors of joint publications.

Structure and volume of the dissertation. This work consists of an introduction, four chapters, conclusion, list of abbreviations, references, and one supplementary material. Chapter 1 is dedicated to the review of literature data on the crystal chemistry of borates in the BaO—M_2O_3––B_2O_3 (M = Y, Eu^{3+}, Bi^{3+}) and the mineralogy of alkaline earth and rare earth borates, Chapter 2 - description of synthesis methods and studies, Chapters 3 and 4 - consideration of research results.

The total volume of the dissertation is 153 pages, 72 figures, 33 tables, 14 abbreviations, 150 references.

The work of the conducted research corresponds to points 2 "Physics, chemistry, and thermodynamics of minerals, modern physicochemical methods of mineral research"; point 5 "Mineralogy of non-traditional and potentially new types of minerals, mineral materials science and synthesis of mineral-like materials"; point 8 "Crystallography and crystal chemistry of minerals, their technogenic and synthetic analogs"; point 11 " Single crystal X-ray diffraction and other methods of studying crystal structures" of the specialty passport 1.6.4. Mineralogy, crystallography. Geochemistry, geochemical methods of mineral exploration and the requirements of criteria 9-14 "Regulations on the award of academic degrees".

The work was carried out at branch of the National Research Center "Kurchatov Institute" - Petersburg Institute of Nuclear Physics - I.V. Grebenshchikov Institute of Silicate Chemistry (branch of the National Research Center KI - PINP - ISC) in the laboratory of oxide structural chemistry and at the crystallography department of the Institute of Earth Sciences at St. Petersburg State University. X-ray diffraction studies were conducted at the St. Petersburg State University research park "Centre for X-ray Diffraction Studies" ("Centre XRD") and at the branch of the National Research Center KI - PINP - ISC. Measurement of luminescence, Raman spectroscopy, and IR spectra were carried out at the St. Petersburg State University research park "OLMIV".

Main scientific results.

1. For the first time, 6 series of solid solutions of 32 compositions activated and co-activated by REE^{3+} ions (the author's personal contribution being 100%, see chapter 2.1.1): $BaBi_{2-x-y-z}REE_{x,x,z}B_2O_7$ (REE = Eu^{3+}, Sm^{3+}, Tb^{3+}, Tm^{3+}) were obtained and comprehensively studied (Shablinskii et al., 2022, Demina et al., 2024).

1.2. The existence regions of continuous solid solutions have been established: $BaBi_{2-x-y-z}REE_{x,x,z}B_2O_7$ (x_{Eu} = 0—0.45, x_{Sm} = 0—0.35, x_{Tb} = 0—0.45), $BaBi_{2-x-0.05}Eu_xSm_{0.05}B_2O_7$ (x_{Eu} + y_{Sm} = 0—0.45), $BaBi_{2-0.15-y}Eu_{0.15}Sm_yB_2O_7$ (x_{Eu} + y_{Sm} = 0—0.375), $BaBi_{2-x-0.3}Eu_xTb_{0.15}Tm_{0.15}B_2O_7$ (x_{Eu} + y_{Tb} + z_{Tm}= 0—0.475), a personal contribution of at least 100%, 3.1.1, 3.2.1, 3.3.1, 3.4.1, 3.5.1, 3.6.1, 3.7.1 (Shablinskii et al., 2022, Demina et al., 2024).

1.3. Eight crystal structures of the $BaBi_{2-x}Eu_xB_2O_7$ (x = 0.1, 0.2, 0.4), $BaBi_{2-x}Sm_xB_2O_7$ (x = 0.05, 0.3), $BaBi_{2-x}Tb_xB_2O_7$ (x = 0.1, 0.3, 0.4) borates have been refined based on single-crystal data. According to XRD data, the regularity of the distribution of REE^{3+} atoms over sites of the crystal structure during isomorphic substitution has been established: larger atoms Sm and Eu in terms of ionic radius replace Bi atoms in the largest volume polyhedra $M1$ and $M2$ sites, while smaller Tb atoms occupy the smallest volume polyhedra $M3$ site, a personal contribution of at least 60%, see chapters 3.1.2, 3.2.2, 3.5.2, 3.7.2 (Shablinskii et al., 2022, Demina et al., 2024).

1.4. Substitution of Bi^{3+} atoms with Tb^{3+} in the $M1M2M3B_2O_7$ (where the occupancy of $M1$, $M2$, $M3$ is 1/3Ba, 2/3Bi) crystalline matrix leads to a decrease in the degree of disordering of the (Bi,Ba)(Bi,Ba)(Tb,Bi,Ba)B_2O_7 solid solutions, the author's personal contribution estimated at no less than 70%, see chapter 3.5.2 (Demina et al., 2024).

1.5. Comparison of the thermal expansion of the $BaBi_2B_2O_7$ and $BaBi_{1.7}Sm_{0.3}B_2O_7$ borates allowed to establish that the bends in the temperature dependence of the unit cell parameters at 450°C in the borate activated by Sm^{3+} are associated with the redistribution of Bi and Sm cations over sites, a personal contribution of not less than 80%, see chapter 3.2.4 (Demina et al., 2024).

1.6. Optimal concentrations of the activator ion were determined for all investigated concentration series by measuring the excitation spectra of luminescence, luminescence, and evaluating the intensity of the emitted radiation from the phosphors: $BaBi_{1.6}Eu_{0.4}B_2O_7$, $BaBi_{1.95}Sm_{0.05}B_2O_7$, $BaBi_{1.7}Tb_{0.3}B_2O_7$, $BaBi_{1.75}Eu_{0.15}Sm_{0.1}B_2O_7$, $BaBi_{1.7}Eu_{0.15}Tb_{0.15}Tm_{0.15}B_2O_7$. Promising tunable phosphors for white light-emitting diodes were obtained. The author's personal contribution is not less than 50%, see chapters 3.1.5, 3.2.6, 3.3.2, 3.4.2, 3.5.4, 3.6.2 (Demina et al., 2024).

2. A new $Ba_3Y_{2-x}Er_x(BO_3)_4$ (x = 0.01—0.3) series of solid solutions and the $Ba_3Eu_2(BO_3)_4$ borate were synthesized by crystallization from melt (The author's personal contribution is 100%. Refer to chapter 2.1.2) and comprehensively studied (Demina et al., 2021, Demina et al., 2023).

2.1. The crystal structure of the $Ba_3Y_2(BO_3)_4$ borate was refined for the first time in an anisotropic approximation; the distribution of cations over sites was determined. A regularity in the isomorphic substitution of borates of the $A_3M_2(BO_3)_4$ (A = Ca, Sr, Ba, M = *REE*, Bi^{3+}) family was revealed. Atoms with smaller ionic radii predominantly occupy the smallest $M3$ site, while $M1$ and $M2$ sites with the largest volume are mainly occupied by cations with larger ionic radii. A description of the isomorphism of the presented family from the perspective of structural diversity factor is proposed. The personal contribution is at least 70%. Refer to chapters 4.2, 4.8.1 (Demina et al., 2023).

2.2. The nature of bends in the temperature dependencies of the unit cell parameters of the $Ba_3Eu_2(BO_3)_4$ and $Ba_3Y_2(BO_3)_4$ borates has been determined in the temperature ranges of 500–640 °C and 600–740 °C, respectively. Based on the refinement of the $Ba_3Y_2(BO_3)_4$ crystal structure over a wide temperature range, it has been determined that the bends in borates of the $A_3M_2(BO_3)_4$ (A = Ca, Sr, Ba, M = *REE*, Bi^{3+}) family are associated with the redistribution of cations over sites with increasing temperature. The personal contribution is at least 70%, see chapters 4.3, 4.8.2 (Demina et al., 2021, Demina et al., 2023).

2.3. Analysis of the thermal expansion of seven borates of the $A_3M_2(BO_3)_4$ (A = Ca, Sr, Ba, M = *REE*, Bi^{3+}) family demonstrates that the borates studied in this work and from literary sources

have maximum thermal expansion along the *a*-axis, except for the $Ca_3Eu_2(BO_3)_4$ borate, where it is maximum along the *b*-axis. The connection has been established with some differences in the orientation of BO_3 triangular radicals, as well as coordination number of the *M*1, *M*2, *M*3 sites. The personal contribution is at least 80%, see chapter 4.8.2 (Demina et al., 2023).

2.4. The luminescent and thermoluminescent properties of the $Ba_3Y_{2-x}Er_x(BO_3)_4$ solid solutions have been studied. The optimal concentration of the activator ion $x = 0.1$ has been determined. Promising luminescent thermometers have been developed. The author's personal contribution is at least 50%, see chapters 4.6 and 4.7 (Demina et al., 2023).

Thesis statements to be defended:

1. In the new series of solid solutions $BaBi_{2-x}REE_xB_2O_7$ (*REE* = Eu^{3+}, Sm^{3+}, Tb^{3+}), rare earth elements atoms occupy the most suitable sites in terms of volume within the polyhedron: larger atoms of samarium and europium are located in larger volume *M*2 and *M*1 sites respectively, while the smallest atoms of terbium occupy *M*3 site. Specifically, in the $(Bi,Ba,Eu)(Bi,Ba,Eu)(Bi,Ba)B_2O_7$ solid solutions, it is established that Eu^{3+} ions replace Bi^{3+} in *M*1 site at $x = 0.10$—0.30 and in *M*1 and *M*2 sites at $x = 0.40$. The entry of europium ions into *M*2 site leads to a reduction in the distance between activator ions, thus causing concentration quenching of photoluminescence in this series of solid solutions. The entry of the smallest Tb^{3+} ions into the crystal structure leads to increasing the degree of orderliness of the studied solid solutions $(Bi,Ba)(Bi,Ba)(Tb,Bi,Ba)B_2O_7$.

2. With increasing temperature in the $A_3M_2(BO_3)_4$ (*A* = Ca, Sr, Ba, *M* = *REE*, Bi^{3+}) borate, there is a redistribution of large cations among *M*1, *M*2, *M*3 sites, which is reflected in bends in the temperature dependencies of the unit cell parameters.

3. The anisotropy of thermal expansion in $A_3M_2(BO_3)_4$ (*A* = Ca, Sr, Ba, *M* = *REE*, Bi^{3+}) borates is dictated by the preferred orientation of boron-oxygen triangles BO_3 and the articulation of polyhedra, which depends on the size of the cations within them.

The work was carried out within the framework of a state assignment (No. 1023033000085-7-1.4.3) and supported by the Russian Foundation for Basic Research (RFBR) No. 18-29-12106 (2019-2021), 18-03-00679 (2020), the grant of the President of the Russian Federation No. MK-2724.2021.1.3 (2020-2022), the Russian Science Foundation (RSF) No. 21-77-00069 (2021-2023), No. 22-13-00317 (2022-present), No. 23-77-10066 (2023-present).

Acknowledgments. The author of this work expresses deep gratitude to the scientific supervisor, Doctor in geology and mineralogy, Professor Stanislav Konstantinovich Filatov, and scientific advisors, Doctor in chemistry Rimma Sergeevna Bubnova and PhD in in geology and mineralogy Andrey Pavlovich Shablinskii, for the proposed topic of the research, scientific consultation, contribution to the development of the work. The author also thanks Vera

Alexandrovna Firsova for consultations on processing experimental data using the Rietveld method, PhD in in geology and mineralogy, Associate Professor Maria Georgievna Krzhizhanovskaya (Institute of Earth Sciences, St. Petersburg State University) for conducting High-temperature powder X-ray diffraction experiments, Doctor in physics and math, Professor Alexey Valeryevich Povolotsky ("OLMIV") for conducting experiments on measuring optical properties, as well as all co-authors of joint works.

Chapter 1. Crystal chemistry of borates in the BaO–M_2O_3–B_2O_3 (M = Y, Eu^{3+}, Bi^{3+}) systems

1.1 General features of borate crystal chemistry

Boron is a chemical element belonging to the third group of the main subgroup of the periodic table of chemical elements by D.I. Mendeleev, with an electronic configuration of $1s^2 2s 2p_x 2p_y$. The valence electrons of a neutral boron atom possess different characteristics due to their placement on *s*- and *p*-types orbitals. This leads to the formation of various types of bonds. By mixing different orbitals of the central boron atom, it can form either three coplanar bonds (sp^2 hybridization) or four tetrahedral bonds (sp^3 hybridization) (Bubnova, Filatov, 2008). Boron is commonly found in two coordination polyhedra with oxygen surroundings: in BO_3 triangles and BO_4 tetrahedra. Additionally, linear (double) boron coordination has been observed (Hawthorne, 1996; Lin et al., 2022; Noeth et al., 1982; Shoji et al., 2014). In triangular coordination, the B—O bond lengths range from 1.351 to 1.403 Å, with an average bond length of 1.370 Å, and the O—B—O angles vary between 114 and 126°. The valence bond strengths average one valence unit (v.u.), with B–O bond strength values in BO_3 ranging from 1.19 to 0.86 v.u. (Hawthorne et al., 1996). In tetrahedral coordination, the B—O bond lengths range from 1.462 to 1.512 Å, with an average bond length of 1.476 Å, and the O—B—O angles vary between 104 and 115°. The average <O–B–O> angle is close to the angle in a regular tetrahedron, at 109.5° (Bubnova, Filatov, 2008). The average bond strength is 0.75 v.u. (Hawthorne et al., 1996).

1.2 Classification of borates

By dimensionality, the class of borates is divided into six subclasses (Burns et al., 1995): 1) borates with isolated polyhedra; 2) borates with isolated clusters; 3) chain borates; 4) layered borates; 5) framework borates; 6) mixed salts (borosilicates, borosulfates, borophosphates, borarsenates, borocarbonates, and boroberyllates).

According to the number of boron atoms in the classification by H. Strunz (Strunz, 1997), borates are divided into subclasses: 6.A. Monoborates. 6.B. Diborates. 6.C. Triborates. 6.D. Tetraborates. 6.E. Pentaborates. 6.F. Hexaborates. 6.G. Heptaborates, and other megaborates; where the value 6 denotes the class of borates in mineral systematics. Further division occurs based on the dimensionality of the borate anion: within each subclass, subdivisions corresponding to island (A), chain (B), layered (C), and framework (D) borates are identified. The next division is based on the number of boron atoms in triangular and tetrahedral coordination, for example:

6.EA.05. 5(4Δ+ 1T) – island pentaborates (szaibelyite, santite, ammonioborite). This classification highlights only one main block and does not consider the number of groupings in the repeating part of the anion. Therefore, the concept of a branched block is used for further division, which is separately identified, for instance: 6.EB.25. 5(2Δ+ 3T) + Δ (branched units). Additionally, the systematic classification lacks a class of borates containing various polyanions. To denote such borates, the main categorization is indicated with an added specification (isolated units), for example: 6.EC.10. 5(2Δ+ 3T) + Δ (isolated units).

In the crystal structures of anhydrous borates, especially binary and more complex compounds, isolated BO_3 triangles predominate at around 65% (Leonyuk, 2008). Among other borates, nearly half are represented by framework structures containing triangular BO_3 radicals, followed by island, layered, and chain structures. There are approximately fifty types of boron-oxygen anions and polyanions and around a dozen borosilicate, boron-aluminate, and boroberyllate anions (Leonyuk et al., 2020).

1.3 Main boron-oxygen groups

The boron coordination polyhedra tend to polymerize, forming various groups that are often repeated in different structures. The presence of two types of coordination polyhedra plays a key role in the formation of diverse groupings unique to borates. They are capable of forming various B-O groups, in which the polyhedra are interconnected at the vertices. The main rigid boron-oxygen groups include non-cyclic, simple cyclic, double, and multiple cyclic structures.

Simple cyclic groups consist of triborate rings containing three boron atoms, with four types of triborate rings: 3 triangles, 2 triangles and a tetrahedron, triangle and 2 tetrahedra, 3 tetrahedra. Crystalline structures are also known to contain rings of four interconnected B-O polyhedra with island or layered structures. In layers following the quadruple rings with the fewest polyhedra, there are hexagonal, octagonal, and decagonal rings, while frameworks consist only of hexagonal rings (Bubnova, Filatov, 2008).

Non-cyclic groups are formed by various combinations of BO_3 triangles and BO_4 tetrahedra, including single polyhedra, diorthogroups, and interconnections of two tetrahedra and a triangle and chains of BO_3 triangles (Bubnova, Filatov, 2008).

Double and multiple cyclic groups are created by combining triborate rings through shared polyhedra, resulting in the formation of stronger B-O groups through the generalization of tetrahedra.

The articulation of polyhedra along edges

The articulation of polyhedra along edges has previously been observed only in borates during synthesis under high pressure and temperature conditions, exemplified by the $Dy_4B_6O_{15}$ (Huppertz, Eltz, 2002) and $Ho_4B_6O_{15}$ (Huppertz, 2003) compounds. In 2010, the $KZnB_3O_6$ borate (Wu et al., 2010) was discovered with polyhedra connected along edges under atmospheric conditions. Since then, several similar compounds have been identified, such as $Li_4Na_2CsB_7O_{14}$ (Mutailipu et al., 2019), $BaAlBO_4$, $BaGaBO_4$ (Guo et al., 2019).

1.4 Thermal expansion of borates with isolated triangular BO_3 radicals and triborate B_3O_6 groups

In this study, special attention is given to the thermal expansion of borates containing isolated triangular BO_3 radicals in their crystal structure. Often, raising the temperature of a crystalline material leads to increased symmetry and decreased coordination number (c.n.) (Filatov, 1990). Elements are divided into two groups: with "rigid" (stable) and "soft" (variable) coordination (Filatov, 1990). "Rigid" coordination polyhedra demonstrate high bond strength (0.7 v.e.) and stability under various thermodynamic conditions, for example, BO_3 triangles (1 v.e.) and BO_4 tetrahedra (0.75). "Soft" coordination polyhedra have weaker bond strength (0.03–0.3 v.e.) and exhibit variability over a wide range of temperatures depending on thermodynamic conditions.

In monographs (Bubnova, Filatov, 2008; Bubnova, Filatov, 2013), it has been experimentally shown that the thermal expansion of borates with isolated triangular BO_3 radicals and triborate B_3O_6 groups is highly anisotropic. Maximum expansion occurs along an axis perpendicular to the plane of the triangular radicals and pseudo-layers of triborate rings formed by three BO_3 triangles. This expansion aligns with the direction of maximum atomic displacements of oxygen and boron occurring along an axis perpendicular to the plane of the triborate rings.

1.5 Basic principles of high-temperature crystal chemistry of borates

The principles of high-temperature borate crystal chemistry formulated by Bubnova and Filatov (2008; 2013) are driven by the nature of thermal transformations, taking into account the characteristics of crystal structure and thermal vibrations of atoms. Special attention is given to the thermal behavior of boron-oxygen polyatomic anions, which differentiate oxygen compounds of various classes.

1. Significantly covalent (and therefore strong and short) B-O chemical bonds induce thermal vibrations of boron and oxygen atoms predominantly perpendicular to these bonds, determining many aspects of borate formation, structure, properties, and transformations.

2. Strong boron-oxygen polyhedra - BO_3 triangles and BO_4 tetrahedra - remain almost unchanged with temperature, although the amplitude of atom vibrations perpendicular to B-O bonds significantly increases with temperature rise.

3. In strong fragments of the crystal structure (BO_3, BO_4, and rigid boron-oxygen cyclic groups composed of three to six B-O polyhedra, formed by the articulation of three polyhedra), bond lengths and angles practically do not change with temperature; thermal vibrations of boron and oxygen atoms perpendicular to B-O bonds are also perpendicular to the planes of BO_3 triangles and rigid triborate groups B_3O_6.

4. Strong structural fragments of borates, connected into polyanions through common vertices, can rotate relative to each other like hinges, determining the unique "viscosity" of borate crystals, glasses, and melts, which dictates the nature of their thermal behavior.

5. At high temperatures, especially near the substance's melting point, isolated boron-oxygen triangles and tetrahedra can undergo restrained or complete rotation around a point or axis passing through the center; to a lesser extent, rotational thermal motion may be inherent in rigid groups.

1.6 Borates in nature

Compared to minerals of other classes (silicates - 998 known minerals, aluminosilicates - 635, phosphates - 712, arsenates and arsenides - 527, sulfates - 690, sulfides - 623, etc.), borates (170 minerals) and borosilicates (129 minerals) are less common in nature (rruff.info). They form various deposits, the main ones being contact-metasomatic, volcanogenic-sedimentary, and halogenic. The average boron content in the Earth's crust is 950 ppm (WebElements.com). Global identified boron reserves amount to about 9.4 million tons (web.archive.org). Boron is almost never found as an impurity in other minerals (Grew et al., 2017).

This study focuses particularly on synthetic borates containing alkaline earth metals (specifically barium), rare earth elements, and Bi. Currently, there are no known minerals among barium-containing borates. Strontium borates are more common in nature and include 7 known minerals, while calcium borates are the most common among alkaline earth metal borates - with 70 known minerals. Additionally, there are 4 borates with rare earth elements (rruff.info database).

The structure, properties, and occurrence in nature of alkaline earth metal and rare earth borates are discussed below.

Since the compounds studied in this work belong to island borates with isolated triangular radicals, preference was also given to strontium and calcium borates in selecting objects for the literature review, the structures of which are based on triangular BO_3 radicals.

1.6.1 Alkaline earth metal borates

Nordenskiöldine $CaSn^{4+}[BO_3]_2$ (6.AA 1Δ) is a rare mineral belonging to the class of borates, classified as island monoborates. It is isostructural to tusionite and carbonates of the dolomite group. The mineral forms crystals ranging from thin to thick prismatic habitus, often appearing as tabular crystals and their subparallel intergrowths. Nordenskiöldine is colorless, yellow, transparent with white streaks, glassy pearly luster, and conchoidal fracture. It exhibits perfect cleavage on {0001} and indistinct on {1011}. With a hardness of 5.5–6 on the Mohs scale and a density of 4.22 g/cm3 (Brögger, 1887).

It crystallizes in the trigonal crystal system with space group *R*3, a = 4.858(1), c = 16.080(2) Å, V = 328.65(3) Å³, Z = 3. The crystal structure consists of structural blocks, SnO_6 and CaO_6 octahedra (Figure 1a), each linked to six triangular BO_3 radicals. These blocks are interconnected through the vertices of octahedra and triangles with neighboring triangles and octahedra (Liebau, 1985).

Nordenskiöldine is found in alkaline pegmatites (Norway) associated with melanophanite, hamiltoite, zircon, molybdenite, cancrinite, analcime. It also occurs in skarns (e.g., Uchkoshkon, Kyrgyzstan; Titovskoe deposit, Russia) in association with scapolite, diopside, cassiterite, danburite, datolite, calcite. Discoveries of nordenskiöldine are also known in Namibia, USA, China, Canada, Germany.

Gaudefroyite $Ca_4Mn^{3+}{}_3(BO_3)_3(CO_3)O_3$ (6.AB (1Δ) + O) a chain monoborate belonging to the carbonate-borates group. It is characterized by prismatic needle-shaped crystals with cleavage on the prism faces. Typically appearing black and opaque with a brown streak color, Gaudefroyite has a hardness of 6 on the Mohs scale (Jouravsky, Perminge et al., 1964).

It crystallizes in the hexagonal crystal system with space group P63/m, with lattice parameters *P*6₃/*m*, a = 10.608(3), c = 5.886(2) Å, V = 574.11(3) Å³, Z = 2. The structure of Gaudefroyite contains CO_3 triangles in the *ab* plane and BO_3 triangles in the *ac* plane. The $Mn^{3+}O_6$ octahedra are connected by edges to form chains along the *c*-axis. These chains are linked to the BO_3 triangles in a framework, within which Ca atoms and CO_3 groups are located in cavities (Figure 1b) (Hoffmann et al., 1997).

Gaudefroyite is primarily found in manganese hydrothermal deposits (such as Tachgagalt in the Anti-Atlas Mountains of Morocco and the Kalahari manganese deposit in South Africa), where its formation is associated with metasomatism at high temperatures and low pressures.

The mineral **Tunellite** $SrB_6O_9(OH)_2 \bullet 3H_2O$ is a layered hexaborate that can form crystals up to 10 cm in size, elongated along [001] or flattened along {100}. These crystals typically form colorless fine-grained cryptocrystalline aggregates with a white streak color. It is exhibit a glassy pearly luster and demonstrate perfect cleavage along {100} and distinct cleavage along {001}. Tunellite has a hardness of 2.5 on the Mohs scale and a density of 2.391 g/cm3 (Erd et al., 1961).

It crystallizes in the monoclinic crystal system, space group $P2_1/b$, with unit cell parameters a = 14.390(3), b = 8.213(2), c = 9.934(2) Å, V = 1075.8(3) Å^3, Z = 4. The crystal structure consists of layers composed of borate polyions, with strontium cations and water molecules located between them. The layers are connected by hydrogen bonds of water molecules. Borate polyions consist of individual borate groups, each containing three independent BO_4 tetrahedra and three independent triangular BO_3 radicals, linked together by sharing vertices to form six-membered rings. Each ring consists of two tetrahedra and one triangle (Clark, 1964). Strontium atoms are coordinated by ten oxygen atoms.

Tunellite is primarily found as a secondary mineral in borate deposits: 9 known deposits in the USA and 7 deposits in Turkey.

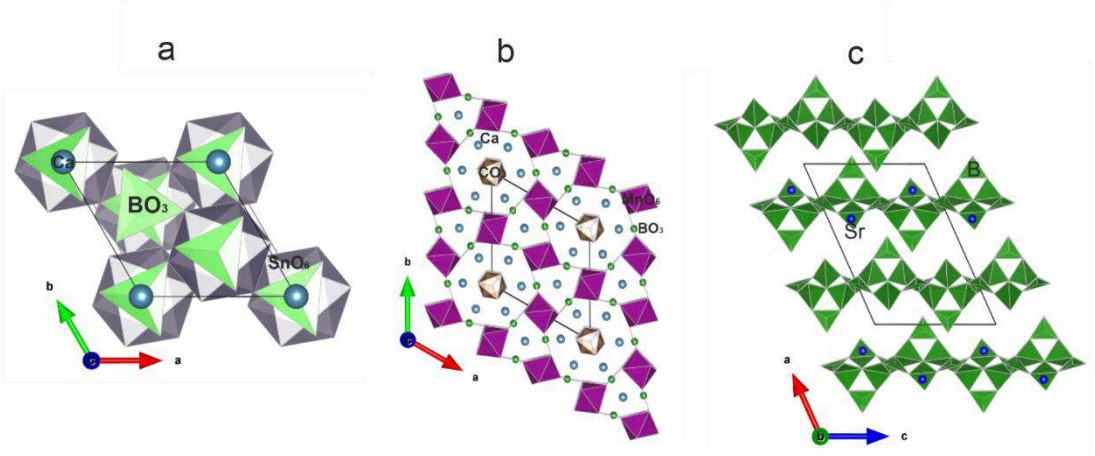

Figure 1 – The crystal structures of minerals include: Nordenskiöldine $CaSn^{4+}[BO_3]_2$ (a); Gaudefroyite $Ca_4Mn^{3+}{}_3(BO_3)_3(CO_3)O_3$ (b); Tunellite $SrB_6O_9(OH)_2 \bullet 3H_2O$ (c). The structures are visualized using the Vesta program.

1.6.2 Rare earth borates

Moydite-(Y) $Y[B(OH)_4](CO_3)$ (6.AC 1T) belongs to the group of layered mono-carbonate-borates. This mineral forms yellow plate-like crystals up to 1 mm in size. It exhibits a streak color ranging from light yellow to white and a glassy luster. The mineral displays perfect cleavage along {010} and has a hardness of 1-2. Its density is 3.13 g/cm3 (Grice et al., 1986).

It crystallizes in a orthorhombic crystal system, in the *Pbca* space group, with unit cell parameters a = 9.089(1), b = 12.244(1), c = 8.926(1) Å, V = 993.34(3) Å³, Z = 8. It features a layered structure composed of YO_9 polyhedra connected by vertices, linking flat triangular carbonate groups (Figure 2a). The alternating layers are linked by isolated $B(OH)_4$ tetrahedra (Grice et al., 1986).

Moydite is found in granite pegmatites rich in rare earth elements. Currently, the only known deposit of muadite is in Canada.

Peprossite-(Ce) is a mineral with the chemical formula $Ce_2(Al_3O)^2/_3B_4O_{10}$ (6.CA 3(3T), belonging to the group of layered triborates. It exhibits a light yellow color with a white streak and forms small platy crystals with hexagonal outlines. The mineral is characterized by a glassy luster and shows perfect cleavage along {0001} and distinct cleavage along {110}. It has a Mohs hardness of 2 and a density of 3.467 g/cm3 (Della et al., 1993).

It crystallizes in the hexagonal crystal system with $P6_2m$ space group, a = 4.612(1), c = 9.374(3) Å, V = 172.6(2) Å³, Z = 1. Peprossite is a layered borate with layers consisting of hexagonal rings of tetrahedra BO_4, alternating with interlayer cations *REE* and layers of Al polyhedra. The Al atoms are coordinated by five oxygen atoms, forming an almost tetragonal pyramid, the base of which is formed by pairs of apical oxygen atoms. Three of these pyramids share their apical oxygen atoms and form Al_3O groups with an occupancy of 2/3 (Figure 2b). In terms of structure, the mineral is similar to dioctahedral micas, with the main difference being the presence of layers composed not of octahedra, but of pyramids (Callegari et al., 2000).

Peprossite is found in pyroclastic deposits within voids among sanidine crystals. It forms due to the circulation of pneumatolytic fluids in hydrothermal solutions, likely at temperatures exceeding 350 °C. Currently, there are two known deposits of peprossite in Italy.

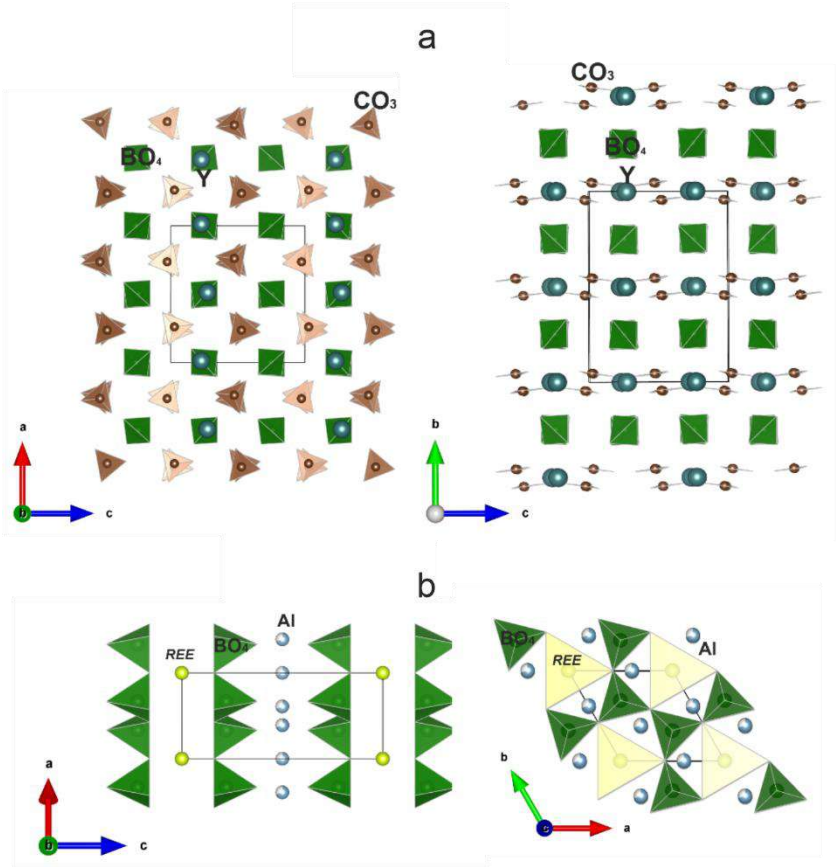

Figure 2 – Crystal structures of minerals: **Moydite-(Y)** $Y[B(OH)_4](CO_3)$ (a); **Peprossite-(Ce)** $Ce_2(Al_3O)^2/_3B_4O_{10}$ (b). The structures are visualized using the Vesta program.

1.7 Borates in the BaO– Bi_2O_3–B_2O_3 system

1.7.1 Synthetic borates in the BaO– Bi_2O_3–B_2O_3 system

At present, there are 6 known borates that belong to the ternary system BaO– Bi_2O_3–B_2O_3 (Figure 3). The borates in this system consist of isolated B–O groups: BO_3 triangles, BO_4 tetrahedra, and triborate B_3O_6 groups.

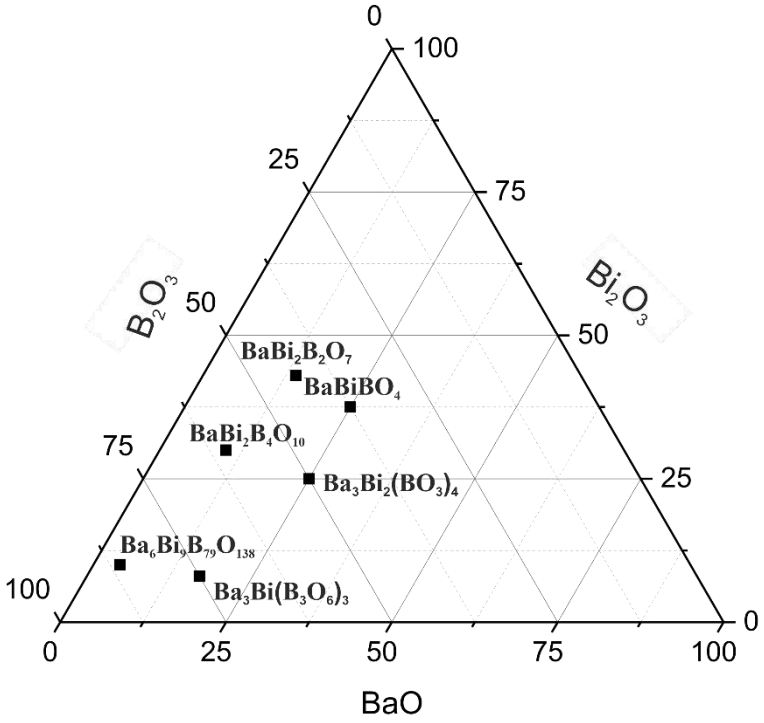

Figure 3 – Known compounds in the ternary BaO–Bi_2O_3–B_2O_3 system.

$Ba_3Bi(B_3O_6)_3$ (165926-ICSD) belongs to island borates. It crystallizes in a hexagonal crystal system, space group $P6_3/m$ with unit cell parameters a = 7.1999(2), c = 17.3567(6) Å, V = 779.2(3) Å^3, Z = 2 (Cai et al., 2009). The crystal structure contains flat isolated triborate groups B_3O_6, parallel to the *ab* plane, composed of three triangular BO_3 radicals (Figure 4a). Bismuth atoms are coordinated by six oxygen atoms, barium atoms by six and nine oxygen atoms.

$Ba_6Bi_9B_{79}O_{138}$ (380533-ICSD) (Krivovichev et al., 2012) is a layered borate, forming a continuous series of solid solutions with the **$Ba_6Eu_9B_{79}O_{138}$** borate (Cong et al., 2015). The borates crystallize in a trigonal crystal system, space group $R3$, with unit cell parameters a = 7.851(2), c = 46.20(1) Å, V = 2466.58(3) Å^3, Z = 3 (Cong et al., 2015). Clusters consist of six triborate rings connected at the vertices, forming layers. In the interlayer cavities, there are two independent Ba atoms and two independent Bi atoms.

$Ba_3Bi_2(BO_3)_4$ (189254-ICSD) is an island borate, crystallizing in orthorhombic crystal system, space group *Pnma*, with unit cell parameters a = 7.9508(5), b = 17.399(1), c = 8.9791(5) Å, V = 1242.13(4) Å^3, Z = 4 (Volkov et al., 2013). The crystal structure contains three independent crystallographic sites for cations, two general and one special, as well as isolated triangular BO_3 radicals, preferably oriented in the *bc* plane (Figure 4b). All large cations are disordered over three sites.

$BaBi_2B_4O_{10}$ (417181-ICSD) is a chain borate, crystallizing in a monoclinic crystal system, space group $P2_1/c$, with unit cell parameters a = 10.150(2), b = 6.3620(9), c = 12.485(2) Å, β = 102.87(1), V = 785.98(8) Å^3, Z = 4 (Bubnova et al., 2007). The crystal structure contains three crystallographic sites for large cations, each surrounded by eight oxygen atoms. Polyhedra $M1$, $M2$, and $M3$ form a three-dimensional framework. Polyhedra $M1$ and $M3$ form single chains, while polyhedra $M2$ form double chains along the a direction (Figure 4c). Ba and Bi atoms are disordered over three crystallographic sites. The borate chains consist of triborate $[B_3O_8]^{7-}$ groups, composed of three BO_4 tetrahedra and one BO_3 triangle.

$BaBiBO_4$ (424596-ICSD) is an island borate. The crystal structure of the borate was determined by neutron diffraction on a polycrystalline sample in orthorhombic crystal system, space group $Pna2_1$, with unit cell parameters a = 8.5817(7), b = 9.6802(7), c = 5.1505(4) Å, V = 427.86(7), Z = 4 (Barbier, Penin, 2005). Later, based on X-ray diffraction data, the space group $Pnam$ was selected, with unit cell parameters a = 8.5556(8), b = 5.1569(5), c = 9.6677(7) Å, V = 426.54(3) Å^3, Z = 4 (Dong et al., 2015). The crystal structure consists of a three-dimensional framework composed of BiO_5, BaO_9 polyhedra, and BO_3 triangles (Figure 4d). BiO_5 polyhedra and BO_3 triangles form infinite one-dimensional chains along the crystallographic b axis.

The island **$BaBi_2B_2O_7$** borate crystallizes in a hexagonal crystal system, space group $P6_3$, with unit cell parameters a = 5.3378(8), c = 13.583(2) Å, V = 335.15(9) Å^3, Z = 2 (Bubnova et al., 2016). The crystal structure contains two crystallographic sites for BO_3 triangles, three sites for large cations ($M1$, $M2$, $M3$), each split into Ba and Bi subpositions, one site for an additional oxygen atom not bonded to boron. The $M1$ and $M2$ sites are coordinated by ten oxygen atoms, while $M3$ site is coordinated by nine. The crystal structure figure is provided in section 3.1.2, page 58.

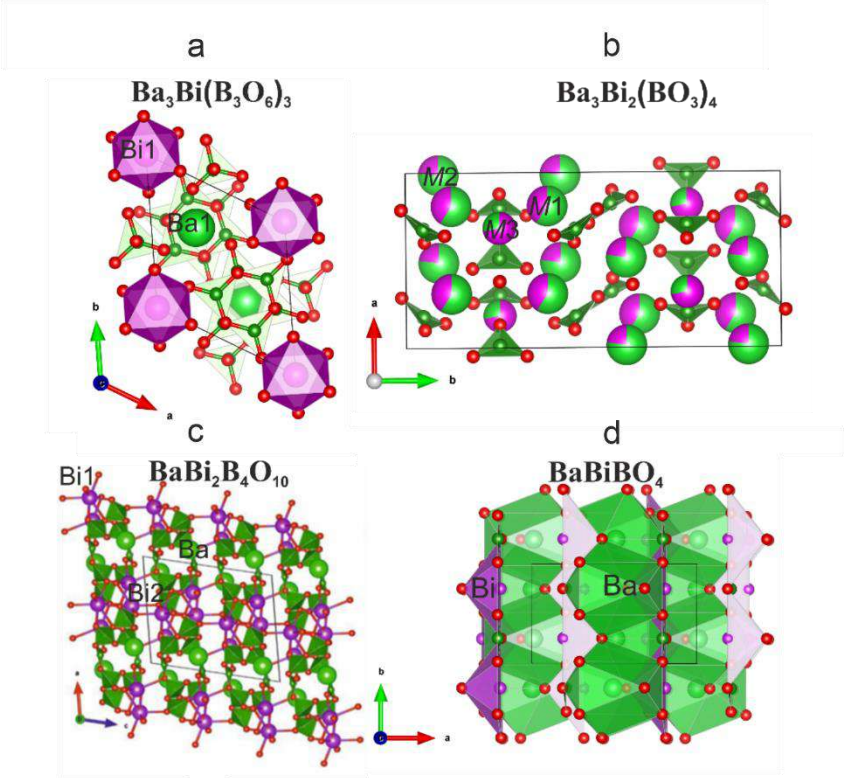

Figure 4 – The crystal structures of borates $Ba_3Bi(B_3O_6)_3$ (165926-ICSD) (a), $Ba_3Bi_2(BO_3)_4$ (189254-ICSD) (b), $BaBi_2B_4O_{10}$ (417181-ICSD) (c), $BaBiBO_4$ (424596-ICSD). The structures are visualized using the Vesta program.

1.7.2 Borates of the ABi$_2$B$_2$O$_7$ (A = Ca, Sr, Ba) family

In the present study, a significant amount of work has been carried out on the synthesis, refinement of crystalline structures, investigation of thermal behavior, and luminescent properties of borate matrices activated and co-activated by rare earth ions according to the formula $BaBi_{2-x}REE_xB_2O_7$ (*REE* = Eu^{3+}, Sm^{3+}, Tb^{3+}). This section is dedicated to the overview of crystal structures, thermal behavior, and luminescence of known ABi$_2$B$_2$O$_7$ (A = Ca, Sr, Ba) compounds.

CaBi$_2$B$_2$O$_7$ was first synthesized in (Barbier, Cranswick, 2006). The crystal structure was refined in orthorhombic crystal system, space group $Pna2_1$. Subsequently, in the work (Volkov et al., 2020), a re-refinement of the crystal structure of the $CaBi_2B_2O_7$ borate was conducted in orthorhombic crystal system, space group *Pnma*.

The structure contains $\{CaBi_2B_2O_7\}_\infty$ layers, consisting of BO_3 triangles, CaO_6 trigonal prisms, and distorted $Bi\psi O_3$ tetrahedra, one of which contains a stereoactive lone electron pair ψ at one vertex (Figure 5). The layers are connected by weak Bi–O bonds with a length of 2.902(11) Å. The BO_3 triangles are linked to three CaO_6 trigonal prisms and two BiO_3 groups through shared vertices. The CaO_6 polyhedra are connected by shared vertices to six BO_3 triangles and by shared

edges to two BiO_3 groups. The "extra" O_3 atom, not bonded to boron, coordinates with two Bi atoms and two Ca atoms, forming OBi_2Ca_2 tetrahedra. Overall, the refined structural model by (Volkov et al., 2020) in space group *Pnma* is close to $Pna2_1$ by (Barbier, Cranswick, 2006). The presence of a mirror plane leads to a reduction in the number of symmetrically independent sites (Volkov et al., 2020).

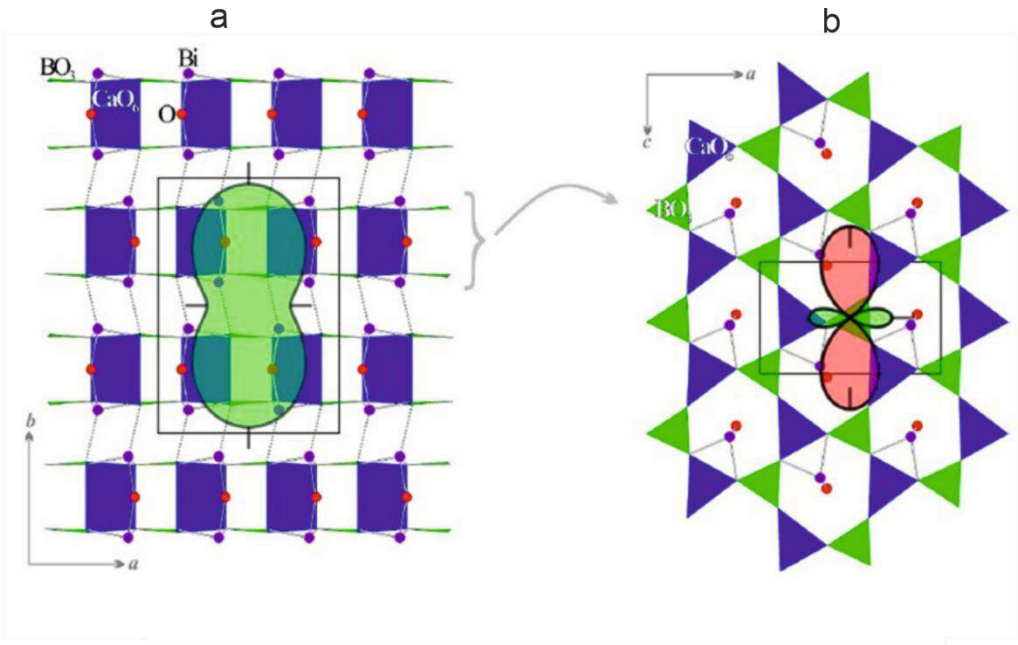

Figure 5 – Projections of the crystal structure of $CaBi_2B_2O_7$ on the planes *ab* (a) and *ac* (b). The figure shows correlations between the thermal expansion tensor at 600 °C and the structure (Volkov et al., 2020).

The $Sr_{1-x}Ba_xBi_2B_2O_7$ (x = 0—1) borates

The $SrBi_2B_2O_7$ borate were first reported by (Barbier, Cranswick, 2006). The $SrBi_2B_2O_7$ crystallizes in the hexagonal crystal system, space group $P6_3$. In 2012, a $Sr_{1-x}Ba_xBi_2B_2O_7$ (x = 0—1) glass-ceramic material was synthesized by (Shablinskii et al., 2012). Cooling the melt resulted in the formation of grains within the glass phase with sizes ranging from 0.7–1.0 μm, exhibiting a radial-radiating structure. Crystals with sizes of 0.1–0.2 μm were observed at the center of the grains. The crystalline phase constitutes approximately 10% of the material. The $Sr_{1-x}Ba_xBi_2B_2O_7$ (x = 0—1) crystal structures, including the new $BaBi_2B_2O_7$ compound, were refined by (Bubnova et al., 2016) in the hexagonal crystal system, space group $P6_3$. Notably, superstructural reflections were detected in the diffraction patterns (reciprocal space sections) of $Sr_{1-x}Ba_xBi_2B_2O_7$ (x = 0—0.65) solid solutions (Figure 6). Increasing the Ba content led to a weakening of the superstructural reflections. The refinement of borates with x = 0.70 and x = 1 was carried out in a reduced cell

with $a_{Ba} = a_{Sr}/\sqrt{3}$ (Figure 7). The unit cell volumes of the $Sr_2Bi_2B_2O_7$ and $BaBi_2B_2O_7$ borates are $V = 946.44(6)$ Å^3 and $V = 335.15(9)$ Å^3, respectively.

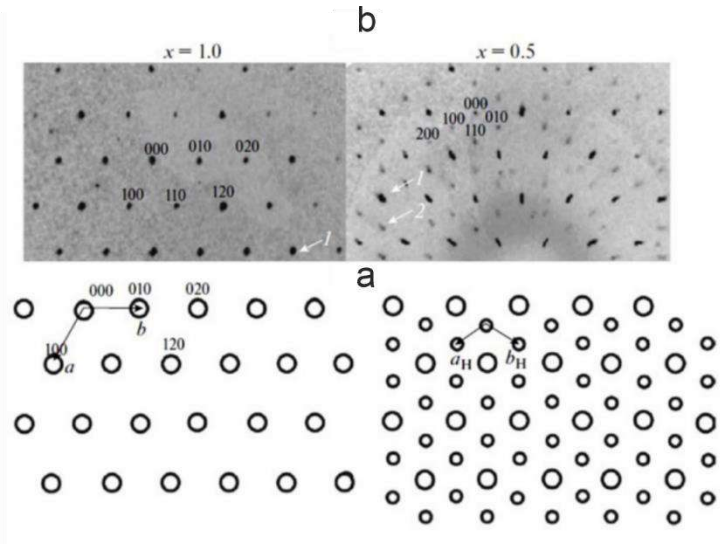

Figure 6 – Diffraction patterns of $Sr_{0.5}Ba_{0.5}Bi_2B_2O_7$ and $BaBi_2B_2O_7$ samples: actual image (a); *1* – reflections ($a_{Ba} = a_{Sr}/\sqrt{3}$), *2* – superstructural reflections (a_{Sr}) (b) (Bubnova et al., 2016).

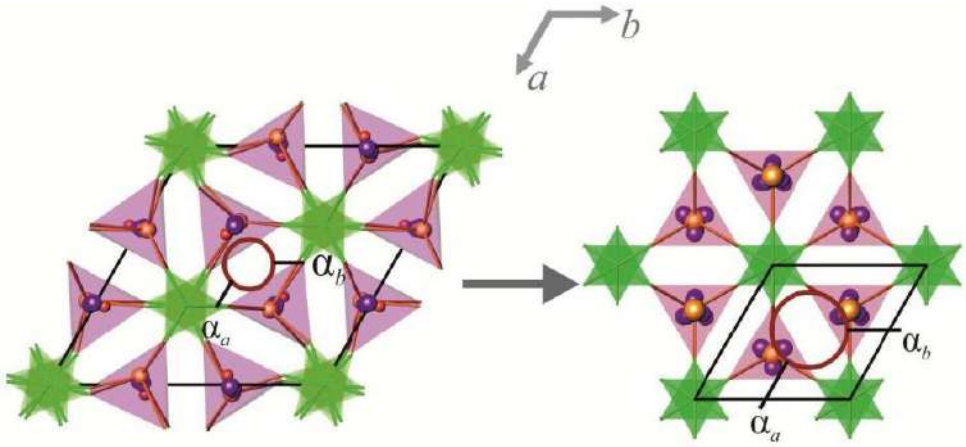

Figure 7 – Transition to a reduced cell ($SrBi_2B_2O_7 \rightarrow BaBi_2B_2O_7$). The crystal structure is compared with the of the thermal expansion tensor (Bubnova et al., 2016).

In the $SrBi_2B_2O_7$ crystal structure, the Sr and Ba atoms are ordered in three sies (*M*1, *M*2, and *M*3), while in the $BaBi_2B_2O_7$ structure they are almost completely disordered. In the solid solution at $x = 0.70$, the sites with the smallest polyhedral volume (*M*3) contains only Sr and Bi atoms. Increasing the content of Sr in this sites leads to a structural transition caused by the disruption of the statistical distribution of cations among sites (Figure 8). The parameters of the unit cell of borates from the $ABi_2B_2O_7$ (*A* = Ca, Sr, Ba) family are provided in the Table 1.

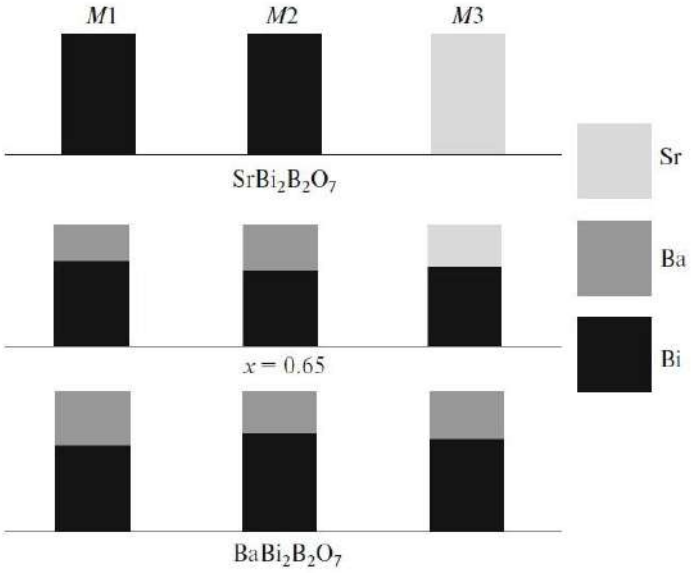

Figure 8 – Distribution of cations among sites in $Sr_{1-x}Ba_xBi_2B_2O_7$ (Bubnova et al., 2016).

According to (Bubnova et al., 2016), in the $Sr_{1-x}Ba_xBi_2B_2O_7$ crystal structures, just like in $CaBi_2B_2O_7$, there is an additional oxygen atom present.

All three types of splitting are present in the oxocentered pentagonal pyramid OM_5, formed around the atom O3 (Figure 9). Both end members of the $Sr_{1-x}Ba_xBi_2B_2O_7$ (x = 0—1) series have an additional oxygen atom in different coordination (Figure 9). Site splitting occurs as a result of the need to narrow the limits of isomorphic mixing, arising from the cooling of Bi^{3+} and Ba^{2+} atoms of different sizes and electronic structures, containing a stereoactive unshared electron pair (Bubnova et al., 2016).

In the $SrBi_2B_2O_7$ crystal structure, the Sr atoms fully occupy $M$3 site and are bonded to oxygen at the vertices of a trigonal prism. The transition from a hexagonal pyramid to a nonagonal pyramid occurs when Sr is replaced by Ba.

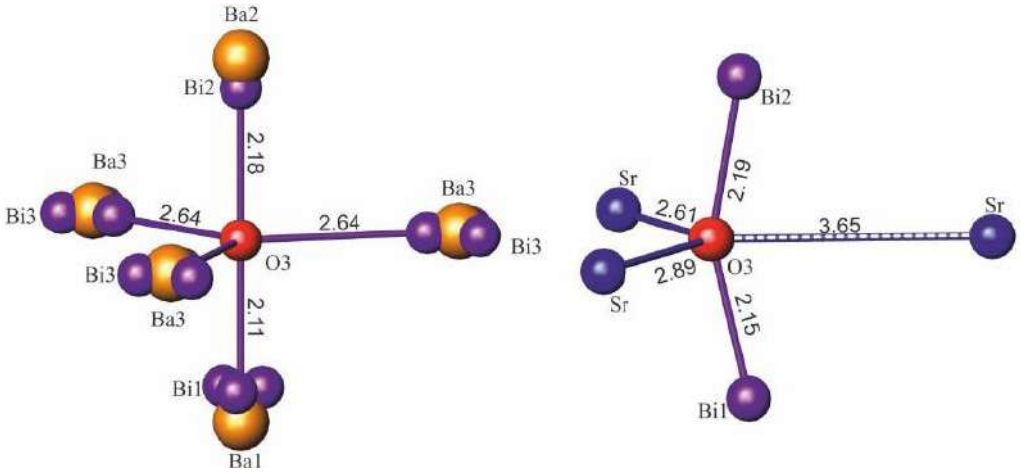

Figure 9 – Oxocentered polyhedra in the $BaBi_2B_2O_7$ and $SrBi2B_2O_7$ crystal structures (Bubnova et al., 2016).

In the (Volkov et al., 2020, an analysis of similar structural motifs of $CaBi_2B_2O_7$ (space group *Pnma*), $SrBi_2B_2O_7$, and $BaBi_2B_2O_7$ (space group $P6_3$) borates was conducted (Figure 10).

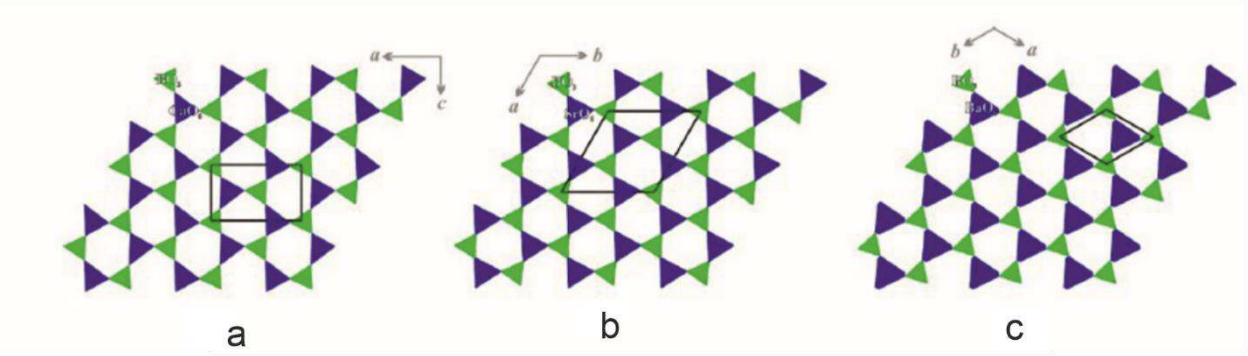

Figure 10 – The crystal structures of $CaBi_2B_2O_7$ (a), $SrBi_2B_2O_7$ (b), and $BaBi_2B_2O_7$ (c) (Volkov et al., 2020).

The study by (Shablinsky et al., 2022) refined the crystal structure of the $Sr_{0.5}Ba_{0.5}Bi_2B_2O_7$ borate. The crystal structure contains six symmetrically independent sites for BO_3 triangles, three sites for large cations *M*1, *M*2, *M*3, and one site for an additional oxygen atom. Site *M*1 is split into Sr, Ba, and two Bi sub-positions, site *M*2 is split into Ba and three Bi sub-positions, and site *M*3 is split into two Bi and Sr sub-positions. Sites *M*1, *M*2, *M*3 are coordinated by eight, ten, and nine oxygen atoms, respectively. The crystal structure of the $Sr_{0.5}Ba_{0.5}Bi_2B_2O_7$ borate is highly disordered compared to $SrBi_2B_2O_7$. It is also shown that strong disorder is observed in $Sr_{1-x}Ba_xBi_2B_2O_7$ solid solutions with a Ba concentration less than $x = 0.65$, suggesting that the $SrBi_2B_2O_7$ crystal structure, previously refined as ordered, is also characterized by slight disorder.

Table 1 – The unit cell parameters of borates in the $ABi_2B_2O_7$ (A = Ca, Sr, Ba) family

Compound	Space Group	a, Å	b, Å	c, Å	V, Å^3	Z	Reference
$CaBi_2B_2O_7$	$Pna2_1$	8.9371(5)	5.4771(3)	12.5912(7)	616.33(6)	4	(Barbier, Cranswick, 2006)
$CaBi_2B_2O_7$	*Pnma*	8.9123(5)	12.5412(7)	5.4786(3)	946.44(7)	4	(Volkov et al., 2020)
$SrBi_2B_2O_7$	$P6_3$	8.9123(5)	8.9123(5)	12.5412(7)	612.35(6)	6	(Barbier, Cranswick, 2006)
$SrBi_2B_2O_7$	$P6_3$	9.1404(4)	9.1404(4)	13.0808(6)	946.44(6)	6	(Bubnova et al., 2016)
$Sr_{0.5}Ba_{0.5}Bi_2B_2O_7$	$P6_3$	9.1937(14)	9.1937(14)	13.299(3)	973.5(3)	6	(Bubnova et al., 2016)
$Sr_{0.3}Ba_{0.7}Bi_2B_2O_7$	$P6_3$	5.3246(3)	5.3246(3)	5.3246(3)	329.04(1)	2	(Bubnova et al., 2016)
$BaBi_2B_2O_7$	$P6_3$	5.3378(8)	5.3378(8)	13.583(2)	335.15(9)	2	(Bubnova et al., 2016)

1.7.3 Behavior of borates in the $ABi_2B_2O_7$ (A = Ca, Sr, Ba) family at high temperatures

The thermal analysis data of the $Sr_{1-x}Ba_xBi_2B_2O_7$ (x = 0—1) series of solid solutions revealed the following thermal effects on DSC curves in the (Bubnova et al., 2016): glass transition temperature, crystallization from glass, melting upon heating, or crystallization upon cooling (Table 2). Based on the obtained data, it was concluded that the melting temperature decreases with an increase in the barium content in the composition of solid solutions.

Table 2 – Melting and crystallization temperatures of $Sr_{1-x}Ba_xBi_2B_2O_7$ according to DSC data during heating and cooling, respectively (Bubnova et al., 2016).

Compound	T_{melt}, °C	T_{cryst}, °C
$SrBi_2B_2O_7$	776	777
$Sr_{0.75}Ba_{0.25}Bi_2B_2O_7$	755	745
$Sr_{0.5}Ba_{0.5}Bi_2B_2O_7$	740	699
$Sr_{0.35}Ba_{0.65}Bi_2B_2O_7$	675	620
$Sr_{0.25}Ba_{0.75}Bi_2B_2O_7$	687	637
$Sr_{0.15}Ba_{0.85}Bi_2B_2O_7$	648	563
$BaBi_2B_2O_7$	630	*

* Not detected

Thermal expansion of borates from the $ABi_2B_2O_7$ (A = Ca, Sr, Ba) family.

In the $CaBi_2B_2O_7$ crystal structure (Volkov et al., 2020) (Figure 10a) reveals rigid boron-oxygen triangles oriented approximately parallel to the *ac* plane. Thermal expansion in this plane is minimal (Table 3). The anisotropy of thermal expansion in $CaBi_2B_2O_7$ sharply increases upon heating. The crystal structure exhibits negative expansion along [001] in the temperature range of 30–700 °C. The authors attribute the strong anisotropy to the tendency of the structure to become hexagonal, like $SrBi_2B_2O_7$, upon heating. As a result, the ratio of the unit cell parameters *a*/*c* approaches the value of √3, corresponding to the hexagonal aristotype (Figure 11). The temperature dependence of the *a*/*c* ratio is highly nonlinear and exponential. The authors suggest that the transition from orthorhombic to hexagonal crystal system may occur around 950 °C (Figure 11), although the melting temperature of $CaBi_2B_2O_7$ (765 °C) is lower than the calculated temperature of the polymorphic transition.

Table 3 – Thermal expansion coefficients α (10^{-6} °C^{-1}) of borates from the $ABi_2B_2O_7$ (*A* = Ca, Sr, Ba) family at different temperatures.

Compound	α_a	α_b	α_c	α_V	Reference
			25 °C		
$SrBi_2B_2O_7$	3.8	3.8	23	30	(Bubnova et al., 2016)
$Sr_{0.75}Ba_{0.25}Bi_2B_2O_7$	2.6	2.6	23	28	(Bubnova et al., 2016)
$Sr_{0.5}Ba_{0.5}Bi_2B_2O_7$	3.3	3.3	22	29	(Bubnova et al., 2016)
$Sr_{0.35}Ba_{0.65}Bi_2B_2O_7$	3.9	3.9	18	26	(Bubnova et al., 2016)
$Sr_{0.3}Ba_{0.7}Bi_2B_2O_7$	3.1	3.1	21	27	(Bubnova et al., 2016)
$BaBi_2B_2O_7$	5.6	5.6	20	31	(Bubnova et al., 2016)
			100 °C		
$CaBi_2B_2O_7$	10.0(2)	18.3(4)	−6.7(6)	21.6(3)	(Volkov et al., 2020)
			300 °C		
$CaBi_2B_2O_7$	10.7(1)	24.8(1)	-3.5(2)	32.0(1)	(Volkov et al., 2020)
			325 °C		
$SrBi_2B_2O_7$	5.8	5.8	27	38	(Bubnova et al., 2016)
$Sr_{0.75}Ba_{0.25}Bi_2B_2O_7$	5.9	5.9	27	39	(Bubnova et al., 2016)
$Sr_{0.5}Ba_{0.5}Bi_2B_2O_7$	6	6	27	40	(Bubnova et al., 2016)
$Sr_{0.35}Ba_{0.65}Bi_2B_2O_7$	7.3	7.3	26	40	(Bubnova et al., 2016)
$Sr_{0.3}Ba_{0.7}Bi_2B_2O_7$	6.5	6.5	28	40	(Bubnova et al., 2016)
$BaBi_2B_2O_7$	6.9	6.9	27	41	(Bubnova et al., 2016)
			600 °C		
$CaBi_2B_2O_7$	11.8(1)	34.2(3)	−25.7(4)	20.3(2)	(Volkov et al., 2020)
			625 °C		
$SrBi_2B_2O_7$	7.9	7.9	30	46	(Bubnova et al., 2016)
$Sr_{0.75}Ba_{0.25}Bi_2B_2O_7$	9.3	9.3	32	50	(Bubnova et al., 2016)
$Sr_{0.5}Ba_{0.5}Bi_2B_2O_7$	8.6	8.6	33	50	(Bubnova et al., 2016)
$Sr_{0.35}Ba_{0.65}Bi_2B_2O_7$	10.6	10.6	33	54	(Bubnova et al., 2016)
$Sr_{0.3}Ba_{0.7}Bi_2B_2O_7$	9.6	9.6	34	53	(Bubnova et al., 2016)
$BaBi_2B_2O_7$	8.3	8.3	34	50	(Bubnova et al., 2016)
			650 °C		
$CaBi_2B_2O_7$	11.9(2)	35.8(3)	−32.6(6)	15.1(3)	(Volkov et al., 2020)

According to (Bubnova et al., 2016), the $Sr_{1-x}Ba_xBi_2B_2O_7$ solid solutions exhibit significantly anisotropic thermal expansion: the *c* parameter increases more intensively than the *a* parameter (Table 3). Maximum thermal expansion is observed along the axis perpendicular to the orientation plane of the BO_3 triangles (*ab*). The thermal expansion coefficients of solid solutions are provided in Table 3.

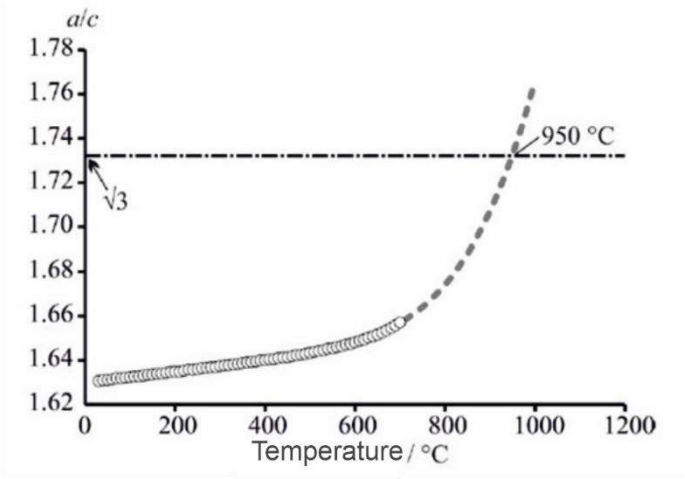

Figure 11 – Temperature dependence of the *a*/*c* unit cell parameters for $CaBi_2B_2O_7$. The dashed line indicates the ideal value of √3, corresponding to the hypothetical hexagonal aristotype structure (Volkov et al., 2020).

1.7.4 Luminescent properties of borates of the $ABi_2B_2O_7$ (*A* = Ca, Sr, Ba) family, activated by REE^{3+} ions

In the study conducted by (Li et al., 2016a), the $CaBi_2B_2O_7:Eu^{3+}$ phosphors emitting in the orange-red region of the spectrum were successfully synthesized. These phosphors are efficiently excited by near ultraviolet light. The chromaticity coordinates are (0.601, 0.392), indicating color purity close to the standard. The $CaBi_2B_2O_7:Eu^{3+}$ phosphors are considered promising for application in w-LEDs with near UV excitation.

In a subsequent study (Li et al., 2016c), the $CaBi_2B_2O_7:Tm^{3+}$ phosphors emitting in the blue region of the spectrum and exhibiting high color purity were first obtained. It was found that the color purity of $CaBi_2B_2O_7:Tm^{3+}$ is higher than that of the commercial blue phosphor $BaMgAl_{10}O_{17}:Eu^{2+}$ (BAM: Eu^{2+}), making them potential candidates for use in w-LEDs with near UV excitation.

Additionally, in the (Li et al., 2017), novel phosphors $CaBi_2B_2O_7:Dy^{3+}$ emitting in the bluish-white region of the spectrum were first obtained. The CIE chromaticity coordinates under near UV excitation are (0.226, 0.228).

The $SrBi_2B_2O_7:Eu^{3+}$ phosphors emitting in the orange-red region of the spectrum were obtained (Li et al., 2018a). Excitation and emission spectra show that this phosphor can be efficiently excited by near ultraviolet light and exhibit bright yellow and red luminescence.

In the (Wu et al., 2017), co-activation of the $SrBi_2B_2O_7$ borate with Eu^{3+} and Sm^{3+} atoms was conducted, leading to improved thermal stability of the phosphors due to the addition of Sm^{3+} ions as sensitizers for Eu^{3+}.

A comparison of the concentration quenching magnitude in the $ABi_2B_2O_7$ (*A* = Ca, Sr, Ba): Eu^{3+} family was carried out in section 3.1.5, page 63.

However, the luminescent properties of the borate matrix $BaBi_2B_2O_7$ and the crystal structures of this matrix activated by rare earth elements have not been previously studied. This work aims to fill existing gaps in the study of the luminescent properties of borate $BaBi_2B_2O_7$, activated and co-activated by rare earth elements, refinement of crystal structures, analysis of cation distribution over sites, and investigation of thermal expansion.

1.8 Borates in the BaO–M_2O_3–B_2O_3 (*M* = Y, Eu) systems

1.8.1 Synthetic borates of the BaO–M_2O_3–B_2O_3 (*M* = Y, Eu) systems

In BaO–M_2O_3–B_2O_3 (*M* = Y, Eu) systems, there are known to be 5 compositions (Figure 12), one of which is represented by high- and low-temperature modifications. All borates in these systems contain isolated B–O groups: BO_3 triangles, B_2O_5 diorthogroups, or B_3O_6 triborate groups.

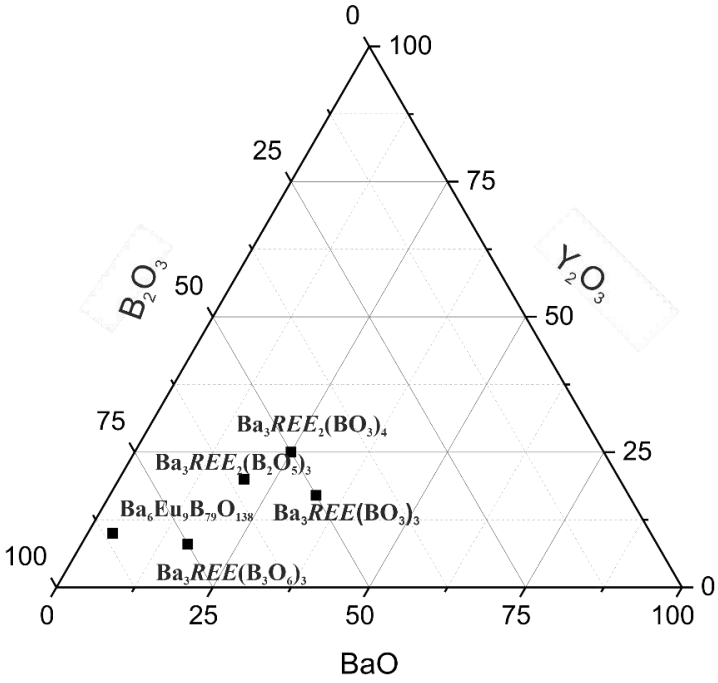

Figure 12 – Known compounds in the ternary BaO–M_2O_3–B_2O_3 systems.

$Ba_3Y(B_3O_6)_3$ (170217-ICSD) is an island borate, crystallizing in a hexagonal crystal system, space group $P6_3/m$, with unit cell parameters a = 7.1766(9), c = 16.9657(6) Å, V = 756.1(1) Å^3, Z = 2 (Li et al., 2004). The crystal structure contains flat isolated triborate groups B_3O_6, parallel to the *ab* planes, composed of three BO_3 triangles. Yttrium atoms are coordinated by six oxygen atoms, while barium atoms are coordinated by six and nine oxygen atoms (Figure 13a).

$Ba_6Eu_9B_{79}O_{138}$ (Cong et al., 2015) is a layered borate. It forms a continuous series of solid solutions with **$Ba_6Bi_9B_{79}O_{138}$** (Krivovichev et al., 2012). The borates crystallize in a trigonal crystal system, space group $R3$. The $Ba_6Eu_9B_{79}O_{138}$ crystal structure is not specified, but it is likely isostructural to $Ba_6Bi_9B_{79}O_{138}$.

The **α-$Ba_3M(BO_3)_3$** modification (97761-ICSD) belongs to island borates, crystallizing in a trigonal crystal system, space group $R\bar{3}$, with unit cell parameters a = 13.028(2), c = 9.4992(2) Å, V = 1396.1(5) Å^3, Z = 6 (Pan et al., 2004). The structure consists of isolated BO_3 triangles (Figure 13b). Yttrium atoms are coordinated by six oxygen atoms, forming nearly perfect YO_6 octahedra, while barium atoms are coordinated by nine oxygen atoms.

The **β-$Ba_3Y(BO_3)_3$** modification (99537-ICSD) also belongs to island borates, crystallizing in a hexagonal crystal system, space group $P6_3cm$, with unit cell parameters a = 9.416(3), c = 17.536(8) Å, V = 1346.6(8) Å^3, Z = 6 (Pan, Wang, 2003). The crystal structure also contains isolated BO_3 triangles and has three independent sites for Ba and Y cations, one of which occupied

both atoms with Ba occupancy at 83.3% and Y at 16.7%. Yttrium atoms are coordinated by six oxygen atoms, while barium atoms are coordinated by nine (Figure 13c).

$Ba_3Y_2(B_2O_5)_3$ (261704-ICSD) is an island borate, crystallizing in a cubic crystal system, which is very rare for borates (approximately 1.18% of compounds), space group $Ia\bar{3}$, with unit cell parameters a = 14.253 (6) Å, V = 2895(2) Å^3, Z = 8 (Zhao et al., 2011). Two flat BO_3 triangles are connected through a common vertex, forming pyroborate B_2O_5 groups. Y atoms are coordinated by six oxygen atoms, forming regular $Y1O_6$ and $Y2O_6$ octahedra. The BO_3 triangles are linked to the YO_6 octahedra by vertices and to the BaO_9 polyhedra by vertices and edges (Figure 13d). The crystal structure forms a framework consisting of large distorted BaO_9 polyhedra.

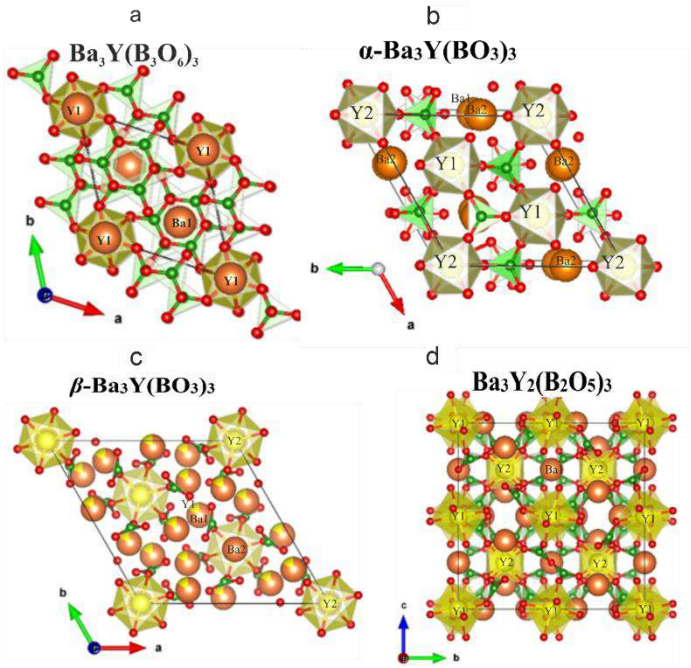

Figure 13 – Crystal structures of $Ba_3Y(B_3O_6)_3$ (170217-ICSD) (a), $Ba_3M(BO_3)_3$ (97761-ICSD) (b), β-$Ba_3Y(BO_3)_3$ (99537-ICSD) (c), $Ba_3Y_2(B_2O_5)_3$ (261704-ICSD) (d) borates are visualized in the Vesta program.

$Ba_3M_2(BO_3)_4$ (M = Y, Eu^{3+}) belong to island borates. The $Ba_3Y_2(BO_3)_4$ borate (155327-ICSD) crystallizes in a orthorhombic crystal system, space group *Pnma*, with unit cell parameters a = 7.6860, b = 16.4968, c = 8.9959 Å, V = 1140.630 Å^3. The structure contains three independent crystallographic sites for cations, two of which are general ($M$1 and $M$2), and one is special ($M$3) (Figure 14). All large cations are disordered over three sites. According to (Ma et al., 2005), the occupancy of sites is as follows: $M$1: Ba – 75.21 %, Y – 24.79 %; $M$2: Ba – 59.49 %, Y – 40.51 %;

*M*3: Ba – 69.39 %, Y – 30.6 %. The **$Ba_3Eu_2(BO_3)_4$** borate (a = 7.6970(15), b = 16.554(3), c = 8.9300(18) Å, V = 1137.8(3) $Å^3$) is isostructural to $Ba_3Y_2(BO_3)_4$ (Chen et al., 2020).

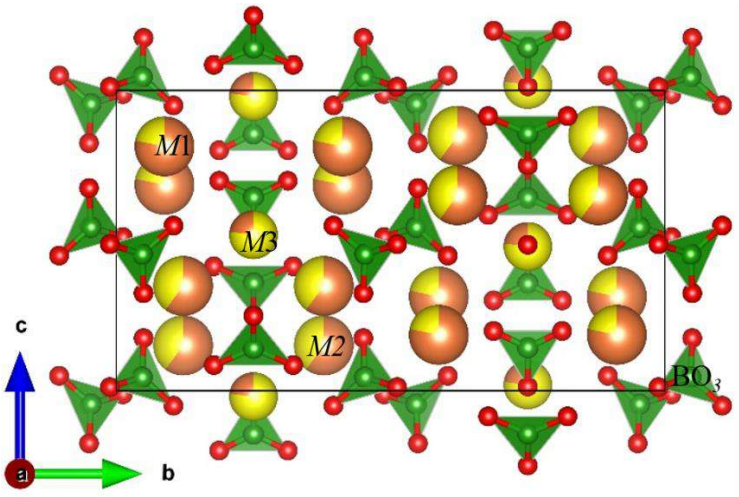

Figure 14 – Crystal structure of $Ba_3Y_2(BO_3)_4$ borate. The structure is visualized in the Vesta program based on data from (155327-ICSD).

1.8.2 Borates of the $A_3M_2(BO_3)_4$ (A = Ca, Sr, Ba, M = *REE*, Bi^{3+}) family

In this section, an analysis of the crystal structures, thermal expansion, and luminescent properties of borates belonging to the $A_3M_2(BO_3)_4$ (A = Ca, Sr, Ba, M = *REE*, Bi^{3+}) family is presented.

In earlier studies, the crystal structures of Sr-containing borates in this family were refined in the space group $Pc2_1n$ (Bambauer, Kindermann, 1978; He, Wang, 2007). Currently, the crystal structures are being refined in the orthorhombic crystal system space group *Pnma* (Khamaganova, 1990; Mill et al., 1998; Pan et al., 2004; Ma et al., 2005; Höppe et al., 2013; Volkov et al., 2013; Shablinskii et al., 2017; Sun et al., 2017; Kosyl et al., 2020). In the borates of the $A_3M_2(BO_3)_4$ (A = Ca, Sr, Ba, M = *REE*, Bi^{3+}) family, atoms of A and M types are disordered over three crystallographic sites. In borates M = Bi^{3+}, site splitting may be observed due to the presence of a stereochemically active lone electron pair. For example, in the $Ba_3Bi_2(BO_3)_4$ borate (Volkov et al., 2013), the *M*1, *M*2, and *M*3 sites are split into Ba and Bi sub-positions. The asymmetry of sites is more pronounced for cationic sites with a higher number of Bi^{3+} atoms. However, in the $Sr_3Bi_2(BO_3)_4$ borate (Shablinskii et al., 2017), cations are disordered over three crystallographic sites, and no splitting is observed, attributed to the smaller difference in ionic radii between $^{[8]}$Ba (1.56 Å) and $^{[8]}$Sr (1.40 Å) compared to $^{[8]}$Bi (1.31 Å) and $^{[8]}$Ba (1.56 Å) (Shannon, 1976). A similar phenomenon was also observed in the $ABi_2B_2O_7$ (A = Sr, Ba) borates studied in this work:

in the $BaBi_2B_2O_7$ borate, atoms of Ba and Bi are disordered over three crystallographic sites (Bubnova et al., 2016), while in the $SrBi_2B_2O_7$ borate (Bubnova et al., 2016), sites splitting is either not observed or is minimal (Shablinskii et al., 2023) (see section 1.7.2, page 26).

The unit cell parameters of the borates belonging to the $A_3M_2(BO_3)_4$ family are presented in Table 4. In the $A_3M_2(BO_3)_4$ (A = Ca, Sr, Ba, M = *REE*, Bi^{3+}) borates, as the ordinal number of the rare earth element increases, the unit cell parameters decrease due to the reduction in atomic and ionic radii (the phenomenon of lanthanide contraction). The (Volkov et al., 2013) provides a graph showing the dependence of the unit cell volume on the ionic radius of the element in the $A_3Ln_2(BO_3)_4$ (A = Ca, Sr, Ba) family (Figure 15).

Table 4 – Unit cell parameters of borates belonging to the $A_3M_2(BO_3)_4$ (A = Ca, Sr, Ba, M = *REE*, Bi^{3+}) family

Compound	*a*, Å	*b*, Å	*c*, Å	*V*, Å^3	Space Group	Reference
$Ca_3La_2(BO_3)_4$	7.279(1)	16.033(3)	8.670(1)	1011.8(2)	*Pc*2$_1$*n*	(Bambauery et al, 1978)
$Ca_3La_2(BO_3)_4$	7.242(1)	16.129(1)	8.688(1)	1014.81	*Pnma*	(Mill et al., 1998)
$Ca_3Pr_2(BO_3)_4$	7.252(1)	15.785(2)	8.664(1)	991.9(2)	*Pc*2$_1$*n*	(Bambauery et al, 1978)
$Ca_3Nd_2(BO_3)_4$	7.235(1)	15.731(2)	8.661(1)	985.79(1)	*Pc*2$_1$*n*	(Bambauery et al, 1978)
$Ca_3Sm_2(BO_3)_4$	7.213(1)	15.603(2)	8.643(1)	972.7(2)	*Pc*2$_1$*n*	(Bambauery et al, 1978)
$Ca_3Eu_2(BO_3)_4$	7.196(1)	15.584(2)	8.633(1)	968.0(2)	*Pc*2$_1$*n*	(Bambauery et al, 1978)
$Ca_3Eu_2(BO_3)_4$	7.20378(2)	15.57492(5)	8.63406(3)	968.7(6)	*Pnma*	(Kosyl et al., 2020)
$Ca_3Gd_2(BO_3)_4$	7.185(1)	15.549(1)	8.617(1)	962.7(1)	*Pc*2$_1$*n*	(Bambauery et al, 1978)
$Ca_3Tb_2(BO_3)_4$	7.176(1)	15.520(2)	8.600(1)	957.8(2)	*Pc*2$_1$*n*	(Bambauery et al, 1978)
$Ca_3Dy_2(BO_3)_4$	7.162(1)	15.487(2)	8.583(1)	952.1(1)	*Pc*2$_1$*n*	(Bambauery et al, 1978)
$Ca_3Y_2(BO_3)_4$	7.153(1)	15.481(2)	8.562(1)	948.1(2)	*Pc*2$_1$*n*	(Bambauery et al, 1978)
$Ca_3Y_2(BO_3)_4$	7.1690(4)	15.4758(8)	8.5587(6)	949.5(1)	*Pnma*	(Wang et al., 2004)
$Ca_3Ho_2(BO_3)_4$	7.149(1)	15.473(2)	8.564(1)	947.4(2)	*Pc*2$_1$*n*	(Bambauery et al, 1978)
$Ca_3Er_2(BO_3)_4$	7.138(1)	15.460(1)	8.547(1)	943.2(1)	*Pc*2$_1$*n*	(Bambauery et al, 1978)
$Ca_3Tm_2(BO_3)_4$	7.143(1)	15.425(1)	8.530(1)	939.8(1)	*Pc*2$_1$*n*	(Bambauery et al, 1978)
$Ca_3Yb_2(BO_3)_4$	7.148(1)	15.359(2)	8.505(1)	933.7(2)	*Pc*2$_1$*n*	(Bambauery et al, 1978)
$Ca_3Lu_2(BO_3)_4$	7.148(1)	15.356(3)	8.491(1)	932.0(2)	*Pc*2$_1$*n*	(Bambauery et al, 1978)

$Sr_3Bi_2(BO_3)_4$	7.5107(5)	16.274(1)	8.8163(5)	1077.6(1)	*Pnma*	(Shablinskii et al., 2017)
$Sr_3La_2(BO_3)_4$	7.435(1)	16.488(2)	8.896(1)	1090.6(1)	$Pc2_1n$	(Bambauery et al, 1978)
$Sr_3Pr_2(BO_3)_4$	7.37(2)	16.45(4)	8.80(2)	1066.9(2)	$Pc2_1n$	(Palkina et al., 1974)
$Sr_3Gd_2(BO_3)_4$	7.406(1)	16.041(1)	8.754(1)	1040.0(1)	$Pc2_1n$	(Bambauery et al, 1978)
$Sr_3Gd_2(BO_3)_4$	7.3859(5)	15.9445(12)	8.7003(6)	1024.5(1)	*Pnma*	(Sun et al., 2017)
$Sr_3Ho_2(BO_3)_4$	7.3845(7)	15.915(1)	8.7103(9)	1023.7(2)	*Pnma*	(Höppe et al., 2013)
$Sr_3Er_2(BO_3)_4$	7.22(2)	15.80(5)	8.57(3)	977.6(2)	$Pc2_1n$	(Abdullaev, Mamedov, 1976)
$Sr_3Er_2(BO_3)_4$	7.3808(2)	15.8894(4)	8.6781(2)	1017.7(4)	*Pnma*	(Höppe et al., 2013)
$Sr_3Yb_2(BO_3)_4$	7.377(1)	15.891(1)	8.664(1)	1015.7(1)	$Pc2_1n$	(Bambauery et al, 1978)
$Sr_3Yb_2(BO_3)_4$	7.3750(8)	15.9265(14)	8.6776(9)	1019.2(2)	*Pnma*	(Lin et al., 2013)
$Sr_3Y_2(BO_3)_4$	8.6936(3)	15.9706(6)	7.3912(3)	1025.6(2)	*Pnma*	(Zhang, Li, 2004)
$Sr_{1.5}Ba_{1.65}Bi_2(BO_3)_4$	7.7649(4)	16.836(1)	8.8317(6)	1154.6(1)	*Pnma*	(Шаблинский и др., 2022)
$Ba_3Bi_2(BO_3)_4$	7.9508(5)	17.399(1)	8.9791(5)	1242.1(1)	*Pnma*	(Volkov et al., 2013)
$Ba_3La_2(BO_3)_4$	7.758(1)	17.097(2)	9.025(1)	1197.0(2)	$Pc2_1n$	(Bambauery et al, 1978)
$Ba_3La_2(BO_3)_4$	7.734(2)	17.043(4)	9.056(3)	1193.6(8)	*Pnma*	(Khamaganova, 1990)
$Ba_3Pr_2(BO_3)_4$	7.733(1)	16.843(2)	9.009(1)	1173.2(7)	*Pnma*	(Khamaganova, 1990)
$Ba_3Nd_2(BO_3)_4$	7.7143(1)	16.7790(3)	8.948(1)	1158.2(2)	*Pnma*	(Yan, Hong, 1987)
$Ba_3Eu_2(BO_3)_4$	7.697(1)	16.554(3)	8.930(2)	1137.8(4)	*Pnma*	(Chen et al., 2020)
$Ba_3Gd_2(BO_3)_4$	7.708(1)	16.578(2)	8.943(1)	1142.8(2)	$Pc2_1n$	(Bambauery et al, 1978)
$Ba_3Y_2(BO_3)_4$	7.68(1)	16.51592)	9.009(1)	1142.7(2)	*Pnma*	(Ma et al., 2005)

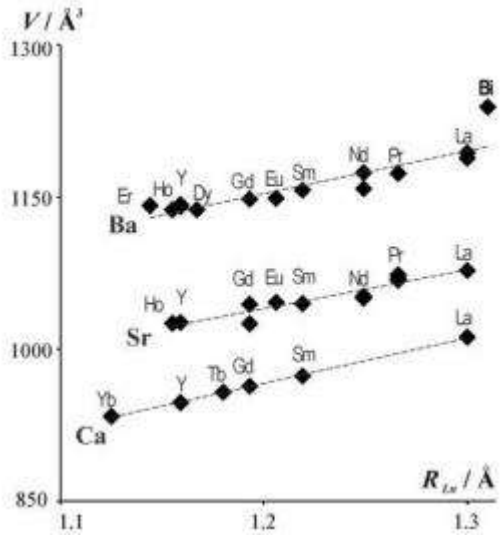

Figure 15 – Graph showing the dependence of volume on the ionic radii of the atom in the $A_3Ln_2(BO_3)_4$ (A = Ca, Sr, Ba) family (Volkov et al., 2013).

This work pays significant attention to the distribution of cations over *M*1-*M*3 sites. A comparison of the site occupancies in $A_3M_2(BO_3)_4$ borates, along with an analysis and discussion of the results, are presented below (see section 4.8.1, page 114).

1.8.3 Thermal expansion of borates of the $A_3M_2(BO_3)_4$ (*A* = Ca, Sr, Ba, *M* = *REE*, Bi^{3+}) family

One of the characteristic features of borates of the $A_3M_2(BO_3)_4$ (*A* = Ca, Sr, Ba, *M* = *REE*, Bi^{3+}) family is their thermal expansion. This section presents an analysis of the literature data regarding the behavior of borates in the family with increasing temperature, as one of the aims of this study is to identify patterns and the nature of such thermal properties.

The thermal expansion of the **$Ba_3Bi_2(BO_3)_4$** borate was investigated in the study (Volkov et al., 2013). Maximum thermal expansion is observed along the *a*-axis, perpendicular to the preferred orientation of the triangular BO_3 radicals. Analysis of the temperature dependence graphs of the unit cell parameters reveals a bend at a temperature of 600 °C (Figure 16a). The authors suggest that at 600 °C, there may be a redistribution of Ba and Bi atoms among the *M* sites. Furthermore, all three cation sites are split, and with increasing temperature, the split sites are believed to pairwise merge into one.

In the graphs showing the temperature dependence of the unit cell parameters for the **$Sr_3Bi_2(BO_3)_4$** borate (Figure 16b), bends are observed at approximately 500 °C. This phenomenon is explained by the possible redistribution of Sr-Bi cations among the sites. Sr atoms predominantly occupy *M*1 and *M*2 sites, while Bi^{3+} atoms occupy the smallest polyhedral *M*3 site. Heating may lead to an increase in the size of the polyhedron at *M*3 site due to increased thermal vibrations, resulting in the redistribution of Sr^{2+} and Bi^{3+} among *M*1, *M*2, and *M*3 sites. Maximum thermal expansion is also observed along the *a*-axis.

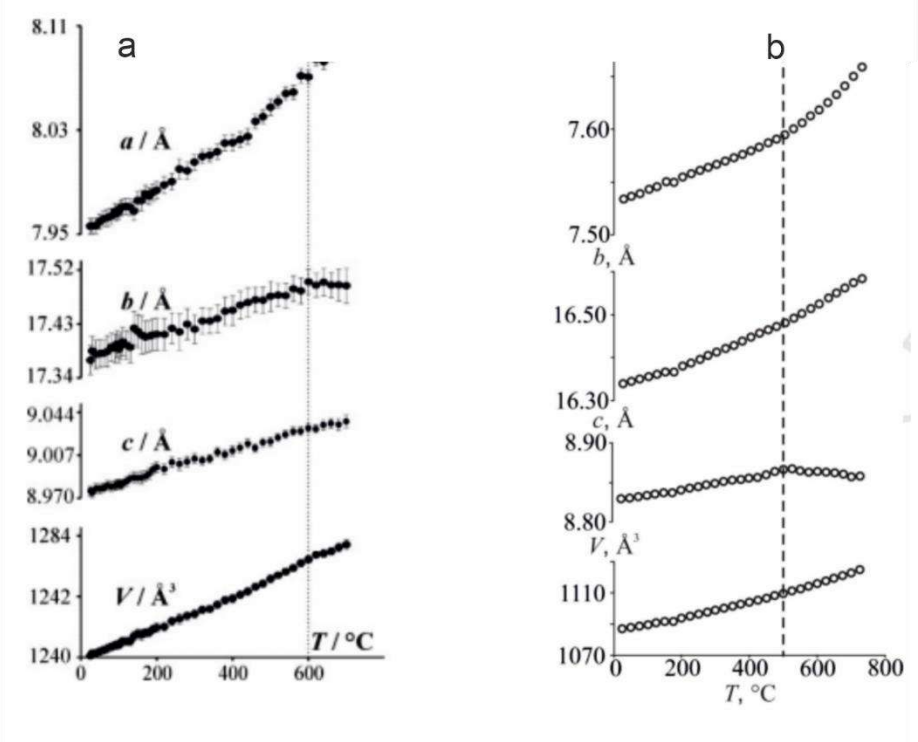

Figure 16 – Dependencies of the unit cell parameters on the temperature of the $Ba_3Bi_2(BO_3)_4$ (Volkov et al., 2013) (a) and $Sr_3Bi_2(BO_3)_4$ (Shablinskii et al., 2017) (b) borates.

In the study conducted by (Shablinskii et al., 2022), the thermal expansion of the **$Sr_{1.5}Ba_{1.5}Bi_2(BO_3)_4$** borate was investigated. Distortions are observed in the dependencies of the unit cell parameters at a temperature of 500 °C (Figure 17). The authors of the study identify several possible reasons for the observed phenomenon: firstly, the redistribution of cations among sites may have an influence. In the $Sr_{1.35}Ba_{1.65}Bi_2(BO_3)_4$ crystal structure, the *M*1 and *M*3 sites are split, and *M*2 site with a larger polyhedron size is occupied by Ba atoms with a larger ionic radius. As the temperature increases, the atomic displacements parameters increase, which may lead to the partial erasure of boundaries between cations. Additionally, it is found that at a temperature of 450 °C, the $(Sr,Ba)Bi_2B_2O_7$ phase crystallization occurs, which may affect the nature of thermal expansion.

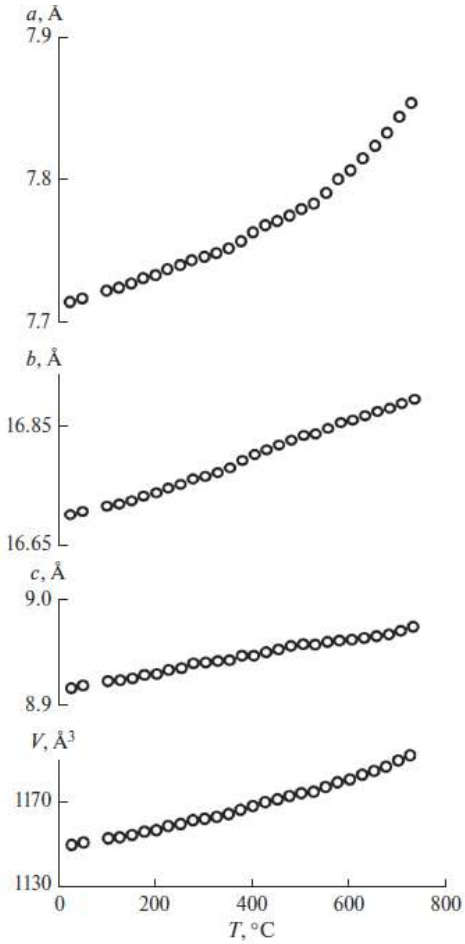

Figure 17 – Dependencies of the unit cell parameters on the temperature of the $Sr_{1.5}Ba_{1.5}Bi_2(BO_3)_4$ borate 4 (Shablinskii et al., 2022).

The thermal expansion of the **$Ca_3Eu_2(BO_3)_4$** borate has been studied by (Kosyl et al., 2020). A bend in the graphs of the dependencies of the unit cell parameters on temperature is observed at 650 °C (Figure 18a). The authors explain this phenomenon by suggesting that the bend may be caused by changes in the occupancies of the *M*1-*M*3 sites with increasing temperature (Figure 18b). Approximately up to 923 K (650 °C), the distribution of Ca/Eu atoms remains relatively constant. As the temperature increases, the occupancy of Eu atoms in the *M*2 site increases, while in the *M*3 site it decreases. The occupancy of Ca/Eu atoms in *M*1 site remains approximately constant. At temperatures above 650 °C, the distribution of Ca/Eu atoms becomes increasingly homogeneous with increasing temperature. The maximum thermal expansion of the $Ca_3Eu_2(BO_3)_4$ borate is observed along the *b*-axis, which differs from the expansion of other borates in the $A_3M_2(BO_3)_4$ (*A* = Ca, Sr, Ba, *M* = *Ln*, Y, Bi) family. In section 4.8.2, page 117, data on the analysis of the thermal expansion of borates in the family and possible reasons for the deviation in the behavior of the $Ca_3Eu_2(BO_3)_4$ borate from other borates in the family are presented.

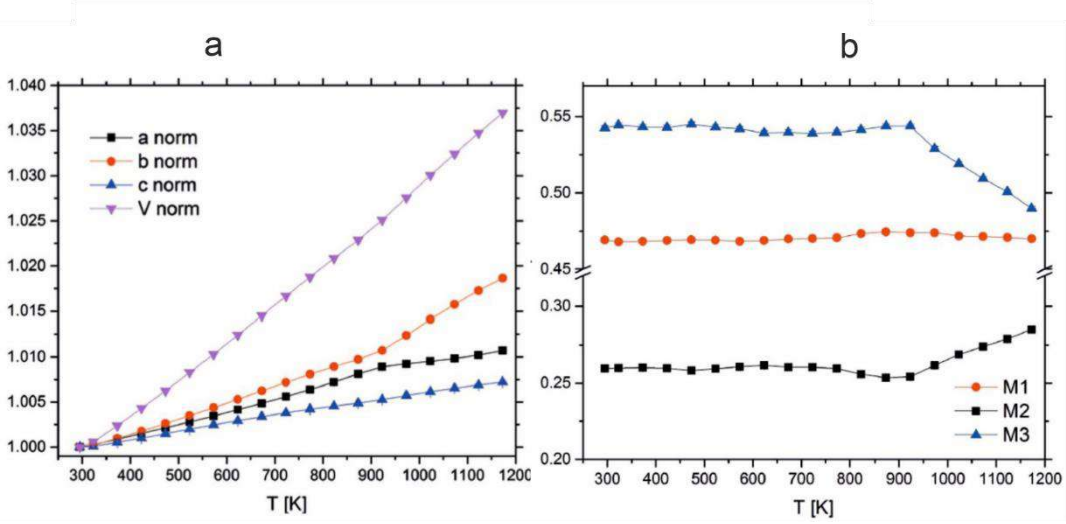

Figure 18 – Graphs of the dependencies of normalized unit cell parameters on temperature (a) and sites occupancies on temperature in the $Ca_3Eu_2(BO_3)_4$ borate (b) (Kosyl et al., 2020).

1.8.4 Luminescent properties of borates of the $A_3M_2(BO_3)_4$ (*A* = Ca, Sr, Ba, *M* = *REE*, Bi^{3+}) family

The first known phosphors in the $A_3M_2(BO_3)_4$ (*A* = Ca, Sr, Ba, *M* = *REE*, Bi^{3+}) family (were discovered in the (Postolov, Benderskaya,1975) based on borates $A_3M_2(BO_3)_4$ activated by Tb^{3+} atoms, leading to the development of green-emitting phosphors. These photoluminescent materials exhibit stability and luminescent properties comparable to industrial phosphor $ZnS:Mn^{2+}$. Testing samples of $Sr_3La_2(BO_3)_4:Tb^3$ under high-density excitation in fluorescent lamps (W = 150 W) showed a luminous efficacy of 82.3% after 100 hours of illumination. Subsequently, these studies initiated active research on phosphors within this family.

One of the main applications of these phosphors is in the creation of materials for white light-emitting diodes (wLEDs), achieved through the combination of red, green, and blue colors (RGB). Recent research, such as (Chen et al., 2020), led to the development of red-emitting phosphors $Ba_3Eu_2(BO_3)_4$ and $Sr_3Eu_2(BO_3)_4$, closely resembling industrial phosphor $Y_2O_2S:Eu^{3+}$ in color but demonstrating significantly higher quantum efficiency values of 90.09% and 44.48%, respectively. Additionally, studies by (Shablinskii et al., 2017; Shablinskii et al., 2019) on $Sr_3Bi_2(BO_3)_4:Eu^{3+}$ and $Ba_3Bi_2(BO_3)_4:Eu^{3+}$ borates yielded promising thermally stable red-emitting phosphors comparable in emission intensity to industrial YAG and Y_2O_3. Investigations by (Su et al., 1993) focused on the highly sensitive transitions of Dy^{3+} ions in polycrystalline $A_3M_2(BO_3)_4$ (*A* = Ca, Sr, Ba, *M* = *REE*, Bi^{3+}) matrices, as Dy^{3+} ions emit light in the blue and yellow spectra,

making them potential activators for dual-color phosphors. The $Sr_3Y_2(BO_3)_4$: Dy^{3+} borates characterized by white emission (Li et al., 2008) could be utilized in white LED production.

Furthermore, the $A_3M_2(BO_3)_4$ (*A* = Ca, Sr, Ba, *M* = *REE*, Bi^{3+}) family phosphors are being studied for materials suitable for solid-state lasers. For instance, spectroscopic studies on $Ca_3Gd_2(BO_3)_4$ and $Ca_3La_2(BO_3)_4$ crystals activated by Er^{3+}/Yb^{3+} ions (Wei et al., 2004) revealed high absorption coefficients (22 and 14.5 nm^{-1}, respectively) and full width at half maximum (7 and 9 nm) for the absorption band in the 900—1050 nm range, suitable for InGaAs laser diode pumping. The fluorescence lifetime (τ) of these borate crystals was significantly shorter compared to other compounds like yttrium aluminum garnet $Y_3Al_5O_{12}$ (YAG). The $Ba_3Y_2(BO_3)_4$ (Ma et al., 2007), $Sr_3Gd_2(BO_3)_4$ (Sun et al., 2017), $Sr_3La_2(BO_3)_4$ (Yuan et al., 2017),:$Sr_3Y_2(BO_3)_4$:Er^{3+},Yb^{3+} (Huang et al., 2013) borates have also been considered as promising laser media.

Therefore, the $A_3M_2(BO_3)_4$ (*A* = Ca, Sr, Ba, *M* = *REE*, Bi^{3+}) family borates hold potential for applications in wLEDs and as prospective media for solid-state lasers, underscoring their versatility and significance in optoelectronics.

1.8.5 Natural and synthetic compounds isostructural to $A_3M_2(BO_3)_4$ (*A* = Ca, Sr, Ba, *M* = *REE*, Bi^{3+}) borates

At present, the mineral compositions of $A_3M_2(BO_3)_4$ (*A* = Ca, Sr, Ba, *M* = *REE*, Bi^{3+}) are unknown. However, the existence of the mineral peprossite-(Ce) $Ce_2Al_3(B_4O_{10})O$ (Della et al., 1993) in nature suggests that the formation of borates with rare earth elements is not impossible.

In the study (Rashchenko et al., 2022), the synthesis method under high pressures yielded β-$K_2Ca_3(CO_3)_4$, isotypic to borates of the $A_3M_2(BO_3)_4$ family. The carbonate also crystallizes in the space group *Pnma*, with unit cell parameters *a* = 7.5371(2) Å, *b* = 16.1777(5) Å, *c* = 8.7793(3) Å. The $A_3M_2(BO_3)_4$ borates and β-$K_2Ca_3(CO_3)_4$ carbonate exhibit a similar, disordered motif in their crystal structures: in the β-$K_2Ca_3(CO_3)_4$ structure, there are three independent crystallographic sites for large cations, one of which (*M*2) is occupied only by Ca^{2+} atoms, while the other two (*M*1 and *M*3) are occupied by Ca^{2+} and K^+ atoms. The research on the synthesis and study of the crystal structure of β-$K_2Ca_3(CO_3)_4$ is inspired by recent studies on modeling processes occurring in the mantle (Arefiev et al., 2019), which established that under mantle conditions in the K_2CO_3–$CaCO_3$–$MgCO_3$ system, high-temperature intermediate phases are formed, with $K_2Ca_3(CO_3)_4$ being one of them. Let us delve further into the assumptions and findings of the study of the K_2CO_3–$CaCO_3$–$MgCO_3$ system.

The presence of crystalline carbonates at various mantle levels is due to the presence of magnesite, dolomite, calcite, and/or aragonite in spinel peridotites, xenoliths of eclogites (Pyle,

Haggerty, 1994), primary inclusions in Cr-pyropes (Nikolenko et al., 2017), and in diamonds originating from the base of the continental lithosphere and deeper levels (Shatsky et al., 2019). Ca-Mg carbonates are also found as rock-forming minerals and inclusions in high-pressure minerals in diamond-bearing metamorphic rocks of ultra-high pressure, exhumed from depths of 150—250 km (Sobolev, Shatsky, 1990). The inclusions retain high internal pressure, suggesting a mantle origin of the captured melt (Navon, 1991). Recently, this melt was also discovered as micro-inclusions in the central part of a high-quality gem diamond crystal (Logvinova et al., 2019). Experimental evidence shows that potassium-rich carbonate melts of the upper mantle could have formed through partial melting of carbonate-bearing pelites (Tsuno et al., 2012) at pressures of 5–8 GPa (Figure 19).

Based on the modeling of processes occurring in the mantle, scientists in the work (Arefiev et al., 2019) were able to identify the decomposition products of carbonatite melt in the K_2CO_3–$CaCO_3$–$MgCO_3$ system. It has been established that under mantle conditions, the K_2CO_3–$CaCO_3$–$MgCO_3$ system forms several intermediate compounds, represented by double carbonates of alkali and alkali-earth metals. At a pressure of 3 GPa and 750°C, the low-pressure carbonates include $K_2Mg(CO_3)_2$, $K_2Ca_2(CO_3)_2$, and buchliite $K_2Ca(CO_3)_2$, which is also stable at atmospheric pressure (Figure 20 a, b). At higher pressures and temperatures, the stability field of these compounds changes: $K_2Mg(CO_3)_2$ remains stable up to 1250°C, while the stability of $K_2Ca_2(CO_3)_2$ is limited to approximately 990°C. The decomposition of $K_2Ca(CO_3)_2$ leads to the formation of high-pressure carbonates $K_8Ca_3(CO_3)_7$ and $K_2Ca_3(CO_3)_4$ (Figure 20 c).

Although high-pressure carbonates $K_8Ca_3(CO_3)_7$ and $K_2Ca_3(CO_3)_4$ have not been found in diamonds, their high melting temperatures suggest the possibility of co-crystallization with diamond and entrapment as inclusions (Arefiev et al., 2019).

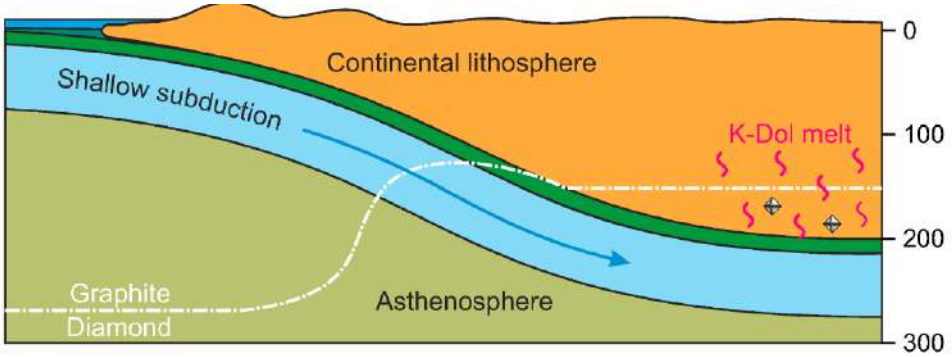

Figure 19 – Geological settings of carbonatite melt formation, embedded in diamonds (Arefiev et al., 2019).

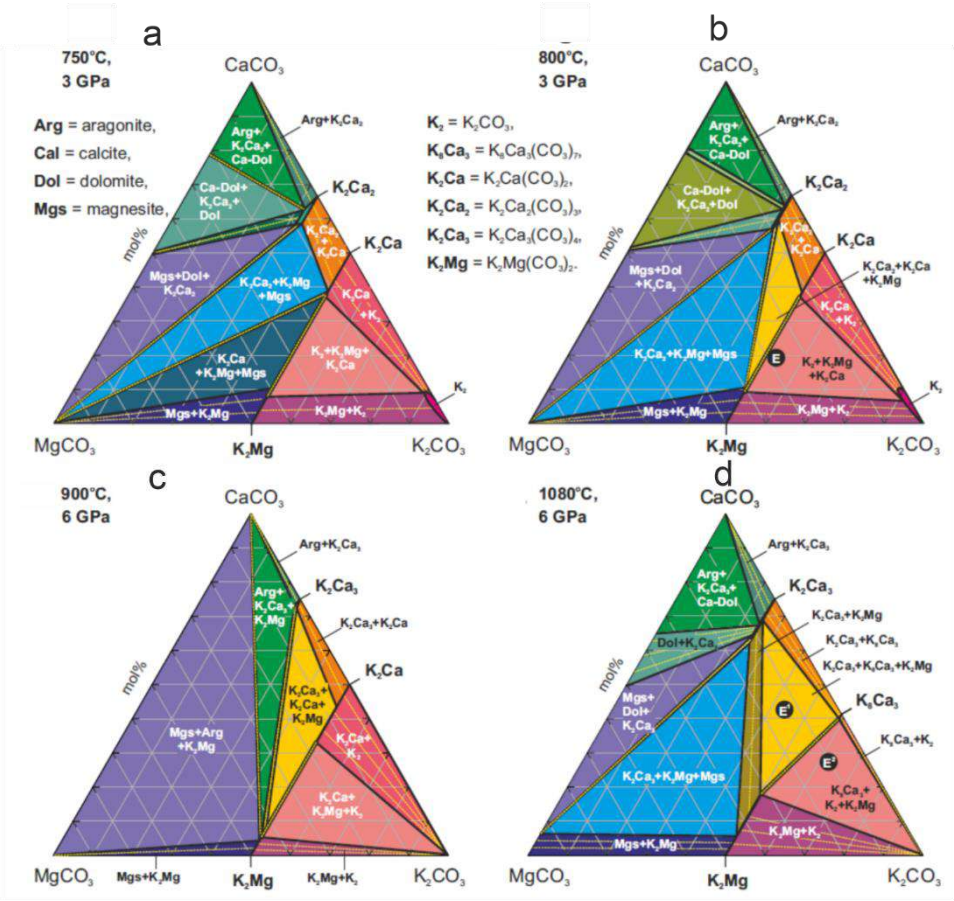

Figure 20 – Isothermal and isobaric sections of the *T-X* diagram of the K_2CO_3–$CaCO_3$–$MgCO_3$ system at 3 GPa, 750°C (a) and 800°C (b) (Arefiev et al., 2019a) and at 6 GPa, 900°C (c) and 1080°C (d) (Arefiev et al., 2019). E, E1, and E2 denote eutectic points.

1.9 Conclusion to the chapter 1

The borates of the $A_3M_2(BO_3)_4$ (A = Ca, Sr, Ba, M = *REE*, Bi^{3+}) family are widely studied for their potential application as matrices for phosphors in white light-emitting diodes and in laser materials (Tu et al., 2004a; Tu et al., 2004b; Wang et al., 2006; Wei et al., 2006; Ma et al., 2007a; Li et al., 2008b; Pan et al., 2013). Some studies have focused on borates such as $Ba_3Eu_2(BO_3)_4$ (Chen et al., 2020) and thermally stable $Ba_3Bi_2(BO_3)_4:Eu^{3+}$ (Shablinskii et al., 2019) for white light-emitting diodes. Incomplete data on the activation of the crystalline matrix $A_3M_2(BO_3)_4$ by rare earth element atoms and the search for effective matrices for phosphors stimulate research development in this area.

The crystal structure of the borate $Ba_3Y_2(BO_3)_4$ has been partially characterized (Ma et al., 2005) only in an isotropic approximation. Data on the thermal expansion of the $Ba_3Eu_2(BO_3)_4$ and $Ba_3Y_2(BO_3)_4$ borates, and the luminescent properties of the borate $Ba_3Y_2(BO_3)_4$ activated by Er^{3+}

are unknown. Based on this, the $Ba_3Eu_2(BO_3)_4$ and $Ba_3Y_2(BO_3)_4:Er^{3+}$ borates were selected as objects of the present study.

The borates of the $ABi_2B_2O_7$ (*A* = Ca, Sr) family have also demonstrated promising luminescent properties: the borates $CaBi_2B_2O_7:Eu^{3+}$ (Li et al., 2016a), $CaBi_2B_2O_7:Tm^{3+}$ (Li et al., 2016c), and $CaBi_2B_2O_7:Dy^{3+}$ (Li et al., 2017) exhibit color purity comparable to or surpassing commercial analogs. These materials are promising for w-LEDs pumped in the near UV. The $SrBi_2B_2O_7:Eu^{3+}$ luminescent phosphors emitting in the orange-red region of the spectrum are known (Li et al., 2018a). In the (Wu et al., 2017), co-activation with Eu^{3+} and Sm^{3+} ions was carried out, leading to increased thermal stability of the phosphor due to the addition of Sm^{3+} ions as sensitizers for Eu^{3+}.

However, the luminescent properties of the $BaBi_2B_2O_7$ borate matrix activated by rare earth elements have not been previously studied, nor have investigations into the occupancies of crystallographic sites during the activation of the crystalline matrix by rare earth elements. Therefore, in the present study, the borates, based on $BaBi_2B_2O_7$ martix, activated and co-activated by rare earths: $BaBi_{2-x-y-z}REE_{x,x,z}B_2O_7$ (*REE* = Eu^{3+}, Sm^{3+}, Tb^{3+}, Tm^{3+}) are the objects of investigation.

Chapter 2. Experimental part and research methodology

In this chapter, the synthesis methods used to obtain the borates studied in this work are described, along with the methods of investigation employed. Specifically, during the research for this dissertation, 42 samples were obtained through crystallization from melt and glass ceramics methods. The author of this work successfully synthesized all the investigated borates: $BaBi_{2-x}Eu_xB_2O_7$ (x = 0.05, 0.1, 0.15, 0.2, 0.3, 0.4, 0.5), $BaBi_{2-x}Sm_xB_2O_7$ (x = 0.05, 0.1, 0.15, 0.2, 0.3, 0.4, 0.5), $BaBi_{2-x-0.05}Eu_xSm_{0.05}B_2O_7$ (x = 0.35, 0.4, 0.45), $BaBi_{2-0.15-y}Eu_{0.15}Sm_yB_2O_7$ (y = 0.05, 0.1, 0.15, 0.2, 0.25), $BaBi_{2-x}Tb_xB_2O_7$ (x = 0.05, 0.1, 0.15, 0.2, 0.3, 0.4, 0.5), $BaBi_{2-x-0.3}Eu_xTb_{0.15}Tm_{0.15}B_2O_7$ (x = 0.05, 0.1, 0.15, 0.2), $Ba_3Eu_2(BO_3)_4$, $Ba_3Y_{2-x}Er_x(BO_3)_4$ (x = 0, 0.01, 0.05, 0.1, 0.15, 0.2, 0.25, 0.3). The synthesis was carried out at branch of the National Research Center "Kurchatov Institute" - Petersburg Institute of Nuclear Physics - I.V. Grebenshchikov Institute of Silicate Chemistry (branch of the National Research Center KI - PINP - ISC) in the laboratory of oxide structural chemistry.

X-ray diffraction experiments, such as powder diffraction (XRPD), high-temperature powder X-ray diffraction, single crystal X-ray diffraction were performed at the St. Petersburg State University research park "Centre for X-ray Diffraction Studies" – "Centre XRD". Powder diffraction data collection was conducted by the author of this work. high-temperature powder X-ray diffraction expriments was performed by Ph.D., Assoc. Prof. M.G. Krzhizhanovskaya. Single crystal selection and experimentation were carried out jointly with Ph.D., Senior Researcher A.P. Shablinskii. Thermal analysis was conducted at the Kurchatov Institute National Research Center, in the I.V. Grebenshchikov Institute of Silicate Chemistry by Ph.D., Senior Researcher V.L. Ugolkov. IR, luminescence and luminescence excitation spectra, and light scattering combination were obtained using equipment from the Resource Center "Optical and Laser Methods of Substance Research" "OLMIV" SPbSU by Dr., Assoc. Prof. A.V. Povolotsky.

Data processing and analysis were carried out at the branch of the National Research Center KI - PINP - ISC.

2.1 Synthesis Methods

In the present study, two synthesis methods were used: the $BaBi_{2-x}Eu_xB_2O_7$, $BaBi_{2-x}Sm_xB_2O_7$, $BaBi_{2-x-0.05}Eu_xSm_{0.05}B_2O_7$, $BaBi_{2-0.15-y}Eu_{0.15}Sm_yB_2O_7$, $BaBi_{2-x}Tb_xB_2O_7$, $BaBi_{2-x-0.3}Eu_xTb_{0.15}Tm_{0.15}B_2O_7$ borates were obtained by crystallization from glass-ceramics, and the $Ba_3Eu_2(BO_3)_4$, $Ba_3Y_{2-x}Er_x(BO_3)_4$ borates were crystallized from melt.

The amounts of initial reagents Y_2O_3 (ACS), Eu_2O_3 (ACS), Sm_2O_3 (ACS), Tm_2O_3 (ACS), Tb_4O_7 (ACS), Er_2O_3 (ACS), $BaCO_3$ (ACS), H_3BO_3 (CP), Bi_2O_3 (ACS) were calculated for the synthesis of borates using the following chemical reaction equations:

$(2\text{-}x)Bi_2O_3 + xREE_2O_3 + 2BaCO_3 + 4H_3BO_3 = 2BaBi_{2-x}REE_xB_2O_7 + 6H_2O + 2CO_2\uparrow$, ($REE$ = Eu^{3+}, Sm^{3+});

$2\cdot(2\text{-}x)Bi_2O_3 + xTb_4O_7 + 4BaCO_3 + 8H_3BO_3 = 4BaBi_{2-x}REE_xB_2O_7 + 12H_2O + 4CO_2\uparrow + (^1/_2\, x)O_2\uparrow$;

$2\cdot(2\text{-}x)Bi_2O_3 + 2xEu_2O_3 + yTb_4O_7 + 2zTm_2O_3 + 4BaCO_3 + 8H_3BO_3 = 4BaBi_{2-x-y-z}REE_xREE_yREE_zB_2O_7 + 12H_2O + 4CO_2\uparrow + (^1/_2\, x)O_2\uparrow$;

$2Y_2O_3 + 6BaCO_3 + 8H_3BO_3 \rightarrow 2Ba_3Y_2(BO_3)_4 + 12H_2O + 6CO_2\uparrow$;

$2Eu_2O_3 + 6BaCO_3 + 8H_3BO_3 \rightarrow 2Ba_3Eu_2(BO_3)_4 + 12H_2O + 6CO_2\uparrow$;

$2\text{-}xY_2O_3 + xEr_2O_3 + 6BaCO_3 + 8H_3BO_3 \rightarrow 2Ba_3Y_{2-x}Er_x(BO_3)_4 + 12H_2O + 6CO_2\uparrow$.

For the synthesis of the $BaBi_{2-x}Tb_xB_2O_7$, $BaBi_{2-x-0.3}Eu_xTb_{0.15}Tm_{0.15}B_2O_7$ borates, a mixed-valence $Tb_4^{3-4+}O_7$ reagent was used. Chemical compounds with oxidation states of 3+ and 4+ are amphoteric and can form anionic forms with oxygen. The formula can also be represented as $Tb_2^{3+}Tb_2^{4+}O_7$. Tb^{4+} atoms can only exist in anionic complexes with oxygen. Thus, introducing $Tb_2^{3+}Tb_2^{4+}O_7$ into the crystal structure with other anionic complexes (in this case – BO_3) leads to redox reactions with the formation of Tb^{3+} and the release of molecular oxygen (Serebrennikov, 1959; Korzanov, Shulgina, 2007).

In order to remove surface water from the reagents, Y_2O_3, Eu_2O_3, Sm_2O_3, Tm_2O_3, Tb_4O_7, and Er_2O_3 were pre-dried in a muffle furnace LOIP LF 7/13-G1 at a temperature of 900 °C/1 h, while $BaCO_3$ and Bi_2O_3 were dried at a temperature of 600 °C/3 h. The dried reagents were weighed using high-precision laboratory analytical balances KERN ABJ 120-4M series (weighing accuracy up to 0.1 mg). The grinding of the reagents was carried out using a planetary ball mill Retsch for one hour. After grinding, the samples were placed in a muffle furnace at 600 °C/3 h for decarbonization, followed by further grinding using agate mortar and pestle. Subsequently, the samples were pressed into tablets using a hydraulic press PGR-10 and round-section press molds from LabTools made of high-quality tool steel, with a diameter of 10 mm. After completing the aforementioned steps, synthesis was conducted using crystallization methods from glass-ceramics and melt.

2.1.1 Crystallization from Glass-Ceramics

The synthesis of borates based on the crystalline matrix $BaBi_2B_2O_7$ was carried out through crystallization from glass-ceramics using the methodology (Shablinskii et al., 2012; Bubnova et al., 2016). During the synthesis of the $Sr_{1-x}BaBi_2B_2O_7$ solid solutions, the cooling of the melt led to the formation of grains inside the glass phase, within which crystals measuring 0.1–0.2 μm were observed at the center (Shablinskii et al., 2012). The x-ray powder diffraction patterns also indicated the presence of amorphous and crystalline phases, which were evaluated in a ratio of 9:1 (Shablinskii et al., 2012). The glass transition temperature of the $BaBi_2B_2O_7$ borate is 369.5 °C, and the temperature of the onset of crystallization is 403 °C (Bubnova et al., 2016).

After the selection of powders, grinding, decarbonization, re-grinding, and pressing into tablets (detailed description provided above), the tablets were placed in platinum crucibles and then into a high-temperature furnace with a hold at 900°C/1 h. The obtained melt was poured onto a cold substrate to obtain glass-ceramics. Below (Figure 21), x-ray powder diffraction patterns of the $BaBi_{2-x}Eu_xB_2O_7$ glass-ceramics are presented, confirming the presence of amorphous and crystalline phases and showing compliance with the literature data (Shablinskii et al., 2012). The obtained samples of glass-ceramics were placed in a high-temperature furnace and held at a temperature of 500 °C/5 h. As a result, homogeneous crystalline samples were obtained.

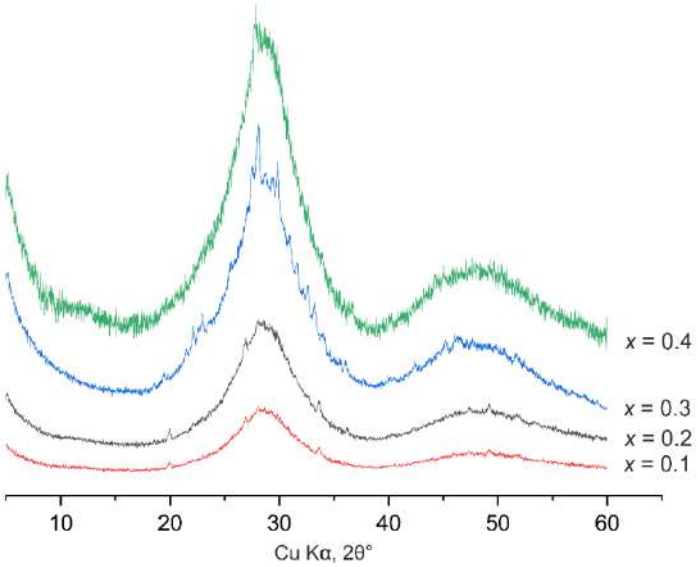

Figure 21 – X-ray powder diffraction patterns of the $BaBi_{2-x}Eu_xB_2O_7$ glass-ceramics.

2.1.2 Obtaining Poly- and Monocrystals from Melt

The $Ba_3Eu_2(BO_3)_4$, $Ba_3Y_2(BO_3)_4$ borates, and the $Ba_3Y_{2-x}Er_x(BO_3)_4$ (x = 0.01, 0.05, 0.1, 0.15, 0.2, 0.25, 0.3) series of solid solutions were obtained through the crystallization from melt method. The synthesis temperatures were selected based on literature data (Ma et al., 2005), which indicate that the melting temperature of the $Ba_3Y_2(BO_3)_4$ borate is 1222 °C. After the selection of powders, grinding, decarbonization, re-grinding, and pressing into tablets (detailed description provided above), the tablets were placed on platinum substrates and placed in a high-temperature furnace for 1 hour at a temperature of 1300 °C, followed by slow cooling over 10 hours. The polycrystals of the obtained samples were separated by mechanically removing the crystallized melt from the platinum substrate.

2.2 Investigation Methods

2.2.1 X-ray Diffraction Methods

In this section, the equipment used for conducting X-ray diffraction studies, experimental conditions, and software packages employed for initial processing of experimental results are listed.

2.2.1.1 X-ray Powder diffraction (XRD)

To investigate the phase composition of the obtained borates, X-ray powder diffraction method was utilized.

Equipment and experimental conditions. Powder diffraction data were collected using the Rigaku MiniFlex II diffractometer. Samples for the experiment were applied to a substrate by deposition from an alcohol suspension.

When capturing the $BaBi_{2-x-y-z}REE_{x,x,z}B_2O_7$ (*REE* = Eu^{3+}, Sm^{3+}, Tb^{3+}, Tm^{3+}) borates, the following conditions were used: CuKα radiation, λ = 1.5406 Å, 2θ = 5–80°, step 0.02°, scanning speed 3 deg./min.

When conducting X-ray powder diffraction of the $Ba_3Y_{2-x}Er_x(BO_3)_4$ and $Ba_3Eu_2(BO_3)_4$ borates, the shooting conditions were as follows: CuKα radiation, λ = 1.5406 Å, 2θ = 5–60°, step 0.02°, heating rate 3 deg./min.

The phase composition was determined by comparing the positions of reflections (2θ) and their intensities between the diffraction patterns from the card index and experimental data. For

this purpose, the PDXL X-ray powder diffraction complex (Sasaki, 2010) and the PDF-2 2016 database (ICDD) were used. Structural files *.cif were taken from the ICSD database.

Calculation of unit cell parameters was performed using the Rietveld To Tensor software package (Bubnova et al., 2018).

2.2.1.2 Single crystal X-ray diffraction

Refinement of the crystal structures based on single crystal data was carried out for the $BaBi_{1.90}Eu_{0.10}B_2O_7$, $BaBi_{1.80}Eu_{0.20}B_2O_7$, $BaBi_{1.60}Eu_{0.40}B_2O_7$, $BaBi_{1.95}Sm_{0.05}B_2O_7$, $BaBi_{1.70}Sm_{0.30}B_2O_7$, $BaBi_{1.90}Tb_{0.10}B_2O_7$, $BaBi_{1.70}Tb_{0.30}B_2O_7$, $BaBi_{1.60}Tb_{0.40}B_2O_7$, $Ba_3Y_2(BO_3)_4$ borates.

Preparation of single crystals. Crystals suitable for analysis were selected using a Leica EZ4 optical microscope. The crystals were attached to a glass fiber using epoxy glue, which was then secured on a sample holder.

Equipment and experimental conditions. Experiments for the $BaBi_{2-x}REE_xB_2O_7$ (*REE* = Eu, Sm, Tb) borates were conducted using the Rigaku XtaLAB Synergy-S single crystal diffractometer equipped with a HyPix-6000HE detector, with MoKα radiation λ = 0.71069 Å., a crystal rotation step of Ω = 0.5°, and an exposure time of 30 s.

Data collection for the $Ba_3Y_2(BO_3)_4$ single crystals was performed on the Bruker Smart APEX II diffractometer, equipped with a CCD detector using MoKα radiation λ = 0.71069 Å., a crystal rotation step of Ω = 0.5°, and an exposure time of 30 s.

Processing of experimental data. Intensity arrays were integrated using the CrysAlisPro 2015 software package (OxfordDiffraction, 2015). Absorption correction was applied using the SCALE3 ABSPACK algorithm. Refinement of the crystalline structures of all investigated borates was carried out using the Jana 2006 software package (Petříček et al., 2016) with the charge flipping method. Atom positions in the crystal structure were determined based on the presence of maxima in the difference Fourier map of the electron density.

To refine the occupancy of the crystallographic sites of the $BaBi_{2-x}REE_xB_2O_7$ (*REE* = Eu, Sm, Tb) borates, the following strategy was employed: Bi sub-positions were clearly identified by the asymmetric coordination of this cation, attributed to the presence of stereochemically active unshared electron pair Bi^{3+}. Initially, the occupancy of Ba sub-positions was refined, and the obtained value was fixed. To refine the occupancy of Bi sub-positions, the site scattering factor was refined. It was assumed that *REE* atoms occupied the Bi sub-positions, as shown in the literature data on the refinement of the crystalline structures of alkaline earth metal borates and Bi (Li et al., 2016a; Shablinskii et al., 2017; Li et al., 2018; Shablinskii et al., 2019; Shablinskii et al., 2020). *REE* atoms were placed in those Bi sub-positions that exhibited a lower scattering factor

value than expected. A restraint was imposed to maintain the occupancy of each position by Ba, Bi, and *REE* atoms at 100%. The occupancy of Bi sub-positions was refined, then the fixing on Ba was removed, and the occupancy of all crystallographic sites was refined again.

For the refinement of the occupancy of crystallographic sites in the $Ba_3Y_2(BO_3)_4$ borate, the following strategy was employed: Ba and Y atoms were placed in the crystallographic *M*1, *M*2, and *M*3 sites in a stoichiometric ratio, followed by refinement of the occupancy while maintaining the stoichiometry of the formula.

Visualization of the crystal structures was performed using the VESTA software (Momma, Izumi, 2011).

2.2.1.3 High-temperature powder X-ray diffraction

The investigation of the $Ba_3Y_2(BO_3)_4$, $Ba_3Eu_2(BO_3)_4$ and $BaBi_{1.7}Sm_{0.3}B_2O_7$ borates over a wide temperature range was conducted *in situ* using the high-temperature powder X-ray diffraction method.

Equipment and experimental conditions. The experiments were carried out using the Rigaku Ultima IV powder diffractometer with the SHT-1500 thermal attachment. To determine the parameters of the unit cell with increasing temperature and further calculate the characteristic surface of the thermal expansion tensor, the following conditions were used: CoKα radiation, λ = 1.7902 Å, atmospheric air, temperature range 25–600 °C for для $BaBi_{1.7}Sm_{0.3}B_2O_7$ and 25–1000 °C for $Ba_3Y_2(BO_3)_4$ and $Ba_3Eu_2(BO_3)_4$, 20 °C step, heating rate 0.6 °C/min, 2θ step 0.02°, 1 sec exposure at the point.

An additional experiment was conducted to refine the crystal structure of the $Ba_3Y_2(BO_3)_4$ borate, including sites occupancy over a wide temperature range using the Rietveld method, under the following shooting conditions: CoKα radiation, λ = 1.7902 Å, atmospheric air, temperature range 600–800 °C, 5 °C step, heating rate 0.6 °C/min, 2θ step 0.02, 5 sec exposure at the point.

Experiment processing, approximation of unt cell parameters depending on temperature, calculation of thermal expansion coefficients, and visualization of the characteristic surface of the thermal expansion tensor were performed using the Rietveld To Tensor software complex (Bubnova et al., 2018). When processing High-temperature powder X-ray diffraction experiments using the Rietveld method, adjustments were made for sample displacement, zero position, crystallite sizes, and unit cell parameters. Additionally, for refining the crystal structure of the $Ba_3Y_2(BO_3)_4$ borate using the Rietveld method at temperatures 600–800 °C, coordinates of large cation atoms, atomic displacement parameters, site occupancy, and peak broadening parameters were refined.

2.2.2 Thermal Analysis: Thermogravimetry (TG) and Differential Scanning Calorimetry (DSC)

In order to determine the temperatures at which endothermic and exothermic effects occur in the $BaBi_{1.7}Sm_{0.3}B_2O_7$ borate, a thermal analysis was conducted *in situ*.

The experiments were carried out using the STA 429 CD NETZSCH instrument under the following conditions: air atmosphere, airflow rate of 50 cm^3 min^{-1}, temperature range from 400 to 1000 °C, heating rate of 20 °C min^{-1}. The temperature determination error did not exceed ±2 °C. Experiment tablets weighing 20 mg were pre-weighed with an accuracy of 0.01 mg and placed in a platinum-rhodium crucible. The temperatures of the thermal effects were determined using the NETZSCH Proteus software package with the first derivative of the DSC curve.

2.2.3 Spectroscopic Methods

2.2.3.1 Light Scattering Spectroscopy (LSS)

The Light Scattering spectra were measured using the Horiba LabRam spectrometer equipped with a confocal microscope. A laser with a wavelength of 488 nm was used as the excitation source, with its emission focused on the surface of the polycrystalline sample by a 50x microobjective. Raman scattering spectra were measured in a backscattering configuration with a resolution of 3 cm^{-1}.

2.2.3.2 Infrared Spectroscopy (IR Spectroscopy)

The measurements were conducted using the Nicolet 8700 IR Fourier spectrometer (Thermo Scientific). The instrument's spectral range is 11000–50 cm^{-1}, with a resolution of 0.1 cm^{-1}, wavelength reproducibility of 0.01 cm^{-1}, and a scanning speed of 90 scans/c at a resolution of 16 cm^{-1}.

2.2.3.3 Luminescent Spectroscopy

Fluorescence, thermoluminescence, excitation fluorescence spectra, kinetic curves, and luminescence kinetics were measured using the Fluorolog-3 spectrofluorimeter (Horiba Jobin Yvon). A xenon lamp with a power of 450 W served as the excitation source, while for kinetic

curves, a pulsed xenon lamp with a power of 150 W was used. Fluorescence and excitation fluorescence spectra were measured with a resolution of 1 nm. To achieve sample homogeneity, the samples were ground in a mortar, then 5 mg of the substance was mixed with 300 mg of KBr. Subsequently, the samples were pressed into tablets under forevacuum.

Chapter 3. The $BaBi_2B_2O_7$ borates, activated and co-activated by REE^{3+} Ions. Results and Discussion

During the course of this study, six series of solid solutions based on the $BaBi_2B_2O_7$ (32 compositions) borate matrix were synthesized: $BaBi_{2-x}Eu_xB_2O_7$ (x = 0.05, 0.1, 0.15, 0.2, 0.3, 0.4, 0.5), $BaBi_{2-x}Sm_xB_2O_7$ (x = 0.05, 0.1, 0.15, 0.2, 0.3, 0.4, 0.5), $BaBi_{2-x}Tb_xB_2O_7$ (x = 0.05, 0.1, 0.15, 0.2, 0.3, 0.4, 0.5), $BaBi_{2-x-0.05}Eu_xSm_{0.05}B_2O_7$ (x = 0.35, 0.4, 0.45), $BaBi_{2-0.15-y}Eu_{0.15}Sm_yB_2O_7$ (y = 0.05, 0.1, 0.15, 0.2), $BaBi_{2-x-0.3}Eu_xTb_{0.15}Tm_{0.15}B_2O_7$ (x = 0.05, 0.1, 0.15, 0.2). Single-crystals were selected and the crystal structures of 8 borate compounds were refined: $BaBi_{1.90}Eu_{0.10}B_2O_7$, $BaBi_{1.80}Eu_{0.20}B_2O_7$, $BaBi_{1.60}Eu_{0.40}B_2O_7$, $BaBi_{1.95}Sm_{0.05}B_2O_7$, $BaBi_{1.70}Sm_{0.30}B_2O_7$, $BaBi_{1.90}Tb_{0.10}B_2O_7$, $BaBi_{1.70}Tb_{0.30}B_2O_7$, and $BaBi_{1.60}Tb_{0.40}B_2O_7$ based on single-crystal data. The thermal behavior of the $BaBi_{1.70}Sm_{0.30}B_2O_7$ borate was studied using High-temperature powder X-ray diffraction, differential scanning calorimetry (DSC), and thermogravimetry (TG). The light scattering spectra for the $BaBi_{2-x}Eu_xB_2O_7$ series and the luminescence spectra of the six series of solid solutions were described.

The synthesis method, starting materials, and equipment used are detailed in section 2.1.1, page 50. This section focuses primarily on research results and discussions.

3.1 The BaBi2−xEuxB2O7 (x = 0.05, 0.1, 0.15, 0.2, 0.3, 0.4, 0.5) borates

This section is dedicated to the investigation of solid solutions in the $BaBi_{2-x}Eu_xB_2O_7$ series: refining their crystal structure, including the analysis of cation distribution sites, luminescent properties, as well as determining the optimal concentrations of Eu^{3+} ions in comparison with the $CaBi_2B_2O_7$ and $SrBi_2B_2O_7$ borates, activated by Eu^{3+}.

3.1.1 Results of Powder X-ray Diffraction of Borates BaBi2−xEuxB2O7

Based on the results of Powder X-ray Diffraction, the $BaBi_{2-x}Eu_xB_2O_7$ (x = 0.05—0.4) borates are found to be homogeneous. The $BaBi_{1.5}Eu_{0.5}B_2O_7$ sample contains 9% (according to Rietveld analysis) of the Eu_2O_3-$C2/m$ impurity phase (Figure 22).

The unit cell parameters of the $BaBi_{2-x}Eu_xB_2O_7$ borates were calculated using the Rietveld method based on powder data. The dependencies of the unit cell parameters on concentration are shown in Figure 23. Further analysis of the $BaBi_{2-x-y-z}REE_{x,x,z}B_2O_7$ (REE = Eu^{3+}, Sm^{3+}, Tb^{3+}, Tm^{3+}) solid solutions is presented in section 3.7.1, page 94.

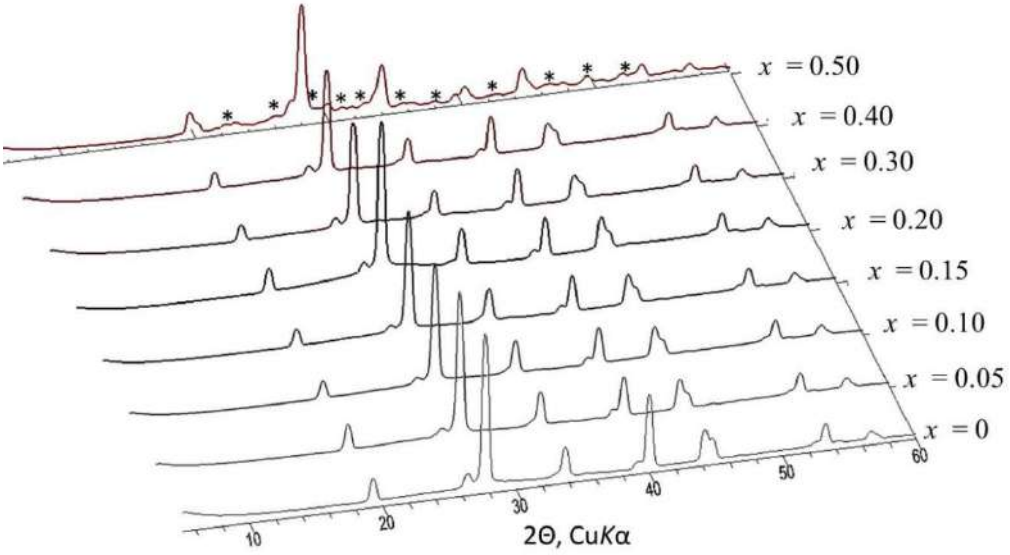

Figure 22 – Diffraction patterns of the $BaBi_{2-x}Eu_xB_2O_7$ borates. The asterisks correspond to the peaks of the Eu_2O_3-*C*2/*m* impurity phase in the $BaBi_{1.5}Eu_{0.5}B_2O_7$ sample.

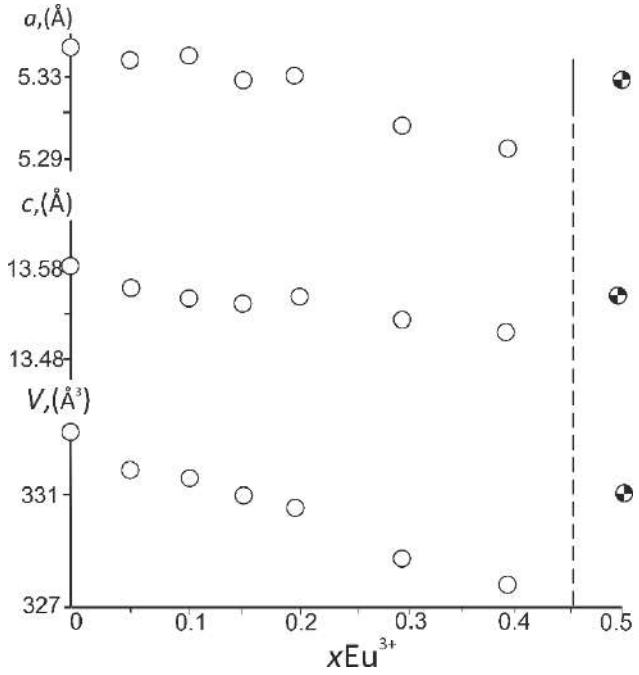

Figure 23 – The dependencies of the unit cell parameters on the content of Eu^{3+} in $BaBi_{2-x}Eu_xB_2O_7$ borates. The non-homogeneous $BaBi_{1.5}Eu_{0.5}B_2O_7$ sample is marked in black and white.

3.1.2 Results of refinement of crystal structures of the $BaBi_{2-x}Eu_xB_2O_7$ (x = 0.1, 0.2, 0.4) borates

Based on single-crystal analysis, a comprehensive refinement of three crystal structures of the new $BaBi_{2-x}Eu_xB_2O_7$ (x = 0.1, 0.2, 0.4) solid solutions has been carried out. These borates crystallize in the structural type of $BaBi_2B_2O_7$ ($P6_3$, a = 5.3378(8), c = 13.583(2) Å, V = Å^3, Z =2) (Bubnova et al., 2016). Refined based on single-crystal data, the formulas of the $BaBi_{1.89}Eu_{0.11}B_2O_7$, $Ba_{1.02}Bi_{1.80}Eu_{0.19}B_2O_7$ and $Ba_{1.02}Bi_{1.60}Eu_{0.38}B_2O_7$ crystal structures are close to the formulas of the initial $BaBi_{1.90}Eu_{0.10}B_2O_7$, $BaBi_{1.80}Eu_{0.20}B_2O_7$, $BaBi_{1.60}Eu_{0.40}B_2O_7$ compositions. Crystal data and refinement details of refinement are presented in Table 5. Atomic coordinates, occupancy of crystallographic sites, and anisotropic and equivalent atomic displacement parameters are provided in Appendix A (Table S 1, Table S 2, pp. 143—144), bond lengths in Table 6.

Table 5 – Crystal data and details of refinement of the $BaBi_2B_2O_7$*, $BaBi_{1.90}Eu_{0.10}B_2O_7$, $BaBi_{1.80}Eu_{0.20}B_2O_7$, $BaBi_{1.60}Eu_{0.40}B_2O_7$ borates

Stoichiometric formula	$BaBi_2B_2O_7$	$BaBi_{1.90}Eu_{0.10}B_2O_7$	$BaBi_{1.80}Eu_{0.20}B_2O_7$	$BaBi_{1.60}Eu_{0.40}B_2O_7$
Refined formula	$BaBi_2B_2O_7$	$BaBi_{1.89}Eu_{0.11}B_2O_7$	$Ba_{1.02}Bi_{1.80}Eu_{0.19}B_2O_7$	$Ba_{1.02}Bi_{1.60}Eu_{0.38}B_2O_7$
Crystal system, space group	Hexagonal, $P6_3$			
Temperature (K)	293			
a (Å)	5.3378(8)	5.3282(8)	5.3021(8)	5.2956(8)
c (Å)	13.583(2)	13.569(2)	13.503(2)	13.490(2)
V (Å^3)	335.15(9)	333.61(9)	328.74(9)	327.61(9)
Z	2			
Radiation type	Mo $K\alpha$			
μ (mm^{-1})	58.18	56.473	55.72	52.372
Crystal size (mm)	0.04×0.04×0.03	0.04×0.05×0.1	0.03×0.04×0.07	0.04×0.04×0.09
Diffractometer	Bruker Smart Apex II	Rigaku XtaLab Synergy-S		
No. of measured, independent and observed [$I > 3\sigma(I)$] reflections	1872/398/280	4543/795/372	1552/696/296	3478/506/316
R_{int}	0.031	0.0936	0.0343	0.0553
$(\sin\theta/\lambda)_{max}$ (Å^{-1})	0.593	0.773	0.805	0.775
Refinement				
R (obs), wR(obs), S	0.026, 0.056, 1.04	0.0442, 0.0535, 1.42	0.0399, 0.0520, 1.21	0.0315, 0.0405, 1.41
No. of reflections	398	372	296	316
No. of parameters	57	52	49	58

*Data from (Bubnova et al., 2016)

Table 6 – Selected bond lengths (Å) for $BaBi_2B_2O_7$*, $BaBi_{1.89}Eu_{0.11}B_2O_7$, $Ba_{1.02}Bi_{1.80}Eu_{0.19}B_2O_7$ and $Ba_{1.02}Bi_{1.60}Eu_{0.38}B_2O_7$ borates.

Bond length/*x*	**0**	**0.10**	**0.20**	**0.40**
Ba1—O3	2.48(5)	2.50 (3)	2.53 (4)	2.47 (3)
Ba1—O2×3	2.71(3)	2.72 (2)	2.73 (1)	2.72 (2)
Ba1—O2×3	2.79(3)	2.80 (2)	2.74 (1)	2.76 (2)
Ba1—O2×3	2.98(2)	2.94 (2)	3.04 (1)	3.01 (2)
<Ba1—O>$_{10}$	**2.79**	**2.79**	**2.81**	**2.79**
Bi1(Eu1)—O3	2.11(5)	2.07 (3)	2.06 (5)	2.02 (3)
Bi1(Eu1)—O2	2.37(2)	2.40 (3)	2.44 (3)	2.38 (3)
Bi1(Eu1)—O2	2.45(3)	2.44 (2)	2.52 (2)	2.54 (3)
Bi1(Eu1)—O2	2.65(4)	2.60 (3)	2.59 (3)	2.59 (4)
Bi1(Eu1)—O2	2.72(4)	2.76 (3)	2.77 (3)	2.78 (3)
Bi1(Eu1)—O2	2.96(3)	2.944 (19)	2.79 (3)	2.79 (4)
Bi1(Eu1)—O2	3.03(2)	3.01 (2)	2.88 (3)	2.94 (3)
Bi1(Eu1)—O1	3.24(2)	3.24 (2)	3.35 (2)	3.28 (2)
Bi1(Eu1)—O1	3.25(2)	3.27 (2)	3.47 (3)	3.41 (3)
Bi1(Eu1)— O1	3.51(2)	3.50 (2)	3.54 (3)	3.51 (3)
<Bi1—O>$_{10}$	**2.83**	**2.82**	**2.84**	**2.82**
Ba2—O3	2.52(5)	2.58 (3)	2.53 (4)	2.67 (3)
Ba2—O1×3	2.72(2)	2.747 (10)	2.769 (13)	2.819(12)
Ba2—O1×3	2.79(2)	2.767 (10)	2.784 (14)	2.764 (13)
Ba2—O2×3	2.98(2)	2.957 (15)	2.89 (2)	2.846 (19)
<Ba2—O>$_{10}$	**2.80**	**2.80**	**2.79**	**2.80**
Bi2(Eu2)—O3	2.18(5)	2.17 (3)	2.13 (5)	2.19 (3)
Bi2(Eu2)—O1×3	2.66(2)	2.674 (11)	2.681 (13)	2.709 (12)
Bi2(Eu2)—O1×3	2.73(2)	2.695 (10)	2.697 (14)	2.652 (12)
Bi2(Eu2)—O2×3	3.26(2)	3.298 (14)	3.223 (19)	3.249 (18)
<Bi2(Eu2)—O>$_{10}$	**2.81**	**2.82**	**2.79**	**2.80**
Ba3—O2×3	2.49(2)	2.518 (17)	2.60 (3)	2.51 (2)
Ba3—O1×3	2.57(2)	2.52 (2)	2.39 (3)	2.42 (3)
Ba3—O3×3	3.083(1)	3.0766 (7)	3.0631 (18)	3.0582 (9)
<Ba3—O>$_9$	**2.71**	**2.70**	**2.68**	**2.66**
Bi3—O1	2.38(3)	2.369 (17)	2.58 (3)	2.57 (4)
Bi3—O1	2.39(2)	2.392 (18)	2.28 (3)	2.20 (3)
Bi3—O2	2.44(2)	2.424 (16)	2.65 (2)	2.66 (4)
Bi3—O2	2.46(2)	2.463 (15)	2.37 (2)	2.31 (3)
Bi3—O3	2.643(4)	2.665 (4)	2.973 (15)	2.88 (4)
Bi3—O1	2.82(2)	2.792 (17)	2.54 (3)	2.53 (3)
Bi3—O2	2.88(2)	2.844 (14)	2.61 (3)	2.63 (3)
Bi3—O3	3.321(6)	3.286 (6)	2.909 (15)	2.93 (4)
Bi3—O3	3.325(4)	3.320 (4)	3.319 (3)	3.387 (19)

<Bi3—O>$_9$	**2.74**	**2.73**	**2.69**	**2.68**
O3—Ba1	2.48(5)	2.50 (3)	2.53 (4)	2.47 (3)
O3—Ba2	2.52(5)	2.58 (3)	2.53 (4)	2.67 (3)
O3—Ba3×3	3.083(1)	3.0766 (7)	3.0631 (18)	3.0582 (9)
<O3—Ba>$_5$	**2.85**	**2.86**	**2.85**	**2.86**
O3—Bi1(Eu1)	2.11(5)	2.07 (3)	2.06 (5)	2.02 (3)
O3—Bi2(Eu2)	2.18(5)	2.17 (3)	2.13 (5)	2.19 (3)
O3—Bi3x3	2.643(4)	2.665 (4)	2.909 (15)	2.88 (4)
<O3—Bi>$_5$	**2.45**	**2.45**	**2.58**	**2.57**
B1—O1×3	1.36(2)	1.36 (2)	1.31 (2)	1.37 (2)
<B1—O>$_3$	**1.36(2)**	**1.36 (2)**	**1.31 (2)**	**1.37 (2)**
B2—O2×3	1.38(2)	1.36 (1)	1.39 (1)	1.37 (1)
<B2—O>$_3$	**1.38(2)**	**1.36 (1)**	**1.39 (1)**	**1.37 (1)**

*Data from (Bubnova et al., 2016)

The crystal structures of $CaBi_2B_2O_7$ (Barbier, Cranswick, 2006; Volkov et al., 2020), $SrBi_2B_2O_7$ (Barbier, Cranswick, 2006), and $BaBi_2B_2O_7$ (Bubnova et al., 2016) borates consist of layers $\{ABi_2B_2O_7\}_\infty$ where *A* = Ca, Sr, Ba. Each layer is composed of isolated BO_3 triangles, BiO_3 groups, and CaO_6 or SrO_6 triangular prisms. The layers are connected by weak Bi–O bonds with a length of approximately 2.9 Å.

The crystal structure contains three symmetrically independent crystallographic sites for large cations (*M*1, *M*2, *M*3), each of which is split into Ba and Bi subpositions, two symmetrically independent BO_3 triangular radicals, and one site for an "additional" oxygen atom (O3) not bonded to boron (Figure 24). The *M*2 site is split into two subpositions (Ba (2b), Bi (2b)), while *M*1 and *M*3 are split into two subpositions with different symmetries (Ba (2b), Bi (6c)). The splitting of the *M*1, *M*2, *M*3 sites is minor, and the Ba–Bi distances range from 0.416(9) Å (*M*2) to 0.558(9) Å (*M*1) (Bubnova et al., 2016), from 0.408(9) Å (*M*2) to 0.556(9) Å (*M*1), from 0.402(9) Å (*M*2) to 0.529(9) Å (*M*1), and from 0.485(9) Å (*M*2) to 0.525(9) Å (*M*1) in the crystal structures of $BaBi_2B_2O_7$, $BaBi_{1.90}Eu_{0.10}B_2O_7$, $BaBi_{1.80}Eu_{0.20}B_2O_7$ and $BaBi_{1.60}Eu_{0.40}B_2O_7$, respectively.

The “additional” oxygen atom O3 forms five O–*M* bonds (Figure 25), leading to the formation of OM_5 polyhedra. Bi^{3+} atoms are closer to the central oxygen atom than Ba^{2+} in the oxocentered polyhedron. This can be explained by the average bond lengths in borate and $BaBi_2B_2O_7$ (Bubnova et al., 2016) Bi^{3+}—O) = 2.290 Å < (Ba^{2+}—O) = 2.738 Å, as well as by electrostatic interactions, since the Bi^{3+} cation is more electropositive among the atoms surrounding the oxygen at O3 site.

The *M*1 and *M*2 sites are coordinated by ten oxygen atoms, while *M*3 site is coordinated by nine. $B1O_3$ shares vertices with $M1O_{10}$ polyhedra and edges with $M2O_{10}$, while B_2O_3 is connected

by edges to $M1O_{10}$ polyhedra and vertices to $M2O_{10}$. $B1O_3$ and $B2O_3$ are only connected to $M3O_9$ polyhedra through vertices.

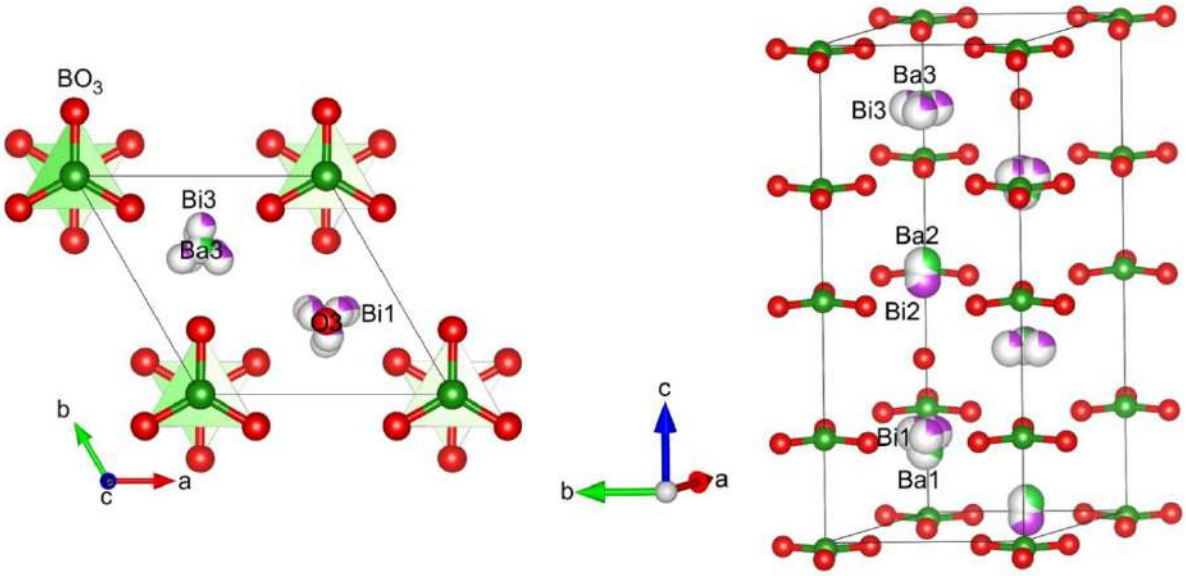

Figure 24 – Crystal structure of $BaBi_{2-x}Eu_xB_2O_7$ (x = 0, 0.1, 0.2, 0.4) borates.

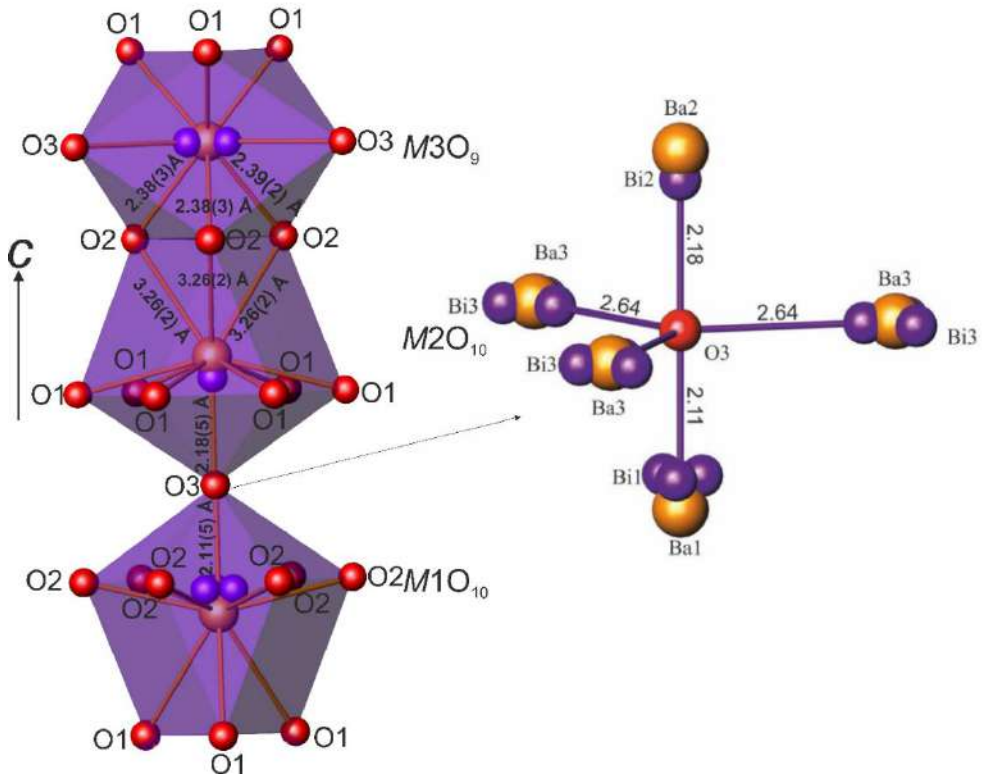

Figure 25 – Coordination polyhedra of the $M1$, $M2$ and $M3$, OM_5 sites in $BaBi_{2-x}Eu_xB_2O_7$ (x = 0, 0.1, 0.2, 0.4) borates. Signed values of bond lengths for $BaBi_2B_2O_7$ (Bubnova et al., 2016)

3.1.3 Distribution of Eu^{3+} cations over *M*1, *M*2, *M*3 sites

In the crystal structure of $BaBi_2B_2O_7$, the *M*1, *M*2, *M*3 sites are predominantly occupied by 2/3 Bi^{3+} and 1/3 Ba^{2+} ions (Bubnova et al., 2016). A similar ratio is maintained in the crystalline structures of (Bi,Ba,Eu)(Bi,Ba,Eu)(Bi,Ba)B_2O_7 solid solutions: in the $BaBi_{1.90}Eu_{0.10}B_2O_7$ and $BaBi_{1.80}Eu_{0.20}B_2O_7$ borates, Eu^{3+} atoms occupy approximately 10% and 20% of the *M*1 site, respectively. When the occupancy of Eu^{3+} atoms in the *M*1 site reaches 20%, they begin to occupy around 30% of the *M*2 site and 10% of the *M*1 in the crystal structure of $BaBi_{1.60}Eu_{0.40}B_2O_7$ (Figure 26). Eu^{3+} and Bi^{3+} atoms occupy the same split subpositions in the *M*1 and *M*2 sites.

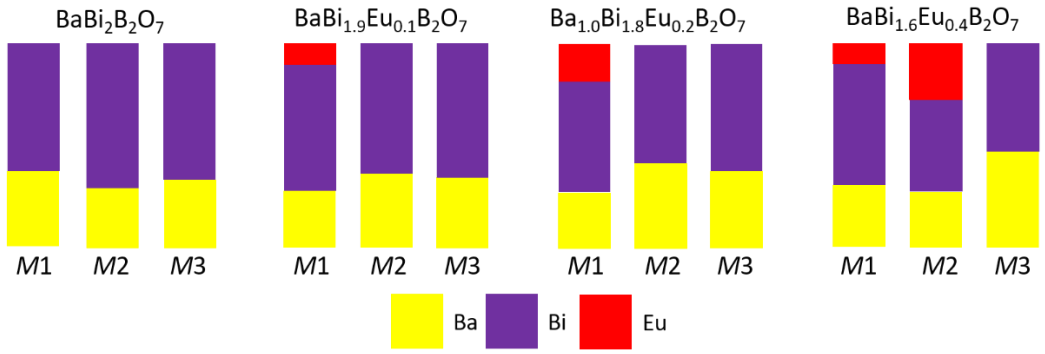

Figure 26 – Occupancy (%) of cation sites in the crystal structures of $BaBi_{2-x}Eu_xB_2O_7$ (x = 0.10, 0.20, 0.40) borates.

As mentioned in section 3.1.1 (page 56), at europium concentrations above x = 0.45, it is presumed that the limit of the solid solution's isomorphic capacity is reached. The immiscibility of the $BaBi_{2-x}Eu_xB_2O_7$ solid solution may have a structurally dependent nature. The crystal structure of $BaBi_2B_2O_7$ consists of $ABi_2B_2O_7\}_\infty$ layers, connected by weak bonds (approximately 2.9 Å) Bi–O in the *M*1 and *M*2 sites. Since in the $BaBi_{2-x}Eu_xB_2O_7$ solid solutions, Eu atoms replace Bi, the connection of layers in the crystal structures is also carried out by Eu–O bonds. These bonds are quite large for Eu^{3+} ions, as the ionic radius $^{[8]}Eu^{3+}$ (1.206 Å) is smaller than that of $^{8]}Bi^{3+}$ (1.31 Å) (Shannon, 1976). According to the bond valence theory (Brown, 1981), long Eu–O bonds are weaker than long Bi–O bonds, therefore, an increase in Eu^{3+} concentration leads to Eu^{3+} not being able to fully incorporate into the crystalline structure. As a result, immiscibility of solid solutions occurs at x = 0.50, and the solid solution miscibility range of $BaBi_{2-x}Eu_xB_2O_7$ can be defined as x = 0–0.45.

3.1.4 Results of light scattering spectroscopy of $BaBi_{2-x}Eu_xB_2O_7$ borates

The Raman spectra demonstrate a consistent set of bands for borates with x = 0.05-0.30 (Figure 27). The presence of broad bands in the spectra confirms the disordering of the crystal structure. The main structural units in the spectra are triangular BO_3 radicals (Table 7). Further increase in the concentration of the activator ion leads to a slight change in the structure of the crystalline matrix. Perhaps, such a change is associated with the redistribution of cations among the three cation sites *M*1, *M*2, and *M*3 when $x > 0.30$.

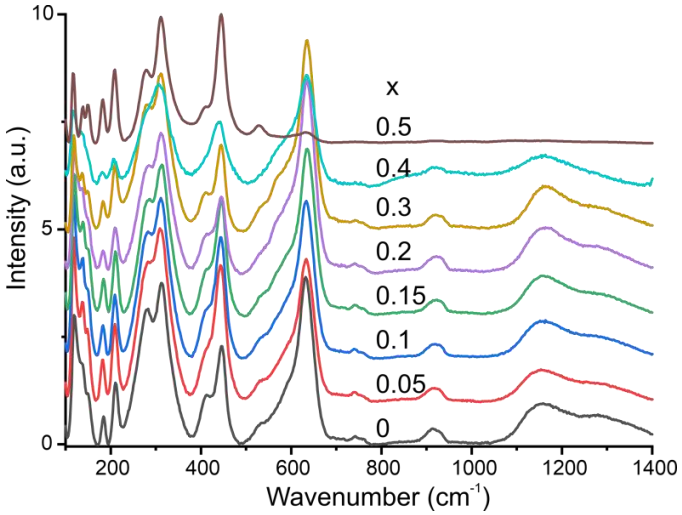

Figure 27 – Raman spectra of $BaBi_{2-x}Eu_xB_2O_7$ borates.

Table 7 – Raman bands assignment for $BaBi_{2-x}Eu_xB_2O_7$ phosphors.

Raman band, cm^{-1}	Assignment
136, 146, 150, 183, 210, 278, 311	γ (BO_3)
410, 445, 528, 571, 635, 740	δ(BO_3)
920	ν_s(BO_3)

3.1.5 Results of luminescent spectroscopy of $BaBi_{2-x}Eu_xB_2O_7$ borates

Excitation spectra of a $BaBi_{2-x}Eu_xB_2O_7$ series of solid solutions at a wavelength of 615 nm are presented (Figure 28a). In the excitation spectra of luminescence, broad bands in the spectral range of 300–350 nm are interpreted as interband transitions of the crystalline matrix, corresponding to the position of the edge of the main optical absorption and energy transfer to

europium ions. The crystalline matrix effectively absorbs light up to 350 nm. Narrow bands in the excitation spectra in the spectral range of 350–550 nm correspond to transitions of europium ions from the ground to excited states.

Luminescence spectra were measured at an excitation wavelength of 300 nm (Figure 28b). All bands in the spectra correspond to radiative transitions of Eu^{3+} ions.

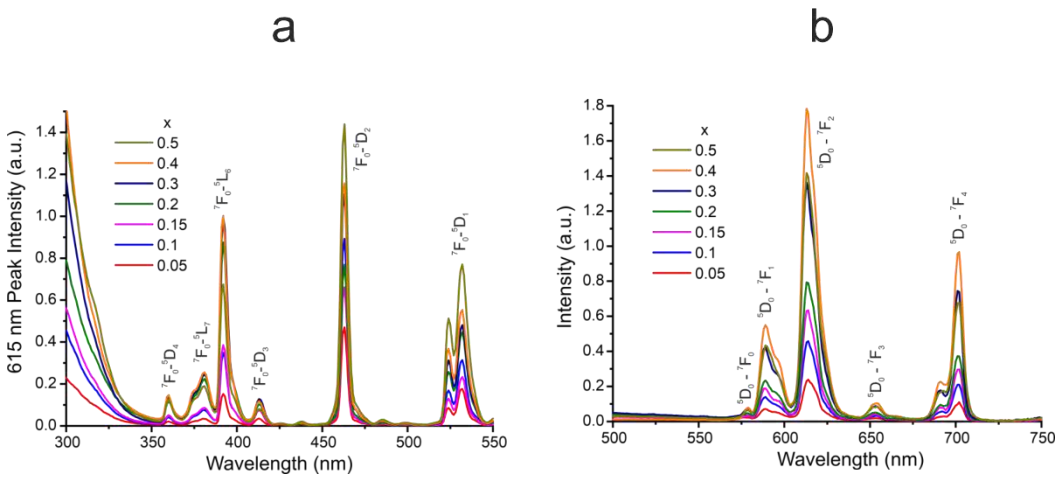

Figure 28 – Excitation spectra (λ_{em} = 616 nm) (a) and photoluminescence spectra (λ_{ex} = 300 nm) (b) of the $BaBi_{2-x}Eu_xB_2O_7$ concentration series.

The concentration dependence of luminescence intensity at a wavelength of 615 nm is shown in Figure 29. The optimal concentration of Eu^{3+} ions, at which the maximum luminescence intensity is observed, is x = 0.40. With further increase in europium concentration, the intensity of luminescence decreases, which can be explained by reaching the immiscibility region of the solid solution, as the sample x = 0.50 is two-phase, and its unit cell parameters increase relative to the composition x = 0.40 (Figure 23). As a result of increasing the unit cell parameters of the sample x = 0.50, the distance between active ions increases. The quenching of luminescence is explained by the dipole-dipole interaction between Eu^{3+} ions, the probability of which increases with decreasing distance between active ions.

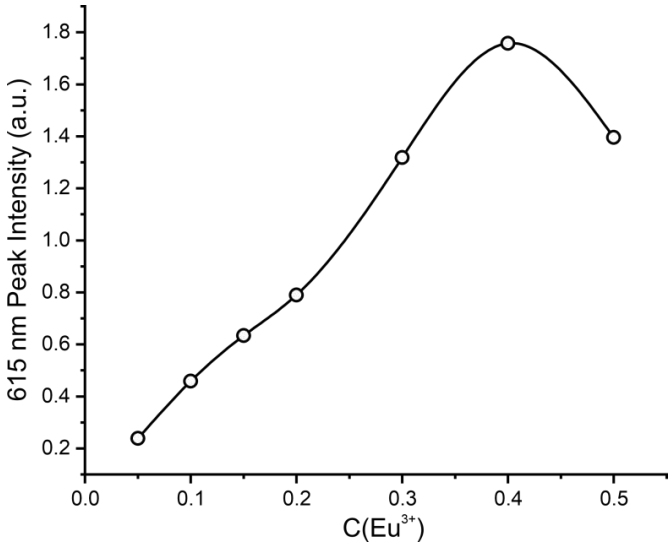

Figure 29 – Concentration dependence of the luminescence intensity of the $^5D_0$-$^7F_2$ transition in $BaBi_{2-x}Eu_xB_2O_7$.

The luminescence kinetic curves were used to measure the lifetime of the excited level of europium ions $^5D_0$. The temporal dependence of the $^5D_0$ level on the concentration of europium ions is shown in (Figure 30). It has been established that within the margin of error, the lifetime remains unchanged for all examined samples and amounts to 1.2±0.1 ms.

The CIE color coordinates (Table 8 and Figure 31) demonstrate that with an increase in the concentration of europium ions, the spectrum shifts from the red-orange region to the red, which is associated with an increase in the intensity of fluorescence of active ions and a decrease in the intensity of the intrinsic fluorescence of the crystalline matrix relative to the concentration of activator ions.

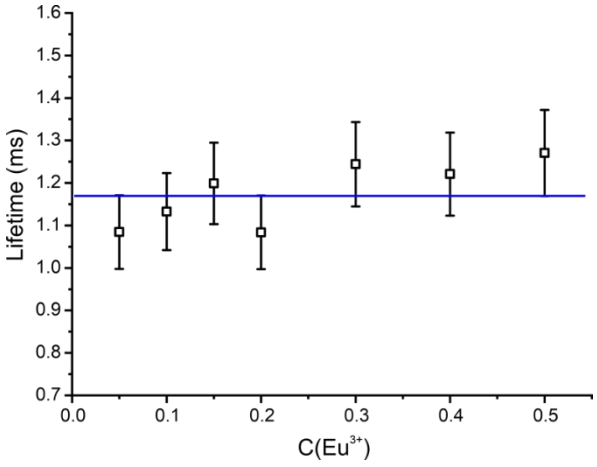

Figure 30 – Concentration dependence of the lifetime of the 5D0 level of europium ions in $BaBi_{2-x}Eu_xB_2O_7$.

Table 8 – CIE (CIE 1931) chromaticity coordinates of $BaBi_{2-x}Eu_xB_2O_7$ concentration series

$C(Eu^{3+})$	x	y
0.05	0.37	0.28
0.1	0.42	0.29
0.15	0.50	0.31
0.2	0.49	0.31
0.3	0.52	0.32
0.4	0.62	0.35
0.5	0.57	0.33

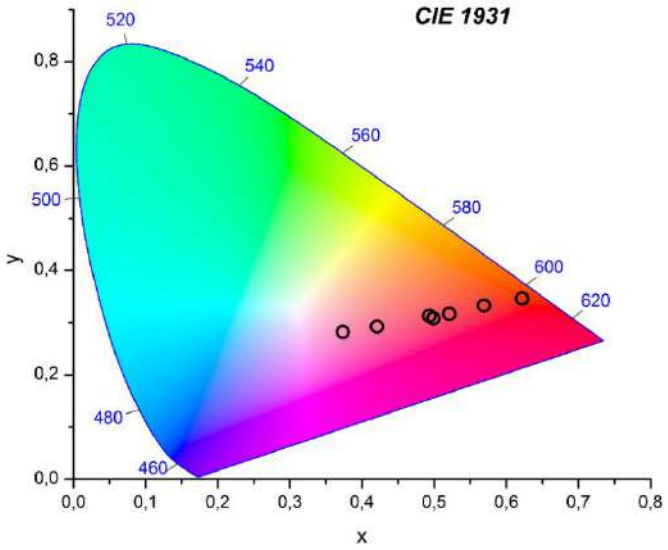

Figure 31 – CIE chromaticity coordinates of $BaBi_{2-x}Eu_xB_2O_7$ concentration series.

3.2 The $BaBi_{2-x}Sm_xB_2O_7$ (x = 0.05, 0.1, 0.15, 0.2, 0.3, 0.4, 0.5) borates

3.2.1 Results of powder X-ray diffraction of $BaBi_{2-x}Sm_xB_2O_7$ borates

According to the results of powder X-ray diffraction, the $BaBi_{2-x}Sm_xB_2O_7$ (x = 0.05, 0.1, 0.15, 0.2, 0.3) borates are homogeneous. Further increase in the concentration of samarium ions leads to the appearance of a significant amount of impurity phase Sm_2O_3-*C*2/*m* (11% according to the Rietveld method) in the $BaBi_{1.6}Sm_{0.4}B_2O_7$ and $BaBi_{1.5}Sm_{0.5}B_2O_7$ borates. Below are the diffraction patterns of homogeneous borates from the $BaBi_{2-x}Sm_xB_2O_7$ series of solid solutions (Figure 32).

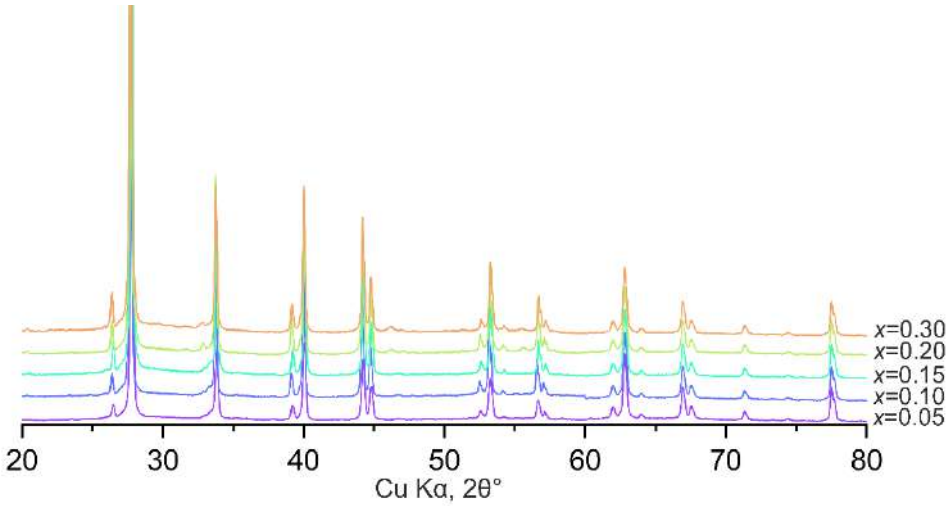

Figure 32 – Diffraction patterns of the $BaBi_{2-x}Sm_xB_2O_7$ borates.

Using the Rietveld method based on powder data, the unit cell parameters were calculated and graphs of the dependencies of the parameters on the concentration of Sm^{3+} were constructed (Figure 33). The analysis of concentration dependencies of the unit cell parameters, determination of the regions of existence of solid solutions, is presented in the discussion of the results (see section 3.7.1, page 94).

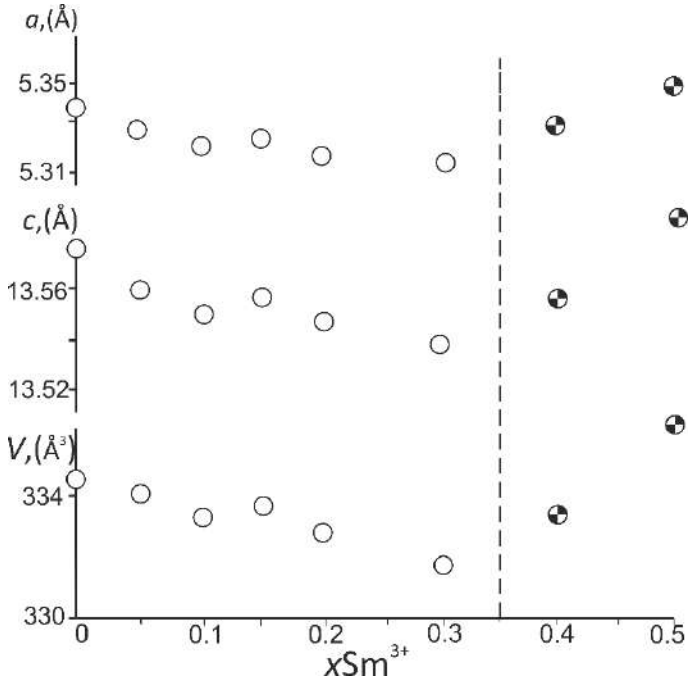

Figure 33 – The dependencies of the unit cell parameters on the content of Sm^{3+} in $BaBi_{2-x}Sm_xB_2O_7$ borates. The non-homogeneous $BaBi_{1.6}Sm_{0.4}B_2O_7$ and $BaBi_{1.5}Sm_{0.5}B_2O_7$ samples are marked in black and white.

3.2.2 Results of refinement of crystal structures of $BaBi_{2-x}Sm_xB_2O_7$ (x = 0.05, 0.3) borates

The refinement results of the crystal structures demonstrate that (Bi,Ba)(Bi,Ba,Sm)(Bi,Ba)B_2O_7 borates also crystallize in the structural type of $BaBi_2B_2O_7$ (Bubnova et al., 2016). A detailed description of the crystal structure is presented in section 3.1.2, page 58. The refined single-crystal data formulas of the crystal structures $Ba_{0.99}Bi_{1.956}Sm_{0.05}B_2O_7$, $Ba_{1.00}Bi_{1.71}Sm_{0.30}B_2O_7$ are close to the formulas of the initial charge: $BaBi_{1.95}Sm_{0.05}B_2O_7$, $Ba_{1.00}Bi_{1.70}Sm_{0.30}B_2O_7$. Below are the crystallographic data and refinement parameters of the crystal structures (Table 9). Atomic coordinates, occupancy of crystallographic sites, anisotropic and equivalent parameters of atomic displacements are provided in Table S 3 and Table S 4, pages 145-146, bond lengths in Table 10.

Table 9 – Crystal data and details of refinement of the $BaBi_2B_2O_7$*, $BaBi_{1.95}Sm_{0.05}B_2O_7$, $Ba_{1.00}Bi_{1.70}Sm_{0.30}B_2O_7$ borates

Stoichiometric formula	$BaBi_2B_2O_7$	$BaBi_{1.95}Sm_{0.05}B_2O_7$	$BaBi_{1.70}Sm_{0.30}B_2O_7$
Refined formula	$BaBi_2B_2O_7$	$Ba_{0.99}Bi_{1.96}Sm_{0.05}B_2O_7$	$Ba_{1.00}Bi_{1.71}Sm_{0.30}B_2O_7$
Crystal system, space group	Hexagonal, $P6_3$		
Temperature (K)	293		
a (Å)	5.3378(8)	5.3326(5)	5.3129(8)
c (Å)	13.583(2)	13.564(1)	13.534(2)
V (Å^3)	335.15(9)	334.28(5)	330.85(9)
Z	2		
Radiation type	Mo $K\alpha$		
μ (mm^{-1})	58.18	57.66	54.03
Crystal size (mm)	0.04×0.04×0.03	0.04×0.05×0.1	0.04×0.04×0.09
Diffractometer	Bruker Smart Apex II	Rigaku XtaLab Synergy-S	
No. of measured, independent and observed [$I > 3\sigma(I)$] reflections	1872/398/261	4543/795/372	2820/481/329
R_{int}	0.031	0.094	0.039
$(\sin\theta/\lambda)_{max}$ (Å^{-1})	0.593	0.773	0.764
Refinement			
R (obs), wR(obs), S	0.026, 0.056, 1.04	0.059, 0.072, 1.89	0.054, 0.071, 2.48
No. of reflections	398	795	481
No. of parameters	57	40	32

*Data from (Bubnova et al., 2016)

Table 10 – Selected bond lengths (Å) for $BaBi_2B_2O_7$*, $Ba_{0.99}Bi_{1.96}Sm_{0.05}B_2O_7$, and $Ba_{1.00}Bi_{1.71}Sm_{0.30}B_2O_7$ borates

Bond length/*x*	**0**	**0.05**	**0.30**
Ba1—O3	2.48(5)	2.47(3)	2.35(4)
Ba1—O2×3	2.71(3)	2.726(14)	2.71(2)
Ba1—O2×3	2.79(3)	2.779(14)	2.73(2)
Ba1—O1×3	2.98(2)	3.968(18)	3.06(2)
<Ba1—O>$_{10}$	**2.79**	**2.79**	**2.79**
Bi1—O3	2.11(5)	2.08(3)	2.01(4)
Bi1—O2	2.37(2)	2.39(2)	2.39(2)
Bi1—O2	2.45(3)	2.464(15)	2.46(3)
Bi1—O2	2.65(4)	2.67(3)	2.64(2)
Bi1—O2	2.72(4)	2.69(3)	2.70(2)
Bi1—O2	2.96(3)	2.925(15)	2.91(3)
Bi1—O2	3.03(2)	2.990(18)	2.97(3)
Bi1—O1	3.24(2)	3.244(19)	3.29(2)
Bi1—O1	3.25(2)	3.256(19)	3.32(2)
Bi1—O1	3.51(2)	3.490(18)	3.53(2)
<Bi1—O>$_{10}$	**2.83**	**2.82**	**2.82**
Ba2—O3	2.52(5)	2.70(3)	2.78(5)
Ba2—O1×3	2.72(2)	2.784(17)	2.79(2)
Ba2—O1×3	2.79(2)	2.789(16)	2.83(2)
Ba2—O2×3	2.98(2)	2.838(18)	2.79(3)
<Ba2—O>$_{10}$	**2.80**	**2.80**	**2.80**
Bi2(Sm2′)—O3	2.18(5)	2.19(3)	2.24(2)
Bi2(Sm2′)—O1×3	2.66(2)	2.684(9)	2.67(2)
Bi2(Sm2′)—O1×3	2.73(2)	2.690(9)	2.70(1)
Bi2(Sm2′)—O2×3	3.26(2)	3.263(18)	3.24(2)
<Bi2(Sm2)—O>$_{10}$	**2.80**	**2.81**	**2.81**
Ba3—O2×3	2.49(2)	2.544(17)	2.48(2)
Ba3—O1×3	2.57(2)	2.520(18)	2.52(2)
Ba3—O3×3	3.083(1)	3.078(1)	3.069(2)
<Ba3—O>$_9$	**2.71**	**2.71**	**2.69**
Bi3—O2	2.38(3)	2.329(18)	2.39(2)
Bi3—O2	2.39(2)	2.36(2)	2.46(2)
Bi3—O1	2.44(2)	2.489(19)	2.34(2)
Bi3—O1	2.46(2)	2.508(19)	2.42(2)
Bi3—O3	2.643(4)	2.653(3)	2.71(9)
Bi3—O2	2.82(2)	2.763(16)	2.78(3)
Bi3—O1	2.88(2)	2.911(18)	2.75(2)
Bi3—O3	3.321(6)	3.297(6)	3.22(7)
Bi3—O3	3.325(4)	3.320(6)	3.31(7)
<Bi3—O>$_9$	**2.74**	**2.74**	**2.71**
O3—Ba1	2.48(5)	2.47(3)	2.35(4)
O3—Ba2	2.52(5)	2.70(3)	2.78(5)
O3—Ba3×3	3.083(1)	3.078(1)	3.069(2)

<O3—Ba>$_5$	**2.85**	**2.88**	**2.86**
O3—Bi1	2.11(5)	2.08(3)	2.01(4)
O3—Bi2(Sm2)	2.18(5)	2.19(3)	2.24(2)
O3—Bi3x3	2.643(4)	2.653(3)	2.71(9)
<O3—Bi>$_5$	**2.44**	**2.44**	**2.48**
B1—O1×3	1.36(2)	1.338(17)	1.35(2)
<B1—O>$_3$	**1.36(2)**	**1.338(17)**	**1.35(2)**
B2—O2×3	1.38(2)	1.396(13)	1.37(1)
<B2—O>$_3$	**1.38(2)**	**1.396(13)**	**1.37(1)**

*Data from (Bubnova et al., 2016)

3.2.3 Distribution of Sm^{3+} cations over *M*1, *M*2, *M*3 sites

According to the refinement results of the crystal structures of $BaBi_{2-x}Sm_xB_2O_7$ (x = 0.05, 0.30) borates, Sm^{3+} atoms replace Bi^{3+} only in *M*2 site (Figure 34). Below (section 3.7.2, page 96) is an analysis of the occupancy of crystallographic sites by REE^{3+} atoms in the crystal structures of $BaBi_{2-x}Eu_xB_2O_7$ (x=0.10, 0.20, 0.40), $BaBi_{2-x}Sm_xB_2O_7$ (x=0.05, 0.30), $BaBi_{2-x}Tb_xB_2O_7$ (x = 0.10, 0.30, 0.40).

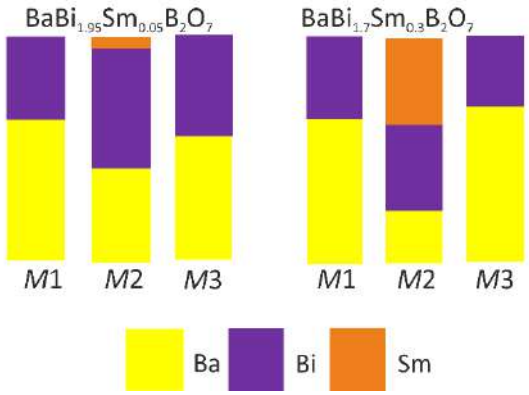

Figure 34 – Occupancy (%) of cation sites in the crystal structures of $BaBi_{2-x}Sm_xB_2O_7$ (x = 0.05, 0.30) borates.

3.2.4 Results of High-temperature powder X-ray diffraction of $BaBi_{1.7}Sm_{0.3}B_2O_7$ borate

The thermal expansion of the single-phase borate from the $BaBi_{2-x}Sm_xB_2O_7$ series of solid solutions with the maximum content of Sm^{3+} – $BaBi_{1.7}Sm_{0.3}B_2O_7$ was investigated using High-temperature powder X-ray diffraction. No visible changes indicating a polymorphic transition or high-temperature decomposition of the phase were observed in the HTXRD patterns (Figure 35).

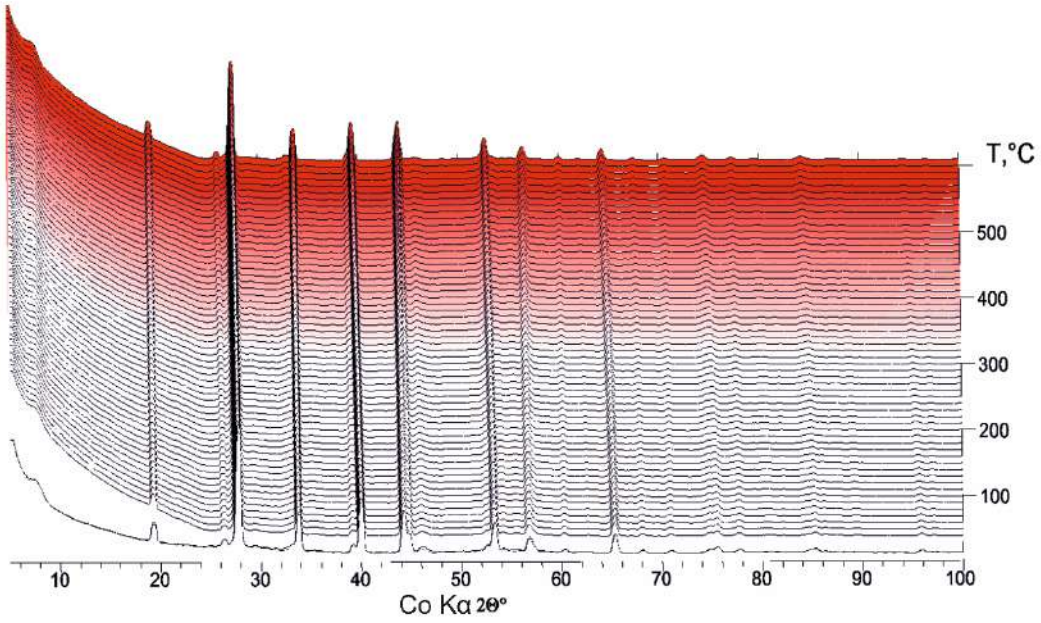

Figure 35 – 3D image of HTXRD patterns of the $BaBi_{1.7}Sm_{0.3}B_2O_7$ borate at high temperatures.

The temperature dependence graphs of the unit cell parameters show a slight inflection at 450 °C (Figure 36). The dependency graphs were approximated by second-degree polynomials in two temperature intervals. The approximation equations are provided in (Table 11).

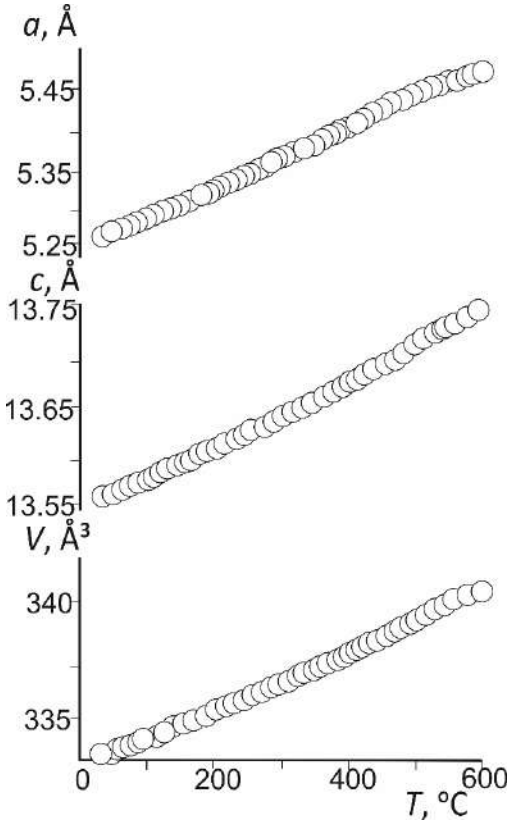

Figure 36 – Temperature dependencies of unit cell parameters of $BaBi_{1.7}Sm_{0.3}B_2O_7$ borate.

Table 11 – Equations of approximation of temperature dependencies of unit cell parameters of $BaBi_{1.7}Sm_{0.3}B_2O_7$ ($a_0 + a_1 \times 10^{-3}t + a_2 \times 10^{-6}t^2$)

Parameter	Interval	a_0	a_1	a_2
$a(t)$ (Å)	25–450 °C	5.31642(8)	0.0349(7)	0.010(1)
	450–600°C	5.314(6)	0.060(2)	-0.033(2)
$c(t)$ (Å)	25–450 °C	13.5305(5)	0.280(4)	0.085(9)
	450–600°C	13.64(3)	–0.15(1)	0.52(9)
$V(t)$ (Å^3)	25–450 °C	331.19(1)	11.21(1)	3.50(2)
	450–600°C	333.52(7)	3.8(3)	8.7(2)

The coefficients of thermal expansion were calculated over a wide temperature range (Table 12), and the data were compared with the $BaBi_2B_2O_7$ borate (Bubnova et al., 2016). The coefficients of thermal expansion increase until reaching the temperature of 450 °C, corresponding to the inflection point on the temperature dependence graphs (Figure 36). The thermal expansion is maximal along the *c*-axis, perpendicular to the preferred orientation of the BO_3 radicals (*ab*). According to the principles of high-temperature crystal chemistry of borates with isolated triangular BO_3 radicals (Bubnova, Filatov, 2008), the thermal expansion is maximal along the axis perpendicular to the preferred orientation of boron-oxygen radicals. The tensor figures of thermal

expansion of the $BaBi_{1.7}Sm_{0.3}B_2O_7$ borate compared with the crystal structure are presented in (Figure 37).

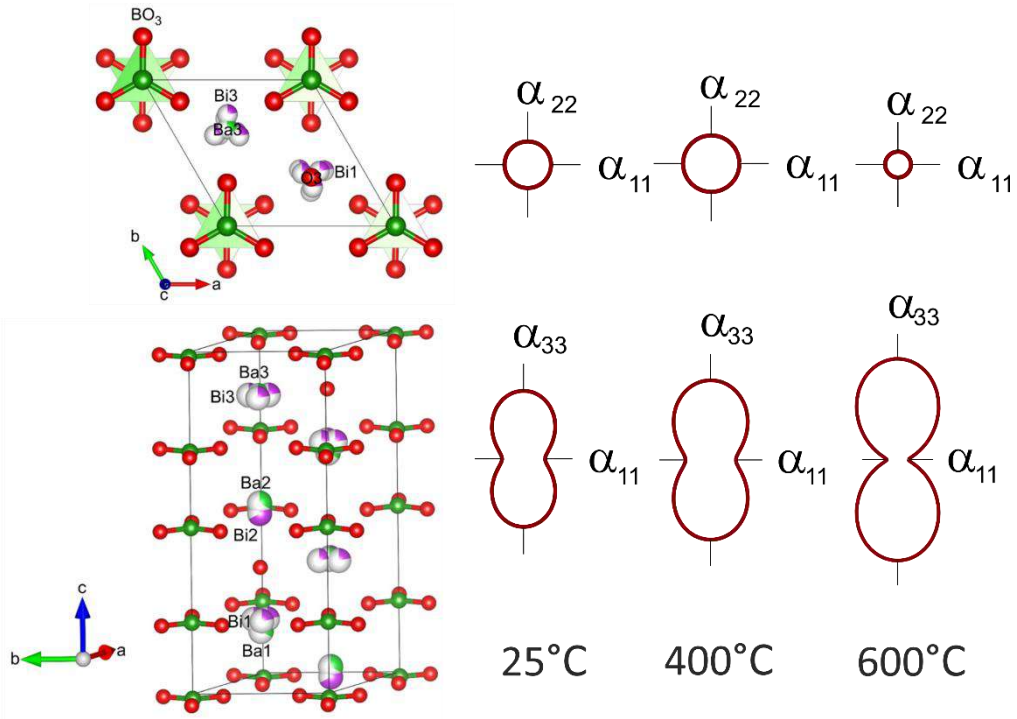

Figure 37 – Crystal structure of the $BaBi_{1.7}Sm_{0.3}B_2O_7$ borate in comparison with the thermal expansion tensor figures at different temperatures.

The $BaBi_{1.7}Sm_{0.3}B_2O_7$ and $BaBi_2B_2O_7$ (Bubnova et al., 2016) borates exhibit a similar thermal expansion behavior: it is maximal along the *c*-axis, and the coefficients of thermal expansion are comparable up to a temperature of 450 °C. Since an inflection point is observed in the temperature dependence of the unit cell parameters in $BaBi_{1.7}Sm_{0.3}B_2O_7$, at temperatures above 450 °C, the unit cell parameters begin to decrease. The presence of an inflection point in the dependencies of the parameters of the elementary cell in the borate $BaBi_{1.7}Sm_{0.3}B_2O_7$ and its absence in $BaBi_2B_2O_7$ suggests that the observed phenomenon occurs due to the redistribution of cations in sites, which occurs with partial substitution of Bi atoms by Sm.

Table 12 – Thermal expansion coefficients of $BaBi_{1.7}Sm_{0.3}B_2O_7$ and $BaBi_2B_2O_7$ (Bubnova et al., 2016) at some temperatures

***T*, ˚C**	$BaBi_{1.7}Sm_{0.3}B_2O_7$			$BaBi_2B_2O_7$		
	$\alpha_a = \alpha_b$ (10^{-6} °C^{-1})	α_c	α_V	$\alpha_a = \alpha_b$ (10^{-6} °C^{-1})	α_c	α_V
25	6.7(1)	21.0(3)	34.4(4)	5.6	20	31

200	7.32(4)	23.14(9)	38.18(8)	6.3	23	36
325	7.79(5)	24.63(2)	40.22(1)	6.9	27	41
400	8.08(9)	25.5(2)	42.4(3)	7.2	28	43
500	4.9(3)	30.0(3)	36.8(5)	7.7	31	46
600	3.7(6)	34.5(1)	41.8(1)	8.1	33	49

3.2.5 Results of thermal analysis of $BaBi_{1.7}Sm_{0.3}B_2O_7$ borate

A thermal analysis of the $BaBi_{1.7}Sm_{0.3}B_2O_7$ borate was conducted. No mass losses were observed according to the TG data. The borate was studied under heating conditions followed by cooling at a rate of 20 °C/min. The DSC curves (Figure 38) show melting effects during heating and crystallization effects during cooling. The data obtained in this study were compared with literature data for the $BaBi_2B_2O_7$ glass-ceramic (Bubnova et al., 2016). The temperatures of the onset and maximum effects during heating and cooling, determined by the change in the first derivative, are presented in Table 13. According to (Egorysheva et al., 2010), a Sr-containing analogue $SrBi_2B_2O_7$ with a similar crystal structure can decompose during melting into SrB_2O_4 and Bi_2O_3 + melt. Since the studied borate contains an additional component, it may decompose during melting into BaB_2O_4 and $(Bi,Sm)_2O_3$ + melt. The DSC curves confirm this assumption: at a temperature of 635 °C, a peak is observed, which can be attributed to the onset of melting of the borate $BaBi_{1.7}Sm_{0.3}B_2O_7$ with decomposition into phases BaB_2O_4 and $(Bi,Sm)_2O_3$ + melt. At 727 °C, a peak related to the melting of the BaB_2O_4 phase with the formation of $(Bi,Sm)_2O_3$ + melt is observed. At 829 °C, the melting of $(Bi,Sm)_2O_3$ with the formation of melt occurs. Crystallization from the melt begins upon cooling to 660 °C. Comparing with the glass-ceramic $BaBi_2B_2O_7$, it can be concluded that the activation of the crystalline matrix by Sm^{3+} ions leads to an increase in the crystallization temperature from the melt from 540 to 660 °C and a slight increase in the melting temperature from 630 to 635 °C.

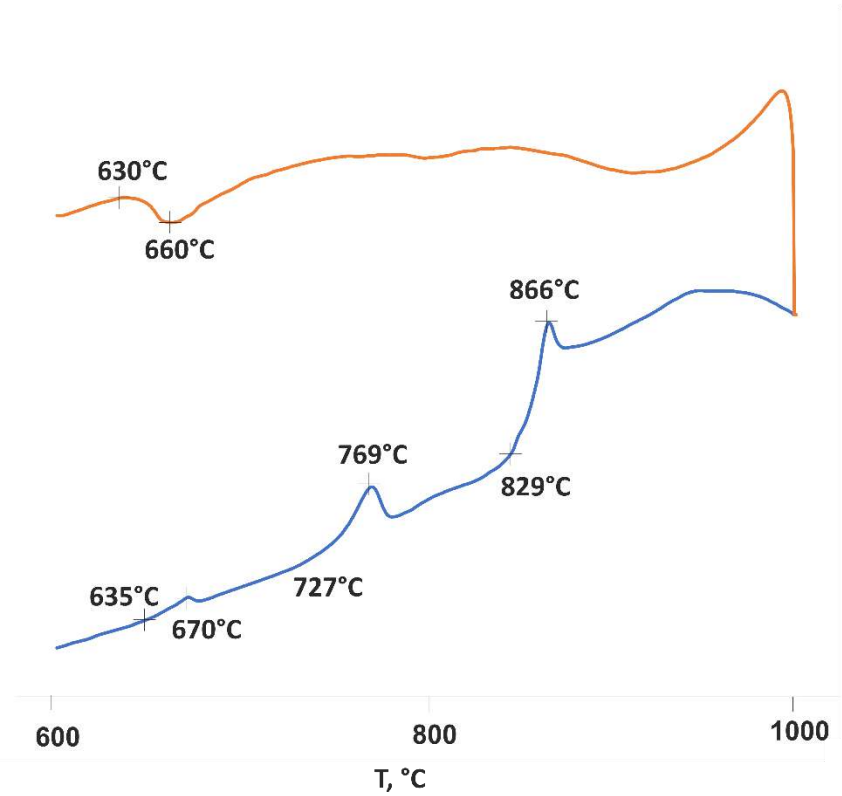

Figure 38 – DSC curves for $BaBi_{1.7}Sm_{0.3}B_2O_7$ borate: heating (blue) and cooling (orange).

Table 13 – Melting point $BaBi_{1.7}Sm_{0.3}B_2O_7$ borate according to DSC data upon heating and crystallization temperature from the melt upon cooling

$BaBi_{1.7}Sm_{0.3}B_2O_7$								$BaBi_2B_2O_7$			
Melting when heated, °C						Crystallization on cooling, °C		Melting when heated, °C		Crystallization on cooling, °C	
T_{beg}	T_{max}	T_{beg}	T_{max}	T_{beg}	T_{max}	T_{beg}	T_{max}	T_{beg}	T_{max}	T_{beg}	T_{max}
635	670	727	769	829	866	660	630	630	677	540	560

3.2.6 Results of luminescent spectroscopy of $BaBi_{2-x}Sm_xB_2O_7$ borates

The borates of the $BaBi_{2-x}Sm_xB_2O_7$ concentration series were excited at a wavelength of 601 nm. Narrow bands are observed in the excitation spectra, corresponding to the transitions of samarium ions from the ground to the excited state (Figure 39a). The narrow bands in the photoluminescence spectra (Figure 39b) correspond to the radiative transitions of Sm^{3+} ions. An increase in the concentration of Sm^{3+} ions in the solid solution leads to a decrease in the intensity

of photoluminescence. The spectra of non-homogeneous samples with x = 0.4, 0.5 demonstrate the lowest emission intensity.

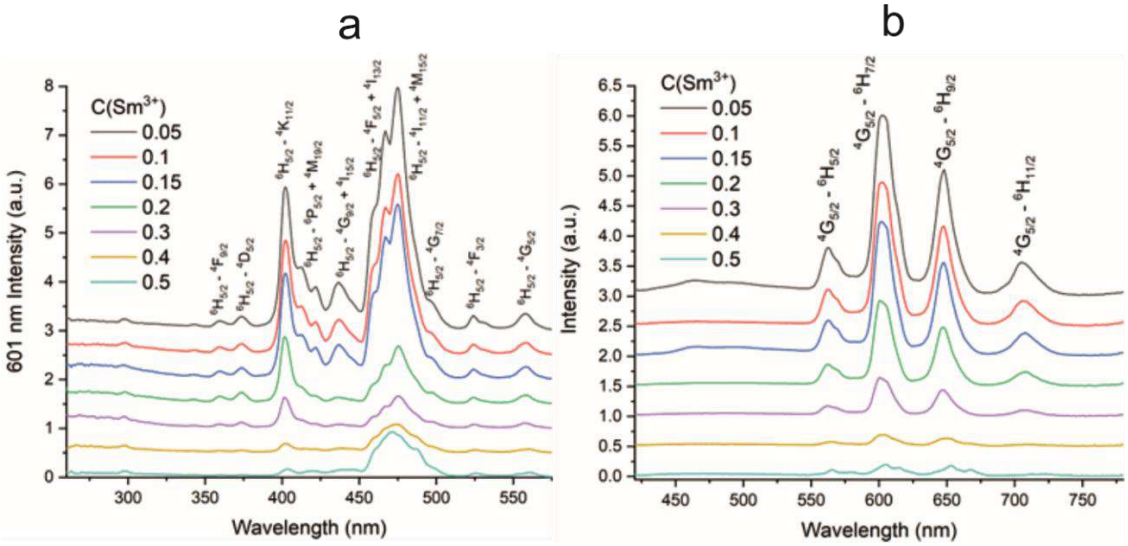

Figure 39 – Excitation spectra (λ_{em} = 601 nm) (a) and photoluminescence spectra (λ_{ex} = 402 nm) (b) of the $BaBi_{2-x-0.05}Eu_xSm_{0.05}B_2O_7$ concentration series.

The concentration dependence of the integral luminescence intensity at a wavelength of 601 nm is presented below (Figure 40a). It has been established that the optimal concentration of Sm^{3+} ions in the $BaBi_{2-x}Sm_xB_2O_7$ solid solutions is x = 0.05. Further increase in the samarium content leads to concentration quenching of luminescence.

The luminescence lifetime for the $^4G_{5/2}$ level of Sm^{3+} is maximal at x = 0.05 and is 0.8±0.1 ms (Figure 41b). The phosphor may be a promising red-emitting materials when co-activated with the crystalline matrix $BaBi_2B_2O_7$ by Sm^{3+} and Eu^{3+} ions (see section 1.7.4, page 33).

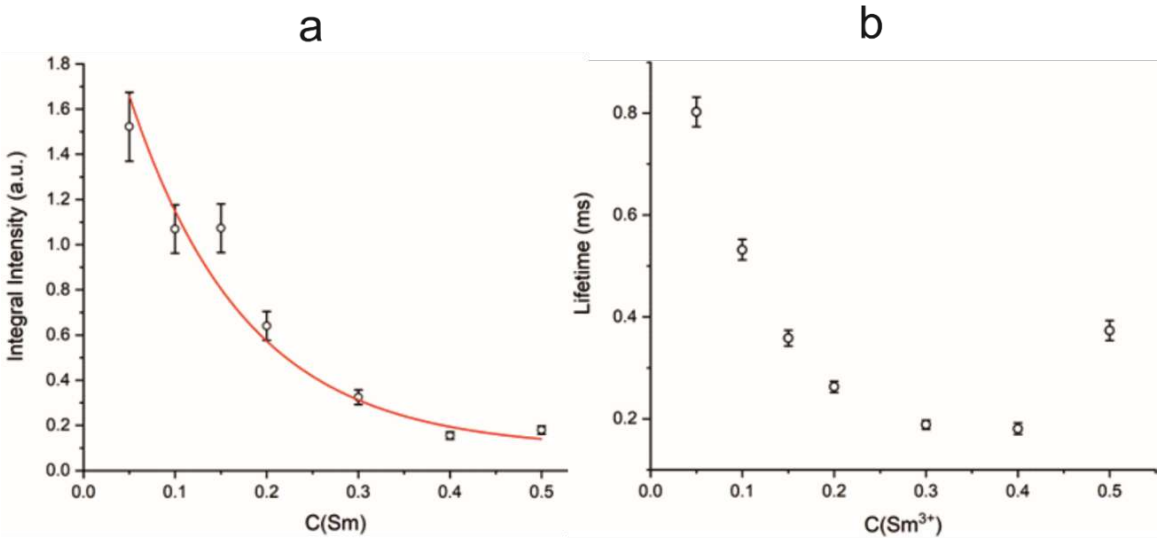

Figure 40 – Concentration dependence of the integral luminescence intensity of the $^4G_{5/2}$-$^6H_{5/2}$ transition (a), Concentration dependence of the lifetime of the $^4G_{5/2}$ level of europium ions in $BaBi_{2-x}Sm_xB_2O_7$ (b).

3.3 The $BaBi_{2-x-0.05}Eu_xSm_{0.05}B_2O_7$ (x = 0.35, 0.4, 0.45) borates

From the analysis of the luminescence intensity of $BaBi_{2-x}Sm_xB_2O_7$ borates (see section 3.2.6, page 75) and $BaBi_{2-x}Eu_xB_2O_7$ (see section 3.1.5, page 63) and based on the data (Wu et al., 2017), the optimal concentration of Sm^{3+} and Eu^{3+} ions is found to be x = 0.05 and x = 0.4, respectively. Therefore, the optimal composition for co-activation could be: $BaBi_{2-x-0.05}Eu_xSm_{0.05}B_2O_7$ (x = 0.35, 0.4, 0.45; y = 0.05).

3.3.1 Results of powder X-ray diffraction of the $BaBi_{2-x-0.05}Eu_xSm_{0.05}B_2O_7$ borates

Analysis of the diffraction patterns of the $BaBi_{2-x-0.05}Eu_xSm_{0.05}B_2O_7$ (x = 0.35, 0.4, 0.45) borates shows that samples with concentrations x = 0.35, 0.4 contain a small amount (3% according to Rietveld method) of Eu_2O_3 (*C2/m*) impurity phase. Further increase in the concentration of Eu^{3+} ions in the solid solution leads to an increase in the intensity of peaks of the impurity phase Eu_2O_3 (*C2/m*) and the appearance of a third phase – $BaBiBO_4$ (*Pnma*). The diffraction patterns of the $BaBi_{2-x-0.05}Eu_xSm_{0.05}B_2O_7$ (x = 0.35, 0.4) borates, containing 97% of the main phase, are presented in (Figure 41).

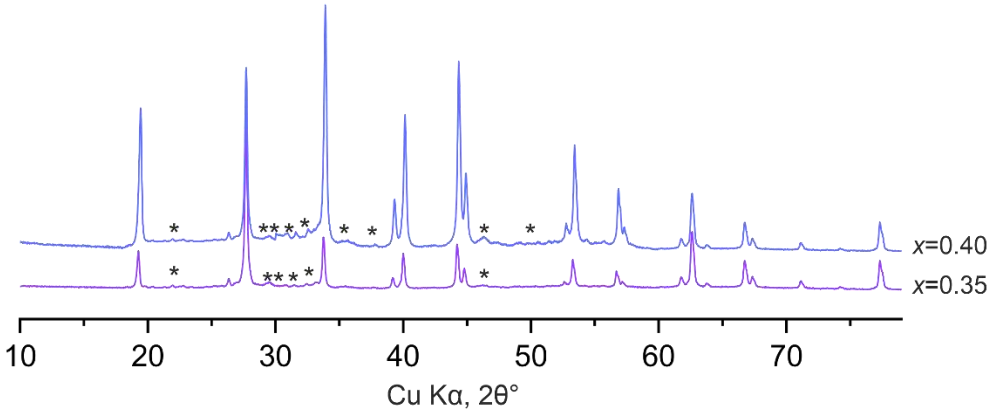

Figure 41 – Diffraction patterns of the $BaBi_{2-x-0.05}Eu_xSm_{0.05}B_2O_7$ borates. The asterisks correspond to the peaks of the Eu_2O_3-*C*2/*m* impurity phase (5%).

The unit cell parameters of the $BaBi_{2-x-0.05}Eu_xSm_{0.05}B_2O_7$ borates were calculated using powder data by the Rietveld method (Table 14). The parameters decrease with increasing concentration of Eu^{3+} ions in solid solutions, as the ionic radius $^{[8]}Eu^{3+}$ (1.206 Å) is smaller than $^{[8]}Bi^{3+}$ (1.31 Å) (Shannon, 1976), and the parameters in the sample with a concentration of $x = 0.45$ sharply increase, indicating a limit to the isomorphic capacity of the solid solution.

Table 14 – The unit cell parameters of the $BaBi_{2-x-0.05}Eu_xSm_{0.05}B_2O_7$ borates

Compound	*a*, Å	*b*, Å	*V*, Å^3
x =0 (Shabliskii et al., 2012)	5.3378(8)	13.583(2)	335.15(9)
x =0.35	5.3094(6)	13.519(2)	330.04(1)
x =0.40	5.3051(6)	13.507(2)	329.23(1)
x =0.45	5.3107(6)	13.519(2)	330.21(8)

3.3.2 Results of luminescent spectroscopy of the $BaBi_{2-x-0.05}Eu_xSm_{0.05}B_2O_7$ borates

Upon excitation of the $BaBi_{2-x-0.05}Eu_xSm_{0.05}B_2O_7$ solid solutions at a wavelength of 615 nm, broad bands in the range of 300—350 nm (Figure 42 a) corresponding to the interband transition of the crystalline matrix were observed. Narrow bands in the spectral range of 350—600 nm correspond to transitions of europium and samarium ions from the ground to the excited states.

In the photoluminescence spectra upon excitation at a wavelength of 401 nm for Sm^{3+} and 392 nm for Eu^{3+}, narrow bands (Figure 42 b) related to the radiative transitions of Sm^{3+} and Eu^{3+} ions were observed. The emission intensity of bands in the spectral range of 300—350 nm for the composition $x = 0.40$ is significantly lower compared to $x = 0.35$, which may be attributed to

approaching the immiscibility region of solid solutions, previously identified for $BaBi_{2-x}Eu_xB_2O_7$ borates in the region (x = 0.40-0.50). In the borate with a concentration of x = 0.40, the $^4G_{5/2}$-$^6H_{5/2}$ transition at 550 nm is not observed, which is present in the sample with x = 0.35 (Figure 42 b, circled). This observation may also be linked to nearing the immiscibility region of the solid solution.

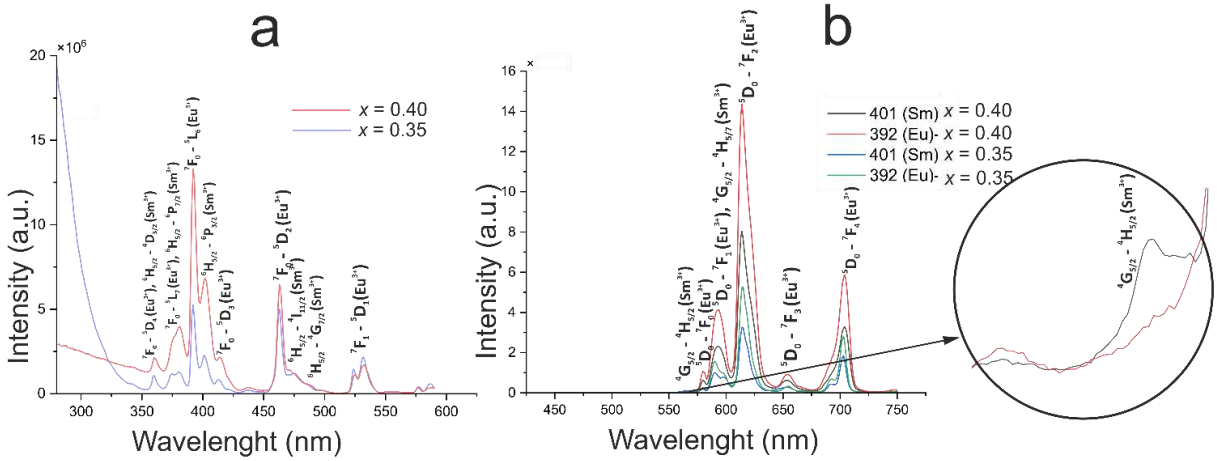

Figure 42 – Excitation spectra (λ_{em} = 615 nm) (a) and photoluminescence spectra (λ_{ex} = 392 (Eu^{3+}), 401 (Sm^{3+}) (b) of the $BaBi_{2-x-0.05}Eu_xSm_{0.05}B_2O_7$ concentration series.

3.4 The $BaBi_{2-0.15-y}Eu_{0.15}Sm_yB_2O_7$ (y = 0.05, 0.1, 0.15, 0.2, 0.3) borates

As soon as in the $BaBi_{2-x-0.05}Eu_xSm_{0.05}B_2O_7$ concentration series low-intensity radiative transitions of Sm^{3+} were observed, the novel series of solid solutions $BaBi_{2-0.15-y}Eu_{0.15}Sm_yB_2O_7$ (y = 0.05, 0.1, 0.15, 0.2, 0.3) with varying concentrations of samarium ions developed to achieve effective energy transfer from samarium to europium.

3.4.1 Results of powder X-ray diffraction of the $BaBi_{2-0.15-y}Eu_{0.15}Sm_yB_2O_7$ borates

Based on powder X-ray diffraction results, the $BaBi_{2-0.15-y}Eu_{0.15}Sm_yB_2O_7$ (y = 0.05, 0.1, 0.15, 0.2) borates are homogeneous. Further incorporation of Sm^{3+} atoms into the crystal structure leads to the formation of a secondary Sm_2O_3 (*C*2/*m*) phase. The diffraction patterns of homogeneous borates $BaBi_{2-0.15-y}Eu_{0.15}Sm_yB_2O_7$ (y = 0.05, 0.1, 0.15, 0.2) are presented below (Figure 43).

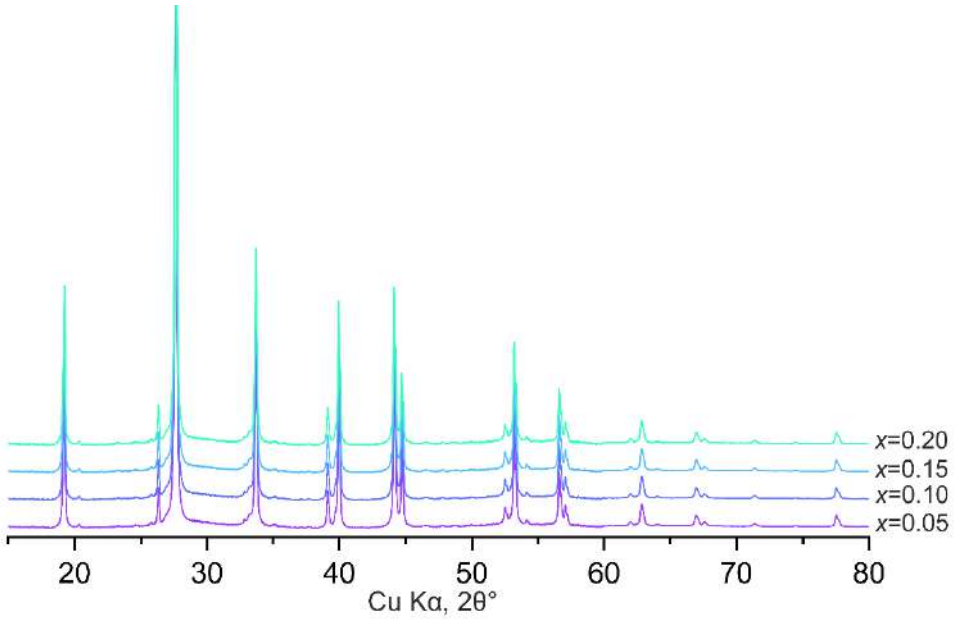

Figure 43 – Diffraction patterns of the $BaBi_{2-0.15-y}Eu_{0.15}Sm_yB_2O$ borates.

The dependencies of the unit cell parameters on the concentrations of Eu^{3+} and Sm^{3+} presented at Figure 44. Analysis of the concentration-dependent graphs allows for the identification of regions where continuous solid solutions exist (see 3.7.1, page 94).

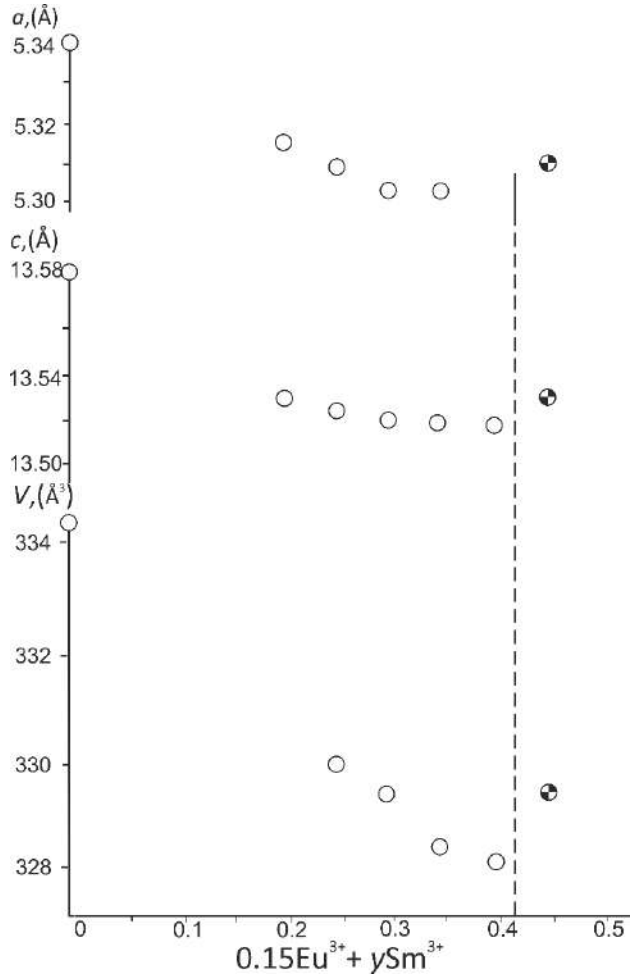

Figure 44 – The dependencies of the unit cell parameters on the content of Eu^{3+} in $BaBi_{2-x}Eu_xB_2O_7$ borates. The non-homogeneous $BaBi_{1.5}Eu_{0.5}B_2O_7$ sample is marked in black and white.

3.4.2 Results of luminescent spectroscopy of the $BaBi_{2-0.15-y}Eu_{0.15}Sm_yB_2O_7$ borates

The $BaBi_{2-0.15-y}Eu_{0.15}Sm_yB_2O_7$ borates were excited at a wavelength of 614 nm (Figure 45a). Excitation in the spectral range of 300—350 nm is associated with interband transition of the crystalline matrix. Narrow bands in the spectral range of 350—550 nm are attributed to transitions of Eu^{3+} and Sm^{3+} ions from the ground to the excited state. The fluorescence spectra under excitation at a wavelength of 295 nm are shown in Figure 45b. Wide bands in the spectral range of 300—400 nm correspond to the intrinsic emission of the crystalline matrix, while narrow bands in the spectral range of 450—750 nm are related to radiative transitions of Eu^{3+} and Sm^{3+} ions. The bands corresponding to samarium transitions, although less intense than the Eu^{3+} bands, have increased intensity compared to the $BaBi_{2-x-0.05}Eu_xSm_{0.05}B_2O_7$ concentration series.

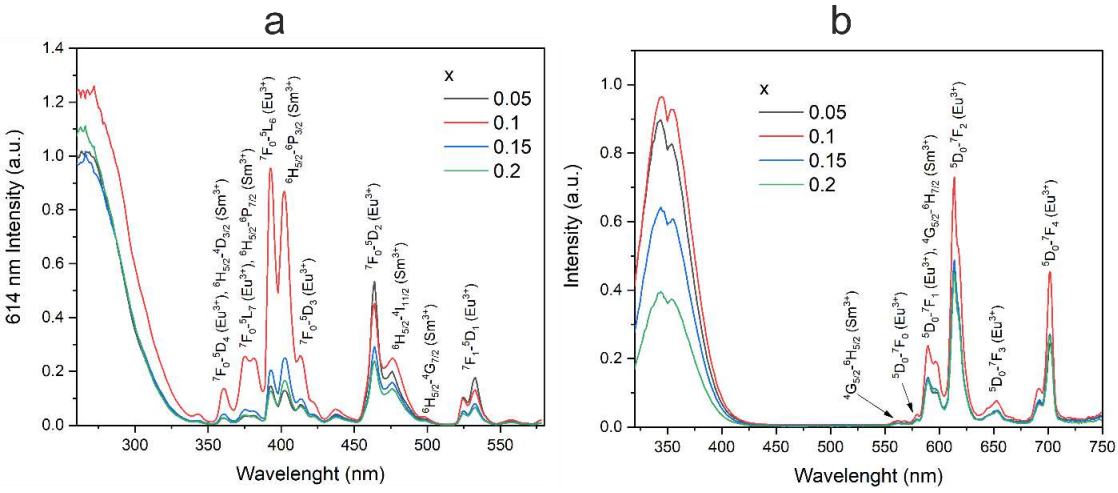

Figure 45 – Excitation spectra (λ_{em} = 614 nm) (a) and photoluminescence spectra (λ_{ex} = 295 (Eu^{3+}) nm) (b) of the $BaBi_{2-0.15-y}Eu_{0.15}Sm_yB_2O_7$ concentration series.

The optimal concentration of Sm^{3+} ions is x = 0.1 (Figure 46a). Co-activation of the crystalline matrix according to the formula $BaBi_{2-0.15-y}Eu_{0.15}Sm_yB_2O_7$ allowed to increase the optimal concentration of Sm^{3+} ions from x = 0.05 in $BaBi_{2-x}Sm_xB_2O_7$ (see section 3.2.6, page 75). The increase in optimal concentration can be explained by exchange interactions. The most effective energy transfer in phosphors through exchange mechanisms is achieved when the angle of the chemical bond *M*—O—*M* is 180°, providing maximum overlap of atomic orbitals. A similar energy transfer mechanism was observed in the phosphor $YVO_4:Eu^{3+}$ from $[VO_4]^{3-}$ to the Eu^{3+} ion, where the V–O–Eu angle is 170° (West, 1984). In the $BaBi_{2-x}Eu_xB_2O_7$ concentration series, Eu^{3+} atoms occupy *M*1 site (subposition *M*1') at x = 0.1—0.3, while in the $BaBi_{2-x}Sm_xB_2O_7$ borates, Sm^{3+} atoms only occupy *M*2 site (subposition *M*2'). Based on this analysis, it can be assumed that in the $BaBi_{2-0.15-y}Eu_{0.15}Sm_yB_2O_7$ borates, Eu*3*+ atoms also occupy *M*1' site, and Sm^{3+} occupies *M*2'. The average angles between *M*1'–O–*M*1', *M*2'–O–*M*2', *M*3'–O–*M*3', *M*1'–O–*M*2', *M*1'–O–*M*3', *M*2'–O– *M*3' are 164.8°, 162.8°, 127.2°, 171.3°, 102.9°, 105.2°, 106.3° respectively. Therefore, the most efficient energy transfer occurs between *M*1'–O–*M*2' (171.3°), where the rare earth elements are most abundant in the solid solution series $BaBi_{2-0.15-y}Eu_{0.15}Sm_yB_2O_7$ and $BaBi_{2-x}Eu_xB_2O_7$.

The luminescence lifetime decreases with increasing concentration of Sm^{3+} (Figure 46b).

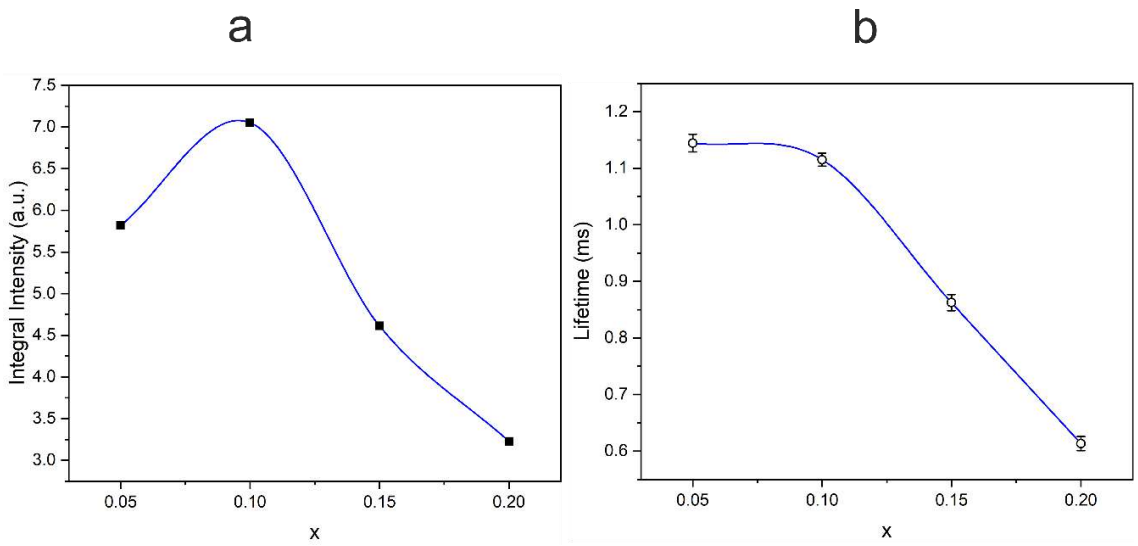

Figure 46 – Concentration dependence of the integral luminescence intensity of the luminescence (a), Concentration dependence of the lifetime of the luminescence (b)in $BaBi_{2-0.15-y}Eu_{0.15}Sm_yB_2O_7$ phosphors.

In the $BaBi_{2-0.15-y}Eu_{0.15}Sm_yB_2O_7$ phosphors, increasing the concentration of Eu^{3+} ions leads to a color change from red-orange to red (Figure 47, Table 15).

Table 15 – CIE (CIE 1931) chromaticity coordinates of the $BaBi_{2-0.15-y}Eu_{0.15}Sm_yB_2O_7$ concentration series

***C*(Eu^{3+})**	***x***	***y***
0.05	0.58333	0.33918
0.1	0.60429	0.34469
0.15	0.60156	0.34502
0.2	0.61377	0.34681

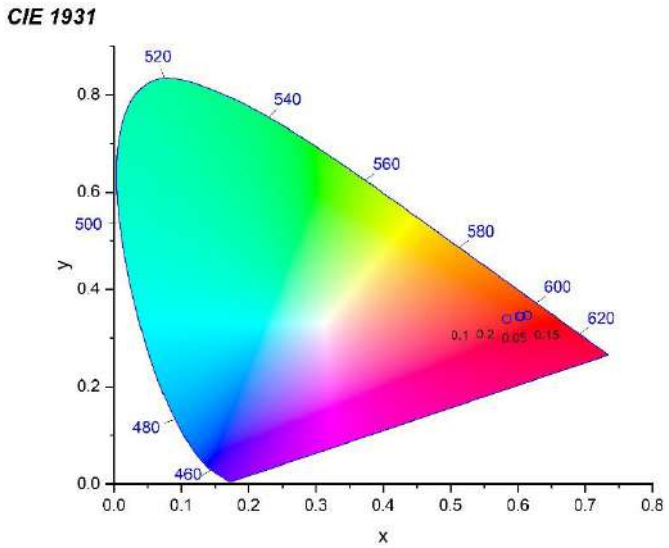

Figure 47 – CIE chromaticity coordinates of the $BaBi_{2-0.15-y}Eu_{0.15}Sm_yB_2O_7$ concentration series.

3.5 The $BaBi_{2-x}Tb_xB_2O_7$ (x = 0.05, 0.1, 0.15, 0.2, 0.3, 0.4, 0.5) borates

In order to obtain promising matrices for white light-emitting diodes, the $BaBi_{2-x}Tb_xB_2O_7$ green-emitting phosphors were synthesized, and their crystal structure and luminescent properties were studied.

3.5.1 Results of powder X-ray diffraction of the$BaBi_{2-x}Tb_xB_2O_7$ borates

The diffraction patterns of the $BaBi_{2-x}Tb_xB_2O_7$ (x = 0.05—0.4) borates are presented in Figure 48. Borates with x = 0.05—0.3 are homogeneous. In the $BaBi_{1.6}Tb_{0.4}B_2O_7$, a small amount of the Tb_2O_3-$C2/m$ impurity phase is observed (2% according to the Rietveld method). Further increase in the Tb^{3+} ion content in the $BaBi_{1.5}Tb_{0.5}B_2O_7$ borate leads to an increase in the intensity of the Tb_2O_3-$C2/m$ impurity phase (10% according to Rietveld).

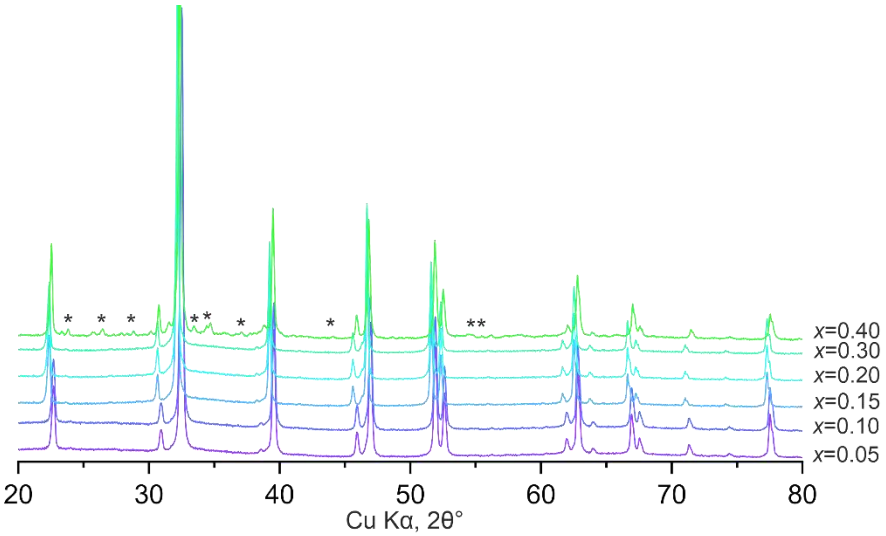

Figure 48 – Diffraction patterns of the $BaBi_{2-x}Tb_xB_2O_7$ borates. The asterisks correspond to the peaks of the Tb_2O_3-*C*2/*m* impurity phase (2%).

The concentration dependence of the unit cell parameters is shown in Figure 49. Section 3.7.1 (page 94) provides an analysis of the dependence of the unit cell parameters on the concentration of REE^{3+} ions, as well as describes the regions of existence of continuous solid solutions of $BaBi_{2-x-y}REE_xREE'_yB_2O_7$ (*REE, REE'*= Eu^{3+}, Sm^{3+}, Tb^{3+}, Tm^{3+}).

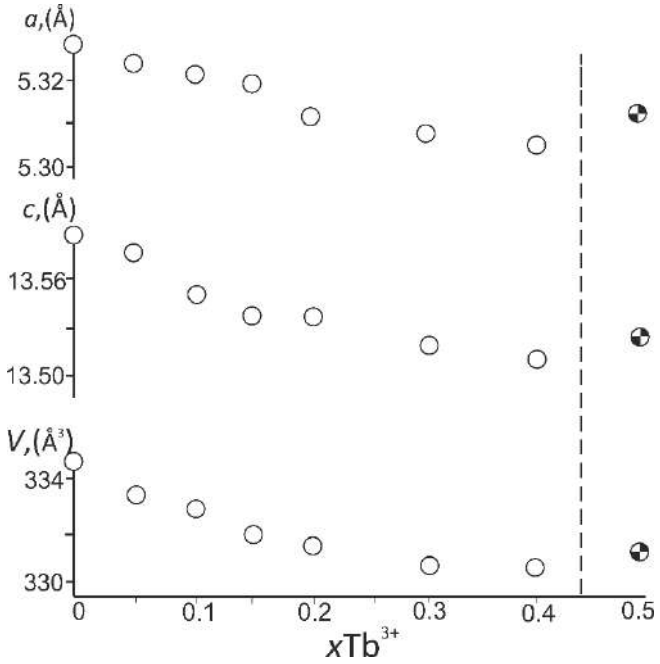

Figure 49 – The dependencies of the unit cell parameters on the content of Tb^{3+} in $BaBi_{2-x}Tb_xB_2O_7$ borates.

3.5.2 Results of refinement of crystal structures of the $BaBi_{2-x}Tb_xB_2O_7$ (x = 0.1, 0.3, 0.4) borates

The (Bi,Ba)(Bi,Ba)(Tb,Bi,Ba)B_2O_7 borates also crystallize in the structural type of $BaBi_2B_2O_7$ ($P6_3$, a = 5.3378(8), c = 13.583(2) Å, V = Å^3, Z =2) (Bubnova et al., 2016). Refined by single-crystal data, the formulas of the crystal structures $Ba_{0.99}Bi_{1.90}Tb_{0.11}B_2O_7$, $Ba_{1.00}Bi_{1.71}Tb_{0.30}B_2O_7$, and $Ba_{1.02}Bi_{1.60}Tb_{0.38}B_2O_7$ are close to the formulas of the initial charge $BaBi_{1.90}Tb_{0.10}B_2O_7$, $BaBi_{1.70}Tb_{0.30}B_2O_7$, $BaBi_{1.60}Tb_{0.40}B_2O_7$. Below are presented crystallographic data, experimental conditions, and refinement parameters of the crystal structures (Table 16). Atom coordinates, anisotropic and equivalent atomic displacement parameters are presented in (Table S 5, p. 146, Table S 6, p. 147), bond lengths – in Table 17. Activation of the crystalline matrix by Tb^{3+} atoms leads to increasing the degree of orderliness of solid solutions – (Bi,Ba)(Bi,Ba)(Tb,Bi,Ba)B_2O_7, characterized by the occupancy nature of the sites: due to the smaller size of Tb^{3+} atoms and the volume of the $M3O_9$ polyhedron, the $M3$ site is predominantly occupied by these atoms, whereas in the (Bi,Ba,Eu)(Bi,Ba,Eu)(Bi,Ba)B_2O_7 and (Bi,Ba)(Bi,Ba,Sm)(Bi,Ba)B_2O_7 solid solutions all sites are predominantly occupied by Bi atoms.

The crystal structure of this structural type is described in detail above (see section 3.1.2, p. 58).

Table 16 – Crystal data and details of refinement of the $BaBi_2B_2O_7$*, $BaBi_{1.90}Tb_{0.10}B_2O_7$, $BaBi_{1.70}Tb_{0.30}B_2O_7$, $BaBi_{1.60}Tb_{0.40}B_2O_7$ borates

Stoichiometric formula	$BaBi_2B_2O_7$	$BaBi_{1.90}Tb_{0.10}B_2O_7$	$BaBi_{1.70}Tb_{0.30}B_2O_7$	$BaBi_{1.60}Tb_{0.40}B_2O_7$
Refined formula	$BaBi_2B_2O_7$	$Ba_{0.99}Bi_{1.90}Tb_{0.11}B_2O_7$	$Ba_{1.00}Bi_{1.71}Tb_{0.30}B_2O_7$	$Ba_{1.02}Bi_{1.60}Tb_{0.38}B_2O_7$
Crystal system, space group	Hexagonal, $P6_3$			
Temperature (K)	293			
a (Å)	5.3378(8)	5.3291(8)	5.3106(8)	5.3143(8)
c (Å)	13.583(2)	13.558(2)	13.520(2)	13.548(2)
V (Å^3)	335.15(9)	333.45(9)	330.22(9)	331.36(9)
Z	2			
Radiation type	Mo $K\alpha$			
μ (mm^{-1})	58.18	56.87	54.69	52.41
Crystal size (mm)	0.04×0.04×0.03	0.04×0.05×0.1	0.03×0.04×0.07	0.04×0.04×0.09
Diffractometer	Rigaku XtaLab Synergy-S			
No. of measured, independent and observed [$I > 3\sigma(I)$] reflections	1872/398/261	3970/789/412	3780/775/371	3611/761/462
R_{int}	0.031	0.041	0.043	0.036
$(\sin\theta/\lambda)_{max}$ (Å^{-1})	0.593	0.774	0.768	0.775
Refinement				
R (obs), wR(obs), S	0.026, 0.056, 0.052, 0.068, 2.01		0.044, 0.060, 1.68	0.056, 0.076, 2.86

	1.04			
No. of reflections	398	789	775	761
No. of parameters	57	42	42	42

*Data from (Bubnova et al., 2016)

Table 17 – Selected bond lengths (Å) for $BaBi_2B_2O_7$*, $BaBi_{1.90}Tb_{0.10}B_2O_7$, $BaBi_{1.70}Tb_{0.30}B_2O_7$, $BaBi_{1.60}Tb_{0.40}B_2O_7$ borates

Bond length/*x*	**0**	**0.10**	**0.30**	**0.40**
Ba1—O3	2.48(5)	2.46(3)	2.37(3)	2.44(2)
Ba1—O2×3	2.71(3)	2.740(15)	2.705(9)	2.733(13)
Ba1—O2×3	2.79(3)	2.761(19)	2.743(9)	2.784(13)
Ba1—O1×3	2.98(2)	2.945(19)	3.066(16)	2.939(18)
<Ba1—O>$_{10}$	**2.79**	**2.78**	**2.79**	**2.78**
Bi1—O3	2.11(5)	2.08(3)	2.00(3)	2.03(2)
Bi1—O2	2.37(2)	2.418(13)	2.413(16)	2.437(16)
Bi1—O2	2.45(3)	2.448(17)	2.454(16)	2.486(17)
Bi1—O2	2.65(4)	2.68(2)	2.646(13)	2.645(15)
Bi1—O2	2.72(4)	2.69(2)	2.684(13)	2.704(14)
Bi1—O2	2.96(3)	2.944(16)	2.906(16)	2.894(17)
Bi1—O2	3.03(2)	2.972(13)	2.947(16)	2.944(17)
Bi1—O1	3.24(2)	3.21(2)	3.337(17)	3.239(18)
Bi1—O1	3.25(2)	3.22(2)	3.341(17)	3.242(18)
Bi1—O1	3.51(2)	3.451(18)	3.552(17)	3.446(18)
<Bi1—O>$_{10}$	**2.83**	**2.81**	**2.83**	**2.81**
Ba2—O3	2.52(5)	2.65(3)	2.64(3)	2.63(3)
Ba2—O1×3	2.72(2)	2.765 (14)	2.758(14)	2.746(9)
Ba2—O1×3	2.79(2)	2.769 (14)	2.799(9)	2.756(9)
Ba2—O2×3	2.98(2)	2.881(16)	2.885(16)	2.961(15)
<Ba2—O>$_{10}$	**2.80**	**2.79**	**2.80**	**2.80**
Bi2—O3	2.18(5)	2.16(3)	2.18(3)	2.18(2)
Bi2—O1×3	2.66(2)	2.679(8)	2.661(8)	2.669(8)
Bi2—O1×3	2.73(2)	2.683(8)	2.703(8)	2.679(8)
Bi2—O2×3	3.26(2)	3.296(16)	3.273(16)	3.340(14)
<Bi2—O>$_{10}$	**2.81**	**2.81**	**2.81**	**2.82**
Ba3—O2×3	2.49(2)	2.495(18)	2.699(17)	2.594(15)
Ba3—O1×3	2.57(2)	2.567(16)	2.290(18)	2.423(17)
Ba3—O3×3	3.083(1)	3.0795(19)	3.082(4)	3.077(2)
<Ba3—O>$_9$	**2.71**	**2.71**	**2.69**	**2.70**
Bi3(Tb3)—O1	2.44(2)	2.522(19)	2.389(16)	2.462(17)
Bi3(Tb3)—O1	2.46(2)	2.526(19)	2.396(15)	2.473(17)
Bi3(Tb3)—O2	2.38(3)	2.326(19)	2.398(15)	2.361(14)
Bi3(Tb3)—O2	2.39(2)	2.333(16)	2.400(14)	2.355(14)

Bi3(Tb3)—O3	2.643(4)	2.685(2)	2.745(8)	2.728(9)
Bi3(Tb3)—O1	2.88(2)	2.899(17)	2.715(16)	2.800(17)
Bi3(Tb3)—O2	2.82(2)	2.725(14)	2.719(14)	2.703(14)
Bi3(Tb3)—O3	3.321(6)	3.289(6)	3.238(6)	3.244(7)
Bi3(Tb3)—O3	3.325(4)	3.293(6)	3.240(6)	3.260(7)
<Bi3(Tb3)—O>$_9$	**2.74**	**2.73**	**2.69**	**2.71**
O3—Ba1	2.48(5)	2.46(3)	2.37(3)	2.44(2)
O3—Ba2	2.52(5)	2.65(3)	2.64(3)	2.63(3)
O3—Ba3×3	3.083(1)	3.0795(19)	3.082(4)	3.077(2)
<O3—Ba>$_5$	**2.85**	**2.87**	**2.85**	**2.86**
O3—Bi1	2.11(5)	2.08(3)	2.00(3)	2.03(2)
O3—Bi2	2.18(5)	2.16(3)	2.18(3)	2.18(2)
O3—Bi3(Tb3)x3	2.643(4)	2.685(2)	2.745(8)	2.728(9)
<O3—Bi>$_5$	**2.45**	**2.46**	**2.48**	**2.48**
B1—O1×3	1.36(2)	1.375(16)	1.37(1)	1.38(2)
<B1—O>$_3$	**1.36(2)**	**1.375(16)**	**1.37(1)**	**1.38(2)**
B2—O2×3	1.38(2)	1.386(11)	1.37(3)	1.37(1)
<B2—O>$_3$	**1.38(2)**	**1.386(11)**	**1.37(3)**	**1.37(1)**

3.5.3 Distribution of Tb^{3+} cations over *M*1, *M*2, *M*3 sites

In the $BaBi_{2-x}Tb_xB_2O_7$ (x = 0.10, 0.30, 0.40) crystal structures, Tb^{3+} atoms occupy only the *M*3 site (Figure 50). A comparison of the occupancies of the sites in studied borates is presented below (see section 3.7.2, p. 96).

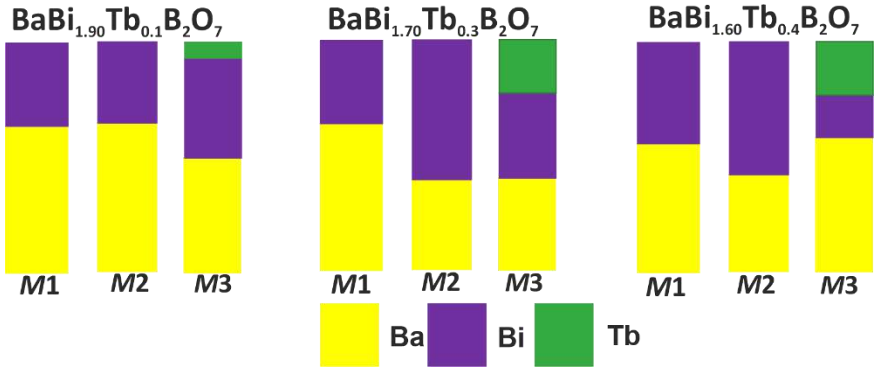

Figure 50 – Occupancy (%) of cation sites in the crystal structures of $BaBi_{2-x}Tb_xB_2O_7$ (x = 0.10, 0.30, 0.40) borates.

3.5.4 Results of luminescent spectroscopy of the $BaBi_{2-x}Tb_xB_2O_7$ borates

When excited at a wavelength of 545 nm, narrow bands are observed in the $BaBi_{2-x}Tb_xB_2O_7$ concentration series (Figure 51a), corresponding to transitions of Tb^{3+} ions from the ground state to the excited state. Below are the fluorescence spectra when excited at a wavelength of 480 nm (Figure 51b). All narrow bands in the spectra correspond to radiative transitions of Tb^{3+} ions.

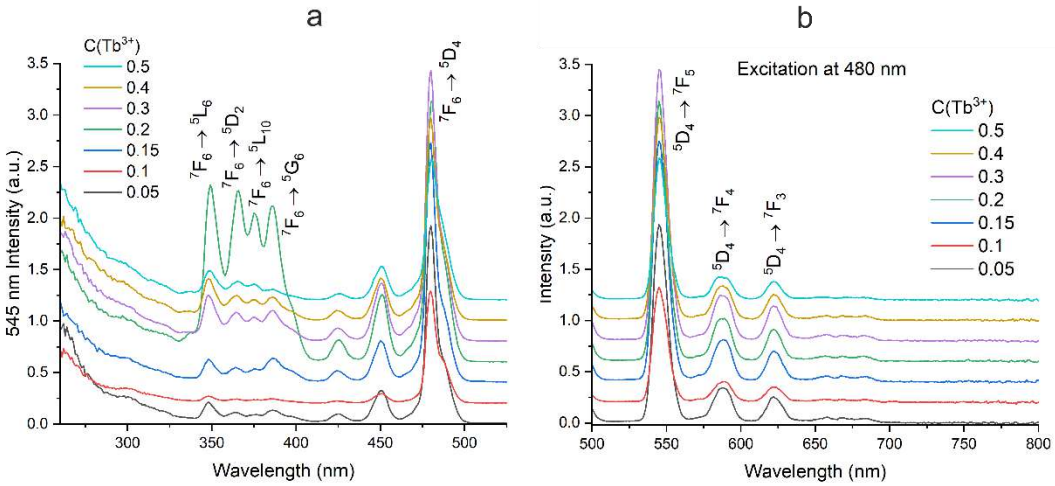

Figure 51 – Excitation spectra (λ_{em} = 545 nm) (a) and photoluminescence spectra (λ_{ex} = 480 nm) (b) of the $BaBi_{2-x}Tb_xB_2O_7$ concentration series.

The optimal concentration of Tb^{3+} ions in the $BaBi_{2-x}Tb_xB_2O_7$ solid solution is x = 0.3 (Figure 52). The $BaBi_{2-x}Tb_xB_2O_7$ phosphors emit in the green region of the spectrum (Figure 53, Table 18).

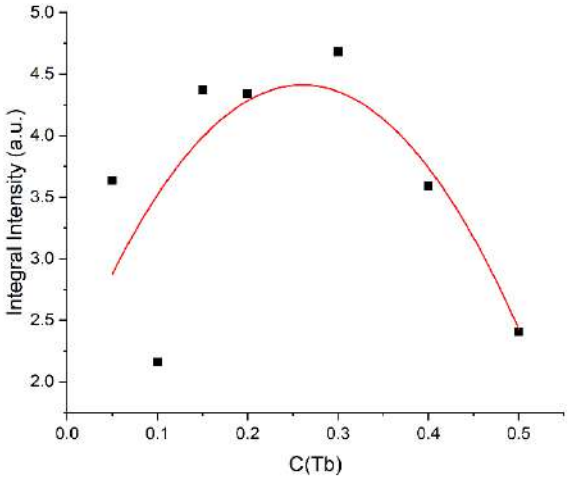

Figure 52 – Concentration dependence of the integral luminescence intensity of the $BaBi_{2-x}Tb_xB_2O_7$ borates

Table 18 – CIE (CIE 1931) chromaticity coordinates of the $BaBi_{2-x}Tb_xB_2O_7$ concentration series

***C*(Eu^{3+})**	***x***	***y***
0.05	0.37451	0.61584
0.1	0.37725	0.6135
0.15	0.37221	0.61805
0.2	0.37264	0.61786
0.3	0.37413	0.61649
0.4	0.37386	0.61645
0.5	0.37583	0.61452

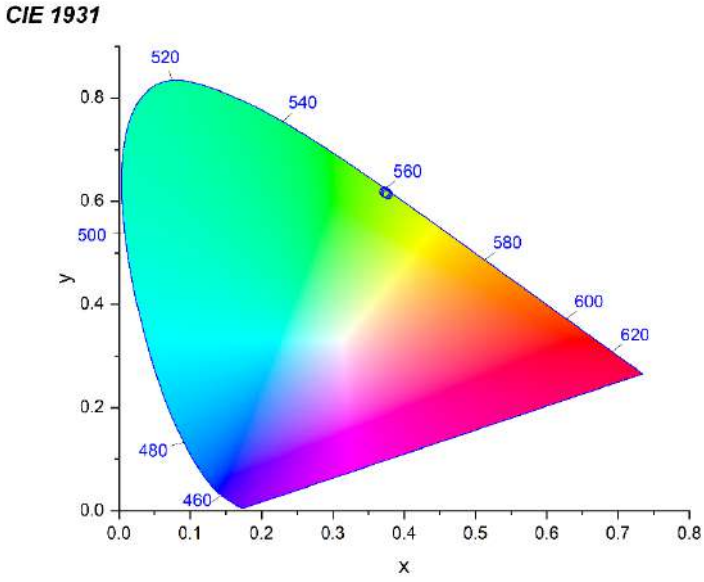

Figure 53 – CIE chromaticity coordinates of the $BaBi_{2-x}Tb_xB_2O_7$ concentration series.

3.6 The $BaBi_{2-x-0.3}Eu_xTb_{0.15}Tm_{0.15}B_2O_7$ (x = 0.05, 0.1, 0.15, 0.2) borates

As the $BaBi_{2-x}Eu_xB_2O_7$ borates are promising tunable phosphors emitting in the red spectral region, and the $BaBi_{2-x}Tb_xB_2O_7$ borates are green-emitting phosphors, it is suggested that promising matrices for white LED devices could be created based on them by adding a blue-emitting rare-earth element ion to the matrix. From literature data, it is known that the $CaBi_2B_2O_7$: Tm^{3+} borate (Li et al., 2016c) is a promising blue-emitting phosphor with high thermal stability (see section 1.7.4, page 33), leading to the conclusion that its presence in the crystalline matrix $BaBi_2B_2O_7$ will provide the necessary blue color for use in w-LEDs. Since the $BaBi_{2-x}Eu_xB_2O_7$ borates are capable of changing color depending on the concentration of Eu^{3+} ions, it has been decided to obtain the $BaBi_{2-x-0.3}Eu_xTb_{0.15}Tm_{0.15}B_2O_7$ (x = 0.05, 0.1, 0.15, 0.2) solid solutions with variable concentrations of europium ions for further color tuning in white LED devices.

3.6.1 Results of powder X-ray diffraction of the $BaBi_{2-x-0.3}Eu_xTb_{0.15}Tm_{0.15}B_2O_7$ borates

Analysis of the powder diffraction patterns of the $BaBi_{2-x-0.3}Eu_xTb_{0.15}Tm_{0.15}B_2O_7$ borates shows that samples with concentrations x = 0.05—0.15 are homogeneous (Figure 54). Further increase in the content of Tb^{3+} ions in the $BaBi_{1.5}Eu_{0.20}Tb_{0.15}Tm_{0.15}B_2O_7$ borate leads to the formation of a Tb_2O_3-$C2/m$ secondary phase (11% according to the Rietveld method).

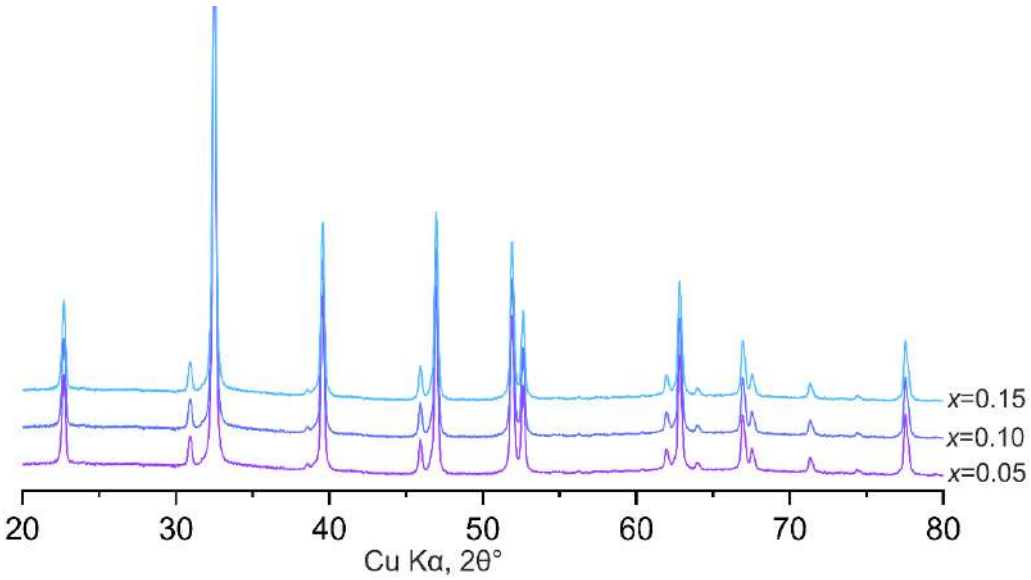

Figure 54 – Diffraction patterns of the $BaBi_{2-x-0.3}Eu_xTb_{0.15}Tm_{0.15}B_2O_7$ borates.

Based on refining of the unit cell parameters of the $BaBi_{2-x-0.3}Eu_xTb_{0.15}Tm_{0.15}B_2O_7$ borates using the Rietveld method with powder data (Figure 55), the miscibility regions of solid solutions have been determined. The results are presented in section 3.7.1 (page 94).

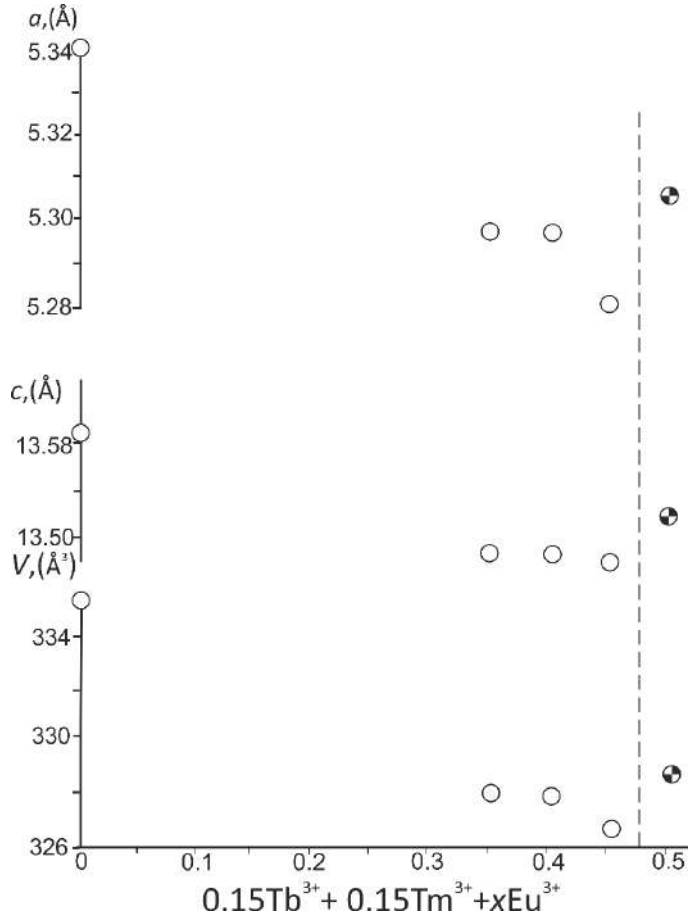

Figure 55 – The dependencies of the unit cell parameters on the content of REE^{3+} in $BaBi_{2-x-0.3}Eu_xTb_{0.15}Tm_{0.15}B_2O_7$ borates.

3.6.2 Results of luminescent spectroscopy of the $BaBi_{2-x-0.3}Eu_xTb_{0.15}Tm_{0.15}B_2O_7$ borates

When excited in the $BaBi_{2-x-0.3}Eu_xTb_{0.15}Tm_{0.15}B_2O_7$ concentration series of at a wavelength of 614 nm (Figure 56a), broad bands in the spectral range of 250—350 nm are observed, corresponding to interband transitions of the crystalline matrix. In the photoluminescent spectra (Figure 56b), broad bands in the range of 300—400 nm, related to the emission of the crystalline matrix, and narrow bands in the range of 450—750 nm, corresponding to radiative transitions of Eu^{3+}, Tb^{3+}, and Tm^{3+} ions, are observed. The emission bands of Eu^{3+} exhibit significantly higher intensity.

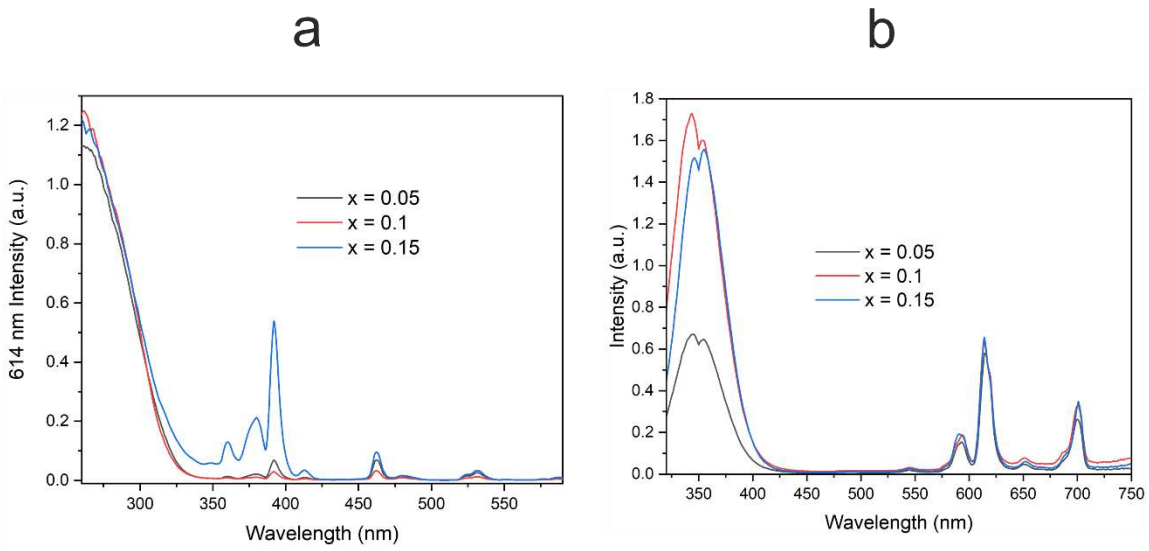

Figure 56 – Excitation spectra (λ_{em} = 614 nm) (a) and photoluminescence spectra (λ_{ex} = 295 (Eu^{3+}) nm) (b) of the $BaBi_{2-x-0.05}Eu_xSm_{0.05}B_2O_7$ concentration series.

According to the CIE color coordinates (Figure 57, Table 19), the $BaBi_{2-x-0.3}Eu_xTb_{0.15}Tm_{0.15}B_2O_7$ borates are tunable red-emitting phosphors

Table 19 – CIE (CIE 1931) chromaticity coordinates of the $BaBi_{2-x-0.3}Eu_xTb_{0.15}Tm_{0.15}B_2O_7$ concentration series

***C*(Eu^{3+})**	***x***	***y***
0.05	0.64768	0.34528
0.1	0.64662	0.35336
0.15	0.64256	0.35683

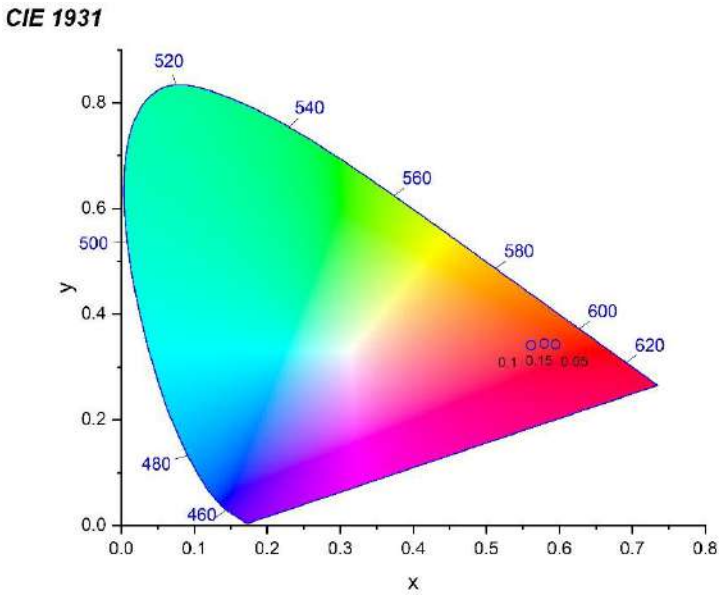

Figure 57 – CIE chromaticity coordinates of the $BaBi_{2-x-0.3}Eu_xTb_{0.15}Tm_{0.15}B_2O_7$ concentration series.

3.7 Results and discussion

3.7.1 Areas of continuous solid solutions existence $BaBi_{2-x-y-z}REE_{x,x,z}B_2O_7$ (*REE* = Eu^{3+}, Sm^{3+}, Tb^{3+}, Tm^{3+})

The concentration dependencies of the unit cell parameters of the $BaBi_{2-x-y-z}REE_{x,x,z}B_2O_7$ (*REE* = Eu^{3+}, Sm^{3+}, Tb^{3+}, Tm^{3+}) borates are shown in Figure 58. For all series of solid solutions, a decrease in the unit cell parameters is observed when $^{[8]}Bi^{3+}$ atoms (1.310 Å) (Shannon, 1976) are replaced by smaller REE^{3+} atoms. Additionally, as the ordinal number of the rare earth element decreases, the unit cell parameters of the corresponding solid solutions also decrease ($^{[8]}Sm^{3+}$ (1.219 Å), $^{[8]}Eu^{3+}$ (1.206 Å), $^{[8]}Tb^{3+}$ (1.18 Å), $^{[8]}Tm^{3+}$ (1.134 Å) (Shannon, 1976). The existence regions of continuous solid solutions $BaBi_{2-x-y-z}REE_{x,x,z}B_2O_7$ (*REE* = Eu^{3+}, Sm^{3+}, Tb^{3+}, Tm^{3+}) have been determined. The unit cell parameters of two-phase formations $BaBi_{1.5}Eu_{0.5}B_2O_7$, $BaBi_{1.6}Sm_{0.4}B_2O_7$, $BaBi_{1.5}Sm_{0.5}B_2O_7$, $BaBi_{1.5}Tb_{0.5}B_2O_7$, $BaBi_{1.5}Eu_{0.45}Sm_{0.05}B_2O_7$, $BaBi_{1.55}Eu_{0.15}Sm_{0.25}B_2O_7$, $BaBi_{1.5}Eu_{0.20}Tb_{0.15}Tm_{0.15}B_2O_7$ sharply increase, indicating a decrease in the content of the REE^{3+} ions in the solid solutions and reaching the limits of isomorphic capacity. Thus, the existence regions of continuous solid solutions are estimated as follows: $BaBi_{2-x}Sm_xB_2O_7$ (x = 0—0.35), $BaBi_{2-x}Eu_xB_2O_7$ (x = 0—0.45), $BaBi_{2-x}Tb_xB_2O_7$ (x = 0—0.5), $BaBi_{2-0.15-y}Eu_{0.15}Sm_yB_2O_7$ ($x + y$ = 0—0.375), $BaBi_{2-x-0.3}Eu_xTb_{0.15}Tm_{0.15}B_2O_7$ ($x + y + z$ = 0—0.475). The maximum concentration of the REE^{3+} ions in the $BaBi_{2-x}Sm_xB_2O_7$ solid solutions is x = 0.3, and in $BaBi_{2-x}Eu_xB_2O_7$ it is x = 0.4. According to Vegard's rule, formulated in 1921, the unit

cell parameters of solid solutions change within a series linearly in the first approximation. The Sm^{3+} atoms, which are closer in size to Bi^{3+} than Eu^{3+}, should more predominantly enter the crystal structure of $BaBi_2B_2O_7$. However, since this rule is valid for the simplest isomorphic substitutions in one system of sites, polarity of compositional deformations is manifested, leading to deviation from additivity. Thus, in addition to the ionic radius of the substituting atom, the crystallographic site occupied by this atom also influences the boundaries of solid solution existence.

Co-activation of the crystalline matrix $BaBi_2B_2O_7$ has allowed for the expansion of the boundaries of solid solution existence: in $BaBi_{2-x-0.05}Eu_xSm_{0.05}B_2O_7$, the miscibility range is estimated as x = 0—0.475, while in $BaBi_{2-x}Eu_xB_2O_7$, x = 0—0.45; in $BaBi_{2-0.15-y}Eu_{0.15}Sm_yB_2O_7$, the maximum concentration of REE^{3+} has increased to x = 0—0.375 compared to $BaBi_{2-x}Sm_xB_2O_7$ (x= 0—0.35); and in $BaBi_{2-x-0.3}Eu_xTb_{0.15}Tm_{0.15}B_2O_7$, the maximum content of REE^{3+} has increased to x = 0—0.475, while in $BaBi_{2-x}Tb_xB_2O_7$, it was (x = 0—0.45).

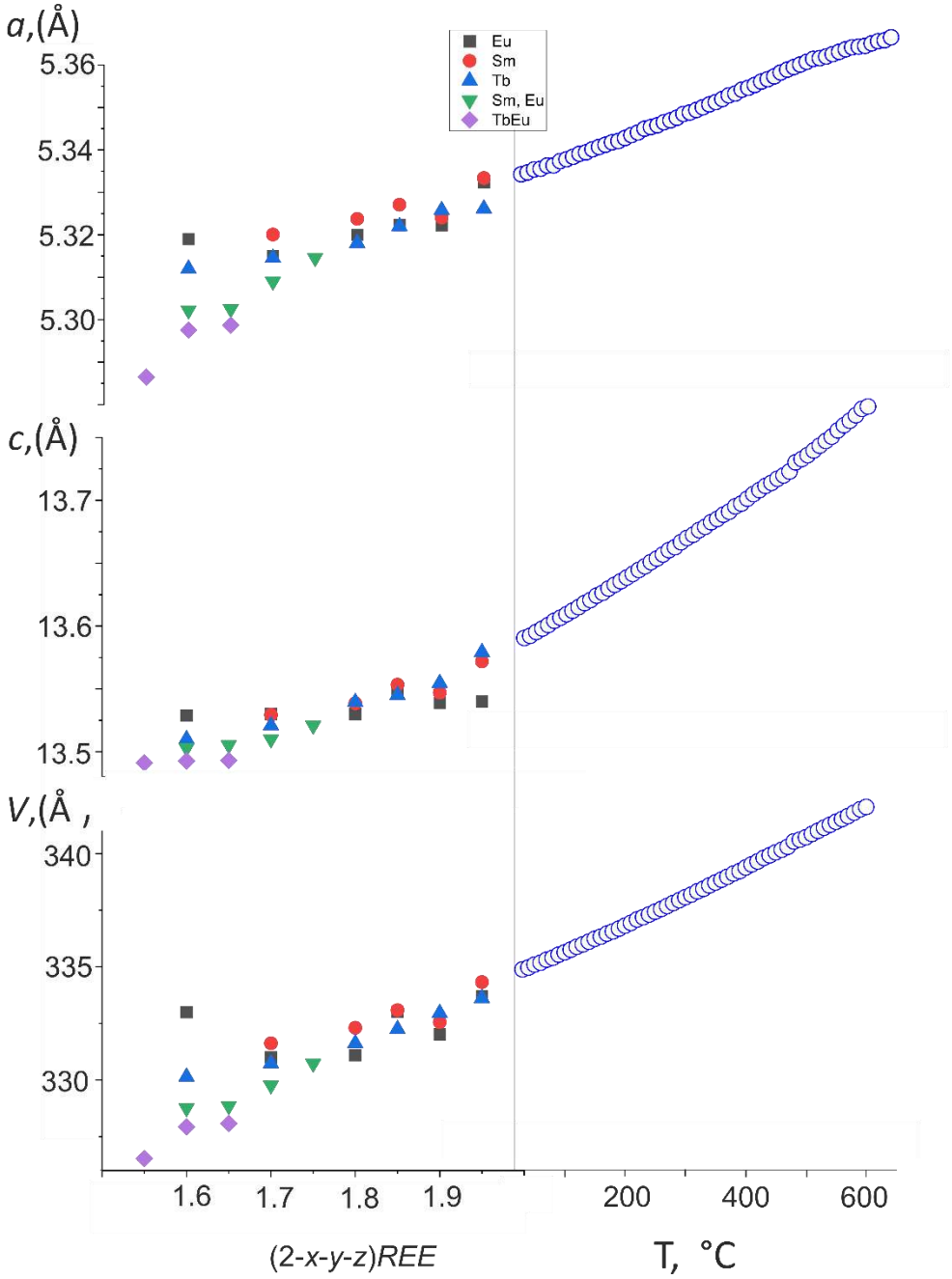

Figure 58 – The dependencies of the unit cell parameters on the content of REE^{3+} (left) and on the temperature (right) in the $BaBi_{2-x-y-z}REE_{x,x,z}B_2O_7$ (*REE* = Eu^{3+}, Sm^{3+}, Tb^{3+}, Tm^{3+}) borates.

3.7.2 Analysis of the occupancies of crystallographic sites of the $BaBi_{2-x}REE_xB_2O_7$ (*REE* = Eu^{3+}, Sm^{3+}, Tb^{3+}) borates

As previously mentioned (see section 3.1.2, page 58), the crystal structure of the $BaBi_2B_2O_7$ contains three crystallographic sites for large cations, each of which is disordered into Ba and Bi subpositions. In the crystalline structures of the $BaBi_{2-x}REE_xB_2O_7$ (*REE* = Eu^{3+}, Sm^{3+}, Tb^{3+})

borates, the REE^{3+} atoms occupy the same split Bi subpositions. The distribution of cations in sites differs. This section provides an analysis of the cation distribution in sires and describes possible reasons for this phenomenon.

In the $BaBi_{2-x}Sm_xB_2O_7$ (x = 0.05, 0.30) solid solutions, Sm^{3+} atoms replace Bi^{3+} in $M2$ site (Figure 34).

In the crystal structures of the $BaBi_{2-x}Eu_xB_2O_7$ (x = 0.10, 0.20, 0.40) solid solutions, Eu^{3+} atoms occupy $M1$ site at concentrations x = 0.10—0.30, and with an increase in the concentration of the activator ion to x = 0.40 in the solid solution, Eu^{3+} atoms occupy around 30% of $M2$ and 10% of $M1$ site (Figure 26).

In the $BaBi_{2-x}Tb_xB_2O_7$ (x = 0.10, 0.30, 0.40) borates, Tb^{3+} atoms only occupy $M3$ site (Figure 50).

Such differences in the occupancy of crystallographic sites can be explained from the perspective of the size criterion (Filatov, 1990). The $M3O_9$ polyhedron has the smallest volume (V = 39.06 Å^3), while the volumes of the $M1O_{10}$ (V = 44.64 Å^3) and $M2O_{10}$ (V = 44.18 Å^3) polyhedron are practically the same (the difference is 1%). Since the $^{[8]}Sm^{3+}$ (1.219 Å) and $^{[8]}Eu^{3+}$ (1.206 Å) atoms are also comparable in size, the likelihood of their entry into $M1$ and $M2$ sites is presumably the same. The $^{[8]}Tb^{3+}$atoms have the smallest ionic radius (1.18 Å) (Shannon, 1976), therefore, they occupy the $M3$ site with the smallest polyhedron volume.

3.7.3 Chemical deformations in the $BaBi_{2-x}REE_xB_2O_7$ (REE = Eu^{3+}, Sm^{3+}, Tb^{3+}) borates

The quantitative comparison of thermal equivalents of chemical deformations of the $BaBi_{2-x}REE_xB_2O_7$ borates is of interest. Results of calculations for chemical deformation coefficients (γ_v) and thermal equivalents of chemical deformations, computed using the formula γ_v/α_v, are presented in Table 20. The methodology for conducting such calculations is described in (Filatov, 1990). The thermal expansion coefficient α_V value for the $BaBi_2B_2O_7$ crystalline matrix (Bubnova et al., 2016) is accepted as $38 \cdot 10^{-6}$ °C^{-1}. The ratio of equivalents is shown in Figure 59 and Table 20. A consistent distribution of equivalent values is observed: for the $BaBi_{2-x}Sm_xB_2O_7$ solid solutions, the equivalent values are higher because Sm atoms have a larger ionic radius. Introducing 1% Sm in crystal structure corresponds to a temperature increase of 0.12 °C. The thermal equivalents of chemical deformations for the $BaBi_{2-x}Tb_xB_2O_7$ are the lowest, and introducing 1% Tb in crystal structure is equivalent to a temperature increase of 0.08 °C. For the $BaBi_{2-x}Eu_xB_2O_7$ and $BaBi_{2-0.15-y}Eu_{0.15}Sm_yB_2O_7$ solid solutions, these values correspond to temperature increases of 0.09 and 0.11 °C, respectively.

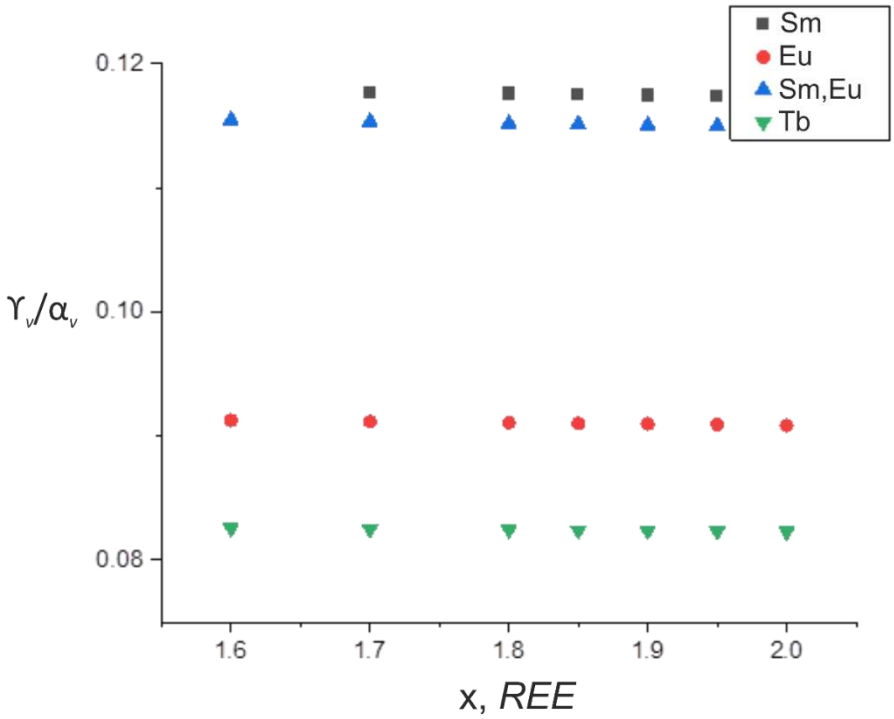

Figure 59 – The ratio of thermal equivalents of chemical deformations (γ_v/α_v) of the $BaBi_{2-x}REE_xB_2O_7$ borates.

Table 20 – Values of chemical deformation coefficients (γ_v) and thermal equivalents of chemical deformations (γ_v/α_v) of the $BaBi_{2-x}REE_xB_2O_7$ borates

x Bi		γ_v		
	Sm	Eu	Tb	Sm+Eu
1.6	-	2.7381	2.4769	3.4643
1.7	3.5314	2.735	2.4748	3.4602
1.8	3.5273	2.732	2.4728	3.4561
1.85	3.5252	2.7305	2.4718	3.454
1.9	3.5231	2.729	2.4708	3.452
1.95	3.5211	2.7275	2.4697	3.4499
2	3.519	2.726	2.4687	0.8548
		γ_v/α_v		
1.6	-	0.09127	0.082563	0.115477
1.7	0.117713	0.091167	0.082493	0.11534
1.8	0.117577	0.091067	0.082427	0.115203
1.85	0.117507	0.091017	0.082393	0.115133
1.9	0.117437	0.090967	0.08236	0.115067
1.95	0.11737	0.090917	0.082323	0.114997
2	0.1173	0.090867	0.08229	0.114493

3.8 Conclusion for the section 3

Based on the conducted synthesis and research highlighted in sections 3.1-3.7, the following results can be distinguished:

1. Three new series of solid solutions activated by REE^{3+} ions have been obtained: $BaBi_{2-x}Eu_xB_2O_7$ (x = 0.05—0.5), $BaBi_{2-x}Sm_xB_2O_7$ (x = 0.05—0.5), $BaBi_{2-x}Tb_xB_2O_7$ (x = 0.05—0.5), and three series of solid solutions co-activated by multiple REE^{3+} ions: $BaBi_{2-x-0.05}Eu_xSm_{0.05}B_2O_7$ (x = 0.35, 0.4, 0.45), $BaBi_{2-0.15-y}Eu_{0.15}Sm_yB_2O_7$ (y = 0.05—0.2), $BaBi_{2-x-0.3}Eu_xTb_{0.15}Tm_{0.15}B_2O_7$ (x = 0.05—0.3) (32 compositions). The existence regions of continuous solid solutions have been determined, and it has been established that co-activation of the $BaBi_2B_2O_7$ crystalline matrix has allowed expanding the solid solution miscibility regions to x = 0.025-0.05.

2. Eight crystal structures have been refined based on single-crystal data for $BaBi_{2-x}Eu_xB_2O_7$ (x = 0.1, 0.2, 0.4), $BaBi_{2-x}Sm_xB_2O_7$ (x = 0.05, 0.3), $BaBi_{2-x}Tb_xB_2O_7$ (x = 0.1, 0.3, 0.4). Borates crystallize in the structural type of $BaBi_2B_2O_7$, in hexagonal crystal system, space group $P6_3$. The crystal structure contains three symmetrically independent crystallographic sies for large cations, each of which are split into Ba and Bi subpositions. The REE^{3+} atoms occupy Bi subpositions. A regularity in isomorphic substitution upon activation of the crystalline matrix by REE^{3+} atoms has been discovered: larger atoms Sm and Eu occupy $M1$ and $M2$ sites with the largest polyhedral volumes, while Tb atoms with the smallest ionic radius occupy $M3$ site with the smallest polyhedral volume. Raman spectra for the $BaBi_{2-x}Eu_xB_2O_7$ borates have been studied. The obtained results further confirm the disordered model of the crystal structure.

3. According to high-temperature powder X-ray diffraction, the $BaBi_{1.7}Sm_{0.3}B_2O_7$ borate exhibits the greatest expansion along the c-axis, perpendicular to the preferred orientation of the BO_3 radicals (ab) in accordance with the principles of high-temperature crystal chemistry of borates with isolated triangular radicals. At a temperature of 450°C, a bend is observed in the temperature dependencies of the unit cell parameters, which may be associated with the redistribution of Sm and Bi cations over sites with increasing temperature. Melting and crystallization temperatures have been determined through thermal analysis. Based on the combined results of these methods, the thermal stability of the $BaBi_{1.7}Sm_{0.3}B_2O_7$ borate has been identified up to a temperature of 635°C, significantly higher than the operating temperatures for white light-emitting diodes.

4. Excitation spectra, photoluminescence spectra of the $BaBi_{2-x}Eu_xB_2O_7$, $BaBi_{2-x}Sm_xB_2O_7$, $BaBi_{2-x}Tb_xB_2O_7$, $BaBi_{2-x-0.05}Eu_xSm_{0.05}B_2O_7$, $BaBi_{2-0.15-y}Eu_{0.15}Sm_yB_2O_7$, $BaBi_{2-x-0.3}Eu_xTb_{0.15}Tm_{0.15}B_2O_7$ solid solutions have been studied. The regions of miscibility (x_{Eu}

= 0—0.45, x_{Sm} = 0—0.35, x_{Tb} = 0—0.45), $BaBi_{2-x-0.05}Eu_xSm_{0.05}B_2O_7$ (x_{Eu} + y_{Sm} = 0—0.45), $BaBi_{2-0.15-y}Eu_{0.15}Sm_yB_2O_7$ (x_{Eu} + y_{Sm} = 0—0.375), $BaBi_{2-x-0.3}Eu_xTb_{0.15}Tm_{0.15}B_2O_7$ (x_{Eu} + y_{Tb} + z_{Tm}= 0—0.475) have been determined. It has been established that co-activation of the crystalline matrix increases the optimal concentration of the activator due to the incorporation of the REE^{3+} atoms into *M*1 and *M*2 sites, between which an optimal bond angle is achieved for maximum energy transfer efficiency. Promising tunable phosphors for white light-emitting diodes have been developed with the ability to adjust color for technological purposes.

Chapter 4. The $Ba_3Eu_2(BO_3)_4$ and $Ba_3Y_{2-x}Er_x(BO_3)_4$ borates. Results and discussion

In this chapter, the results of the synthesis and investigation of the $Ba_3Eu_2(BO_3)_4$ and $Ba_3Y_{2-x}Er_x(BO_3)_4$ (x = 0, 0.01, 0.05, 0.1, 0.15, 0.2, 0.25, 0.3) borates are described. The 9 borates were obtained and single crystals of the $Ba_3Y_2(BO_3)_4$ were selected for refining the crystal structure of the $Ba_3Y_2(BO_3)_4$ borate using single crystal data. The results of thermal expansion of the $Ba_3Eu_2(BO_3)_4$ and $Ba_3Y_2(BO_3)_4$ are presented for the first time. The behavior of the $Ba_3Y_2(BO_3)_4$ borate at 40 different temperatures was investigated based on powder data using the Rietveld method, as well as changes in structural parameters (site occupancy, volume, average bond lengths in polyhedra) with increasing temperature. The luminescent, thermoluminescent properties, Raman and IR spectra of the new $Ba_3Y_{2-x}Er_x(BO_3)_4$ (x = 0—0.3) series of solid solutions are described. A review and analysis of a large volume of literature data were conducted to identify differences in site occupancies and thermal expansion coefficients of borates in the $A_3M_2(BO_3)_4$ (A = Ca, Sr, Ba, M = *Ln*, Y, Bi) family.

The synthesis method, starting reagent and equipment are detailed in section 2.1.2, page 51. This section focuses primarily on research results and discussion.

4.1 Results of powder X-ray diffraction of the $Ba_3Eu_2(BO_3)_4$ and $Ba_3Y_{2-x}Er_x(BO_3)_4$ borates

According to the results of powder X-ray diffraction, all obtained borates $Ba_3Eu_2(BO_3)_4$ and $Ba_3Y_{2-x}Er_x(BO_3)_4$ (x = 0, 0.01, 0.05, 0.1, 0.15, 0.2, 0.25, 0.3) are homogeneous (Figure 60).

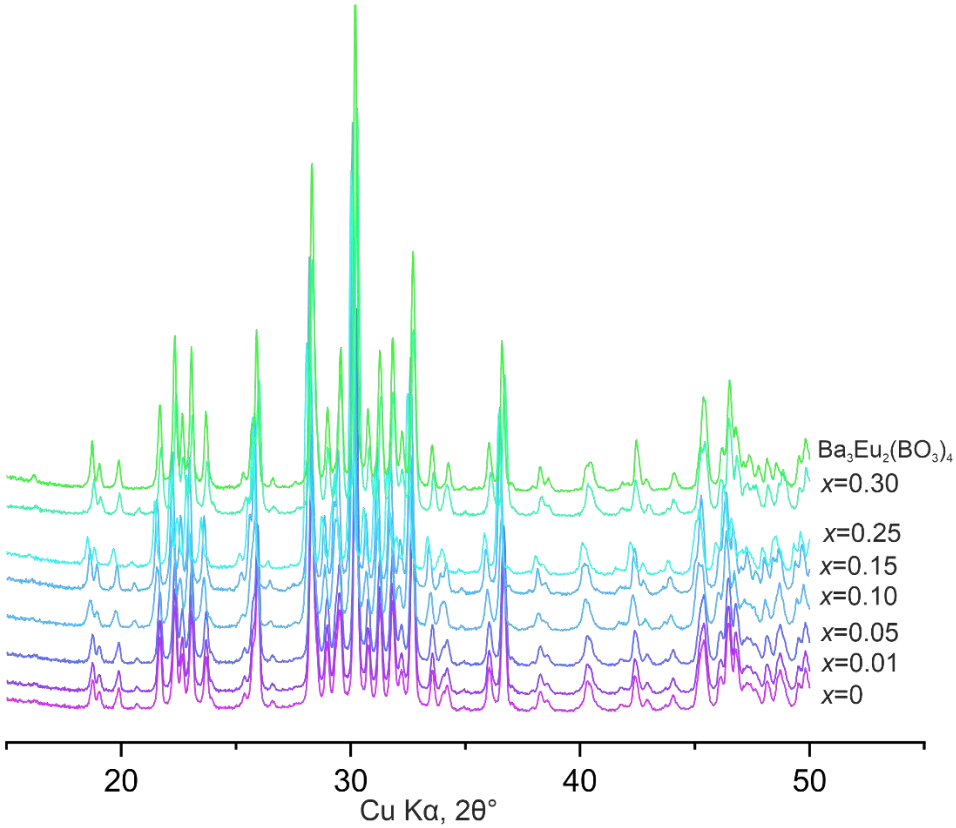

Figure 60 – Diffraction patterns of the $BaBi_{2-x}Eu_xB_2O_7$ borates

4.2 Results of refinement of the crystal structure of the $Ba_3Y_2(BO_3)_4$ borate

According to the refinement of the crystal structure, the $Ba_3Y_2(BO_3)_4$ borate crystallizes in a orthorhombic crystal system, space group *Pnma*, a = 7.6729(13), b = 16.439(3), c = 8.9770(16) Å, V = 1132.3(3) Å^3, Z = 4. The data obtained in this study are consistent with the refinement results from the literature (Ma et al., 2005). The crystallographic data and refinement parameters of the crystal structure of the $Ba_3Y_2(BO_3)_4$ borate are presented in Table 21, atomic coordinates are in Supplementary (Table S 7), and the occupancy of cation sites is presented in (Table 22).

The crystal structure of the $Ba_3Eu_2(BO_3)_4$ was refined in the (Chen et al., 2020). The $Ba_3Eu_2(BO_3)_4$ borate (*Pnma*, a = 7.6970(15), b = 16.554(3), c = 8.9300(18) Å, V = 1137.8(4) Å^3, Z = 4) is isostructural to $Ba_3Y_2(BO_3)_4$.

It is worth noting that errors in the atomic coordinates (Table S 7) of the refinement of the crystal structure of the $Ba_3Y_2(BO_3)_4$ borate were half as much as in (Ma et al., 2005). Additionally, in the (Ma et al., 2005), the parameters of atomic displacements in the crystal structure were refined only in an isotropic approximation. Anisotropic parameters of atomic displacements for all atoms were first obtained by us in this study (Table S 8). The parameters of atomic displacements for

oxygen atoms O3–O7 exceed standard values, both in our refinement and in the literature data. This phenomenon is not uncommon for disordered crystal structures, as occupies crystallographic sites with two cations causes librational vibrations that affect the change in B–O bond lengths in polyhedra. A similar phenomenon was also observed in the $BaBi_{2-x}REE_xB_2O_7$ borates with a disordered crystal structure, as described above (section 3.1.2, page 58).

The crystal structure of the $Ba_3REE_2(BO_3)_4$ (*REE* = Y, Eu) contains three independent crystallographic sites for large cations: two general (*M*1, *M*2) and one special (*M*3). Barium and *REE* atoms are disordered over three sites (Figure 61). The *M*1 and *M*2 sites are predominantly occupied by Ba atoms, while *M*3 site is more occupied by *REE* atoms. The Ba(*REE*')1, Ba(*REE*')2, *REE*(Ba')3 sites are coordinated by eight oxygen atoms.

In section 4.8 (page 114), the sites occupancies in the $A_3M_2(BO_3)_4$ (*A* = Ca, Sr, Ba, *M* = *REE*, Bi^{3+}) family are compared (Table 28).

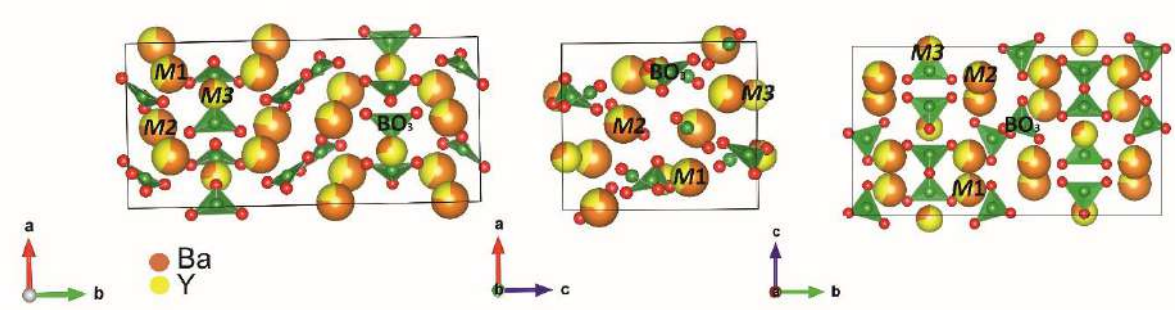

Figure 61 – Refined crystal structure of the $Ba_3Y_2(BO_3)_4$ borate.

Table 21 – Crystal data and details of refinement of the $Ba_3Y_2(BO_3)_4$ borate

Refined formula	$Ba_3Y_2(BO_3)_4$
*M*r	825.1
Crystal system, space group	Orthorhombic, *Pnma*
Temperature (K)	293
a, *b*, *c* (Å)	7.673(1), 16.439(3), 8.977(2)
V (Å^3)	1132.3(3)
Z	4
Radiation type	Mo *K*α
μ (мм$^{-1}$)	20.48
Crystal size (mm)	0.04×0.04×0.03
Diffractometer	Bruker Smart APEX II
No. of measured, independent and observed [$I > 3\sigma(I)$] reflections	10645/1696/1212
*R*int	0.039
(sin θ/λ)max (Å^{-1})	0.851
R (obs), wR(obs), S	0.037, 0.042, 1.87
No. of reflections	1696

No. of parameters	94
(Δ/σ)max	0.047

Table 22 – Distribution of cations sites for the $Ba_3Y_2(BO_3)_4$ borate

Atom	Occupancy
Ba1	0.768(3)
Y1′	0.232(3)
Ba2	0.59(3)
Y2′	0.409(3)
Y3	0.718(10)
Ba3′	0.282(10)

Taking into account the mixed occupancies of the *M*1, *M*2, *M*3 sites and the different valences of barium and yttrium atoms, the bond valence sum have been calculated for the $Ba_3Y_2(BO_3)_4$ borate (Table 23). Thus, the calculated bond valence sum is 2.23, 2.41, and 2.72 v.u. for the *M*1O_8, *M*2O_8, *M*3O_8 polyhedra, respectively. The Ba/Y1–O bond lengths in the (Ba,Y)1O_8 polyhedra range from 2.491 to 2.934 Å. The next bond length is 3.643 Å, therefore it does not contribute to the formation of this polyhedron. The calculated bond valence sum in this polyhedron is 2.29 v.u., which is in agreement with the "theoretical" value (2.23 v.u.). The "theoretical" bond valence sum was calculated as the sum of the occupancy fractions of each atom in one site, multiplied by their valence. The Ba/Y2–O bond lengths in (Ba,Y)2O_8 range from 2.369 to 3.128 Å, and the bond valence sum is 2.35 v.u. (compared to the "theoretical" value of 2.41 v.u.). The Ba/Y3–O bond lengths in the (Ba,Y)3O_8 polyhedra range from 2.347 to 2.849 Å, with the next bond length being 3.772 Å. The bond valence sum in the (Ba,Y)3O_8 polyhedra is 2.63 v.u. (compared to the "theoretical" 2.72 v.u.). Therefore, the bonds in the (Ba,Y)3O_8 polyhedra are the strongest.

Table 23 – Selected bond lengths (Å) and bond valence sum (BVS) for $Ba_3Y_2(BO_3)_4$

Bond	Distance (Å)	BVS (v.u.)	Bond	Distance (Å)	BVS (v.u.)
Ba/Y)—O7^{vi}	2.491(12)	0.49	Ba/Y3—O3	2.347(11)	0.50
Ba/Y1—O7^{ix}	2.577(11)	0.39	Ba/Y3—O4	2.379(8)	0.46
Ba/Y1—O5^{vii}	2.662(10)	0.31	Ba/Y3—O4^{vi}	2.379(8)	0.46
Ba/Y1—O4^{vi}	2.685(9)	0.29	Ba/Y3—O2^{xiv}	2.455(10)	0.37
Ba/Y)—O6^{viii}	2.718(11)	0.26	Ba/Y)—O1^{vi}	2.554(6)	0.29
Ba/Y)—O6^{v}	2.778(11)	0.22	Ba/Y3—O1	2.554(6)	0.29
Ba/Y1—O1^{v}	2.864(7)	0.18	Ba/Y3—O7^{ix}	2.849(17)	0.13
Ba/Y1—O4	2.934(9)	0.15	Ba/Y3—O7^{ii}	2.849(17)	0.13
<Ba/Y1—O>$_8$	2.68	∑2.29*	< Ba/Y3—O>$_8$	2.55	∑2.63***

Ba/Y2—O6^{viii}	2.369(11)	0.59	B1— O2	1.361(15)	1.03
Ba/Y2—O5^{xiii}	2.493(10)	0.43	B1— O1	1.363(8)	1.02
Ba/Y2—O5^{ix}	2.574(11)	0.34	B1— O1	1.363(8)	1.02
Ba/Y2—O3^{ix}	2.615(6)	0.31	<B1—O>$_3$	1.36	∑3.07****
Ba/Y2—O2^{v}	2.646(6)	0.28	B2— O3	1.33(14)	1.12
Ba/Y2—O1^{xiii}	2.768(7)	0.20	B2—O7	1.33(12)	1.12
Ba/Y2—O1	2.947(7)	0.12	B2—O7^{vi}	1.33(12)	1.12
Ba/Y2—O4	3.128(9)	0.08	<B2—O>$_3$	1.33	∑3.35****
<Ba/Y2—O>$_8$	2.58	∑2.35**	B3— O4	1.327(11)	1.13
			B3— O5	1.33(10)	1.12
			B3— O6	1.345(12)	1.07
			<B3—O>$_3$	1.33	∑3.32****

* The "theoretical" meaning of bond valence sum – 2.232

** The "theoretical" meaning of bond valence sum – 2.41

*** The "theoretical" meaning of bond valence sum – 2.72

**** The "theoretical" meaning of bond valence sum – 3

4.3 Results of High-temperature powder X-ray diffraction of the $Ba_3Eu_2(BO_3)_4$ and $Ba_3Y_2(BO_3)_4$ borates

In the diffraction patterns of the $Ba_3Eu_2(BO_3)_4$ and $Ba_3Y_2(BO_3)_4$ borates in the temperature range of 25–1000 °C, no peaks corresponding to phase transitions or high-temperature decomposition are observed – the borates are stable within the investigated temperature ranges. Figure 62 shows 2D image of HTXRD patterns for the $Ba_3Eu_2(BO_3)_4$ and $Ba_3Y_2(BO_3)_4$ borates.

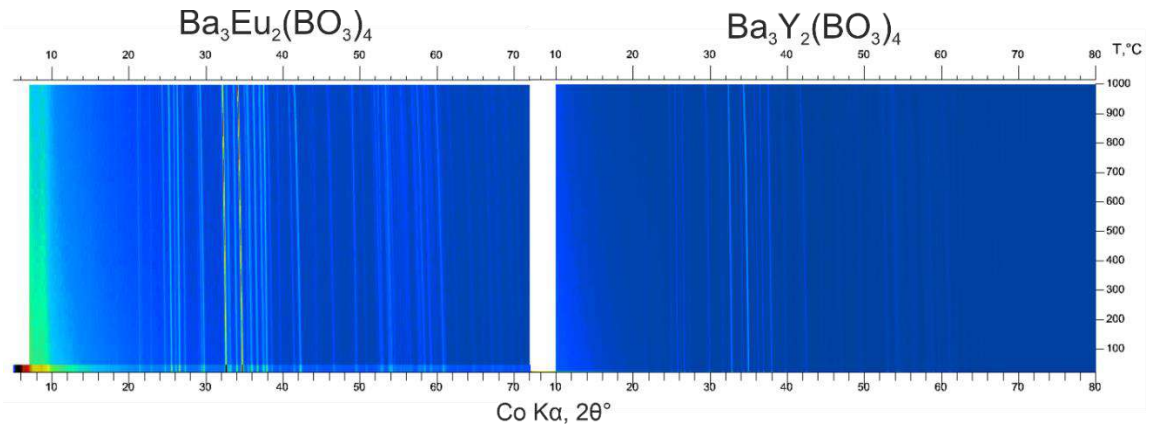

Figure 62 – 2D images of HTXRD patterns of the $Ba_3Y_2(BO_3)_4$ and $Ba_3Eu_2(BO_3)_4$ borates.

The thermal dependence graphs of the unit cell parameters (Figure 63) exhibit inflections in the temperature ranges of 500–640 °C and 600–740 °C for the $Ba_3Eu_2(BO_3)_4$ and $Ba_3Y_2(BO_3)_4$, respectively.

Similar inflections are characteristic of the $A_3M_2(BO_3)_4$ (A = Ca, Sr, Ba, M = *Ln*, Y, Bi) borate family and are described in a number of studies (Volkov et al., 2013; Shablinskii et al., 2019; Kosyl et al., 2020).

It is worth noting that the inflections in the temperature dependence graphs of the unit cell parameters of the $Ba_3Y_2(BO_3)_4$ borate are more clearly distinguished in all parameters, whereas in the $Ba_3Eu_2(BO_3)_4$ borate, these inflections are clearly visible only in parameter *b*. This may be related to the difference in ionic radii of atoms: since the ionic radius of Eu^{3+} (1.206 Å) is larger than that of Y^{3+} (1.159 Å) and closer in size to the radius of Ba^{2+} (1.56 Å) (кч = 8) (coordination number = 8) (Shannon, 1976), the disordering of cations over sites may be less in the $Ba_3Eu_2(BO_3)_4$ borate.

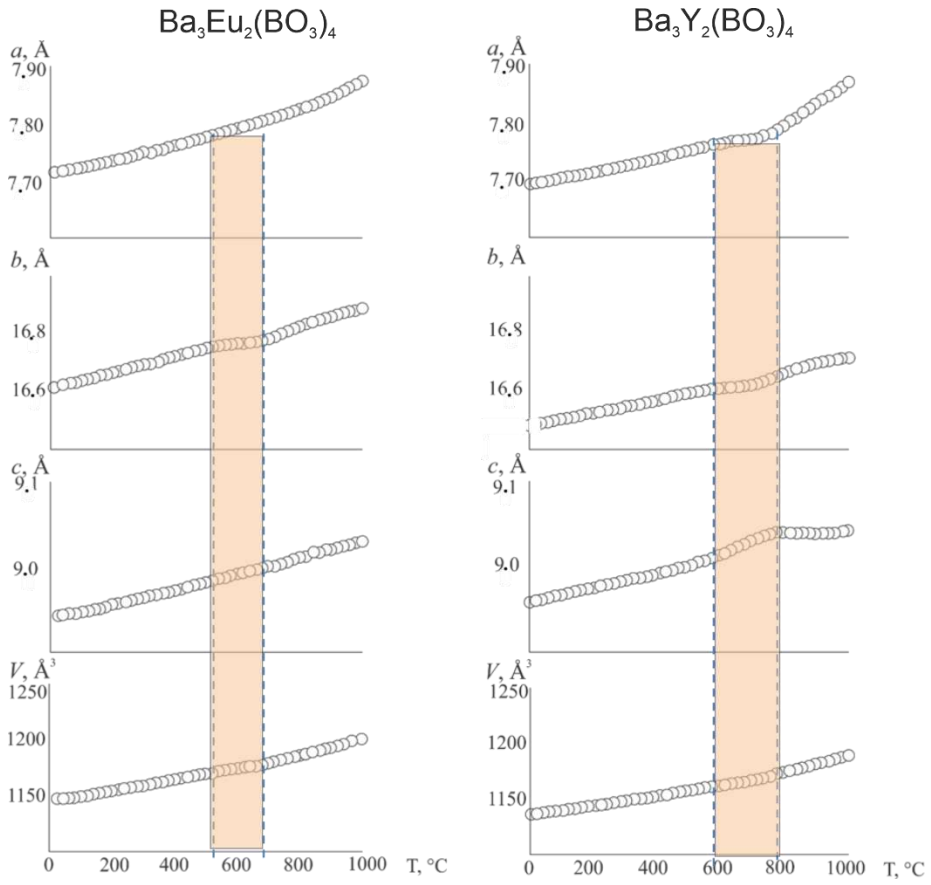

Figure 63 – Temperature dependencies of unit cell parameters of the $Ba_3Y_2(BO_3)_4$ and $Ba_3Eu_2(BO_3)_4$ borates.

It is assumed that at temperatures of 500–640 °C and 600–740 °C in the $Ba_3Eu_2(BO_3)_4$ and $Ba_3Y_2(BO_3)_4$ borates, respectively, the processes of "order-disorder" occur, which are superimposed on thermal expansion. Therefore, in the ranges of the presumed localization of these processes, the coefficients of thermal expansion cannot be reliably calculated. For this reason, the

approximation of the unit cell parameters of the $Ba_3Y_2(BO_3)_4$ borate was carried out using second-degree polynomials for two temperature intervals. Since in the $Ba_3Eu_2(BO_3)_4$ borate a vizible bend in the thermal dependencies of the unit cell parameters is observed only for the parameter *b*, the approximation was carried out in two temperature intervals for this parameter, and for *a*, *c*, *V* – in one (Table 24).

Table 24 – Equations of approximation of temperature dependencies of unit cell parameters of the $Ba_3Y_2(BO_3)_4$ and $Ba_3Eu_2(BO_3)_4$ borates ($a_0 + a_1 \times 10^{-3}t + a_2 \times 10^{-6}t^2$)

Cell parameter	Range	a_0	a_1	a_2
		$Ba_3Eu_2(BO_3)_4$		
$a(t)$ (Å)	25–1000 °C	7.7139(7)	0.000090(3)	0.000000064(3)
$b(t)$ (Å)	25–500 °C	16.6111(7)	0.000263(6)	0.000000032(1)
	640–1000 °C	16.43(4)	0.00062(9)	-0.00000016(6)
$c(t)$ (Å)	25–1000 °C	8.9393(3)	0.000078(1)	0.000000013(1)
$V(t)$ (Å^3)	25–1000 °C	1145.9(3)	0.039(1)	0.000015(1)
		$Ba_3Y_2(BO_3)_4$		
$a(t)$ (Å)	25–600 °C	7.6932(3)	0.000090(2)	0.000000049(4)
	740–1000°C	7.66(2)	0.00002(5)	0.00000019(3)
$b(t)$ (Å)	25–600 °C	16.4728(8)	0.000211(6)	0.00000002(1)
	740–1000 °C	15.84(3)	0.00164(8)	–0.00000076(5)
$c(t)$ (Å)	25–600 °C	8.9574(4)	0.000072(3)	0.000000029(5)
	740–1000 °C	9.06(4)	–0.00006(9)	0.00000004(5)
$V(t)$ (Å^3)	0–1000 °C	1135.9(3)	0.031(1)	0.000022(1)

The values of the thermal expansion coefficients of the $Ba_3Eu_2(BO_3)_4$ and $Ba_3Y_2(BO_3)_4$ borates in a wide temperature range are presented in (Table 25), the comparison of thermal expansion with the crystal structure is shown in (Figure 64).

In the $Ba_3Eu_2(BO_3)_4$ borate, the maximum thermal expansion is observed along the *a* axis (α_a changes from 12.1(4) at 25 °C to 27.8(4) $\times 10^{-6}$ °C^{-1} at 1000 °C) and is minimal in the *c* direction (α_c changes from 8.8(1) at 25 °C to 11.5(1) $\times 10^{-6}$ °C^{-1} at 1000 °C). At temperatures above 640 °C, a sharp increase in the values of the α_b coefficient is observed after the bend (from 17.6(3) at 500 °C to 24.6(1) $\times 10^{-6}$ °C^{-1} at 650 °C), followed by a decrease in values to 17.6(1) $\times 10^{-6}$ °C^{-1} at 1000 °C.

In the $Ba_3Y_2(BO_3)_4$ borate, the maximum thermal expansion is also observed along the *a*-axis. Prior to the inflection temperature, the α_a values increase from 13.8(3) at 25 °C to 18.5(3)

$\times 10^{-6}$ °C^{-1} at 600 °C. After the inflection point, the α_a values of sharply increase to 37.8(1) $\times 10^{-6}$ °C^{-1} at 750 °C and reach 51.2(1) $\times 10^{-6}$ °C^{-1} at 1000 °C. The values of the coefficients α_b and α_c change insignificantly before the inflection temperature. After the inflection point, the α_b values first increase sharply (from 13.9(4) at 600 °C to 29.1(7) $\times 10^{-6}$ °C^{-1} at 750 °C), and then decrease to α_b = 6.7(7) $\times 10^{-6}$ °C^{-1} at 1000 °C, as observed in the $Ba_3Eu_2(BO_3)_4$ borate. The α_c values decrease to negative values after the inflection point (from 12.5(2) at 600 °C to –0.8(1) $\times 10^{-6}$ °C^{-1} at 750 °C), and then increase to α_c = 3.4(1) at 1000 °C.

Thus, the thermal expansion of both borates is maximal along the *a*-axis, perpendicular to the preferred orientation of the triangular BO_3 radical (*bc*), which is consistent with the principles of high-temperature crystal chemistry of borates with isolated triangular radicals (Bubnova, Filatov, 2008).

Table 25 – Thermal expansion coefficients of the $Ba_3Y_2(BO_3)_4$ and $Ba_3Eu_2(BO_3)_4$ borates at some temperatures

	$Ba_3Eu_2(BO_3)_4$				$Ba_3Y_2(BO_3)_4$			
T, °C	$\alpha_a \times 10^6$ °C^{-1}	α_b	α_c	α_V	$\alpha_a \times 10^6$ °C^{-1}	α_b	α_c	α_V
25	12.1(4)	15.9(3)	8.8(1)	36.9(1)	13.8(3)	14.4(4)	9.1(2)	37.3(1)
200	15.0(1)	16.6(1)	9.3(9)	40.9(7)	15.2(1)	14.3(2)	10.12(9)	39.7(8)
400	18.2(1)	17.3(2)	9.9(4)	45.4(3)	16.9(1)	14.1(2)	11.29(7)	42.3(4)
500	19.8(1)	17.6(3)	10.1(3)	47.6(3)	17.7(2)	14.0(3)	11.9(1)	43.6(3)
550	20.6(1)	17.8(4)	10.3(3)	48.7(3)	18.1(2)	14.0(3)	12.2(2)	44.2(3)
600	21.5(1)	18.0(4)	10.4(4)	49.8(3)	18.5(3)	13.9(4)	12.5(2)	44.9(4)
650	22.3(1)	24.6(1)	10.5(5)	57.3(4)	–	–	–	–
700	23.0(2)	23.5(8)	10.7(6)	57.3(4)	–	–	–	–
750	23.8(2)	22.6(6)	10.8(7)	57.2(5)	37.8(1)	29.1(7)	–0.8(1)	66.1(7)
800	24.6(2)	21.6(4)	10.8(7)	57.1(6)	40.5(7)	24.6(4)	0.02(8)	65.2(8)
1000	27.8(4)	17.6(1)	11.5(1)	57.0(9)	51.2(1)	6.7(7)	3.4(1)	61.3(1)

Below in section 4.8 (page 114), a comparison of the thermal expansion coefficients over a wide temperature range of seven borates from the $A_3M_2(BO_3)_4$ (*A* = Ca, Sr, Ba, *M* = *Ln*, Y, Bi) family is provided, followed by an analysis and discussion of the results.

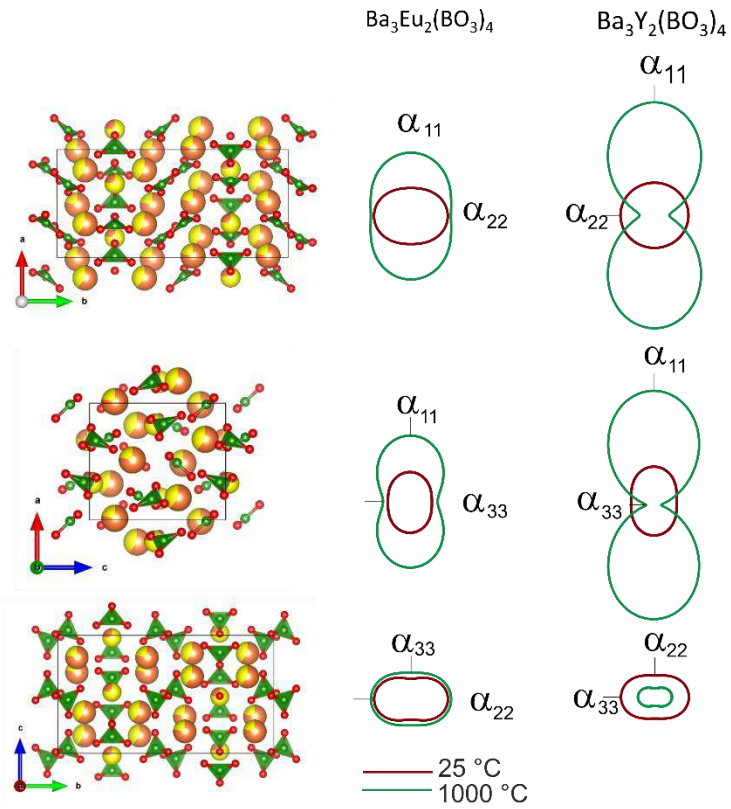

Figure 64 – Crystal structure in comparison with the figures of thermal expansion tensor coefficients of the $Ba_3Y_2(BO_3)_4$ and $Ba_3Eu_2(BO_3)_4$ borates.

4.4 Results of refinement of the crystal structure of the $Ba_3Y_2(BO_3)_4$ borate at high temperatures using the Rietveld method

As mentioned, borates from the $A_3M_2(BO_3)_4$ (*A* = Ca, Sr, Ba, *M* = *REE*, Bi^{3+}) family exhibit bends in the temperature dependencies of the unit cell parameters (Volkov et al., 2013; Shablinskii et al., 2017; Kosyl et al., 2020), which are also observed in the studied $Ba_3Eu_2(BO_3)_4$ and $Ba_3Y_2(BO_3)_4$ borates in this work. In the (Shablinskii et al., 2017), it was suggested that these bends occur due to the redistribution of large cations over the crystallographic sites *M*1–*M*3 with increasing temperature. In this work, an additional refinement of the crystal structure of the $Ba_3Y_2(BO_3)_4$ borate was carried out using powder data by the Rietveld method in the temperature range of 600–800 °C with a step of 5 °C (40 points) to confirm the cation redistribution.

Temperature dependence graphs of the occupancies of Ba and Y atom sites are presented in (Figure 65a), and the volumes and average bond lengths in the polyhedra are shown in (Figure 66b). With increasing temperature, the occupancies of Ba atoms in *M*1 and *M*2 sites increase, while those of Y atoms decrease. The occupancy of Y atoms in *M*3 site with the smallest polyhedron volume increases by 5%, while that of Ba atoms decreases.

Changes in volumes and average bond lengths in the polyhedra occur consistently with changes in occupancy: volumes and average bond lengths in the $M1O_8$ and $M2O_8$ polyhedra increase with higher Ba content with a larger ionic radius and decrease in the $M2O_8$ polyhedron due to the decrease in Ba content.

A detailed analysis, comparison of structural parameter changes with increasing temperature for the $Ba_3Y_2(BO_3)_4$ and $Ca_3Eu_2(BO_3)_4$ borates, as well as discussion of the results are provided below (see section 4.8, page 114).

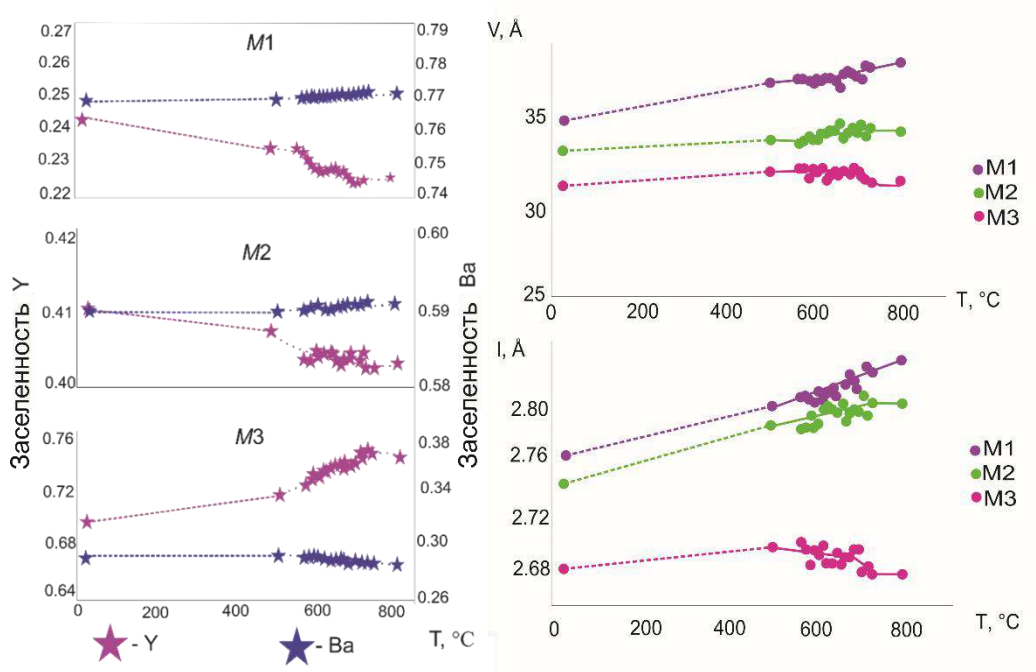

Figure 65 – Temperature dependencies of the site occupancies by the Ba and Y atoms (left), changes in the volumes and bond lengths in the polyhedra with an increase in temperature (right).

4.5 Results of Raman spectroscopy of and infrared spectroscopy of the $Ba_3Y_{2-x}Er_x(BO_3)_4$ borates

In the vibrational spectra (Figure 66a) of the $Ba_3Y_{2-x}Er_x(BO_3)_4$ (x = 0.01—0.2) borates, the same set of bands is observed, indicating the absence of structural changes upon activation of the $Ba_3Y_2(BO_3)_4$ matrix by Er^{3+} ions. $Ba_3Y_{1.7}Er_{0.3}(BO_3)_4$ sample shows the absence of almost all narrow bands, which may be attributed to a strong disorder of cations in sites.

IR spectra (Figure 66b) exhibit a consistent set of bands for all examined samples with corresponding fluctuations. All bands in the Raman and IR spectra correspond to the vibrations of

triangular BO_3 radicals. The IR and Raman bands with corresponding fluctuations are presented below (Table 26).

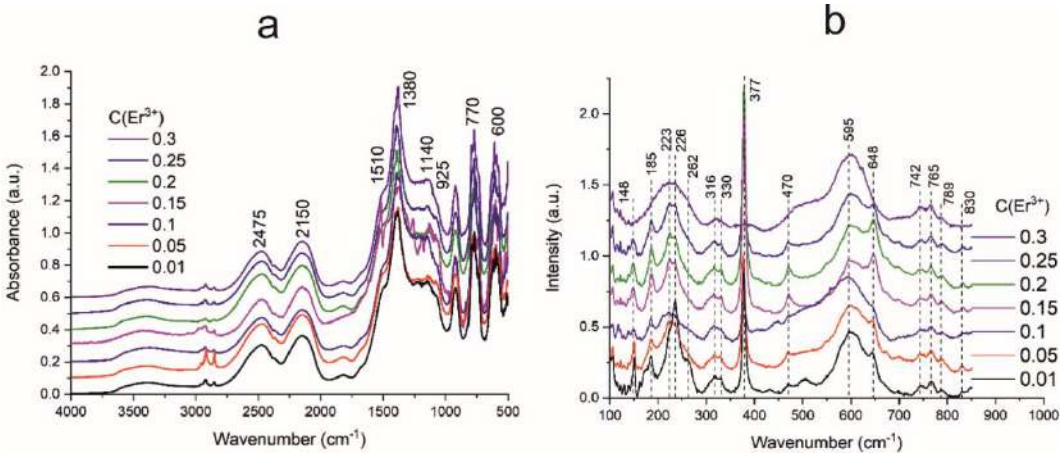

Figure 66 – Raman spectra (a) and IR spectra of the samples $Ba_3Y_{2-x}Er_x(BO_3)_4$.

Table 26 – Assignment of IR and Raman bands of the samples $Ba_3Y_{2-x}Er_x(BO_3)_4$

IR band, cm^{-1}	Raman band, cm^{-1}	Assignment
	148	$\delta(BO_3)$
	185	$\rho_t(BO_3)$
	223, 226, 262, 316, 330	$\gamma(BO_3)$
	377	$\delta(BO_3)$
	470	$\gamma\ (BO_3)$
600	595	$\delta(BO_3)$
	648	$\gamma\ (BO_3)$
770	742, 765, 789	$\gamma(BO_3)$
925		$\nu_s(BO_3)$
1140, 1380		$\nu_{as}\ (BO_3)$
1510		$\gamma(BO_3)$

ν – stretching vibration, δ – bending vibration, γ – out-of-plane vibration, s – symmetrical

4.6 Results of luminescent spectroscopy of the $Ba_3Y_{2-x}Er_x(BO_3)_4$ borates

The excitation spectra of luminescence in $Ba_3Y_{2-x}Er_x(BO_3)_4$ borates (Figure 67) demonstrate the efficiency of pumping the excited electronic states of active ions at various wavelengths. Wide bands in the spectral range of 300—350 nm correspond to interband transitions in the crystalline matrix. Narrow bands in the spectral range of 350–550 nm correspond to direct excitation of Er^{3+} ions.

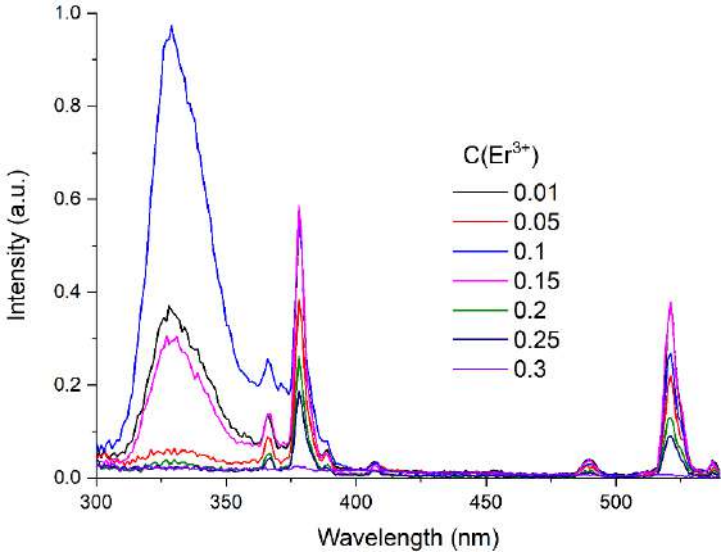

Figure 67 – Excitation spectra of 563 nm luminescence for $Ba_3Y_{2-x}Er_x(BO_3)_4$ samples.

When excited at a wavelength of 377 nm, narrow bands in the spectral range from 500 to 700 nm are observed in the luminescence spectra (Figure 68a), corresponding to radiative transitions of Er^{3+} ions. The graph showing the dependence of the integral intensity of photoluminescence on the concentration of erbium ions when pumped at a wavelength of 377 nm (Figure 68b) indicates that the optimal concentration of erbium ions, resulting in maximum luminescence intensity, is x = 0.1. Increasing the concentration of active centers leads to concentration quenching of luminescence.

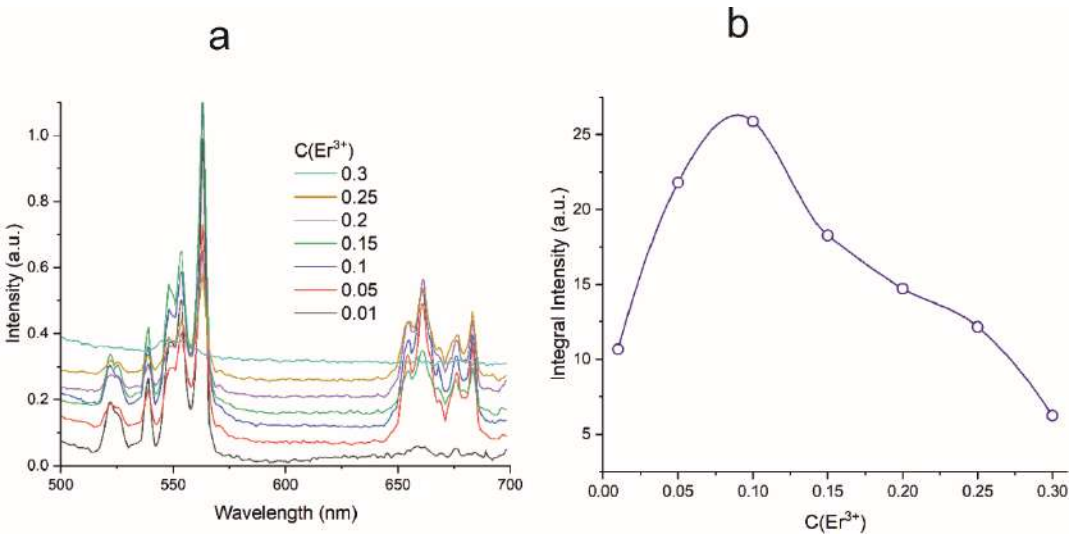

Figure 68 – Photoluminescence spectra of $Ba_3Y_{1-x}Er_x(BO_3)_4$ under 377 nm excitation (a); Concentration dependence of the integrated luminescence intensity (b).

Luminescence kinetic curves were measured. The concentration dependence graph of the lifetime of excited states of erbium ions for the $Ba_3Y_{2-x}Er_x(BO_3)_4$ borates shows a decrease in lifetime with increasing concentration up to $x = 0.1$ (Figure 69). Further increase in the content of Er^{3+} ions results in only a slight change in the lifetime of excited states. The luminescence kinetics data indicate that concentration quenching significantly affects even at the lowest concentrations of active ions.

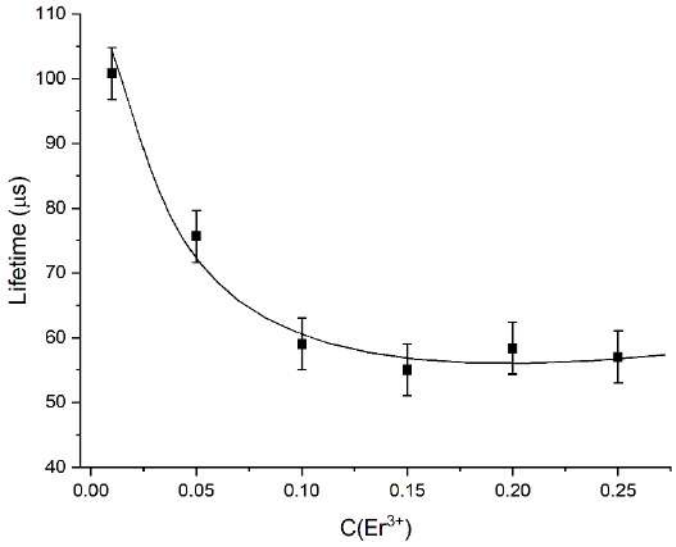

Figure 69 – Dependence of the lifetime of the excited state on the concentration of erbium ions of $Ba_3Y_{1-x}Er_x(BO_3)_4$ borates.

4.7 Results of thermoluminescent spectroscopy of the $Ba_3Y_{2-x}Er_x(BO_3)_4$ borates

In order to evaluate the thermal stability of the $Ba_3Y_{2-x}Er_x(BO_3)_4$ phosphors, the thermoluminescent properties of the $Ba_3Y_{1.9}Er_{0.1}(BO_3)_4$ borate with maximum luminescence intensity were studied. Thermoluminescence spectra were measured under identical experimental conditions (except for temperature) with excitation at a wavelength of 377 nm, in the temperature range of 299—466 K (Figure 70a). As the temperature increases, the intensity of bands in the spectral region of 520 nm increases, while in the regions of 550–560 nm and 650–675 nm, it decreases. The increase in temperature leads to a monotonic decrease in the integral emission intensity due to the interaction of electrons with thermally active phonons.

The temperature dependence of the integral emission intensity is described by the Arrhenius equation (2) (Tang et al., 2017):

$$It = \frac{Io}{1 + Aexp(\frac{\Delta E}{kT})} \qquad (2),$$

where *It* is emission intensity at temperature *T*, I_0 is the initial emission intensity (at *T* = 299 K), *k* is Boltzmann constant, and Δ*E* is the activation energy for thermal quenching process.

The experimental data in the Arrhenius plot are approximated by a linear function (Figure 70b), indicating that the thermal quenching process follows an activated Arrhenius-type model. The activation energy is determined to be 0.18 eV.

The dependence of the luminescence intensity of the $Ba_3Y_{1.9}Er_{0.1}(BO_3)_4$ borate on temperature suggests that these phosphors can be used as fluorescent thermometers, a characteristic feature of phosphors activated by Er^{3+} ions (Aizawa et al., 2005; Manzani et al., 2017; Soler-Carracedo et al., 2020).

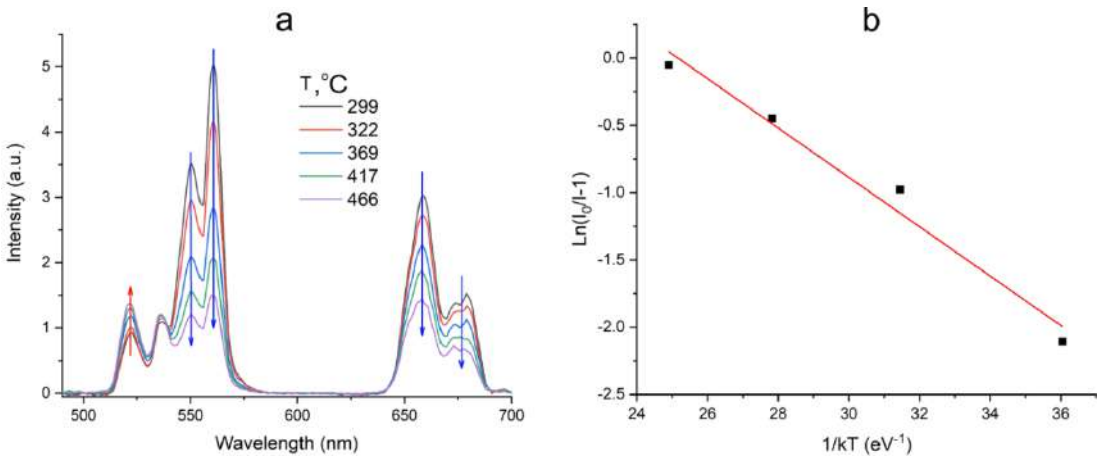

Figure 70 – The emission spectra measured at different temperatures (a) and activation energy (b) for thermal quenching of $Ba_3Y_{1.9}Er_{0.1}(BO_3)_4$ phosphor under 377 nm excitation.

4.8 Results and discussion

4.8.1 Crystal structures of the $A_3M_2(BO_3)_4$ borates at room temperature

In this section, an analysis of the crystal structures of borates from the $A_3M_2(BO_3)_4$ (*A* = Ca, Sr, Ba, *M* = *REE*, Bi^{3+}) family, including site occupancies, polyhedral volumes, and the difference in ionic radii of atoms occupying crystallographic sites, is presented.

The $A_3M_2(BO_3)_4$ (*A* = Ca, Sr, Ba, *M* = *REE*, Bi^{3+}) borates crystallize in the space group *Pnma* (Table 4). In several studies, the $Ca_3M_2(BO_3)_4$ and $Sr_3M_2(BO_3)_4$ borates have been refined in the space group $Pc2_1n$ ((Palkina et al., 1974; Bambauery et al, 1978; Wang et al., 2004; Lin et al.,

2013; Reuther et al., 2015). The crystal structure contains three sites for isolated BO_3 triangles and three independent crystallographic *M*1, *M*2, *M*3 sites for large cations (see section 4.2, page 102), each of which is occupied by *A* (Ca, Sr, Ba) and *M* (*REE*, Bi^{3+}) atoms. In this study, calculations of the bond valence sum were carried out for known crystal structures of $A_3M_2(BO_3)_4$ (*A* = Ca, Sr, Ba, *M* = *REE*, Bi^{3+}) borates, refined in the space group *Pnma* (Table S 9, page 149). Based on the calculations, it is possible to identify coordination polyhedra $M1O_8$, $M2O_9$, $M3O_8$ for $A_3M_2(BO_3)_4$ borates (Table 27).

The volumes of the $M1O_8$, $M2O_9$, and $M3O_8$ polyhedra in the $Ba_3Y_2(BO_3)_4$ borate are 33.13, 38.04, and 27.52 Å3, respectively. Y atoms, with a smaller ionic radius than Ba, predominantly occupy the *M*3 site with the smallest polyhedron volume and minimally occupy the *M*2 site with the largest volume.

Below are the occupancy data for *M*1–*M*3 sites in the crystal structures of 18 borates from the $A_3M_2(BO_3)_4$ (*A* = Ca, Sr, Ba, *M* = *REE*, Bi^{3+}) family (Table 28) based on literature and data obtained in this study. Site occupancies in $Ca_3Y_2(BO_3)_4$ (Wang et al., 2004), $Sr_3Y_2(BO_3)_4$, $Sr_3Yb_2(BO_3)_4$ (Lin et al., 2013), $Ba_3La_2(BO_3)_4$ и $Ba_3Pr_2(BO_3)_4$ (Khamaganova et al., 1997), $Ba_3Nd_2(BO_3)_4$ (Yan, Hong, 1987a) borates have been previously refined as statistically distributed in the respective works. For the remaining borates presented, there is a sequential occupation by atoms with smaller ionic radius *M* (*M* = *REE*, Bi^{3+}) of the most suitable sites by volume: initially, the majority of atoms enter the *M*3 site with the smallest volume, then the *M*1 site, and finally the *M*2 site with the largest volume. The difference in ionic radii of substituting ions relative to the smaller one by (Goldschmidt, 1926) is presented in (Table 29) (r_{i1}—r_{i2}/r_{i2}, где $r_{i2} < r_{i1}$).

The isomorphism of borates from the $A_3M_2(BO_3)_4$ (*A* = Ca, Sr, Ba, *M* = *REE*, Bi^{3+}) family can be characterized using the rule of structural diversity (Filatov, Bubnova, 1983), which states that from several positions, an atom should successively replace the most suitable one in terms of size.

Table 27 – Coordination and volumes of the $M1O_8$, $M2O_9$, $M3O_8$ polyhedra of borates of the $A_3M_2(BO_3)_4$ (*A* = Ca, Sr, Ba, *M* = *REE*, Bi^{3+}) family

Borate	Coordination			Volumes of the $M1O_8$, $M2O_9$, $M3O_8$ polyhedra, $Å^3$			Reference
	*M*1	*M*2	*M*3	$M1O_8$	$M2O_9$	$M3O_8$	
$Ca_3La_2(BO_3)_4$	8	9	8	27.20	34.75	25.61	(Mill et al., 1998)
$Ca_3Eu_2(BO_3)_4$	8	9	8	25.44	34.34	24.11	(Kosyl et al., 2020)
$Sr_3Bi_2(BO_3)_4$	8	9	8	30.23	36.97	26.64	(Shablinskii et al., 2017)

$Sr_3Eu_2(BO_3)_4$	8	9	8	28.74	33.93	23.44	(Li et al., 2020)
$Sr_3Ho_2(BO_3)_4$	8	9	8	28.11	34.57	25.19	(Höppe et al., 2013)
$Sr_3Er_2(BO_3)_4$	8	9	8	27.89	34.33	24.20	(Höppe et al., 2013)
$Ba_3Pr_2(BO_3)_4$	8	9	8	33.32	40.58	27.86	(Khamaganova, 1990)
$Ba_3Eu_2(BO_3)_4$	8	9	8	32.39	38.99	26.98	(Chen et al., 2020)
$Ba_3Y_2(BO_3)_4$	8	9	8	33.13	38.04	27.52	This work

Table 28 – Occupancies of the *M*1–*M*3 sites of borates of the $A_3M_2(BO_3)_4$ (*A* = Ca, Sr, Ba, *REE*, Bi^{3+}) family

Borate	***M*1 Occ.** ***M***	***M*2 Occ.** ***M***	***M*3 Occ.** ***M***	**Space group**	**Reference**
$Ca_3La_2(BO_3)_4$	0.58	0.4	0.04	*Pnma*	(Mill et al., 1998)
$Ca_3Eu_2(BO_3)_4$	0.469	0.26	0.543	*Pnma*	(Kosyl et al., 2020)
$Ca_3Y_2(BO_3)_4$	0.33	0.33	0.33	*Pnma*	(Wang et al., 2004)
$Sr_3Bi_2(BO_3)_4$	0.208	0.386	0.823	*Pnma*	(Shablinskii et al., 2017)
$Sr_3Gd_2(BO_3)_4$-25	0.4	0.3	0.6	$Pc2_1n$	(Reuther et al., 2015)
$Sr_3Gd_2(BO_3)_4$-700	0.33	0.32	0.7	$Pc2_1n$	(Reuther et al., 2015)
$Sr_3Gd_2(BO_3)_4$	0.36	0.262	0.63	*Pnma*	(Sun et al., 2017)
$Sr_3Ho_2(BO_3)_4$	0.354	0.307	0.678	*Pnma*	(Höppe et al., 2013)
$Sr_3Er_2(BO_3)_4$	0.336	0.316	0.695	*Pnma*	(Höppe et al., 2013)
$Sr_3Yb_2(BO_3)_4$	0.321	0.338	0.681	*Pnma*	(Lin et al., 2013)
$Sr_3Y_2(BO_3)_4$	1	0	0	$Pc2_1n$	(Zhang, Li, 2004)
$Ba_3Bi_2(BO_3)_4$	0.228	0.339	0.866	*Pnma*	(Volkov et al., 2013)
$Ba_3Bi_{1.95}Eu_{0.05}(BO_3)_4$	Bi 0.16	Bi 0.4 Eu 0.05	Bi 0.8	*Pnma*	(Shablinskii et al., 2019)
$Ba_3Bi_{1.65}Eu_{0.35}(BO_3)_4$	Bi 0.34	Bi 0 Eu 0.39	Bi 0.58	*Pnma*	(Shablinskii et al., 2019)
$Ba_3Bi_{1.2}Eu_{0.8}(BO_3)_4$	Bi 0.2 Eu 0.3	Bi 0.07 Eu 0.27	Bi 0 Eu 0.38	*Pnma*	(Shablinskii et al., 2019)
$Ba_3La_2(BO_3)_4$	0.33	0.33	0.33	*Pnma*	(Khamaganova et al., 1997)
$Ba_3Pr_2(BO_3)_4$	0.33	0.33	0.67	*Pnma*	(Khamaganova et al., 1997)
$Ba_3Nd_2(BO_3)_4$	0.25	0.25	1	*Pnma*	(Yan, Hong, 1987a)
$Ba_3Eu_2(BO_3)_4$	0.388	0.352	0.52	*Pnma*	(Chen et al., 2020)
$Ba_3Y_2(BO_3)_4$	0.248	0.405	0.694	*Pnma*	(Ma et al., 2005)
$Ba_3Y_2(BO_3)_4$	0.232	0.410	0.718	*Pnma*	This work

Table 29 – Difference in ionic radii* (in %) (coordination = 8) (Shannon, 1976)

AE	r_i (Å)	*REE* (+ Bi, Y)	r_i (Å)	Difference (%)
Ca	1.26	La	1.30	3.17
		Eu	1.21	4.48
		Y	1.16	8.71
Sr	1.40	Bi	1.31	6.87
		Gd	1.19	17.35
		Y	1.16	20.68
		Ho	1.15	21.21
		Er	1.14	22.38
		Yb	1.125	24.4
Ba	1.56	Bi	1.31	19.08
		La	1.30	20.00
		Pr	1.27	23.22

	Nd	1.25	24.90
	Eu	1.21	28.92
	Y	1.16	34.60

* Calculated by the formula (r_{i1}—r_{i2}/r_{i2}, где $r_{i2} < r_{i1}$) (Goldschmidt, 1926)

4.8.2 Crystal structures of the $A_3M_2(BO_3)_4$ borates at high temperatures

As mentioned earlier (see section 4.3, page 105), the $Ba_3Y_2(BO_3)_4$ and $Ba_3Eu_2(BO_3)_4$ borates exhibit maximum thermal expansion along the *a*-axis (Table 25). This character of thermal expansion may be associated with the preferential orientation of the BO_3 triangles located in the *bc* plane. According to the principle of high-temperature crystal chemistry of borates with isolated BO_3 triangles, thermal expansion is maximal along the axis perpendicular to the plane of preferred orientation of the BO_3 triangles (Bubnova, Filatov, 2008).

Borates from the $A_3M_2(BO_3)_4$ (*A* = Ca, Sr, Ba, *M* = *REE*, Bi^{3+}) family are characterized by bends in the temperature dependence graphs of the unit cell parameters in various temperature ranges. In the $Ba_3Bi_2(BO_3)_4$ borate (Volkov et al., 2013), a bend is observed at a temperature of around 600 °C. Similar bends at temperatures around 500, 450—500 °C and 650 °C are also found in the $Sr_3Bi_2(BO_3)_4$ (Shablinskii et al., 2017), $Sr_{1.5}Ba_{1.5}Bi_2(BO_3)_4$ (Shablinskii et al., 2022), and $Ca_3Eu_2(BO_3)_4$ (Kosyl et al., 2020) borates respectively. In the present study, bends in the temperature dependence of the unit cell parameters are observed in the $Ba_3Y_2(BO_3)_4$ and $Ba_3Eu_2(BO_3)_4$ borates in temperature ranges of 500—640 °C, and 600—740 °C respectively.

The refinement of the crystal structures of $Ba_3Y_2(BO_3)_4$ at various temperatures allowed for the identification of changes in structural parameters with increasing temperature, comparing them to literature data for $Ca_3Eu_2(BO_3)_4$ (Kosyl et al., 2020). The nature of the changes in structural parameters was found to be different: in $Ca_3Eu_2(BO_3)_4$, with increasing temperature, the occupancy of the *M*2 site by Eu atoms increases, while the occupancy of the *M*3 site decreases. The occupancy of the Ca/Eu site in *M*1 remains approximately constant (Figure 15), whereas in the present study, the occupancy of the *M*3 site by Y atoms increases, while the occupancies of *M*1 and *M*2 decrease (Figure 65).

Known data on the thermal expansion of seven borates of the $A_3M_2(BO_3)_4$ family are presented in Table 30. For all borates, except $Ca_3Eu_2(BO_3)_4$ (Kosyl et al., 2020), maximum thermal expansion is observed along the *a*-axis.

Table 30 – Thermal expansion coefficients of borates of the $A_3M_2(BO_3)_4$ (A = Ca, Sr, Ba, M = *REE*, Bi^{3+}) family

Borate	α_a	α_b	α_c	α_V	T, °C	Reference
$Ca_3La_2(BO_3)_4:Nd^{3+}$	22.7	7.49	-4.36	25.83	25	(Pan, Wang, 2003)
$Ca_3Eu_2(BO_3)_4$	11.52(10)	14.70(42)	9.15(40)	35.37(86)	50	(Kosyl et al., 2020)
	11.949(79)	15.31(33)	9.14(31)	36.40(67)	100	
	12.804(40)	16.51(17)	9.13(16)	38.44(34)	200	
	14.505(73)	18.91(30)	9.09(29)	42.50(62)	400	
	15.35(12)	20.10(48)	9.07(47)	44.52(99)	500	
	12.3(1.4)	24.4(2.2)	8.15(32)	44.9(1)	600	
	12.3(1.4)	24.4(2.2)	8.15(32)	44.9(1)	700	
	12.3(1.4)	24.4(2.2)	8.15(32)	44.9(1)	600	
	7.18(83)	31.0(1.2)	7.50(18)	45.68(60)	900	
$Sr_3Bi_2(BO_3)_4$	14(1)	12 (1)	7(1)	37(1)	25	(Shablinskii et al., 2017)
	17(1)	19.7()	9.0(2)	46(1)	300	
	19(1)	25(1)	10(1)	54(1)	500	
	35.7(3)	28.0(3)	-4(1)	59(1)	600	
	46(1)	28(1)	-7(2)	68(2)	700	
$Sr_{1.5}Ba_{1.5}Bi_2(BO_3)_4$	3(1)	12(1)	7(1)	37(2)	25	(Shablinskii et al., 2022)
	19.6(5)	17.2(5)	9.6(3)	46.4(7)	300	
	30.4(5)	16.2(4)	5.0(1)	52(1)	500	
	35.6(6)	15.8(6)	7.7(4)	59.1(1)	600	
	40.9(9)	15.3(9)	10(1)	67(2)	700	
$Ba_3Bi_2(BO_3)_4$	16	11	11	38	25	(Volkov et al., 2013)
	25	10	12	47	300	
	30	10	12	52	500	
	32	7	-2	37	700	
$Ba_3Eu_2(BO_3)_4$	12.1(4)	15.9(3)	8.8(1)	36.9(1)	25	This work
	15.0(1)	16.6(1)	9.3(9)	40.9(7)	200	
	19.8(1)	17.6(3)	10.1(3)	47.6(3)	500	
	21.5(1)	18.0(4)	10.4(4)	49.8(3)	600	
	22.3(1)	24.6(1)	10.5(5)	57.3(4)	650	
	24.6(2)	21.6(2)	10.8(7)	57.1(6)	800	
	27.8(4)	17.6(1)	11.5(1)	57.0(9)	1000	
$Ba_3Y_2(BO_3)_4$	13.8(3)	14.4(4)	9.1(2)	37.3(1)	25	This work
	15.2(1)	14.3(2)	10.12(9)	39.7(8)	200	
	17.7(2)	14.0(3)	11.9(1)	43.6(3)	500	
	18.5(3)	13.9(4)	12.5(2)	44.9(4)	600	
	37.8(1)	29.1(7)	-0.8(1)	66.1(7)	750	
	40.5(7)	24.6(4)	0.02(8)	65.2(8)	800	
	51.2(1)	6.7(7)	3.4(1)	61.3(1)	1000	

To analyze the differences in thermal expansion of isotypic $Ba_3Y_2(BO_3)_4$ and $Ca_3Eu_2(BO_3)_4$ (Kosyl et al., 2020) borates, an analysis was conducted on the changes in bond

lengths, angles between polyhedra as temperature increases, and angles of triangular BO_3 radicals to planes.

The values of dihedral angles O6–O7–O1–O4 (Figure 71) were calculated for borates $Ba_3Y_2(BO_3)_4$ and $Ca_3Eu_2(BO_3)_4$ at temperatures before and after bending on the temperature dependencies of the unit cell parameters (Table 31). The dihedral angle decreases in $Ca_3Eu_2(BO_3)_4$ and increases in $Ba_3Y_2(BO_3)_4$ with increasing temperature (red arrows, Figure 71).

The difference in the thermal behavior of the dihedral angle O6–O7–O1–O4 is due to the fact that the *M*1O_8 and *M*3O_8 polyhedra, connected through this angle, have a common face O1–O4–O7 in $Ba_3Y_2(BO_3)_4$ and a common edge O1–O7 in $Ca_3Eu_2(BO_3)_4$. The ionic radius of the Ca atom is too small compared to the ionic radius of the Ba atom, so the Ca1–O4 bond (3.53 Å) cannot form a polyhedron and create a common face between *M*1 and *M*3 polyhedra. Since the polyhedral bond through faces is stronger than through edges, the thermal expansion along the *b*-axis for $Ba_3Y_2(BO_3)_4$ is smaller than for $Ca_3Eu_2(BO_3)_4$.

The data is also supported by an analysis of the changes in bond lengths with increasing temperature. Since the structural parameters in the *M*2O_9 polyhedron change insignificantly, it is necessary to consider the changes in bond lengths in the *M*1O_8 and *M*3O_8 polyhedra, which form the dihedral angle O6–O7–O1–O4. Thus, it can be seen that in the *M*1O_8 polyhedron, the longest bond *M*1–O4 in the $Ba_3Y_2(BO_3)_4$ borate is oriented along the *a*-axis (Figure 72). The length of this bond increases with temperature (Table 32). In the $Ca_3Eu_2(BO_3)_4$ borate, this bond is very weak due to the small ionic radius of Ca; therefore, it can hardly impede expansion along the *a*-axis. In the *M*3O_8 polyhedron, the *M*3–O3 bond, oriented almost along the *a*-axis, increases and decreases with temperature in $Ba_3Y_2(BO_3)_4$ and $Ca_3Eu_2(BO_3)_4$, respectively. However, the *M*3–O4 bond, oriented approximately along the *b*-axis, increases and hardly changes with temperature in the $Ca_3Eu_2(BO_3)_4$ and $Ba_3Y_2(BO_3)_4$ borates, respectively. Perhaps, such changes in *M*3–O4 and *M*3–O3 bond lengths make a significant contribution to the thermal expansion of $Ca_3Eu_2(BO_3)_4$ along the *b*-axis and $Ba_3Y_2(BO_3)_4$ along the *a*-axis, which may also contribute to the expansion and contraction of the dihedral angle O6–O7–O1–O4 in the $Ba_3Y_2(BO_3)_4$ and $Ca_3Eu_2(BO_3)_4$ borates with increasing temperature.

Table 31 – The values of O6–O7–O1–O4 dihedral angle for $Ba_3Y_2(BO_3)_4$ and $Ca_3Eu_2(BO_3)_4$ borates at different temperatures.

$Ca_3Eu_2(BO_3)_4$*			
T, °C	25	5100	7500
dihedral angle, °	39.2	38.4	37.6
$Ba_3Y_2(BO_3)_4$			
T, °C	25	5100	8400
dihedral angle, °	36.1	36.4	36.7

* structural data for calculation are taken from

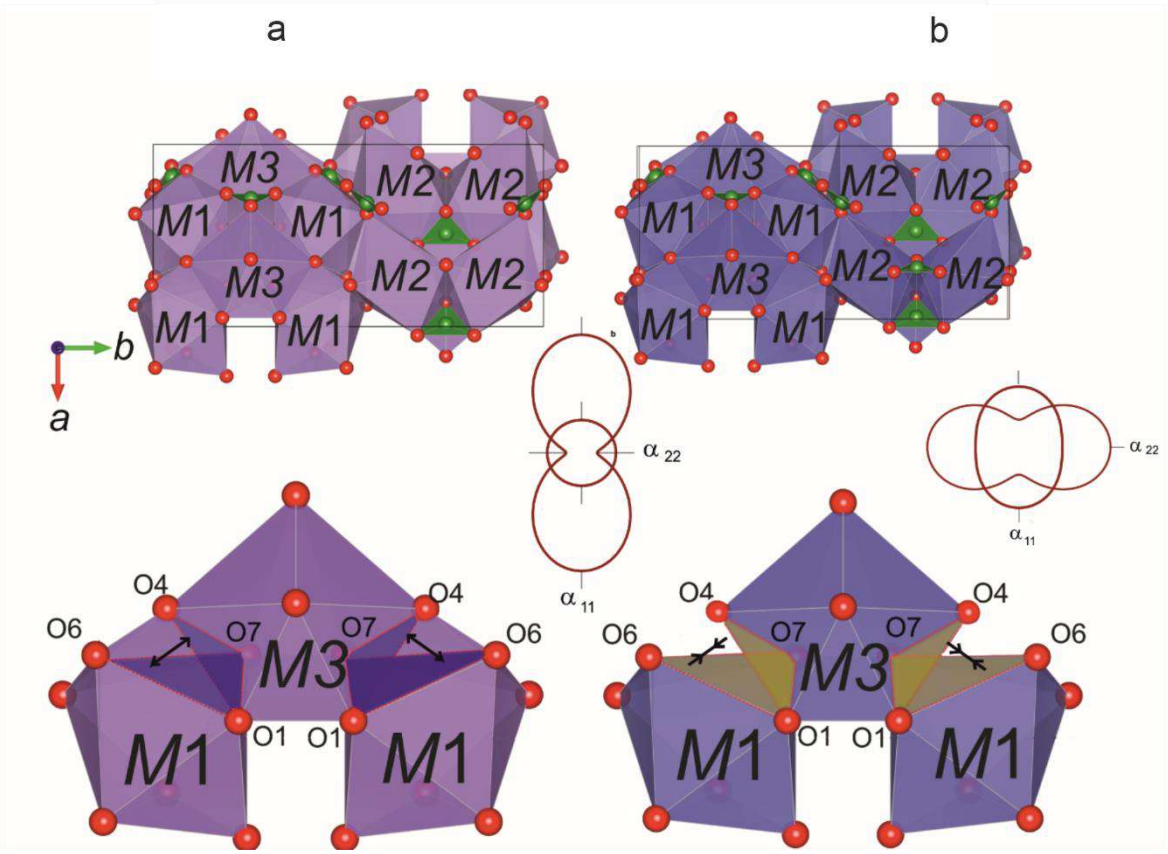

Figure 71 – The O6–O7–O1–O4 dihedral angle. The arrows show the directions of the increase and decrease of the angle with increasing temperature in $Ba_3Y_2(BO_3)_4$ (a) and $Ca_3Eu_2(BO_3)_4$ (b).

Table 32 – The values of bond lengths for $Ba_3Y_2(BO_3)_4$ and $Ca_3Eu_2(BO_3)_4$ borates at different temperatures

	$Ba_3Y_2(BO_3)_4$			$Ca_3Eu_2(BO_3)_4$**		
T, °C	25	500	840	25	500	750
Bond	Distance					
*M*1–O6	2.86	2.89	2.89	2.43	2.47	2.50

*M*1–O4	2.95	2.98	3.01	2.92*	2.91*	2.91*
*M*1–O5	2.63	2.66	2.69	2.55	2.60	2.64
*M*1–O7	2.59	2.60	2.63	2.44	2.46	2.48
*M*1–O1	2.85	2.87	2.88	2.44	2.27	2.28
*M*1–O4	2.63	2.66	2.63	2.36	2.35	2.35
*M*1–O6	2.64	2.70	2.78	2.38	2.38	2.37
*M*1–O7	2.75	2.78	2.78	2.54	2.56	2.58
<***M*1**—**O**>$_8$	2.73	2.77	2.79	2.45	2.44	2.46
*M*2–O5	2.65	2.66	2.66	2.57	2.57	2.58
*M*2–O4	3.13	3.15	3.13	2.79	2.77	2.77
*M*2–O1	2.76	2.79	2.80	2.35	2.37	2.38
*M*2–O3	2.55	2.58	2.59	2.46	2.47	2.47
*M*2–O5	2.49	2.53	2.58	2.71	2.72	2.73
*M*2–O6	2.50	2.47	2.46	2.36	2.39	2.40
*M*2–O2	2.66	2.69	2.70	2.61	2.66	2.66
*M*2–O1	2.98	2.97	3.03	2.89*	2.88*	2.88*
*M*2–O7	3.28	3.27	3.27	2.96*	2.96*	2.95*
<***M*2**—**O**>$_9$	2.71	2.73	2.74	2.55	2.56	2.57
*M*3–O4	2.51	2.51	2.51	2.53	2.56	2.57
*M*3–O4	2.51	2.51	2.51	2.53	2.56	2.57
*M*3–O3	2.46	2.48	2.50	2.42	2.42	2.40
*M*3–O2	2.41	2.44	2.45	2.33	2.33	2.40
*M*3–O7	2.91	2.99	3.07	2.44	2.45	2.48
*M*3–O7	2.91	2.99	3.07	2.44	2.45	2.48
*M*3–O1	2.58	2.58	2.56	2.44	2.48	2.49
*M*3–O1	2.58	2.58	2.56	2.44	2.48	2.49
<***M*3**—**O**>$_8$	2.61	2.63	2.65	2.44	2.47	2.48

* weak bonds of $Ca_3Eu_2(BO_3)_4$ borate are noted

** structural data for calculation are taken from (Kosyl et al., 2020)

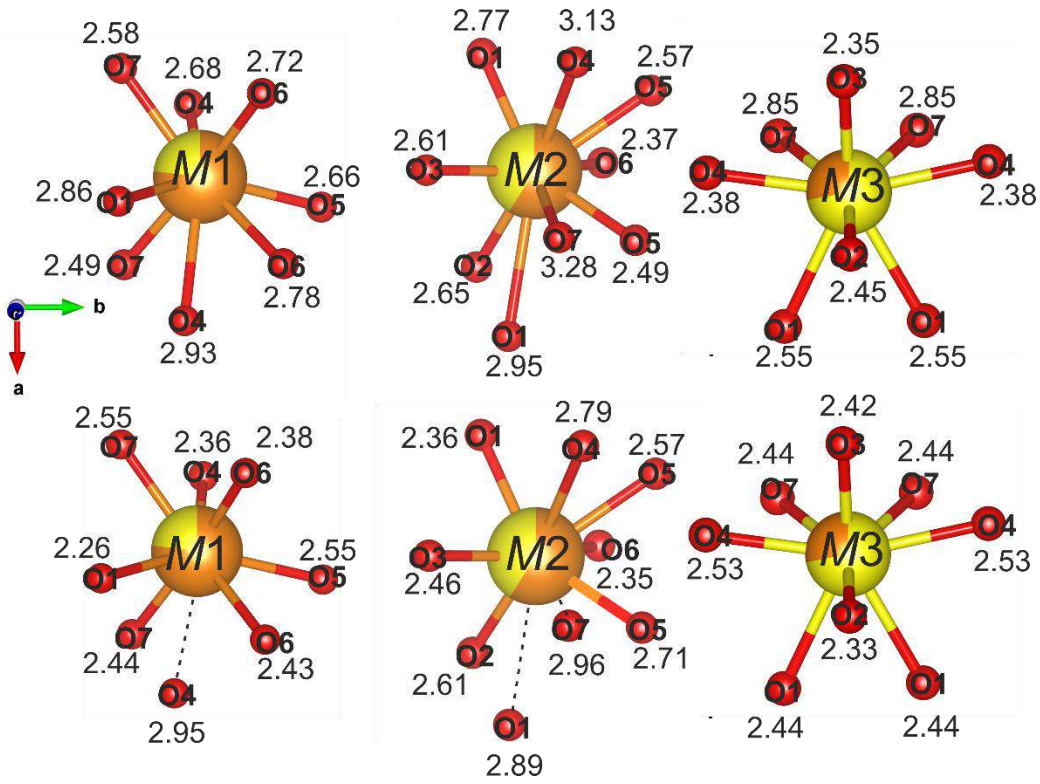

Figure 72 – The *M*1O$_8$, *M*2O$_{7\text{-}9}$ and *M*3O$_8$ polyhedra in the $Ba_3Y_2(BO_3)_4$ (top) and $Ca_3Eu_2(BO_3)_4$ (bottom).

Calculation and analysis of the angles between the planes of BO_3 triangles and the *ab*, *bc*, *ac* planes were conducted (Table 33). In the $Ba_3Y_2(BO_3)_4$ borate, the angles between the triangles B1O$_3$, B2O$_3$, and B3O$_3$ and the *bc* plane are minimal (42.45, 18.22, and 43.04, respectively). It can be concluded that in $Ba_3Y_2(BO_3)_4$, the BO_3 triangular radicals have a preferred orientation in the *bc* plane. In the $Ca_3Eu_2(BO_3)_4$ borate, the B1O$_3$ and B2O$_3$ triangles are predominantly oriented along the *bc* plane, while B3O$_3$ is oriented along *ac*. The difference in the orientation of the BO_3 triangular radicals in the borate $Ca_3Eu_2(BO_3)_4$ may also contribute to the thermal expansion characteristics of this borate, which is maximal along the *b*-axis.

Table 33 – Angles between the planes of the BO_3 triangles and the *ab*, *bc*, *ac* planes in the $Ba_3Y_2(BO_3)_4$ and $Ca_3Eu_2(BO_3)_4$ borates

	$Ba_3Y_2(BO_3)_4$			$Ca_3Eu_2(BO_3)_4$*		
	ab	*bc*	*ac*	*ab*	*bc*	*ac*
B1O$_3$x4	47.55	42.45	90	56.78	33.22	90
B2O$_3$x4	71.78	18.22	90	70.83	19.17	90

$B3O_{3x8}$	74.69	43.04	50.99	76.17	48.65	44.64

* structural data for calculation are taken from (Kosyl et al., 2020)

Thus, the contribution to the anisotropy of thermal expansion in borates of the $A_3M_2(BO_3)_4$ family is made by the preferred orientation of boron-oxygen triangles BO_3, the nature of the articulation of cationic polyhedra sites, and the orientation of the longest bonds.

4.9 Conclusion for the chapter 4

Based on the research results of borates from the $Ba_3REE_2(BO_3)_4$ (*REE* = Y, Eu) family, presented in Chapter 4, the following results can be highlighted:

1. A new $Ba_3Y_{2-x}Er_x(BO_3)_4$ (x = 0—0.3) series of solid solutions was obtained through crystallization from a melt.

2. The crystal structure of the $Ba_3Y_2(BO_3)_4$ borate was refined for all atoms in an anisotropic approach based on single-crystal data up to R = 0.037. The borate crystallizes in a orthorhombic crystal system, space group *Pnma*. Large cations are disordered over three crystallographic sites *M*1, *M*2, *M*3. The disorder in the crystal structure is further confirmed by data from Raman and infrared spectroscopy.

3. The distribution of cations over *M*1, *M*2, and *M*3 sites in the $Ba_3Y_2(BO_3)_4$ borate was refined, and an analysis of the occupancies of sites in the $A_3M_2(BO_3)_4$ (*A* = Ca, Sr, Ba, *M* = *REE*, Bi^{3+}) family at room temperature was conducted. Atoms with smaller ionic radii predominantly occupy the site with the smallest polyhedral volume, while atoms with larger ionic radii occupy the sie with the largest polyhedral volume. Based on the analysis of site occupancies in borates of the $A_3M_2(BO_3)_4$ family, a description of the isomorphism of borates is proposed from the perspective of structural diversity factor – substituting atoms occupy the most suitable sites in terms of size.

4. The temperature dependencies of the unit cell parameters of the $Ba_3Y_2(BO_3)_4$ and $Ba_3Eu_2(BO_3)_4$ borates exhibit bends in the ranges of 600–740 °C and 500–640 °C, respectively. These bends may be associated with the redistribution of cations over *M*1, *M*2, and *M*3 sites with increasing temperature. The redistribution is confirmed by refining the Rietveld method of the $Ba_3Y_2(BO_3)_4$ crystal structure in the temperature range of 600–800 °C (40 points).

5. The thermal expansion of the $Ba_3Y_2(BO_3)_4$ and $Ba_3Eu_2(BO_3)_4$ borates is maximum along the *a*-axis and minimum in the *c*-direction. This character of thermal expansion may be related to the orientation of BO_3 radicals, which have a preferred orientation in the *bc* plane. According to

the principles of high-temperature crystal chemistry of borates with isolated triangular BO_3 radicals, thermal expansion is maximum in the direction perpendicular to the preferred orientation of the BO_3 triangles.

6. An analysis of the thermal expansion of seven borates from the $A_3M_2(BO_3)_4$ family was conducted. The thermal behavior of six borates is similar. A difference is observed in $Ca_3Eu_2(BO_3)_4$, where maximum expansion occurs along the *b*-axis. The orientation of triangular BO_3 radicals plays a crucial role in the anisotropy of thermal expansion. In the $Ba_3Y_2(BO_3)_4$ borate, triangles are preferentially oriented in the *bc* plane, with maximum thermal expansion occurring perpendicular to this plane. In the $Ca_3Eu_2(BO_3)_4$ borate, the preferred orientation of triangles varies: half are predominantly oriented in the *bc* plane and half in *ac*, which may contribute to maximum expansion along the *b*-axis. An analysis of bond length changes in the $Ba_3Y_2(BO_3)_4$ and $Ca_3Eu_2(BO_3)_4$ borates revealed that in $Ba_3Y_2(BO_3)_4$, the lengths of the M1–O4 and M2–O4 bonds oriented along the *a*-axis increase with temperature, while in $Ca_3Eu_2(BO_3)_4$, the lengths of the M1–O5, M2–O3, and M3–O4 bonds oriented along *b* increase. An analysis of the dihedral angle O6–O7–O1–O4 for the $Ba_3Y_2(BO_3)_4$ and $Ca_3Eu_2(BO_3)_4$ borates at increasing temperatures was conducted. Due to the small ionic radius of Ca, the coordination number is smaller, and the nature of polyhedral articulation differs. As polyhedral bonding through faces is stronger than through edges, the thermal expansion along the *b*-axis for $Ba_3Y_2(BO_3)_4$ is less than for $Ca_3Eu_2(BO_3)_4$.

7. The luminescent and thermoluminescent properties of the $Ba_3Y_2(BO_3)_4$: Er^{3+} (x = 0— 0.3) concentration series were investigated. The optimal concentration of the activator ion is x = 0.1. With increasing temperature, the luminescence intensity of the borates decreases. The studied borates (phosphors) can be used as fluorescent thermometers.

Conclusion

Based on the results of the synthesis and studies of activated and co-activated borates based on two borate matrices $BaBi_2B_2O_7$ and $Ba_3Y_2(BO_3)_4$, 7 series of new solid solutions (42 compositions) - promising phosphors were obtained. Nine crystal structures were refined, and the structural data were confirmed by the Raman spectra of two series of solid solutions, as well as the infrared spectra of one series. The thermal expansion of three borates was studied, a thermal analysis of one borate was conducted, the thermoluminescence spectra of one series of solid solutions and the luminescence spectra of 7 series were studied. The following results were identified:

1. For the first time, 6 series of solid solutions (32 compositions) based on the borate matrix $BaBi_2B_2O_7$, activated and co-activated with REE^{3+} ions, were obtained by crystallization from glass-ceramics: $BaBi_{2-x-y-z}REE_{x,x,z}B_2O_7$ (REE = Eu^{3+}, Sm^{3+}, Tb^{3+}, Tm^{3+}).

1.1. The existence regions of continuous solid solutions were established: $BaBi_{2-x}REE_xB_2O_7$ (x_{Eu} = 0—0.45, x_{Sm} = 0—0.35, x_{Tb} = 0—0.45) и $BaBi_{2-x-0.05}Eu_xSm_{0.05}B_2O_7$ (x_{Eu} + y_{Sm} = 0—0.45), $BaBi_{2-0.15-y}Eu_{0.15}Sm_yB_2O_7$ (x_{Eu} + y_{Sm} = 0—0.375), $BaBi_{2-x-0.3}Eu_xTb_{0.15}Tm_{0.15}B_2O_7$ (x_{Eu} + y_{Tb} + z_{Tm}= 0—0.475). Thus, co-activation of the crystalline matrix allowed expanding the miscibility regions of solid solutions.

1.2. Eight crystal structures of the $BaBi_{2-x}Eu_xB_2O_7$ (x = 0.1, 0.2, 0.4), $BaBi_{2-x}Sm_xB_2O_7$ (x = 0.05, 0.3), $BaBi_{2-x}Tb_xB_2O_7$ (x = 0.1, 0.3, 0.4) borates were refined based on single-crystal data. The distribution pattern of REE^{3+} atoms over sites during isomorphic substitution was established based on the occupancy data of crystallographic sites: larger atoms Sm and Eu replace Bi atoms in *M*1 and *M*2 sites with the largest polyhedral volumes, while Tb atoms with the smallest ionic radius occupy *M*3 site with the smallest polyhedral volume. The Raman spectra confirm the disordered model of the crystal structure.

1.3. The thermal expansion of the $BaBi_{1.7}Sm_{0.3}B_2O_7$ borate was studied, revealing inflections in the temperature dependencies of the unit cell parameters at 450°C. The thermal expansion of the $BaBi_2B_2O_7$ and $BaBi_{1.7}Sm_{0.3}B_2O_7$ borates was compared. The presence of inflections in the temperature dependencies of the unit cell parameters in the borate activated by Sm^{3+} and the absence of such in the $BaBi_2B_2O_7$ crystal matrix allow these inflections to be associated with the redistribution of Bi and Sm cations.

1.4. Excitation and luminescence spectra of all series of solid solutions were measured, and optimal concentrations of the activator ion were determined for all investigated concentration series: $BaBi_{1.6}Eu_{0.4}B_2O_7$, $BaBi_{1.95}Sm_{0.05}B_2O_7$, $BaBi_{1.7}Tb_{0.3}B_2O_7$, $BaBi_{1.75}Eu_{0.15}Sm_{0.1}B_2O_7$, $BaBi_{1.7}Eu_{0.15}Tb_{0.15}Tm_{0.15}B_2O_7$. Co-activation of the crystal matrix allowed for the enhancement of

optimal concentrations of activator ions. Promising tunable phosphors for white light-emitting diodes were obtained.

2. A new $Ba_3Y_{2-x}Er_x(BO_3)_4$ (x = 0.01—0.3) series of solid solutions and $Ba_3Y_2(BO_3)_4$, $Ba_3Eu_2(BO_3)_4$ borates were synthesized by crystallization from melt (9 compositions).

2.1. The crystal structure of the $Ba_3Y_2(BO_3)_4$ borate has been refined for the first time in an anisotropic approach, including the distribution of cations over sites based on single-crystal data. A regularity in the isomorphic substitution of borates of the $A_3M_2(BO_3)_4$ (A = Ca, Sr, Ba, M = *REE*, Bi^{3+}) family has been identified. Atoms of type M with smaller ionic radius predominantly occupy $M3$ site with the smallest polyhedron volume, while $M2$ site with the largest volume is mainly occupied by alkaline earth cations (atoms of type A). A description of the isomorphism of the presented family from the perspective of structural diversity factor is proposed. The measured Raman and infrared spectra confirm the disordering of the crystal structure of $Ba_3Y_{2-x}Er_x(BO_3)_4$ (x = 0.0—0.3) solid solutions.

2.2. The thermal expansion of the $Ba_3Eu_2(BO_3)_4$ and $Ba_3Y_2(BO_3)_4$ borates was studied, and inflections in the temperature dependencies of the unit cell parameters were identified in the temperature ranges of 500–640 °C and 600–740 °C, respectively. Based on the refinement of the crystal structure in the $Ba_3Y_2(BO_3)_4$ borate over a wide temperature range (40 points), it was established that similar inflections observed in borates of the $A_3M_2(BO_3)_4$ (A = Ca, Sr, Ba, M = *REE*, Bi^{3+}) family are associated with the redistribution of cations over sites with increasing temperature.

2.3. Analysis of thermal expansion of seven borates from the $A_3M_2(BO_3)_4$ (A = Ca, Sr, Ba, M = *REE*, Bi^{3+}) family demonstrates that the borates studied in this work and from literary sources exhibit maximum thermal expansion along the a-axis, with the exception of the $Ca_3Eu_2(BO_3)_4$ borate, where it is maximal along the b-axis. In order to identify the reasons for differences in the nature of thermal expansion of borates, an analysis of changes in average bond lengths, dihedral angles, and angles between the planes of BO_3 triangles and the *ab*, *bc*, *ac* planes in the borates $Ca_3Eu_2(BO_3)_4$ and $Ba_3Y_2(BO_3)_4$ was conducted. As the temperature increases, the bond lengths $M1$–O4 and $M3$–O3 in the $Ba_3Y_2(BO_3)_4$ borate, oriented along the a-axis, increase, while in the $Ca_3Eu_2(BO_3)_4$ borate, they decrease. Additionally, the bond length $M1$–O4 is excessively large (2.9 Å), accordingly, this bond is weak. In the $Ca_3Eu_2(BO_3)_4$ borate, there is an increase in bond lengths $M3$–O4, oriented along the b-axis, whereas they remain unchanged in the $Ba_3Y_2(BO_3)_4$ borate. This change in bond lengths leads to an increase in the dihedral angle O6–O7–O1–O4 in the $Ba_3Y_2(BO_3)_4$ borate and a decrease in the $Ca_3Eu_2(BO_3)_4$ borate. In the $Ba_3Y_2(BO_3)_4$ borate, the angles between the $B1O_3$, $B2O_3$, and $B3O_3$ triangles and the *bc* plane are minimal, indicating a preferred orientation of the BO_3 triangular radicals in the *bc* plane. In the $Ca_3Eu_2(BO_3)_4$ borate,

the $B1O_3$ and $B2O_3$ triangles are predominantly oriented along the *bc* plane, while $B3O_3$ is oriented along the *ac* plane. The difference in the orientation of the BO_3 triangular radicals in the $Ca_3Eu_2(BO_3)_4$ borate may also contribute to the nature of thermal expansion along the *b*-axis.

2.4. The luminescent and thermoluminescent properties of the $Ba_3Y_{2-x}Er_x(BO_3)_4$ solid solutions were studied. The optimal concentration of the activator ion is $x = 0.1$. An increase in temperature results in a decrease in luminescence intensity. Promising fluorescent thermometers have been developed.

Based on the findings of this study, the following works have been published, indexed in leading scientific publications in WoS and Scopus, and included in the list of HAC:

1) Demina S.V., Shablinskii A.P., Povolotskiy A.V., Bubnova R.S., Biryukov Y.P., Firsova V.A., Filatov S.K. Synthesis, crystal structure, photoluminescence and thermal expansion of $Ba_3Y_{2-x}Er_x(BO_3)_4$(x = 0–0.3) solid solutions // Ceramics. Int. 2023. Vol. 49. P. 6459–6469.
2) Shablinskii A.P., Povolotskiy A.V., Kolesnikov I.E., Biryukov Y.P., Bubnova R.S., Avdontseva M.S., Demina S.V., Filatov S.K. Novel red-emitting color-tunable phosphors $BaBi_{2-x}Eu_xB_2O_7$ (x = 0–0.40): study of the crystal structure and luminescence // Journal of Solid State Chemistry. 2022. Vol. 307. P. 122837.
3) Demina S.V., Shablinskii A.P., Bubnova R.S., Filatov S.K. Thermal expansion of borate $Ba_3Eu_2(BO_3)_4$ // Glass Physics and Chemistry. 2021. Vol. 47(6). P.722–725.

List of abbreviations and symbols

AE – alkaline earth metals

c.n. – Coordination Numbe

CIE – Commission internationale de l'éclairage

cif – crystal structure information file

DSK – Differential Scanning Calorimetry

HTXRD – High-temperature powder X-ray diffraction

ICSD – Inorganic Crystal Structure Database

IR – Infrared Spectroscopy

PXD – powder X-ray diffraction

REE – rare earth elements

RGB – red, green, blue

TG – Thermogravimetry

wLED – white light emitting diode

UV Range – Ultraviolet Radiation Range

References

1. Abdullaev G. K., Mamedov K. S. Crystal structure of the binary orthoborate of erbium and strontium $Sr_3Er_2(BO_3)_4$ // A division of Plenum Publishing Corporation, 1976. P. 166–168.
2. Aizawa H., Takei K., Katsumata T., Komuro S., Morikawa T., Ishizawa H., Toba E. Development of erbium-doped silica sensor probe for fiber-optic fluorescence thermometer // Review of Scientific Instruments. 2005. Vol. 76. № 5.
3. Arefiev A. V., Shatskiy A., Podborodnikov I. V., Bekhtenova A., Litasov K.D. The System K_2CO_3–$CaCO_3$–$MgCO_3$ at 3 GPa: Implications for Carbonatite Melt Compositions in the Shallow Continental Lithosphere // Minerals. 2019a. Vol. 9. № 5. P. 296.
4. Arefiev A. V., Shatskiy A., Podborodnikov I. V., Litasov K.D. The K_2CO_3–$CaCO_3$–$MgCO_3$ System at 6 GPa: Implications for Diamond Forming Carbonatitic Melts // Minerals. 2019b. Vol. 9. № 9. P. 558.
5. Arun Kumar R., Arivanandhan M., Hayakawa Y. Recent advances in rare earth-based borate single crystals: Potential materials for nonlinear optical and laser applications // Progress in Crystal Growth and Characterization of Materials. 2013. Vol. 59. № 3. P. 113–132.
6. Bambauer H. U., Kindermann B. Darstellung und kristallographische Daten von Orthoboraten $(SE)_2Ca_3[BO_3]_4$ // Z Kristallogr Cryst Mater. 1978. V. 147. № 1–4. P. 63–74.
7. Barbier J, Penin N., Denoyer A., Cranswick L. M. D. BaBiBO4, a novel non-centrosymmetric borate oxide // Solid State Sciences. 2005. Vol. 17, № 12. P. 3130–3136.
8. Barbier J., Cranswick L. M. D. The non-centrosymmetric borate oxides, $MBi_2B_2O_7$ (M=Ca, Sr) // J Solid State Chem. 2006. Vol. 179. № 12. P. 3958–3964.
9. Brögger. Geologiska Föeningens I Stockholm // Förhandlinger, Stockholm. 1887. P. 255.
10. Brown, I. D. The Bond-Valence Method: An Empirical Approach to Chemical Structure and Bonding // Structure and Bonding in Crystals. 1981. Vol. 3. P. 49–72.
11. Bubnova R. S., Krivovichev S. V., Filatov S. K., Egorysheva A. V., Kargin Y. F. Preparation, crystal structure and thermal expansion of a new bismuth barium borate, $BaBi_2B_4O_{10}$ // J Solid State Chem. 2007. Vol. 180. № 2. P. 596–603.
12. Bubnova R.S., Filatov S.K. High-temperature crystal chemistry of borates and borosilicates. 2008. Issue. SPb Science. 760 pp. (*In Russian*).
13. Bubnova R. S., Filatov S. K. High-Temperature borate crystal chemistry // Zeitschrift fur Kristallographie. 2013. Vol. 288. № 9. P. 395–427.

14. Bubnova R.S., Shablinskii A.P., Volkov S.N., Filatov S.K. Crystal structures and thermal expansion of $Sr_{1-x}Ba_xBi_2B_2O_7$ solid solutions // Glass physics and chemistry. 2016. Vol. 42. № 4. P. 337–348.

15. Bubnova R.S., Firsova V.A., Volkov S.N., Filatov S.K.. RietveldToTensor: Program for processing powder X-Ray diffraction data under variable conditions // Glass physics and chemistry. 2018. Vol. 44. № 1. P. 33–40.

16. Burns P. S., Grice J. D., Hawthorne F. C. Borate Minerals. I. Polyhedral clusters and fundamental building blocks // Can. Miner. 1995. Vol. 33. P. 1131–1151.

17. Cai G. M., Li M., Liu J., Jin S. F., Wang W. Y., Zheng F., Chen, X. L. Crystal structure and Eu^{3+}/Tb^{3+} doped luminescent properties of a new borate $Ba_3BiB_9O_{18}$ // Mater Res Bull. 2009. Vol. 44. № 12. P. 2211–2216.

18. Callegari A, Caucia F, Mazzi F, Oberti R, Ottolini L, Ungaretti L. The crystal structure of peprossiite-(Ce), an anhydrous *REE* and Al mica-like borate with square-pyramidal coordination for Al // American Mineralogist. 2000. P. 586–593.

19. Chen C., Li R. The anionic group theory of the non-linear optical effect and its applications in the development of new high-quality nlo crystals in the borate series // Int Rev Phys Chem. 1988. Vol. 8. № 1. P. 65–91.

20. Chen X., Zhao L., Chang X., Xiao W. Syntheses, crystal structures, vibrational spectra, and luminescent properties of $M_3Eu_2(BO_3)_4$ (M = Ba, Sr) // J Solid State Chem. 2020. P. 283.

21. Clark J R. The crystal structure of tunellite, $SrB_6O_9(OH)_2.3H_2O$ // American Mineralogist. 1964. P. 1549–1568.

22. Cong R., Zhou Z., Li Q., Sun J., Lin J., Yang T. Approaching the structure of $REBaB_9O_{16}$ (RE = rare earth) by characterizations of its new analogue $Ba_6Bi_9B_{79}O_{138}$ // J Mater Chem C Mater. 2015. Vol. 3. № 17. P. 1–7.

23. Della V. G, Parodi G C, Mottana A, Chaussidon M. Peprossiite-(Ce), a new mineral from Campagnano (Italy): the first anhydrous rare-earth-element borate // European Journal of Mineralogy. 1993, 53–58.

24. Demina S.V., Shablinskii A.P., Bubnova R.S., Filatov S.K. Thermal expansion of borate $Ba_3Eu_2(BO_3)_4$ // Glass Physics and Chemistry. 2021. Vol. 47(6). P.722–725.

25. Demina S.V., Shablinskii A.P., Povolotskiy A.V., Bubnova R.S., Biryukov Y.P., Firsova V.A., Filatov S.K. Synthesis, crystal structure, photoluminescence and thermal expansion of $Ba_3Y_{2-x}Er_x(BO_3)_4$(x = 0–0.3) solid solutions // Ceramics. Int. 2023. Vol. 49. P. 6459–6469.

26. Egorysheva A.V., Volodin V.D., Milenov T. Glass formations in $CaO–Bi_2O_3–B_2O_3$ и $SrO–Bi_2O_3–B_2O_3$ systems // Journal of Inorganic Chemistry. 2010. Vol. 55. № 11. P. 1920–1927. (*In Russian*).

27. Erd R C, Morgan V, Clark J R. Tunellite, a new hydrous strontium borate from the Kramer Borate District, California, U.S. // Geological Survey Professional Paper. 1961. P. 294–297.

28. Filatov S. K., Bubnova R. S. Isomorphism and related crystallochemical phenomena (experiment of systematics) // Zapiski VMO. 1983. Vol. 112. P. 552–556.

29. Filatov S.K. High-temperature crystal chemistry. L.: Nedra, 1990, 288 pp. (*In Russian*).

30. Goldschmidt V. M. Die Gesetze der Krystallochemie // Naturwissenschaften. 1926. Vol. 14. № 21. P. 477–485.

31. Grew, E. S., Hystad, G., Hazen, R. M., Krivovichev, S. V., Gorelova, L. A. How many boron minerals occur in Earth's upper crust? // American Mineralogist. 2017. Vol 102. № 8. P. 1573–1587.

32. Grice J D, Van V. J, Dunn P J, Newbury D E, Etz E S, Nielsen C H. Moydite (Y,*REE*)$[B(OH)_4](CO_3)$, a new mineral species from the Evans-Lou pegmatite, Quebec // The Canadian Mineralogist. 1986. P. 665–673.

33. Guo F., Han J., Cheng S., Yu S., Yang Z., Pan S. Transformation of the B–O Units from Corner-Sharing to Edge-Sharing Linkages in Ba*M*BO_4 (*M* = Ga, Al) // Inorg Chem. 2019. Vol. 58. № 12. P. 8237–8244.

34. Hawtorne, F.C., Burns P.C., Grice J.D. The crystal chemistry of boron // Rev. Miner., 1996. P. 41–116.

35. He L., Wang Y. Synthesis of $Sr_3Y_2(BO_3)_4:Eu^{3+}$ and its photoluminescence under UV and VUV excitation // J Alloys Compd. 2007. T. 431. № 1–2. P. 226–229.

36. Hoffmann C, Armbruster T, Kunz M. Structure refinement of (001) disordered gaudefroyite $Ca_4Mn_3[(BO_3)_3(CO_3)O_3]$: Jahn-Teller-distortion in edge-sharing chains of MnO_6 octahedra // European Journal of Mineralogy. 1997. P. 7–19.

37. Höppe H. A., Kazmierczak K., Grumbt C., Schindler L., Schellenberg I., Pöttgen, R. The Oxonitridoborate $Eu_5(BO_{2.51(7)}N_{0.49(7)})_4$ and the Mixed-Valent Borates $Sr_3Ln_2(BO_3)_4$ (Ln = Ho, Er) // Eur J Inorg Chem. 2013. № 31. P. 5443–5449.

38. Huang X., Han S., Huang W., Liu, X. Enhancing solar cell efficiency: The search for luminescent materials as spectral converters // Chem Soc Rev. 2013. Vol. 42. № 1. P. 173–201.

39. Huppertz H. High-Pressure Preparation, Crystal Structure, and Properties of $RE_4B_6O_{15}$ (*RE* = Dy, Ho) with an Extension of the “Fundamental Building Block”-Descriptors // Zeitschrift für Naturforschung B. 2003. Vol. 58. № 4. P. 278–290.

40. Huppertz H., Eltz B. Multianvil High-Pressure Synthesis of $Dy_4B_6O_{15}$: The First Oxoborate with Edge-Sharing BO_4 Tetrahedra // J Am Chem Soc. 2002. Vol. 124. № 32. P. 9376–9377.

41. Jouravsky G, Permingeat F. La gaudefroyite, une nouvelle espèce minérale // Bulletin de la Société Française de Minéralogie et de Cristallographie. 1964. P. 216–229.

42. Juansheng S. Lighting appliance capable of adjusting color temperature and its adjusting method // 2004.

43. Khamaganova T. N. Crystal structures $Ba_3TR_2(BO_3)_4$ (TR = La, Pr) // Kristallografiya. 1990. P. 856–860.

44. Konidakis I., Karagiannaki A., Stratakis E. Advanced composite glasses with metallic, perovskite, and two-dimensional nanocrystals for optoelectronic and photonic applications // Nanoscale. 2022. Vol. 14. № 8. P. 2966–2989.

45. Korzanov V. S., Shulgina N. P. Chemistry of rare, trace and rare earth elements. 2007. Perm University. 101 pp. (*In Russian*).

46. Kosyl K. M., Paszkowicz W., Shekhovtsov A. N., Kosmyna M. B., Antonowicz J., Olczak A., Fitch A. N. Variation of cation distribution with temperature and its consequences on thermal expansion for $Ca_3Eu_2(BO_3)_4$ // Acta Cryst. B., 2020. P. 554–562.

47. Kosyl K. M., Paszkowicz W., Minikayev R., Shekhovtsov A. N., Kosmyna M. B., Chrunik M., Fitch A. N. Site-occupancy scheme in disordered $Ca_3RE_2(BO_3)_4$: a dependence on rare-earth (*RE*) ionic radius // Acta Crystallogr B Struct Sci Cryst Eng Mater. 2021. T. 77. № 3. C. 339–346.

48. Krivovichev S. V., Bubnova R. S., Volkov S. N., Krzhizhanovskaya M. G., Egorysheva A. V., Filatov, S. K. Preparation, crystal structure and thermal expansion of a novel layered borate, $Ba_2Bi_3B_{25}O_{44}$ // J Solid State Chem. 2012. Vol. 196. P. 11–16.

49. Leonyuk N. I. Growth of new optical crystals from boron-containing fluxed melts // Crystallography Reports. 2008. Vol. 53. № 3. P. 511–518.

50. Leonyuk N. I., Maltsev V. V., Volkova E. A. Crystal Chemistry of High-Temperature Borates // Molecules. 2020. Vol. 25. № 10. P. 2450.

51. Li, C., Chen, J., Gu, F., Hu, Y. Method for preparing long persistence luminescent material with high initial fluorescent intensity // 2008a.

52. Li, G.-H., Yang, N., Guo, J.-G., Wang, Z.-L., Cai, G.-M., Wang, X.-J. Efficient and stable $Sr_3Eu_2B_4O_{12}$ red phosphor benefiting from low symmetry and distorted local environment // Dalton Transactions. 2020. Vol. 49. № 10. P. 3260–3271.

53. Li J., Yan H., Liu W., Yan F., Hu J. Luminescent properties of new bluish white $CaBi_2B_2O_7:Dy^{3+}$ phosphor for white light-emitting diodes // Optoelectronics and advanced materials-rapid communications. 2017. Vol. 11. № 3–4. P. 232–235.

54. Li J., Yan H., Yan F. A novel high color purity blue-emitting phosphor: $CaBi_2B_2O_7:Tm^{3+}$ // Materials Science and Engineering: B. 2016a. Vol. 209. P. 56–59.

55. Li J., Yan H., Yan F. Luminescence properties of a novel orange–red $CaBi_2B_2O_7:Eu^{3+}$ phosphor for near-UV pumped W-LEDs // Optik (Stuttg). 2016b. Vol. 127. № 10. P. 4541–4544.

56. Li, P., Yang, Z., Wang, Z., Guo, Q. White-light-emitting diodes of UV-based $Sr_3Y_2(BO_3)_4:Dy^{3+}$ and luminescent properties // Mater Lett. 2008. Vol. 62. № 10–11. P. 1455–1457.

57. Li Z., Pian Q., Li L., Sun Y., Zheng S. Luminescence properties of $SrBi_2B_2O_7$: Eu^{3+} orange-red phosphor // Optik (Stuttg). 2018. Vol. 161. PC. 38–43.

58. Li X. Z., Wang C., Chen X. L. Syntheses, Thermal Stability, and Structure Determination of the Novel Isostructural $RBa_3B_9O_{18}$ (R = Y, Pr, Nd, Sm, Eu, Gd, Tb, Dy, Ho, Er, Tm, Yb) // Inorg Chem. 2004. Vol. 43. № 26. P. 8555–8560.

59. Liebau F. Structural chemistry of silicates. Berlin; Heidelberg: Springer-Verlag. 1985. P. 347.

60. Lin C. C., Liu R.-S. Advances in Phosphors for Light-emitting Diodes // J Phys Chem Lett. 2011. Vol. 2. № 11. P. 1268–1277.

61. Lin F. L., Huang J. H., Chen Y. J., Gong X. H., Lin Y. F., Luo Z. D., Huang Y. D. Polarized spectral properties and 1.5-1.6 μm laser operation of Er: $Sr_3Yb_2(BO_3)_4$ crystal // Opt Mater (Amst). 2013. Vol. 35. № 12. P. 2314–2319.

62. Lin Y.-J., Liu W.-C., Liu Y.-H., Lee G.-H., Chien S.-Y., Chiu C.-W. A linear Di-coordinate boron radical cation // Nat Commun. 2022. Vol. 13. № 1. P. 7051.

63. Logvinova A.M., Shatskiy A., Wirth R., Tomilenko A.A., Ugap'eva S.S., Sobolev N. V. Carbonatite melt in type Ia gem diamond // Lithos. 2019. Vol. 342–343. P. 463–467.

64. Ma P., Chen J., Hu Z., Lin Z., Wang, G. Structure of $Ba_3Y_2(BO_3)_4$ crystal // Materials Research Innovations. 2005. Vol. 9. № 3. P. 9–11.

65. Ma P., Lin Z., Wang G. Growth and optical properties of Yb^{3+}-doped $Ba_3Y_2(BO_3)_4$ crystal // Opt Mater (Amst). 2007. Vol. 29. № 11. P. 1553–1556.

66. Manzani D., Petruci J.F. S., Nigoghossian K., Cardoso A.A., Ribeiro S.J.L. A portable luminescent thermometer based on green up-conversion emission of Er^{3+}/Yb^{3+} co-doped tellurite glass // Sci Rep. 2017. Vol. 7. P. 41596.

67. Mill B. V., Tkachuk A.M., Belokoneva E.L., Ershova G.I., Mironov D.I., Razumova I.K. Spectroscopic studies of $Ln_2Ca_3B_4O_{12}$-Nd^{3+} (*Ln*=Y, La, Gd) crystals // J Alloys Compd. 1998. T. 275–277.

68. Momma K., Izumi F. VESTA 3 for three-dimensional visualization of crystal, volumetric and morphology data // J Appl Crystallogr. 2011.

69. Mutailipu M., Zhang M., Li H., Fan X., Yang Z., Jin S., Wang G., Pan S. $Li_4Na_2CsB_7O_{14}$: a new edge-sharing $[BO_4]^{5-}$ tetrahedra containing borate with high anisotropic thermal expansion // Chemical Communications. 2019a. Vol. 55. № 9. P. 1295–1298.

70. Mutailipu M., Zhang M., Yang Z., Pan S. Targeting the Next Generation of Deep-Ultraviolet Nonlinear Optical Materials: Expanding from Borates to Borate Fluorides to Fluorooxoborates // Acc Chem Res. 2019b. Vol. 52. № 3. P. 791–801.

71. Navon O. High internal pressures in diamond fluid inclusions determined by infrared absorption // Nature. 1991. Vol. 353. № 6346. P. 746–748.

72. Nikolenko E.I., Sharygin I.S., Alifirova T.A., Korsakov A. V., Zelenovskiy P.S., Shur V.Ya. Graphite-bearing mineral assemblages in the mantle beneath Central Aldan superterrane of North Asian craton: combined confocal micro-Raman and electron microprobe characterization // Journal of Raman Spectroscopy. 2017. Vol. 48. № 11. P. 1597–1605.

73. Noeth H., Staudigl R., Wagner H. U. Contributions to the chemistry of boron. 121. Dicoordinate amidoboron cations // Inorg Chem. 1982. Vol. 21. № 2. P. 706–716.

74. OxfordDiffraction. CrysAlisPRO // Agilent Technologies UK Ltd, Yarnton, England. 2015.

75. Palkina K. K., Kuznetsov V. G., Moruga L. G. Crystal structure of $Sr_3Pr_2(BO_3)_4$ // A division of Plenum Publishing Corporation. 1974. P. 988–992.

76. Pan S., Hu Z., Lin Z., Wang G. Growth and optical properties of Yb^{3+}-doped α-$Ba_3Y(BO_3)_3$ crystal // J Cryst Growth. 2004. Vol. 263. № 1–4. P. 214–217.

77. Pan S., Wang G. Structure of Low Temperature Phase β-$Ba_3Y(BO_3)_3$ Crystal // Jiegou Huaxue. 2003. Vol. 22. № 2. P. 16–19.

78. Pan Z., Cong H., Yu H., Tian L., Yuan H., Cai H., Zhang H., Huang H., Wang J., Wang Q., Wei Z., Zhang Z. Growth, thermal properties and laser operation of Nd:$Ca_3La_2(BO_3)_4$: A new disordered laser crystal // Opt Express. 2013. Vol. 21. № 5. P. 6091–6100.

79. Petříček V., Dušek M., Plášil J. Crystallographic computing system Jana2006: Solution and refinement of twinned structures // Z Kristallogr Cryst Mater. 2016. Vol. 231. № 10.

80. Postolov V.S. Benderskaya L.P. Synthesis and study of luminescent properties of mixed borates of rare earth and alkaline earth metals // Coll. of scientific papers of the All-Russian Research Institute of Luminophores and Highly Pure Substances. Vol. 12. P. 84–87. (*In Russian*).

81. Pyle J. M., Haggerty S. E. Silicate-carbonate liquid immiscibility in upper-mantle eclogites: Implications for natrosilicic and carbonatitic conjugate melts // Geochim Cosmochim Acta. 1994. Vol. 58. № 14. P. 2997–3011.

82. Rashchenko S. V., Ignatov M., Shatskiy A., Arefiev A., Litasov K.D. Coupling between Cation and Anion Disorder in β-$K_2Ca_3(CO_3)_4$ // SSRN. 2022.

83. Reddy V. B., Northrop S. K. Process for Producing Electroluminescent Phosphor With Increased Efficiency // 2000.

84. Reuther C., Möckel R., Götze J., Hengst M., Heide G. Synthesis and optical characterization of Gd-neso-borate single crystals // Chemie der Erde. 2015. Vol. 75. № 3. P. 317–322.

85. Sasaki A. Himeda A., Konaka H., Muroyama N. Ab initio crystal structure analysis based on powder diffraction data used PDXL // Rigaku J. 2010. Vol. 26. P. 10–14.

86. Sasaki, T., Mori, Y., Yoshimura, M., Yap, Y.K., Kamimura, T. Recent development of nonlinear optical borate crystals: key materials for generation of visible and UV light // Materials Science and Engineering: R: Reports. 2000. Vol. 30. № 1–2. P. 1–54.

87. Schubert D. M. Borates in Industrial Use // Group 13 Chemistry III: Industrial Applications 2003. P. 1–40.

88. Serebrennikov V.V. Chemistry of rare earth elements (scandium, yttrium, lanthanides). Vol. 1. Book. 1. 1959. Issue of Tomsk University. 521 pp. (*In Russian*).

89. Shablinskii A. P., Drozdova I. A., Volkov S. N., Krzhizhanovskaya M. G., Bubnova R. S. Obtaining and study of glass ceramics in the $Sr_{1-x}Ba_xBi_2B_2O_7$ system // Glass Physics and Chemistry. 2012. Vol. 38. №. 6. P. 886–889. (*In Russian*).

90. Shablinskii, A.P., Bubnova R.S., Kolesnikov I.E. Novel $Sr_3Bi_2(BO_3)_4:Eu^{3+}$ red phosphor: Synthesis, crystal structure, luminescent and thermal properties // Solid State Sci. 2017. Vol. 70. P. 93–100.

91. Shablinskii, A.P., Kolesnikov I.E, Bubnova R.S. A novel thermally stable $Ba_3Bi_2(BO_3)_4:Eu^{3+}$ red phosphor for solid state lighting application // J Lumin. 2019. Vol. 216. 116714

92. Shablinskii A.P., Povolotskiy,A.V., Kolesnikov I.E., Biryukov Y.P., Bubnova R.S., Avdontceva M.S., Demina S.V., Filatov S.K. Novel red-emitting color-tunable phosphors $BaBi_{2-x}Eu_xB_2O_7$ (x = 0–0.40): Study of the crystal structure and luminescence // J Solid State Chem. 2022. Vol. 307. P. 122837.

93. Shablinskii A. P., Povolotskiy A. V, Yuriev A., Bubnova R. S., Kolesnikov I. E., Filatov S. K. Novel $CaB_{i2}B_4O_{10}:Eu^{3+}$ red phosphor: Synthesis, crystal structure, luminescence and thermal expansion // Solid State Sci. 2020. 106. 106280.

94. Shablinskii A. P., Bubnova R. S., Filatov S. K. Crystal structure and thermal expansion of the solid solution $Sr_{1.5}Ba_{1.5}Bi_2(BO_3)_4$ // Glass Physics and Chemistry. 2022. Vol. 48. №. 6. P. 773–782. (*In Russian*).

95. Shannon R. D. Revised effective ionic radii and systematic studies of interatomic distances in halides and chalcogenides // Acta Crystallogr. 1976. Vol. A32. № 5. P. 925–945.

96. Shatsky V., Zedgenizov D., Ragozin A., Kalinina, V. Silicate Melt Inclusions in Diamonds of Eclogite Paragenesis from Placers on the Northeastern Siberian Craton // Minerals. 2019. Vol. 9. № 7. P. 412.

97. Shen K. K., Kochesfahani S., Jouffret F. Zinc borates as multifunctional polymer additives // Polym Adv Technol. 2008. Vol. 19. № 6. P. 469–474.

98. Shoji Y., Tanaka N., Mikami K., Uchiyama M., Fukushima T. A two-coordinate boron cation featuring C–B+–C bonding // Nat Chem. 2014. Vol. 6. № 6. P. 498–503.

99. Sobolev N. V., Shatsky V. S. Diamond inclusions in garnets from metamorphic rocks: a new environment for diamond formation // Nature. 1990. Vol. 343. № 6260. P. 742–746.

100. Soler-Carracedo K., Martín I.R., Lahoz F., Vasconcelos H.C., Lozano-Gorrín A.D., Martín L.L., Paz-Buclatin F.: Er^{3+}/Ho^{3+} codoped nanogarnet as an optical FIR based thermometer for a wide range of high and low temperatures. // J Alloys Compd. 2020. Vol. 847. P. 156541.

101. Strunz H. Classification of borate minerals // European Journal of Mineralogy. 1997. Vol. 9. № 1. P. 225–232.

102. Su Q., Pei Z., Chi L., Zhang H., Zhang Z., Zou F. The yellow-to-blue intensity ratio (Y/B) of Dy^{3+} emission // J Alloys Compd. 1993. Vol. 192. № 1–2. P. 25–27.

103. Sun S., Wei Q., Lou F., Huang Y., Yuan F., Zhang L., Lin Z. A promising ultrafast pulse laser crystal with a disordered structure: Yb^{3+}:$Sr_3Gd_2(BO_3)_4$ // CrystEngComm. 2017. Vol. 19. № 12. P. 1620–1626.

104. Tang Z. B. Xu C. L., Wei X. R., Zhang X. G., Chen Y. B. Improved photoluminescence intensity and thermal stability brought by increasing Eu^{3+}content in $KBaY_{1-x}Eu_xSi_2O_7$solid-solution phosphors // J Alloys Compd. 2017. Vol. 695. P. 2745–2750.

105. Tsuno K., Dasgupta R., Danielson L., Righter, K. Flux of carbonate melt from deeply subducted pelitic sediments: Geophysical and geochemical implications for the source of Central American volcanic arc // Geophys Res Lett. 2012. Vol. 39. № 16.

106. Tu C., Wang Y., You Z., Li J., Zhu Z., Wu B. The growth and spectroscopic characteristics of $Ca_3Y_2(BO_3)_4$:Er^{3+} laser crystal // J Cryst Growth. 2004a. Vol. 260. № 3–4. P. 410–413.

107. Tu C., Wang Y., You Z., Li J., Zhu Z., Wu B. Growth and spectroscopic characteristics of $Ca_3Gd_2(BO_3)_4$:Yb^{3+} laser crystal // J Cryst Growth. 2004b. Vol. 265. № 1–2. P. 154–158.

108. Volkov S. N., Bubnova R. S., Shorets O. Y., Ugolkov V. L., Filatov S. K. Crystal structure and strong uniaxial negative thermal expansion of $CaBi_2B_2O_7$ borate // Inorg Chem Commun. 2020. Vol. 122. P. 108262.

109. Volkov S.N., Bubnova R.S., Filatov S.K. Synthesis, crystal structure and thermal expansion of a novel borate, $Ba_3Bi_2(BO_3)_4$ // Z Kristallog. 2013. Vol. 288. № 9. P. 436–443.

110. Volkov S.N., Bubnova R.S., Zalesskii V.G., Egorysheva A. V., Volodin V.D., Filatov S.K. Thermal behavior of borate $BaBiBO_4$ // Glass Physics and Chemistry. 2015. Vol. 41. № 6. P. 622–629.

111. Wang Y., Tu C., Huang,C., You Z. Study of crystal Yb^{3+}:$Ca_3Y_2(BO_3)_4$ // J Mater Res. 2004. Vol. 19. № 4. P. 1203–1207.

112. Wang Y., Tu C., You Z., Li J., Zhu Z., Jia G., Lu X., Wu B. Optical spectroscopy of $Ca_3Gd_2(BO_3)_4$:Nd^{3+} laser crystal // J Mod Opt. 2006. Vol. 53. № 8. P. 1141–1148.

113. Wei B., Hu Z., Lin Z., Zhang L., Wang G. Growth and spectral properties of Er^{3+}/Yb^{3+}-codoped $Ca_3Y_2(BO_3)_4$ crystal // J Cryst Growth. 2004. Vol. 273. № 1–2. P. 190–194.

114. Wei Y., Tu C., Jia G., You Z., Wang H., Yang F., Lu X., Li J., Zhu Z., Wang Y. Spectroscopic properties of Tm^{3+} -doped $Ba_3Gd_2(BO_3)_4$ crystal // Solid State Commun. 2006. Vol. 140. № 5. P. 230–235.

115. West. Solid state chemistry and its applications. 1984. John Wiley & Sons. 742 p.

116. Wu L., Bai Y., Wu L., Yi H., Kong Y., Zhang Y., Xu J. Sm^{3+} and Eu^{3+} codoped $SrBi_2B_2O_7$: a red-emitting phosphor with improved thermal stability // RSC Adv. 2017. Vol. 7. № 2. P. 1146–1153.

117. Wu Y., Yao J.-Y., Fu P.-Z. Potassium zinc borate, $KZnB_3O_6$ // Acta Crystallogr Sect E Struct Rep Online. 2010. Vol. 66. № 5. P. i45–i45.

118. Xia Z., Liu Q. Progress in discovery and structural design of color conversion phosphors for LEDs // Prog Mater Sci. 2016. Vol. 84. P. 59–117.

119. Yan J. F., Hong H. Y. P. Crystal structure of a new mini-laser material, $Nd_2Ba_3(BO_3)_4$ // Mater Res Bull. 1987a. Vol. 22. № 10. P. 1347–1353.

120. Ye, S., Xiao, F., Pan, Y.X., Ma, Y.Y., Zhang, Q.Y. Phosphors in phosphor-converted white light-emitting diodes: Recent advances in materials, techniques and properties // Materials Science and Engineering: R: Reports. 2010. Vol. 71. № 1. P. 1–34.

121. Yu Y., Zhao J., Bayly A. E. Development of Surfactants and Builders in Detergent Formulations // Chin J Chem Eng. 2008. Vol. 16. № 4. P. 517–527.

122. Yuan H., Wang L., Ma Y., Dou X., Han W., Xu H., Liu J., Pan Z. Anisotropy in spectroscopic and laser properties of Yb: $Sr_3La_2(BO_3)_4$ disordered crystal // Opt Mater Express. 2017. Vol. 7. № 9. P. 3251.

123. Zhang, W., Chen, X., Bai, S. Phase transitions and microwave dielectric properties of Bi_3NbO_7 ceramics with $Bi_4B_2O_9$ addition // Ceram Int. 2013. Vol. 39. № 4. P.3957–3963.

124. Zhang Y., Li Y. Red photoluminescence and crystal structure of $Sr_3Y_2(BO_3)_4$ // J Alloys Compd. 2004. Vol. 384. № 1. P. 88–92.

125. Zhao S., Yao J., Zhang G. $Ba_3Y_2B_6O_{15}$, a novel cubic borate // Acta Crystallogr C. 2011. Vol. 67. № 7. P. 39.

Other publications with the main scientific results of the dissertation

126) Demina S.V., Shablinskii A.P., Bubnova R.S., Povolotsky A.V., Filatov S.K. New phosphors based on $BaBi_2B_2O_7$ borates activated and co-activated by REE^{3+} atoms // XX International Meeting on Crystal Chemistry, X-ray Diffraction and Spectroscopy of Minerals and VI International Meeting on Organic Mineralogy, St. Petersburg. 17.06.2024–21.06.2024.

127) Demina S.V., Shablinskii A.P., Bubnova R.S., Povolotsky A.V., Filatov S.K. Crystal structures and luminescent properties of new series of solid solutions based on $BaBi_2B_2O_7$ // XIV All-Russian scientific conference "Minerals: structure, properties, research methods" with a youth school, Yekaterinburg. 05.28.2024–06.01.2024.

128) Demina S.V., Shablinskii A.P., Bubnova R.S., Povolotsky A.V., Biryukov Ya.P., Kolesnikov I.E., Avdontseva M.S., Filatov S.K. New phosphors based on $BaBi_2B_2O_7$ borates doped and co-doped with REE^{3+} atoms // All-Russian Conference on Luminescence LUMOS-2024 with international participation, Moscow. 23.04.2024–26.04.2024.

129) Demina S.V. Thermal expansion, crystal structures and luminescent properties of new phosphors based on $BaBi_2B_2O_7$ solid solutions activated by REE^{3+} ions (REE = Eu3+, Sm3+, Tb3+) // Abstract of the report of the 62nd International Scientific Student Conference "ISSC-2024", Novosibirsk. 17.04.2024–23.04.2024.

130) Demina S.V., Shablinskii A.P., Bubnova R.S., Povolotsky A.V., Biryukov Ya.P., Filatov S.K. New phosphors based on Ba-containing borates of rare earths and bismuth: crystal structure, thermal expansion // XXI Youth Scientific Conference of the Institute of Chemical Synthesis of the Russian Academy of Sciences “Functional Materials: Synthesis, Properties, Application”, St. Petersburg, Institute of Chemical Synthesis of the Russian Academy of Sciences. 05.12.2023–07.12.2023. P. 51.

131) Demina S.V., Shablinskii A.P., Bubnova R.S., Povolotsky A.V., Filatov S.K. New phosphors based on Ba-containing borates of rare earths and bismuth for wLEDs // Modern trends in the development of functional materials, Sochi, Sirius University. 07.11.2023–09.11.2023.

132) Demina S.V., Shablinskii A.P., Bubnova R.S., Povolotsky A.V., Kolesnikov I.E., Biryukov Ya.P., Filatov S.K. Red-emitting phosphors based on Ba-containing rare earth and bismuth borates, crystal structure, thermal stability // Abstract of the report of the X All-Russian Conference (with international participation) "High-Temperature Chemistry of Oxide Systems and Materials", St. Petersburg, Institute of Chemical Synthesis of the Russian Academy of Sciences. 25.09.2023–28.09.2023. P. 96–97.

133) Demina S.V. Thermal behavior and luminescent properties of new red-emitting phosphors based on solid solutions $BaBi_2B_2O_7$: Eu^{3+}, Sm^{3+} // Abstract of the report of the 61st International Scientific Student Conference "ISSC-2023". Novosibirsk, NSU. 17.04.2023–26.04.2023.

134) Demina S.V., Shablinskii A.P., Povolotskiy A.V., Biryukov Y.P., Bubnova R.S., Filatov S.K. Eu-Sm co-doped borates of rare-earths elements // Abstract of the report of the Geological International Student Summit «GISS». St. Petersburg, St. Petersburg State University. 2023. P. 257–258.

135) Demina S.V., Shablinskii A.P., Bubnova R.S., Povolotsky A.V., Filatov S.K. New red-emitting phosphors based on Ba-containing Bi borates and rare earths // Abstract of the report of the XVII Kurchatov Interdisciplinary Youth Scientific School. Moscow, National Research Center Kurchatov Institute. 20.03.2023–23.03.2023.

136) Demina S.V., Shablinskii A.P., Bubnova R.S., Povolotsky A.V., Filatov S.K. New red-emitting phosphors based on $BaBi_{2-x}Sm_xB_2O_7$ solid solutions // Abstract of the report of the XX Youth Scientific Conference of the Institute of Chemical Synthesis of the Russian Academy of Sciences "Functional Materials: Synthesis, Properties, Application". St. Petersburg, Institute of Chemical Synthesis of the Russian Academy of Sciences. 05.12.2022–06.12.2022. P. 46.

137) Demina S.V. Crystal-chemical design of new solid-state phosphors based on Ba-containing rare earth borates for LEDs // Abstract of the Youth International Scientific Conference "Modern Trends in the Development of Functional Materials". Sochi, Sirius University. 16.11.2022–18.11.2022. P. 25.

138) Demina S.V. Crystal chemical design of new phosphors based on the $Ba_3REE_2(BO_3)_4$:Er^{3+} (*REE* = Y, Eu) family // Abstract of the report of the 60th International Scientific Student Conference "ISSC-2022". Novosibirsk, NSU. 10.04.2022–20.04.2022. P. 176.

139) Demina S.V., Shablinskii A.P., Povolotskiy A.V., Kolesnikov I.E., Biryukov Y.P., Bubnova R.S., Avdontceva M.S., Filatov S.K. Novel red-emitting color-tunable phosphors $BaBi_{2-x}Eu_xB_2O_7$ (x = 0-0.40): study of the crystal structure and luminescence // Abstract of the report of the Geological International Student Summit «GISS». St. Petersburg, St. Petersburg State University. 2023. P. 257–258.

140) Demina S.V., Shablinskii A.P., Bubnova R.S., Povolotsky A.V., Kolesnikov I.Ya., Filatov S.K., Firsova V.A. Thermal behavior, crystal structure and photoluminescence of borates $Ba_3Eu_2(BO_3)_4$ and $Ba_3Y_2(BO_3)_4$:Er^{3+} // Abstract of the report of the Scientific and Practical Conference "Rare Metals and Materials Based on Them: Technologies, Properties

and Application" ("RedMet-2021"). Moscow, "Giredmet". 08.12.2021–10.12.2021. P. 63-64.

141) Demina S.V., Shablinskii A.P., Bubnova R.S., Povolotsky A.V., Kolesnikov I.Ya., Filatov S.K. New red-emitting phosphors based on $BaBi_{2-x}Eu_xB_2O_7$ solid solutions // Abstract of the report. The Second International Symposium "Chemistry for Biology, Medicine, Ecology and Agriculture" dedicated to the 100th anniversary of the birth of Academician M.G. Voronkov. St. Petersburg, Institute of Chemical Synthesis of the Russian Academy of Sciences. 07.12.2021–08.12.2021. P. 69-70.

142) Demina S.V., Shablinskii A.P., Bubnova R.S., Firsova V.A., Biryukov Ya.P., Povolotsky A.V., Kolesnikov I.E., Filatov S.K. Borates $Ba_3Y_2(BO_3)4$: Er $^{3+}$ and $Ba_3Eu_2(BO_3)_4$: Thermal behavior, crystal structure, photoluminescence // Abstract of the report of the X National Crystal Chemical Conference. Chernogolovka, Institute of Problems of Chemical Physics. 05.07.2021–09.07.2021. P. 115-116.

143) Shablinskii A.P., Bubnova R.S., Kolesnikov I.E., Demina S.V., Povolotsky A.V., Filatov S.K. New $BaBi_{2-x}Eu_xB_2O_7$ solid solutions for red-emitting phosphors: crystal structure and optical properties // Abstract of the report of the X National Crystal Chemical Conference. Chernogolovka, Institute of Problems of Chemical Physics. 05.07.2021–09.07.2021. P. 389-390.

144) Demina S.V. New solid solutions $BaBi_{2-x}Eu_xB_2O_7$ for red-emitting phosphors // Abstract of the report of the 59th International Scientific Student Conference "ISSC-2021". Novosibirsk, NSU. 12.04.2021–23.04.2021. P. 183-184.

145) Demina S.V., Shablinskii A.P., Bubnova R.S., Biryukov Ya.P., Povolotsky A.V., Kolesnikov I.E., Filatov S.K. Thermal expansion, crystal structure and photoluminescence of borates $Ba_3Eu_2(BO_3)_4$ and $Ba_3Y_2(BO_3)_4$:Er^{3+} // Abstract of the report. Conference "Crystal-chemical aspects of creating new materials: theory and practice". Moscow, Moscow State University. 09.23.2021. P. 59-61.

146) Shablinskii A.P., Povolotsky A.V., Demina S.V., Avdontseva M.S., Bubnova R.S., Kolesnikov I.E., Filatov S.K. Red-emitting phosphors $BaBi_{2-x}Eu_xB_2O_7$: synthesis, structure, optical properties // Abstract of the report of the Conference "Crystal-chemical aspects of creating new materials: theory and practice". Moscow, Moscow State University. 09.23.2021. P. 84.

147) Demina S.V., Shablinskii A.P., Bubnova R.S., Biryukov Ya.P., Povolotsky A.V., Kolesnikov I.E., Filatov S.K. Borates $Ba_3Y_2(BO_3)_4$: Er^{3+} and $Ba_3Eu_2(BO_3)_4$: thermal expansion, photoluminescence, crystal structure // Abstract of the report of the XIX All-Russian youth scientific conference "Functional materials: synthesis, properties,

application". St. Petersburg, Institute of Chemical Synthesis of the Russian Academy of Sciences. 01.12.2020–03.12.2020. P. 146.

148) Demina S.V., Shablinsky A.P., Bubnova R.S., Biryukov Ya.P., Filatov S.K. Borates $Ba_3Y_2(BO_3)_4$: Er^{3+} and $Ba_3Eu_2(BO_3)_4$: synthesis, thermal expansion // Abstract of the report. Conference and school for young scientists "Thermal X-ray and Radiography of Nanomaterials (TRPH-4)". St. Petersburg, St. Petersburg State University. 11/19/2020–11/21/2020. P. 60.

149) Shablinskii A.P., Demina S.V., Bubnova R.S. Crystal structure and thermal expansion of the borate $Eu_2Ba_3B_4O_{12}$ // Abstract of the report of the XVII Youth Scientific Conference and School of Young Scientists dedicated to the 100th anniversary of the birth of Academician of the Russian Academy of Sciences M.M. Shultz. St. Petersburg: LEMA Publishing House. St. Petersburg, Institute of Crystallography of the Russian Academy of Sciences. 05.12.2019–06.12.2019. P. 116.

150) Demina S.V., Bubnova R.S., Shablinskii A.P., Biryukov Ya.P., Filatov S.K. Crystal structure and thermal expansion of borate $Y_2Ba_3B_4O_{12}$ // Abstract of the report. Scientific readings dedicated to the 70th anniversary of the Department of Crystallography of Moscow State University, conf. "Crystal chemistry in space and time". Moscow, Moscow State University. Moscow: publishing house "KDU", "Dobrosvet". November 29, 2019. P. 48.

Supplementary materials

Table S 1 – Atomic coordinates, equivalent isotropic displacement parameters (Å^2) and occupancies for $BaBi_{2-x}Eu_xB_2O_7$ (x = 0.10; 0.20; 0.40) phosphors

Atom	*x*	*y*	*z*	U_{iso}*/U_{eq}	Occupancy
$BaBi_{1.9}Eu_{0.1}B_2O_7$					
Ba1	0.333333	0.666667	0.1616 (4)	0.022 (2)	0.2793 (17)
Bi1	0.375 (3)	0.7369 (15)	0.19484 (13)	0.024 (2)	0.2033 (17)
Eu1'	0.375 (3)	0.7369 (15)	0.19484 (13)	0.024 (2)	0.037 (17)
Ba2	−0.333333	0.333333	0.0358 (6)	0.036 (2)	0.365 (7)
Bi2	−0.333333	0.333333	0.0057 (2)	0.0435 (12)	0.635 (7)
Ba3	−0.333333	0.333333	0.3491 (11)	0.0465 (9)	0.345 (7)
Bi3	−0.3820 (9)	0.2439 (7)	0.3524 (6)	0.0465 (9)	0.215 (2)
O1	−0.851 (3)	−0.145 (2)	−0.0148 (11)	0.049 (6)	1
O2	−0.705 (2)	0.139 (3)	0.2133 (11)	0.054 (6)	1
O3	−0.333333	0.333333	−0.1544 (18)	0.088 (6)	1
B1	−1	0	−0.0148 (18)	0.030 (6)	1
B2	−1	0	0.217 (3)	0.056 (11)	1
$BaBi_{1.8}Eu_{0.2}B_2O_7$					
Ba1	0.333333	0.666667	0.1638 (4)	0.017 (2)	0.2479 (8)
Bi1	0.3774 (13)	0.672 (4)	0.1994 (2)	0.0299 (8)	0.1891 (8)
Eu1'	0.3774 (13)	0.672 (4)	0.1994 (2)	0.0299 (8)	0.0616 (8)
Ba2	−0.333333	0.333333	0.0385 (10)	0.047 (4)	0.420 (3)
Bi2	−0.333333	0.333333	0.0087 (5)	0.0299 (8)	0.580 (3)
Ba3	−0.333333	0.333333	0.359 (2)	0.057 (9)	0.351 (3)
Bi3	−0.3894 (5)	0.312 (3)	0.3526 (8)	0.0299 (8)	0.2162 (11)
O1	−0.856 (3)	−0.141 (4)	−0.0203 (13)	0.071 (8)	1
O2	−0.699 (2)	0.151 (3)	0.2124 (15)	0.056 (6)	1
O3	−0.333333	0.333333	−0.149 (3)	0.098 (7)	1
B1	−1	0	−0.021 (5)	0.014 (2)	1
B2	−1	0	0.2221 (18)	0.012 (4)	1
$BaBi_{1.6}Eu_{0.4}B_2O_7$					
Ba1	0.333333	0.666667	0.1636 (6)	0.021 (2)	0.280 (3)
Bi1	0.331 (5)	0.6159 (14)	0.19725 (16)	0.0176 (2)	0.207 (3)
Eu1'	0.331 (5)	0.6159 (14)	0.19725 (16)	0.0176 (2)	0.034 (3)
Ba2	−0.333333	0.333333	0.0440 (5)	0.0255 (2)	0.273
Bi2	−0.333333	0.333333	0.00802 (17)	0.0729 (18)	0.45 (2)
Eu2'	−0.333333	0.333333	0.00802 (17)	0.0729 (18)	0.28 (2)
Ba3	−0.333333	0.333333	0.3511 (10)	0.053 (9)	0.469 (1)
Bi3	−0.405 (4)	0.303 (7)	0.3518 (8)	0.0425 (13)	0.177 (1)
O1	−0.857 (3)	−0.154 (3)	−0.0204 (13)	0.051 (7)	1
O2	−0.702 (3)	0.153 (4)	0.2137 (14)	0.055 (8)	1
O3	−0.333333	0.333333	−0.154 (2)	0.095 (7)	1

B1	−1	0	−0.0300 (19)	0.025 (7)	1
B2	−1	0	0.210 (2)	0.030 (7)	1

Table S 2 – Anisotropic atomic displacement parameters (Å^2) for $BaBi_{2-x}Eu_xB_2O_7$ (x = 0.10; 0.20; 0.40) phosphors

Atom	U^{11}	U^{22}	U^{33}	U^{12}	U^{13}	U^{23}
$BaBi_{1.9}Eu_{0.1}B_2O_7$						
Ba1	0.030 (3)	0.030 (3)	0.005 (3)	0.0152 (15)	0	0
Bi1	0.011 (3)	0.019 (3)	0.029 (2)	−0.001 (3)	0.0011 (12)	0.0001 (9)
Eu1'	0.011 (3)	0.019 (3)	0.029 (2)	−0.001 (3)	0.0011 (12)	0.0001 (9)
Ba2	0.037 (3)	0.037 (3)	0.035 (5)	0.0185 (13)	0	0
Bi2	0.0581 (15)	0.0581 (15)	0.0142 (19)	0.0290 (7)	0	0
Ba3	0.0536 (13)	0.0536 (13)	0.0324 (8)	0.0268 (6)	0	0
Bi3	0.0536 (13)	0.0536 (13)	0.0324 (8)	0.0268 (6)	0	0
O1	0.054 (8)	0.014 (5)	0.084 (10)	0.021 (5)	0.001 (6)	0.009 (4)
O2	0.039 (6)	0.040 (7)	0.058 (8)	0.001 (5)	−0.021 (6)	0.007 (5)
O3	0.116 (8)	0.116 (8)	0.031 (7)	0.058 (4)	0	0
B2	0.030 (9)	0.030 (9)	0.11 (3)	0.015 (5)	0	0
$BaBi_{1.8}Eu_{0.2}B_2O_7$						
Ba1	0.020 (3)	0.020 (3)	0.010 (4)	0.0099 (14)	0	0
Bi1	0.0116 (11)	0.0453 (10)	0.0240 (10)	0.0076 (8)	0.0099 (9)	0.0044 (7)
Eu1'	0.0116 (11)	0.0453 (10)	0.0240 (10)	0.0076 (8)	0.0099 (9)	0.0044 (7)
Ba2	0.046 (3)	0.046 (3)	0.048 (11)	0.0231 (16)	0	0
Bi2	0.0116 (11)	0.0453 (10)	0.0240 (10)	0.0076 (8)	0.0099 (9)	0.0044 (7)
Ba3	0.057 (12)	0.057 (12)	0.018 (6)	0.000	0.000	0.0027 (8)
Bi3	0.0116 (11)	0.0453 (10)	0.0240 (10)	0.0076 (8)	0.0099 (9)	0.0044 (7)
O1	0.040 (8)	0.100 (11)	0.089 (11)	0.048 (8)	0.041 (7)	0.068 (9)
O2	0.015 (5)	0.043 (6)	0.111 (11)	0.016 (5)	0.020 (6)	0.034 (7)
O3	0.127 (10)	0.127 (10)	0.042 (12)	0.063 (5)	0	0
$BaBi_{1.6}Eu_{0.4}B_2O_7$						
Ba1	0.021 (3)	0.021 (3)	0.006 (4)	0.000	0.000	0.0005 (17)
Bi1	0.020 (7)	0.011 (4)	0.014 (3)	−0.0010 (13)	−0.003 (2)	0.002 (8)
Eu1'	0.020 (7)	0.011 (4)	0.014 (3)	−0.0010 (13)	−0.003 (2)	0.002 (8)
Ba2	0.020 (3)	0.020 (3)	0.021 (6)	0.000	0.000	0.0101 (16)
Bi2	0.069 (3)	0.069 (3)	0.034 (4)	0.000	0.000	0.0346 (13)

Eu2'	0.069 (3)	0.069 (3)	0.034 (4)	0.000	0.000	0.0346 (13)
Ba3	0.054 (15)	0.054 (15)	0.016 (6)	0.000	0.000	0.0027 (8)
Bi3	0.033 (3)	0.034 (4)	0.046 (3)	0.006 (4)	0.005 (5)	0.015 (4)
O1	0.022 (8)	0.049 (10)	0.094 (11)	0.027 (7)	0.004 (6)	0.020 (6)
O2	0.035 (8)	0.056 (11)	0.082 (10)	0.028 (8)	−0.021 (7)	0.006 (7)
O3	0.122 (10)	0.122 (10)	0.040 (8)	0.061 (5)	0	0

Table S 3 – Atomic coordinates, equivalent isotropic displacement parameters (Å^2) and occupancies for $BaBi_{2-x}Sm_xB_2O_7$ (x = 0.05, 0.30) phosphors

Atom	*x*	*y*	*z*	U_{iso}*/U_{eq}	Occupancy
			$BaBi_{1.95}Sm_{0.05}B_2O_7$		
Ba1	0.333333	0.666667	0.1631 (4)	0.0424 (4)	0.3472 (12)
Bi1	0.364 (2)	0.7335 (8)	0.19420 (14)	0.0424 (4)	0.2303 (4)
Ba2	−0.333333	0.333333	0.0448 (6)	0.0424 (4)	0.2286 (10)
Bi2	−0.333333	0.333333	0.00702 (12)	0.0424 (4)	0.6938 (3)
Sm2'	−0.333333	0.333333	0.00702 (12)	0.0424 (4)	0.0486 (4)
Ba3	−0.333333	0.333333	0.3533 (5)	0.0424 (4)	0.4142 (16)
Bi3	−0.3820 (13)	0.2415 (5)	0.3443 (3)	0.0424 (4)	0.1905 (5)
O1	−0.857 (2)	−0.144 (2)	−0.0133 (14)	0.052 (6)	1
O2	−0.699 (3)	0.146 (3)	0.2129 (14)	0.051 (6)	1
O3	−0.333333	0.333333	−0.155 (2)	0.093 (9)	1
B1	−1	0	−0.028 (3)	0.033 (9)	1
B2	−1	0	0.204 (3)	0.046 (12)	1
			$BaBi_{1.7}Sm_{0.3}B_2O_7$		
Ba1	0.333333	0.666667	0.1703 (8)	0.0402 (6)*	0.407 (15)
Bi1	0.3579 (18)	0.6257 (16)	0.1970 (2)	0.0402 (6)*	0.226 (5)
Ba2	−0.333333	0.333333	0.0495 (15)	0.0402 (6)*	0.200 (16)
Bi2	−0.333333	0.333333	0.0095 (2)	0.0402 (6)*	0.468 (7)
Sm2'	−0.333333	0.333333	0.0095 (2)	0.0402 (6)*	0.332 (17)
Ba3	−0.333333	0.333333	0.3511 (14)	0.0402 (6)*	0.40 (2)
Bi3	−0.3834 (14)	0.3622 (14)	0.3511 (10)	0.0402 (6)*	0.179 (7)
O1	−0.850 (2)	−0.143 (3)	−0.0169 (16)	0.056 (4)	1
O2	−0.702 (3)	0.151 (3)	0.2131 (17)	0.056 (4)	1
O3	−0.333333	0.333333	−0.156 (3)	0.056 (4)	1
B1	−1	0	−0.029 (4)	0.037 (6)	1

B2	−1	0	0.212 (3)	0.037 (6)	1

Table S 4 – Anisotropic atomic displacement parameters (Å^2) for $BaBi_{2-x}Sm_xB_2O_7$ (x = 0.05, 0.30) phosphors

$Ba_{0.99}Bi_{1.96}Sm_{0.05}B_2O_7$						
Atom	U^{11}	U^{22}	U^{33}	U^{12}	U^{13}	U^{23}
Ba1	0.0497 (5)	0.0497(5)	0.0277(5)	0.0249(3)	0	0
Bi1	0.0497 (5)	0.0497(5)	0.0277(5)	0.0249(3)	0	0
Ba2	0.0497 (5)	0.0497(5)	0.0277(5)	0.0249(3)	0	0
Bi2	0.0497 (5)	0.0497(5)	0.0277(5)	0.0249(3)	0	0
Sm2′	0.0497 (5)	0.0497(5)	0.0277(5)	0.0249(3)	0	0
Ba3	0.0497 (5)	0.0497(5)	0.0277(5)	0.0249(3)	0	0
Bi3	0.0497 (5)	0.0497(5)	0.0277(5)	0.0249(3)	0	0
O1	0.041 (6)	0.023 (5)	0.099(14)	0.020 (5)	0.016 (7)	0.004 (6)
O2	0.023 (6)	0.048 (8)	0.064(10)	0.006 (6)	0.000 (6)	0.018 (7)
O3	0.123 (13)	0.123(13)	0.034 (9)	0.062 (6)	0	0
B1	0.028 (10)	0.028(10)	0.045(17)	0.014 (5)	0	0
B2	0.046 (14)	0.046(14)	0.05 (2)	0.023 (7)	0	0
$Ba_{1.00}Bi_{1.71}Sm_{0.30}B_2O_7$						
O1	0.026(4)	0.071(6)	0.090(5)	0.038(5)	−0.011(5)	−0.014(6)
O2	0.026(4)	0.071(6)	0.090(5)	0.038(5)	−0.011(5)	−0.014(6)
O3	0.026(4)	0.071(6)	0.090(5)	0.038(5)	−0.011(5)	−0.014(6)
B1	0.028(7)	0.028(7)	0.055(14)	0.014(3)	0	0
B2	0.028(7)	0.028(7)	0.055(14)	0.014(3)	0	0

Table S 5 – Atomic coordinates, equivalent isotropic displacement parameters (Å^2) and occupancies for $BaBi_{2-x}Tb_xB_2O_7$ (x = 0.10, 0.30, 0.40) phosphors

Atom	x	y	z	U_{iso}*/U_{eq}	Occupancy
$BaBi_{1.9}Tb_{0.1}B_2O_7$					
Ba1	0.333333	0.666667	0.1652 (6)	0.0374 (4)	0.300 (8)
Bi1	0.3679 (16)	0.7329 (6)	0.19578 (17)	0.0374 (4)	0.246 (3)
Ba2	−0.333333	0.333333	0.0415 (7)	0.0374 (4)	0.329 (8)
Bi2	−0.333333	0.333333	0.0073 (2)	0.0374 (4)	0.642 (8)
Ba3	−0.333333	0.333333	0.3596 (6)	0.0374 (4)	0.359 (11)
Bi3	−0.3761 (11)	0.2464 (5)	0.3466 (3)	0.0374 (4)	0.1728 (11)
Tb3'	−0.3761 (11)	0.2464 (5)	0.3466 (3)	0.0374 (4)	0.037 (4)
O1	−0.8530 (19)	−0.146 (2)	−0.0134 (13)	0.058 (6)	1
O2	−0.699 (2)	0.153 (2)	0.2129 (12)	0.042 (5)	1
O3	−0.333333	0.333333	−0.156 (2)	0.083 (7)	1
B1	−1	0	−0.032 (3)	0.051 (11)	1
B2	−1	0	0.209 (3)	0.048 (10)	1
$BaBi_{1.7}Tb_{0.3}B_2O_7$					

Ba1	0.333333	0.666667	0.1705 (3)	0.0326 (3)	0.417 (8)
Bi1	0.3647 (19)	0.6356 (19)	0.19950 (16)	0.0326 (3)	0.223 (3)
Ba2	−0.333333	0.333333	0.0412 (5)	0.0326 (3)	0.410 (7)
Bi2	−0.333333	0.333333	0.0067 (3)	0.0326 (3)	0.590 (7)
Ba3	−0.333333	0.333333	0.3688 (11)	0.0326 (3)	0.176 (11)
Bi3	−0.3686 (12)	0.3680 (12)	0.3484 (2)	0.0326 (3)	0.1525
Tb3'	−0.3686 (12)	0.3680 (12)	0.3484 (2)	0.0326 (3)	0.100 (4)
O1	−0.848 (2)	−0.144 (2)	−0.0180 (12)	0.053 (6)	1
O2	−0.7024 (5)	0.145 (2)	0.2137 (13)	0.043 (5)	1
O3	−0.333333	0.333333	−0.154 (2)	0.107 (9)	1
B1	−1	0	−0.028 (2)	0.031 (8)	1
B2	−1	0	0.209 (2)	0.043 (10)	1
$BaBi_{1.6}Tb_{0.4}B_2O_7$					
Ba1	0.333333	0.666667	0.1657 (6)	0.0368 (4)	0.288 (8)
Bi1	0.3629 (19)	0.6382 (19)	0.19756 (11)	0.0368 (4)	0.237 (3)
Ba2	−0.333333	0.333333	0.0403 (4)	0.0368 (4)	0.421 (7)
Bi2	−0.333333	0.333333	0.00700 (18)	0.0368 (4)	0.582 (7)
Ba3	−0.333333	0.333333	0.3631 (7)	0.0368 (4)	0.313 (11)
Bi3	−0.3684 (13)	0.3722 (13)	0.3492 (3)	0.0368 (4)	0.1022
Tb3'	−0.3684 (13)	0.3722 (13)	0.3492 (3)	0.0368 (4)	0.127 (4)
O1	−0.852 (2)	−0.146 (2)	−0.0105 (13)	0.069 (6)	1
O2	−0.704 (2)	0.153 (2)	0.2189 (11)	0.047 (4)	1
O3	−0.333333	0.333333	−0.1539 (16)	0.095 (8)	1
B1	−1	0	−0.029 (3)	0.046 (8)	1
B2	−1	0	0.2109 (19)	0.048 (9)	1

Table S 6 – Anisotropic atomic displacement parameters (Å^2) for $BaBi_{2-x}Tb_xB_2O_7$ (x = 0.10, 0.30, 0.40) phosphors

Atom	U^{11}	U^{22}	U^{33}	U^{12}	U^{13}	U^{23}
$BaBi_{1.9}Tb_{0.1}B_2O_7$						
Ba1	0.0443 (4)	0.0443 (4)	0.0238 (7)	0.0221 (2)	0	0
Bi1	0.0443 (4)	0.0443 (4)	0.0238 (7)	0.0221 (2)	0	0
Ba2	0.0443 (4)	0.0443 (4)	0.0238 (7)	0.0221 (2)	0	0
Bi2	0.0443 (4)	0.0443 (4)	0.0238 (7)	0.0221 (2)	0	0
Ba3	0.0443 (4)	0.0443 (4)	0.0238 (7)	0.0221 (2)	0	0
Bi3	0.0443 (4)	0.0443 (4)	0.0238 (7)	0.0221 (2)	0	0
Tb3'	0.0443 (4)	0.0443 (4)	0.0238 (7)	0.0221 (2)	0	0
O1	0.032 (4)	0.040 (5)	0.120 (16)	0.032 (4)	0.002 (6)	−0.008 (7)
O2	0.022 (5)	0.049 (6)	0.052 (8)	0.017 (4)	0.002 (5)	−0.008 (6)
O3	0.110 (9)	0.110 (9)	0.027 (10)	0.055 (4)	0	0
B1	0.044 (10)	0.044 (10)	0.06 (3)	0.022 (5)	0	0
B2	0.064 (13)	0.064 (13)	0.016 (13)	0.032 (7)	0	0
$BaBi_{1.7}Tb_{0.3}B_2O_7$						
Ba1	0.0410 (4)	0.0410 (4)	0.0157 (6)	0.0205 (2)	0	0

Bi1	0.0410 (4)	0.0410 (4)	0.0157 (6)	0.0205 (2)	0	0
Ba2	0.0410 (4)	0.0410 (4)	0.0157 (6)	0.0205 (2)	0	0
Bi2	0.0410 (4)	0.0410 (4)	0.0157 (6)	0.0205 (2)	0	0
Ba3	0.0410 (4)	0.0410 (4)	0.0157 (6)	0.0205 (2)	0	0
Bi3	0.0410 (4)	0.0410 (4)	0.0157 (6)	0.0205 (2)	0	0
Tb3'	0.0410 (4)	0.0410 (4)	0.0157 (6)	0.0205 (2)	0	0
O1	0.043 (5)	0.031 (5)	0.100 (13)	0.030 (4)	−0.002 (7)	−0.006 (6)
O2	0.035 (6)	0.028 (5)	0.058 (8)	0.010 (5)	0.008 (6)	−0.005 (6)
O3	0.152 (12)	0.152 (12)	0.016 (8)	0.076 (6)	0	0
B1	0.028 (8)	0.028 (8)	0.037 (16)	0.014 (4)	0	0
B2	0.063 (14)	0.063 (14)	0.003 (10)	0.031 (7)	0	0
$BaBi_{1.6}Tb_{0.4}B_2O_7$						
Ba1	0.0431 (4)	0.0431 (4)	0.0243 (6)	0.0216 (2)	0	0
Bi1	0.0431 (4)	0.0431 (4)	0.0243 (6)	0.0216 (2)	0	0
Ba2	0.0431 (4)	0.0431 (4)	0.0243 (6)	0.0216 (2)	0	0
Bi2	0.0431 (4)	0.0431 (4)	0.0243 (6)	0.0216 (2)	0	0
Ba3	0.0431 (4)	0.0431 (4)	0.0243 (6)	0.0216 (2)	0	0
Bi3	0.0431 (4)	0.0431 (4)	0.0243 (6)	0.0216 (2)	0	0
Tb3'	0.0431 (4)	0.0431 (4)	0.0243 (6)	0.0216 (2)	0	0
O1	0.044 (5)	0.039 (5)	0.134 (14)	0.028 (4)	0.009 (7)	0.007 (7)
O2	0.025 (5)	0.038 (5)	0.073 (8)	0.013 (4)	0.010 (5)	0.002 (5)
O3	0.126 (11)	0.126 (11)	0.032 (9)	0.063 (5)	0	0
B1	0.033 (9)	0.033 (9)	0.071 (17)	0.017 (4)	0	0
B2	0.059 (13)	0.059 (13)	0.025 (12)	0.030 (6)	0	0

Table S 7 – Atomic coordinates, equivalent isotropic displacement parameters ($Å^2$) and occupancies for $Ba_3Y_2(BO_3)_4$ borate

Atom	*x*	*y*	*z*	*U*iso*/*U*eq	Occupancy
Ba1	01343(6)	0.58766(3)	0.18618(5)	0.03241(16)	0.768(3)
Y1′	0.01343(6)	0.58766(3)	0.18618(5)	0.03241(16)	0.232(3)
Ba2	–0.30964(7)	0.62185(3)	–0.15091(6)	0.0328(18)	0.59(3)
Y2′	–0.30964(7)	0.62185(3)	–0.15091(6)	0.0328(18)	0.409(3)
Y3	–0.1840(1)	0.75	0.4806(1)	0.0373(3)	0.718(10)
Ba3′	–0.1840(1)	0.75	0.4806(1)	0.0373(3)	0.282(10)
O1	–0.4529(8)	0.8221(3)	0.5856(7)	0.06(2)	1
O2	–0.632(1)	0.75	0.750(1)	0.061(3)	1
O3	0.121(2)	0.75	0.490 (1)	0.12(7)	1
O4	–0.141(1)	0.8958(6)	0.451(1)	0.126(4)	1
O5	–0.103(1)	0.9497(7)	0.6756(7)	0.149(5)	1
O6	–0.289(1)	1.0119(6)	0.514(1)	0.143(5)	1

O7	0.243 (2)	0.8216 (6)	0.303 (2)	0.28 (1)	1
B1	–0.512 (2)	0.75	0.64(1)	0.039(3)	1
B2	0.20(2)	0.75	0.356(1)	0.041(3)	1
B3	–0.178(1)	0.9532(5)	0.5445(7)	0.035(2)	1

Table S 8 – Anisotropic atomic displacement parameters ($Å^2$) for $Ba_3Y_2(BO_3)_4$ borate

Atom	U^{11}	U^{22}	U^{33}	U^{12}	U^{13}	U^{23}
Ba1	0.0287(3)	0.0294(3)	0.0392(3)	0.0024(2)	0.0032(2)	0.00188(19)
Y1′	0.0287(3)	0.0294(3)	0.0392(3)	0.0024(2)	0.0032(2)	0.00188(19)
Ba2	0.0354(3)	0.0248(3)	0.0382(3)	0.0064(2)	–0.0042(2)	–0.0028(2)
Y2′	0.0354(3)	0.0248(3)	0.0382(3)	0.0064(2)	–0.0042(2)	–0.0028(2)
Y3	0.036(5)	0.0293(5)	0.0466(6)	0	–0.0084(4)	0
Ba3′	0.036(5)	0.0293(5)	0.0466(6)	0	–0.0084(4)	0
O1	0.064(4)	0.029(3)	0.086(5)	–0.008(3)	0.021(3)	0
O2	0.075(6)	0.051(5)	0.058(5)	0	0.029(5)	0
O3	0.094(9)	0.192(15)	0.075(9)	0	0.004(7)	0
O4	0.104(7)	0.141(8)	0.133(8)	–0.056(6)	0.066(6)	–0.074(6)
O5	0.198(10)	0.2(11)	0.05(5)	–0.104(9)	–0.05(5)	0.056(6)
O6	0.061(6)	0.083(7)	0.284(14)	0.028(5)	0.007(6)	0.03(7)
O7	0.153(12)	0.31(2)	0.38(2)	–0.07(13)	–0.014(13)	0.23(19)

Table S 9 – Calculation of bond valence sum for the $A_3M_2(BO_3)_4$ (*A* = Ca, Sr, Ba, *M* = *REE*, Bi^{3+}) borate family

Bond	length (Å)	valence	Bond	length (Å)	valence
	$Ca_3La_2(BO_3)_4$			$Ca_3Eu_2(BO_3)_4$	
Ca1/La1—O4	2.342 (15)	0.50	Ca1/Eu1—O1	2.261 (8)	0.52
Ca1/La1—O7	2.436 (14)	0.39	Ca1/Eu1—O4	2.359 (8)	0.40
Ca1/La1—O6	2.446 (16)	0.38	Ca1/Eu1—O6	2.379 (8)	0.38
Ca1/La1—O4	2.461 (15)	0.36	Ca1/Eu1—O6	2.430 (8)	0.33
Ca1/La1—O5	2.496 (17)	0.33	Ca1/Eu1—O7	2.438 (8)	0.32
Ca1/La1—O1	2.589 (10)	0.26	Ca1/Eu1—O5	2.546 (8)	0.24
Ca1/La1—O6	2.719 (16)	0.18	Ca1/Eu1—O7	2.547 (7)	0.24
$<Ca1/La1—O>_7$	2.498	∑2.40 (2.58)	$<Ca1/Eu1—O>_7$	2.422	∑2.42 (2.47)
Ca1/La1—O4	2.804 (16)	0.14	Ca1/Eu1—O4	2.953 (8)	0.08
$<Ca1/La1—O>_8$	2.537	∑2.54 (2.58)	$<Ca1/Eu1—O>_8$	2.489	∑2.50 (2.47)
Ca1/La1—O6	3.382 (17)		Ca1/Eu1—O6	3.539(8)	
Ca2/La2—O3	2.385 (10)	0.40	Ca2/Eu2—O6	2.353 (8)	0.38

Ca2/La2—O7	2.436 (14)	0.35	Ca2/Eu2—O1	2.363 (7)	0.37
Ca2/La2—O7	2.465 (15)	0.32	Ca2/Eu2—O3	2.465 (8)	0.28
Ca2/La2—O6	2.499 (15)	0.30	Ca2/Eu2—O5	2.574 (8)	0.21
Ca2/La2—O2	2.567 (14)	0.25	Ca2/Eu2—O2	2.614 (8)	0.19
Ca2/La2—O1	2.791 (10)	0.13	Ca2/Eu2—O5	2.715 (7)	0.14
Ca2/La2—O1	2.793 (14)	0.13	Ca2/Eu2—O4	2.788 (8)	0.12
<Ca2/La2—O>$_7$	2.562	∑1.89 (2.40)	<Ca2/Eu2—O>$_7$	2.553	∑1.69 (2.26)
Ca2/La2—O5	2.858 (16)	0.11	Ca2/Eu2—O1	2.890 (8)	0.09
<Ca2/La2—O>$_8$	2.599	∑2.00 (2.40)	<Ca2/Eu2—O>$_8$	2.595	∑1.78 (2.26)
Ca2/La2—O2	3.107 (17)	0.06	Ca2/Eu2—O7	2.963 (9)	0.07
<Ca2/La2—O>$_9$	2.656	∑2.06 (2.40)	<Ca2/Eu2—O>$_9$	2.636	∑1.85 (2.26)
Ca2/La2—O6	3.659 (16)		Ca2/Eu2—O2	3.396 (8)	
Ca3/La3—O3	2.331 (16)	0.38	Ca3/Eu3—O2	2.33 (1)	0.44
Ca3/La3—O2	2.370 (19)	0.34	Ca3/Eu3—O3	2.42 (1)	0.34
Ca3/La3—O1	2.474 (14)	0.26	Ca3/Eu3—O7	2.442 (7)	0.33
Ca3/La3—O1	2.474 (14)	0.26	Ca3/Eu3—O7	2.442 (7)	0.33
Ca3/La3—O4	2.565 (18)	0.20	Ca3/Eu3—O1	2.445 (7)	0.32
Ca3/La3—O4	2.565 (18)	0.20	Ca3/Eu3—O1	2.445 (7)	0.32
Ca3/La3—O5	2.596 (15)	0.19	Ca3/Eu3—O4	2.525 (8)	0.26
Ca3/La3—O5	2.596 (15)	0.19	Ca3/Eu3—O4	2.525 (8)	0.26
<Ca3/La3—O>$_8$	2.496	∑2.03 (2.04)	<Ca3/Eu3—O>$_8$	2.448	∑2.543 (2.59)
Ca3/La3—O4x2	3.786 (16)		Ca3/Eu3—O5x2	3.673 (8)	
	$Sr_3Bi_2(BO_3)_4$			$Sr_3Eu_2(BO_3)_4$	
Sr1/Bi1—O5	2.478 (18)	0.37	Sr1/Eu1—O3	2.271 (13)	0.64
Sr1/Bi1—O6	2.503 (16)	0.35	Sr1/Eu1—O5	2.395 (15)	0.46
Sr1/Bi1—O3	2.517 (16)	0.33	Sr1/Eu1—O7	2.441 (15)	0.40
Sr1/Bi1—O6	2.559 (16)	0.30	Sr1/Eu1—O6	2.520 (16)	0.32
Sr1/Bi1—O4	2.59 (3)	0.27	Sr1/Eu1—O7	2.5840 (15)	0.27
Sr1/Bi1—O1	2.710 (13)	0.20	Sr1/Eu1—O1	2.666 (15)	0.22
Sr1/Bi1—O3	2.720 (17)	0.19	Sr1/Eu1—O3	2.846 (14)	0.13
<Sr1/Bi1—O>$_7$	2.582	∑2.02 (2.21)	<Sr1/Eu1—O>$_7$	2.532	∑2.43 (2.34)
Sr1/Bi1—O4	3.03 (3)	0.08	Sr1/Eu1—O5	2.882 (15)	0.12
<Sr1/Bi1—O>$_8$	2.638	∑2.10 (2.21)	<Sr1/Eu1—O>$_8$	2.576	∑2.57 (2.34)
Sr1/Bi1—O3	3.580 (17)		Sr1/Eu1—O7	3.530 (16)	
Sr2/Bi2—O3	2.444 (16)	0.40	Sr2/Eu2—O6	2.383 (14)	0.47
Sr2/Bi2—O5	2.45 (2)	0.40	Sr2/Eu2—O7	2.421 (15)	0.42
Sr2/Bi2—O7	2.567 (16)	0.29	Sr2/Eu2—O6	2.435 (16)	0.41
Sr2/Bi2—O5	2.58 (3)	0.28	Sr2/Eu2—O2	2.495 (10)	0.35
Sr2/Bi2—O2	2.660 (14)	0.22	Sr2/Eu2—O4	2.540 (11)	0.31
Sr2/Bi2—O1	2.783 (14)	0.16	Sr2/Eu2—O1	2.668 (15)	0.22
Sr2/Bi2—O1	2.877 (14)	0.12	Sr2/Eu2—O1	2.819 (15)	0.14
<Sr2/Bi2—O>$_7$	2.660	∑1.99 (2.39)	<Sr2/Eu2—O>$_7$	2.537	∑2.32 (2.34)
Sr2/Bi2—O4	2.92 (3)	0.11	Sr2/Eu2—O5	2.985 (15)	0.09
<Sr2/Bi2—O>$_8$	2.638	∑2.10	<Sr2/Eu2—O>$_8$	2.593	∑2.41

		(2.21)			(2.34)
Sr2/Bi2—O2	3.204 (18)	0.05	Sr2/Eu2—O7	3.141 (12)	0.06
<Sr2/Bi2—O>$_9$	2.720	∑2.04 (2.39)	<Sr2/Eu2—O>$_9$	2.654	∑2.47 (2.34)
Sr2/Bi2—O6	3.431 (18)		Sr2/Eu2—O5	3.432 (16)	
Sr3/Bi3—O7	2.41 (3)	0.43	Sr3/Eu3—O3	2.18 (2)	0.79
Sr3/Bi3—O2	2.462 (18)	0.37	Sr3/Eu3—O3	2.429 (15)	0.40
Sr3/Bi3—O4	2.518 (17)	0.32	Sr3/Eu3—O3	2.429 (15)	0.40
Sr3/Bi3—O4	2.518 (17)	0.32	Sr3/Eu3—O1	2.457 (15)	0.37
Sr3/Bi3—O6	2.544 (17)	0.30	Sr3/Eu3—O1	2.457 (15)	0.37
Sr3/Bi3—O6	2.544 (17)	0.30	Sr3/Eu3—O2	2.458 (15)	0.37
Sr3/Bi3—O1	2.567 (14)	0.28	Sr3/Eu3—O5	2.521 (14)	0.31
Sr3/Bi3—O1	2.567 (14)	0.28	Sr3/Eu3—O5	2.521 (14)	0.31
<Sr3/Bi3—O>$_8$	2.509	∑2.59 (2.82)	<Sr3/Eu3—O>$_8$	2.431	∑3.33 (2.63)
Sr3/Bi3—O6x2	3.796 (16)		Sr3/Eu3—O6x2	3.667 (16)	
	$Sr_3Ho_2(BO_3)_4$			$Sr_3Er_2(BO_3)_4$	
Sr1/Ho1—O3	2.44 (2)	0.38	Sr1/Er1—O3	2.419 (14)	0.40
Sr1/Ho1—O3	2.44 (2)	0.38	Sr1/Er1—O3	2.452 (14)	0.37
Sr1/Ho1—O5	2.480(19)	0.34	Sr1/Er1—O7	2.455 (13)	0.36
Sr1/Ho1—O7	2.499 (17)	0.33	Sr1/Er1—O6	2.481 (12)	0.34
Sr1/Ho1—O6	2.511 (19)	0.32	Sr1/Er1—O5	2.514 (15)	0.31
Sr1/Ho1—O7	2.650 (17)	0.22	Sr1/Er1—O7	2.663 (13)	0.21
Sr1/Ho1—O1	2.682 (13)	0.20	Sr1/Er1—O1	2.683 (9)	0.20
<Sr1/Ho1—O>$_7$	2.529	∑2.17 (2.35)	<Sr1/Er1—O>$_7$	2.523	∑2.19 (2.33)
Sr1/Ho1—O5	2.87 (3)	0.12	Sr1/Er1—O5	2.909 (15)	0.11
<Sr1/Ho1—O>$_8$	2.571	∑2.29 (2.35)	<Sr1/Er1—O>$_8$	2.572	∑2.30 (2.33)
Sr1/Ho1—O7	3.594 (17)		Sr1/Er1—O7	3.579(14)	
Sr2/Ho2—O7	2.416 (18)	0.41	Sr2/Er2—O6	2.413(12)	0.41
Sr2/Ho2—O6	2.418 (19)	0.41	Sr2/Er2—O7	2.417 (13)	0.41
Sr2/Ho2—O4	2.463 (11)	0.36	Sr2/Er2—O4	2.463 (7)	0.36
Sr2/Ho2—O6	2.48 (3)	0.35	Sr2/Er2—O6	2.495 (14)	0.33
Sr2/Ho2—O2	2.537 (10)	0.30	Sr2/Er2—O2	2.540 (8)	0.29
Sr2/Ho2—O1	2.673 (13)	0.21	Sr2/Er2—O1	2.649 (9)	0.22
Sr2/Ho2—O1	2.819 (12)	0.14	Sr2/Er2—O1	2.814 (9)	0.14
<Sr2/Ho2—O>$_7$	2.544	∑2.18 (2.31)	<Sr2/Er2—O>$_7$	2.541	∑2.15 (2.31)
Sr2/Ho2—O5	3.07 (3)	0.07	Sr2/Er2—O5	3.009 (15)	0.08
<Sr2/Ho2—O>$_8$	2.609	∑2.24 (2.31)	<Sr2/Er2—O>$_8$	2.600	∑2.24 (2.31)
Sr2/Ho2—O2	3.161 (12)	0.06	Sr2/Er2—O2	3.159 (10)	0.05
<Sr2/Ho2—O>$_9$	2.695	∑2.31 (2.31)	<Sr2/Er2—O>$_9$	2.662	∑2.29 (2.31)
Sr2/Ho2—O3	3.333 (18)		Sr2/Er2—O5	3.793(12)	
Sr3/Ho3—O5	2.42 (2)	0.37	Sr3/Er3—O3	2.377 (12)	0.41
Sr3/Ho3—O5	2.42 (2)	0.37	Sr3/Er3—O5	2.384 (12)	0.40
Sr3/Ho3—O2	2.428 (15)	0.37	Sr3/Er3—O5	2.384 (12)	0.40
Sr3/Ho3—O2	2.434 (17)	0.36	Sr3/Er3—O4	2.385 (15)	0.40
Sr3/Ho3—O1	2.485 (12)	0.31	Sr3/Er3—O1	2.482 (8)	0.31

Sr3/Ho3—O1	2.485 (12)	0.31	Sr3/Er3—O1	2.482 (8)	0.31
Sr3/Ho3—O3	2.598 (18)	0.23	Sr3/Er3—O3	2.541 (15)	0.26
Sr3/Ho3—O3	2.598 (18)	0.23	Sr3/Er3—O3	2.541 (15)	0.26
<Sr3/Ho3—O>$_8$	2.483	∑2.56 (2.68)	<Sr3/Er3—O>$_8$	2.447	∑2.73 (2.70)
Sr3/Ho3—O6x2	3.749 (19)		Sr3/Er3—O6x2	3.770 (12)	
	$Ba_3Pr_2(BO_3)_4$			$Ba_3Eu_2(BO_3)_4$	
Ba1/Pr1—O7	2.586 (87)	0.39	Ba1/Eu1—O4	2.565 (14)	0.39
Ba1/Pr1—O6	2.594 (98)	0.38	Ba1/Eu1—O4	2.573 (14)	0.38
Ba1/Pr1—O4	2.596 (86)	0.38	Ba1/Eu1—O1	2.585 (15)	0.37
Ba1/Pr1—O4	2.643 (1)	0.34	Ba1/Eu1—O2	2.591 (15)	0.36
Ba1/Pr1—O5	2.722 (63)	0.27	Ba1/Eu1—O3	2.690 (14)	0.28
Ba1/Pr1—O6	2.793 (49)	0.22	Ba1/Eu1—O1	2.769 (14)	0.22
Ba1/Pr1—O1	2.804 (95)	0.22	Ba1/Eu1—O6	2.800 (12)	0.21
<Ba1/Pr1—O>$_7$	2.677	∑2.20 (2.33)	<Ba1/Eu1—O>$_7$	2.653	∑2.20 (2.35)
Ba1/Pr1—O5	3.020 (56)	0.12	Ba1/Eu1—O3	3.022 (14)	0.11
<Ba1/Pr1—O>$_8$	2.720	∑2.32 (2.33)	<Ba1/Eu1—O>$_8$	2.699	∑2.32 (2.35)
Ba1/Pr1—O6	3.688 (27)		Ba1/Eu1—O1	3.703(15)	
Ba2/Pr2—O7	2.571 (76)	0.41	Ba2/Eu2—O4	2.540 (15)	0.41
Ba2/Pr2—O3	2.592 (10)	0.38	Ba2/Eu2—O4	2.549 (14)	0.40
Ba2/Pr2—O6	2.600 (35)	0.38	Ba2/Eu2—O1	2.580 (16)	0.36
Ba2/Pr2—O7	2.645 (82)	0.33	Ba2/Eu2—O2	2.613 (11)	0.33
Ba2/Pr2—O2	2.762 (98)	0.24	Ba2/Eu2—O3	2.690 (11)	0.27
Ba2/Pr2—O1	2.825 (77)	0.20	Ba2/Eu2—O1	2.768 (12)	0.22
Ba2/Pr2—O1	3.010 (18)	0.12	Ba2/Eu2—O6	2.987 (11)	0.12
<Ba2/Pr2—O>$_7$	2.715	∑2.07 (2.33)	<Ba2/Eu2—O>$_7$	2.623	∑2.12 (2.39)
Ba2/Pr2—O5	3.039 (58)	0.11	Ba2/Eu2—O3	3.042 (14)	0.10
<Ba2/Pr2—O>$_8$	2.756	∑2.19 (2.33)	<Ba2/Eu2—O>$_8$	2.675	∑2.22 (2.39)
Ba2/Pr2—O2	3.246 (30)	0.07	Ba2/Eu2—O1	3.284 (13)	0.05
<Ba2/Pr2—O>$_9$	2.810	∑2.25 (2.33)	<Ba2/Eu2—O>$_9$	2.683	∑2.27 (2.39)
Ba2/Pr2—O6	3.764 (88)		Ba2/Eu2—O4	3.381 (15)	
Ba3/Pr3—O3	2.495 (52)	0.43	Ba3/Eu3—O5	2.401 (19)	0.55
Ba3/Pr3—O3	2.495 (52)	0.43	Ba3/Eu3—O3	2.453 (14)	0.48
Ba3/Pr3—O5	2.550 (10)	0.37	Ba3/Eu3—O3	2.453 (14)	0.48
Ba3/Pr3—O5	2.550 (10)	0.37	Ba3/Eu3—O7	2.467 (18)	0.46
Ba3/Pr3—O1	2.570 (89)	0.35	Ba3/Eu3—O6	2.535 (11)	0.38
Ba3/Pr3—O1	2.570 (89)	0.35	Ba3/Eu3—O6	2.535 (11)	0.38
Ba3/Pr3—O4	2.604 (47)	0.32	Ba3/Eu3—O4	2.699 (15)	0.25
Ba3/Pr3—O4	2.604 (47)	0.32	Ba3/Eu3—O4	2.699 (15)	0.25
<Ba3/Pr3—O>$_8$	2.564	∑2.96 (2.67)	<Ba3/Eu3—O>$_8$	2.530	∑3.21 (2.52)
Ba3/Pr3—O4x2	3.942 (75)		Ba3/Eu3—O4x2	3.900 (15)	
Ba1/Y1—O7	2.491(12)	0.49			
Ba1/Y1—O7	2.577(11)	0.39			
Ba1/Y1—O5	2.662(10)	0.31			

Ba1/Y1—O4	2.685(9)	0.29
Ba1/Y1—O6	2.718(11)	0.26
Ba1/Y1—O6	2.778(11)	0.22
Ba1/Y1—O1	2.864(7)	0.18
$<Ba1/Y1—O>_7$	2.682	∑2.11 (2.23)
Ba1/Y1—O4	2.934(9)	0.15
$<Ba1/Y1—O>_8$	2.714	∑2.29 (2.23)
Ba1/Y1—O6	3.643 (11)	
Ba2/Y2—O6	2.369(11)	0.59
Ba2/Y2—O5	2.493(10)	0.43
Ba2/Y2—O5	2.574(11)	0.34
Ba2/Y2—O3	2.615(6)	0.31
Ba2/Y2—O2	2.646(6)	0.28
Ba2/Y2—O1	2.768(7)	0.20
Ba2/Y2—O1	2.947(7)	0.12
$<Ba2/Y2—O>_7$	2.631	∑2.27 (2.41)
Ba2/Y2—O4	3.128(9)	0.08
$<Ba2/Y2—O>_8$	2.693	∑2.35 (2.41)
Ba2/Y2—O7	3.283 (17)	0.05
$<Ba2/Y2—O>_9$	2.758	∑2.40 (2.41)
Ba2/Y2—O2	3.368 (8)	
Ba3/Y3—O3	2.347(11)	0.50
Ba3/Y3—O4	2.379(8)	0.46
Ba3/Y3—O4	2.379(8)	0.46
Ba3/Y3—O2	2.455(10)	0.37
Ba3/Y3—O1	2.554(6)	0.29
Ba3/Y3—O1	2.554(6)	0.29
Ba3/Y3—O7	2.849(17)	0.13
Ba3/Y3—O7	2.849(17)	0.13
$<Ba3/Y3—O>_8$	2.547	∑2.63 (2.72)
Ba3/Y3—O5	3.772 (11)	